
This item was submitted to [Loughborough's Research Repository](#) by the author.
Items in Figshare are protected by copyright, with all rights reserved, unless otherwise indicated.

Simulating, fabricating and characterising photoconductive microwave switches for RF applications

PLEASE CITE THE PUBLISHED VERSION

PUBLISHER

© Emma Kristina Kowalczyk

LICENCE

CC BY-NC-ND 4.0

REPOSITORY RECORD

Kowalczyk, Emma K.. 2019. "Simulating, Fabricating and Characterising Photoconductive Microwave Switches for RF Applications". figshare. <https://hdl.handle.net/2134/14968>.

This item was submitted to Loughborough University as a PhD thesis by the author and is made available in the Institutional Repository (<https://dspace.lboro.ac.uk/>) under the following Creative Commons Licence conditions.



For the full text of this licence, please go to:
<http://creativecommons.org/licenses/by-nc-nd/2.5/>

Simulating, Fabricating and Characterising Photoconductive Microwave Switches for RF Applications

By

Emma Kristina Kowalczuk, MEng.

Doctoral Thesis

Submitted in partial fulfilment of the requirements
for the award of
Doctor of Philosophy of Loughborough University
April 2014

© By Emma Kristina Kowalczuk 2014

Dedicated to the friendship and memory of my fellow doctoral candidate

Ajit Yadav

(1983-2014)

Abstract

Photoconductive microwave switches can be used in place of traditional microwave switches to reconfigure antennas and RF circuits. The switch, which consists of a silicon die placed over a gap in transmission line, is controlled by illumination via a fibre optic cable. Hence there is no requirement to design electrical biasing lines which may affect RF performance.

This benefit is the main motivation behind further developing and understanding the photoconductive switch. The second motivation is the growing demand for reconfigurable antennas which necessitate certain switching requirements; one specific area of interest is in cognitive radio applications. However, in order to use such a switch in RF circuitry, the photoconductive nature of the switch must be understood. This is addressed in this thesis presenting and applying analytical equations which dictate the material properties in photoconductive silicon.

These equations are then used to generate a 3D EM simulation model to investigate transmission loss in the photoconductive switch. The concept of signal planarity is investigated so as to give some insight into the best way to package the switch. In order to potentially reduce loss and facilitate a packaged device, the fabrication of the switch is investigated. Namely, the treatment of the silicon and the addition of contacts on the silicon are discussed as possible methods to improve switch performance.

Lastly, linearity, power handling and switching times are presented for the photoconductive switch. This characterisation is important with regards to understanding which types of application the switch can be used in. In particular the single tone and two tone linearity of the switch is measured – these values have not previously been reported for this type of photoconductive switch. The results are encouraging and support further development of the switch into a packaged product to be used in reconfigurable antennas and circuitry.

Acknowledgements

Firstly, this dissertation would not have been possible without the help and guidance from my supervisors Chinthana Panagamuwa and Rob Seager. At every stage they have helped me formulate ideas and taught me such a wide range of skills. Their knowledge has been invaluable. Moreover, our discussions have not only been insightful but also enjoyable – thank you sincerely.

I would like to acknowledge the Electronic, Electrical and Systems Engineering School for providing the funding for me to complete my studies. I am particularly grateful to the members of Loughborough WiCR and CMCR Groups past and present – especially Chinwe, Will, Ajit, Nerijus, Norun, Seun, Shiyu and Alford. The encouragement they have given and memories we've shared over the past years have made my time at Loughborough an unforgettable one.

I would also like to express my gratitude to the following: Piotr Kaminski and Kevin Bass (CREST), Maria Mirgizudoudi and Andrew Sandaver (Wolfson School, Loughborough University), Roger Tomlinson and “Petes” (EESE Loughborough University) and Fiona McEwan (Glasgow University) who all spared time and resource to help me during the fabrication stages. Dr. Chen (Leeds University) also deserves my thanks for his contribution on contact fabrication. I would also like to acknowledge Dr. Budimir (University of Westminster) and Emily Smith (Nottingham University) for facilitating measurements.

I would like to thank my parents and brother for their encouragement on this journey. You have kept my spirits high and helped me keep my goal to finish in sight.

Above all, I thank my partner Mark who has been a pillar of support throughout the duration of my Post-Graduate studies. His patience knows no limits, especially during the write-up stage! His love, understanding and reassurance have given me the confidence to achieve this and much more - I cannot thank him enough.

List of Publications

Journal Publications:

In preparation

E. K. Kowalczyk, C. J. Panagamuwa, R. D. Seager, "Intermodulation Distortion in a Photoconductive Microwave Switch," Unpublished journal

Conference Publications:

E. K. Kowalczyk, C. J. Panagamuwa, R. D. Seager, and J. C. Vardaxoglou. "Characterising the linearity of an optically controlled photoconductive microwave switch." IEEE Loughborough Antennas and Propagation Conference (LAPC), 2010, pp. 597-600, 2010.

E. K. Kowalczyk, R. D. Seager, C. J. Panagamuwa, K. Bass and J. C. Vardaxoglou, "Optimising the performance of an optically controlled photoconductive microwave switch," IEEE Loughborough Antennas and Propagation Conference (LAPC), 2012

E. K. Kowalczyk, C. J. Panagamuwa and R. D. Seager, "Design and operation influences regarding rise and fall time of a photoconductive microwave switch," IEEE Loughborough Antennas and Propagation Conference (LAPC), pp. 149-154, 2013.

Table of Contents

ABSTRACT	I
ACKNOWLEDGEMENTS	II
LIST OF PUBLICATIONS	III
TABLE OF CONTENTS	IV
LIST OF FIGURES	X
GLOSSARY OF ACRONYMS AND SYMBOLS.....	XIX
1 MICROWAVE SWITCHES AND THEIR APPLICATIONS.....	1-1
1.1 Introduction.....	1-1
1.2 Photoconductive Switches	1-2
1.3 Desirable qualities in a microwave switch	1-5
1.4 Motivation.....	1-6
1.4.1 Applications.....	1-7
1.4.2 Types of Microwave switch.....	1-10
1.4.3 Why is Packaging Important?	1-13
1.5 Primary Contributions.....	1-15
1.6 Thesis Structure	1-15
1.7 References	1-17

2	SILICON BEHAVIOUR.....	2-1
2.1	Introduction.....	2-1
2.2	Semiconductor Theory	2-2
2.2.1	Bandgap.....	2-2
2.2.2	Direct or Indirect	2-4
2.2.3	Doping.....	2-5
2.2.4	Mobility and Collision Time	2-6
2.3	Carrier Lifetime	2-8
2.3.1	Shockley Read Hall (SRH) Recombination	2-8
2.3.2	Radiative Recombination	2-9
2.3.3	Auger Recombination	2-9
2.4	Modelling Silicon	2-10
2.4.1	Number of Carriers	2-10
2.4.2	Distribution of Carriers	2-11
2.5	Photoconduction and material properties.....	2-12
2.5.1	Photoconductivity.....	2-13
2.5.2	Factoring in Auger Recombination	2-14
2.5.3	Dielectric Permittivity	2-15
2.5.4	Loss Tangent	2-15
2.6	Photoconductive Material Choice	2-16
2.6.1	Elemental Semiconductors: Si.....	2-17
2.6.2	Group III-V compounds: GaAs and InP	2-18
2.6.3	Group II-VI compounds: CdS and CdSe	2-19
2.6.4	Group II compounds: 6H SiC.....	2-19
2.6.5	Composite Polymers.....	2-20
2.7	Silicon Processing	2-20
2.7.1	Silicon Growth method: Czochralski (CZ) vs. Float-Zone (FZ).....	2-21
2.7.2	Resistivity and Doping	2-22
2.7.3	Thickness of wafer	2-22
2.7.4	Processing the Ingot Polished Surfaces.....	2-23
2.8	Silicon Properties	2-23
2.8.1	Properties and fabrication of the Silicon in this thesis	2-23

2.9	Conductivity Profile (with Auger Recombination)	2-25
2.10	Optimum Wavelength	2-28
2.10.1	Absorption depth and diffusion constant	2-28
2.10.2	Beam Profile	2-33
2.11	Conclusions	2-34
2.12	References	2-35
3	NUMERICAL MODELLING AND PACKAGING DESIGN	3-1
3.1	Introduction	3-1
3.1.1	Electromagnetic Simulation of Silicon	3-1
3.1.2	Switch Topology	3-2
3.2	Transmission Line Topology	3-4
3.2.1	Transmission Line Parameter Simulation	3-5
3.2.2	Results	3-6
3.3	Silicon Conductivity Simulations	3-9
3.3.1	Measurements compared to an Ideal Switch	3-9
3.3.2	Equivalent one layer model	3-14
3.3.3	Six layer model	3-16
3.3.4	Effect of radiant flux on profile	3-21
3.3.5	Silicon Model Limitations	3-24
3.4	Geometry of the Switch and Transmission Line Simulations	3-25
3.4.1	Passivation layer model	3-25
3.4.2	Effects of connector	3-27
3.5	Maintaining Signal Planarity	3-31
3.5.1	Wire bonding	3-32
3.5.2	Flip Chip	3-32
3.5.3	Planarity Study Simulations	3-33
3.5.4	Planarity Study Results	3-35
3.6	Optical Feed Techniques	3-37
3.6.1	Literature Review on Optical Feed techniques	3-37
3.6.2	Through the Substrate Feed Technique	3-41
3.6.3	Fabrication	3-47

3.6.4	Discussion.....	3-50
3.7	Conclusions	3-52
3.8	References	3-53
4	FABRICATION TECHNIQUES FOR PHOTOCONDUCTIVE SWITCHES USING SILICON	4-1
4.1	Introduction.....	4-1
4.2	Overview on Silicon Processing Techniques	4-2
4.2.1	Anti-Reflection Coating (ARC)	4-2
4.2.2	Passivation.....	4-4
4.2.1	Texturing	4-6
4.2.2	Processing techniques for enhancing PCS	4-7
4.3	Variation 1: Passivation and Texturing	4-8
4.3.1	Fabrication	4-8
4.3.2	Using Carrier Lifetime as a Measure of Quality of Passivation	4-11
4.3.3	Results and Discussion	4-14
4.4	Overview on Contact Type.....	4-18
4.4.1	Metal-Semiconductor Junctions	4-18
4.4.2	Ohmic Contacts	4-19
4.4.3	Schottky contact	4-20
4.4.4	Capacitive Contacts	4-20
4.5	Variation 2: Gold Contact Capacitive Switch	4-21
4.5.1	Passivation Analysis	4-21
4.5.2	Fabrication Process	4-23
4.5.3	Results	4-26
4.6	Connection Methods	4-28
4.6.1	Conductive Epoxy vs. Solder.....	4-28
4.6.2	Epoxy Method – Contact Position	4-29
4.6.3	Surface Mounting using Solder.....	4-32
4.6.4	Wire bonding.....	4-38
4.7	Conclusions	4-40

4.8	References	4-41
5	SWITCH CHARACTERISATION.....	5-1
5.1	Introduction.....	5-1
5.2	Linearity	5-2
5.2.1	Single Tone Linearity	5-3
5.2.2	Two-Tone Linearity	5-3
5.3	Switch Linearity and Power Handling Review	5-5
5.4	Single tone linearity test setup.....	5-8
5.4.1	High Directivity Coupler	5-9
5.4.2	Wilkinson Combiner Amplifier.....	5-12
5.4.3	Low Pass Filter	5-14
5.4.4	Conditions and Limitations.....	5-15
5.5	Single Tone Linearity Measurements and Discussion	5-17
5.5.1	Isolation and Insertion Loss	5-17
5.5.2	The SOI / TOI Linearity.....	5-19
5.6	Two Tone Third Order Intermodulation Product.....	5-22
5.6.1	Two Tone Setup	5-22
5.6.2	Two tone Results	5-24
5.6.3	Discussion on two-tone Intermodulation.....	5-27
5.6.4	Two Tone Linearity using separate RF sources	5-29
5.7	1dB Compression Point	5-31
5.7.1	Experiment Setup for 1dB Testing.....	5-32
5.7.2	1dB compression Results	5-33
5.8	Absolute Power Handling	5-34
5.9	Switch Rise and Fall Time.....	5-35
5.9.1	Review of Switching Times.....	5-35
5.9.2	Influences of switching time of a photoconductive switch	5-37
5.9.3	Experimental Switch Time Setup.....	5-38
5.9.4	S-Parameter Performance.....	5-40
5.10	Switching Time Results	5-42

5.10.1	Switch dimensions and radiant flux	5-43
5.10.2	Passivation	5-44
5.10.3	ON-OFF State Voltage Difference.....	5-46
5.10.4	Discussion on switching times.....	5-48
5.11	Conclusions	5-49
5.12	References	5-50
6	CONCLUSIONS AND FUTURE WORK.....	6-1
6.1	Auger term considered in generating conductivity profile	6-2
6.2	Simulating packaging strategy based on conductivity profile	6-2
6.3	Analysing passivation and interconnect methods	6-4
6.4	Linearity and switching time characterisation.....	6-5
6.5	Future Work	6-6
6.5.1	Transparent Materials and Silicon Processing Techniques	6-6
6.5.2	Silicon Quality and Die Size.....	6-6
6.5.3	Ohmic Contacts	6-7
6.5.4	Wire Bonding	6-7
6.5.5	Characterisation.....	6-7

List of Figures

Figure 1.1: Optically controlled attenuator designed on silicon substrate, Flemish <i>et al.</i> [3]	1-3
Figure 1.2: Optically controlled microwave switch incorporating silicon die [7].....	1-4
Figure 1.3: Silicon switches incorporated into a dipole to enable frequency and beam reconfiguration from Panagaumwa <i>et al.</i> [13].....	1-8
Figure 1.4: Top view of the graphene NEMS switch configuration, from Hindle [41]....	1-13
Figure 2.1: Simplified energy band diagram for a metal, insulator and semiconductor [2]	2-3
Figure 2.2: Energy vs. momentum for a semiconductor with an indirect band gap	2-5
Figure 2.3: Atomic structure of silicon	2-17
Figure 2.4: Fabrication process of silicon wafers	2-21
Figure 2.5: Conductivity profile for 10mW, 50mW and 200mW of radiant flux at 980nm. The graph demonstrates the effect the Auger term has on the conductivity profile	2-26
Figure 2.6: Conductivity profile for 10mW of radiant flux at 980nm. The graph demonstrates that the effect the Auger term is only small with relation to the conductivity profile at this radiant flux.....	2-26
Figure 2.7: Real part of the permittivity for Phosphorous doped silicon - carrier density is calculated including the Auger Term	2-27
Figure 2.8: Imaginary part of the permittivity for Phosphorous doped silicon - carrier density is calculated including the Auger Term	2-28
Figure 2.9: Measured data of photon absorption depth in silicon [34].	2-29
Figure 2.10: Conductivity in silicon material at 10mW of radiant flux for varying depths into the silicon.....	2-30
Figure 2.11: Conductivity in silicon material at 10mW of radiant flux at a wavelength of 980nm	2-31
Figure 2.12: Average conductivity in silicon material for depths of 0.3 and 0.53mm at 10mW of radiant flux at a wavelength of 980nm	2-32
Figure 2.13: Beam profile for the fibre-optic coupled laser source which illuminates the silicon in this study	2-33

Figure 3.1: Three switch topologies, (1) chamfered, (2) notch, and (3) interleaved designs investigated by Chauraya <i>et al.</i> [8].....	3-3
Figure 3.2: Basic simulation model of an ideal switch placed between two transmission lines.....	3-6
Figure 3.3: Switch variations and their respective insertion loss and isolation values at 2GHz; markers represent different line and gap widths, particular values of interest are circled as having optimum S21 in ON and OFF states. Details are viewable in Table 3.1.	3-7
Figure 3.4: Basic simulation model of an ideal switch placed between two transmission lines.....	3-10
Figure 3.5: Simulation model of silicon including silver loaded epoxy on a Rogers 3003 substrate with dimensions	3-10
Figure 3.6: Ideal switch simulation results in terms of transmission alongside measured S21 results for various values of radiant flux	3-12
Figure 3.7: Transmission results in the OFF state, comparing simulated ideal switch case and comparing to corresponding measured result for the same topology	3-13
Figure 3.8: Ideal switch simulation results in terms of S11 alongside measured S11 results for 0mW of radiant flux (OFF state)	3-13
Figure 3.9: S-parameter results for an equivalent one layer conductivity simulation model in EMPIRE - based on the average conductivity in the silicon. This is compared to measured results for a 10mW radiant flux.	3-15
Figure 3.10: S-parameter results in OFF state with an OFF state conductivity value of 0.017S/m.....	3-15
Figure 3.11: Layered silicon model including silver epoxy on a Rogers 3003 substrate with dimensions – illumination is from above, applying 10mW of radiant flux.....	3-16
Figure 3.12: CAD model in CST 2013, 6 layer silicon attached over a 0.3mm gap in transmission line (excited by waveguide port: Quasi-TEM mode).....	3-18
Figure 3.13: S21 results comparing 6 layer photoconductive silicon model in EMPIRE (FDTD) and CST (FIT) with measured data under 10mW of radiant flux	3-19
Figure 3.14: S11 results comparing 6 layer photoconductive silicon model in EMPIRE (FDTD) and CST (FIT) with measured data under 10mW of radiant flux	3-20
Figure 3.15: S21 results comparing 6 layer photoconductive silicon model under 10mW, 50mW and 200mW of radiant flux.....	3-23

Figure 3.16: S11 results comparing 6 layer photoconductive silicon model under 10mW, 50mW and 200mW of radiant flux.....	3-24
Figure 3.17: S21 performance of the six layer silicon model with passivation later ...	3-26
Figure 3.18: S11 performance of the six layer silicon model with passivation layer ..	3-27
Figure 3.19: Full optically switched transmission line model in CST including 6 layer silicon, passivation layer and SMA connectors	3-28
Figure 3.20: S21 parameters relating to simulated results for an optically switched transmission line model in CST including six layer silicon, passivation layer and SMA connectors.....	3-29
Figure 3.21: S11 parameters relating to simulated results for an optically switched transmission line model in CST including six layer silicon, passivation layer and SMA connectors.....	3-29
Figure 3.22: S21 relating to simulated results for an optically switched transmission line model in CST including passivation layer and SMA connectors in the OFF state (0mW radiant flux)	3-30
Figure 3.23: S11 relating to simulated results for an optically switched transmission line model in CST including passivation layer and SMA connectors in the OFF state (0mW radiant flux)	3-31
Figure 3.24: Representative model of a wire bonds connecting to a photoconductive silicon die with fibre optic cable	3-32
Figure 3.25: Representative simulation model of a flip-chip method of packaging for a bare silicon die photoconductive switch with fibre optic cable (substrate is made transparent so as to see the optical fibre)	3-33
Figure 3.26: Layered silicon model including silver epoxy on a Rogers 3003 substrate with an Passivation (oxide) coating– illumination is from above (a) and below (b) – diagram is not to scale.....	3-34
Figure 3.27: S21 performance of optically controlled transmission line with silicon illuminated from above and below. Measured result corresponds to illumination from above.	3-35
Figure 3.28: S11 performance of optically controlled transmission line with silicon illuminated from above and below. Measured result corresponds to illumination from above.	3-36

Figure 3.29: Waveguide light delivery system for reconfigurable bowtie antenna [29]	3-38
Figure 3.30: (a) Front and (b) back views of antenna element integrated with the photoconductive attenuator [34]	3-40
Figure 3.31: CAD model of optically switched transmission line with an optical fibre providing illumination to the silicon from below	3-41
Figure 3.32: S21 performance of an optically controlled transmission line with varying diameter of fibre optic cable	3-43
Figure 3.33: S11 performance of the optically switched transmission line under different fibre optic cable diameters	3-43
Figure 3.34: Surface currents on the topside of the ground plane and metallisation at 2GHz. Plot (a) shows the switch without a fibre. Plot (b) shows a switch with fibre inserted through ground plane and substrate. There is a higher level of surface current in the case where a fibre is inserted – noticeable on the SMA connectors and towards the corners of the board.	3-45
Figure 3.35: E-Field distribution on the underside of the switch at 10GHz. Plot (a) shows the switch without a fibre. Plot (b) shows a switch with fibre inserted through ground plane and substrate. There is a higher level of electric field coupling to the edge of the board in the case where a fibre is inserted.	3-46
Figure 3.36: E-Field distribution for a cross section of the switch with (a) and without (b) fibre at 2GHz with the same scaling as in Figure 3.35	3-47
Figure 3.37: Transmission line topology including a hole in the substrate, copper has been given a slight transparency so as to demonstrate that the hole is in the ground plane and substrate only.	3-48
Figure 3.38: Transmission line dimensions including hole in substrate, the diagram is not to scale	3-48
Figure 3.39: Measured S21 result of an optically switched transmission line controlled from above and below under 200mW of radiant flux	3-49
Figure 3.40: Measured S11 result of an optically switched transmission line controlled from above and below under 200mW of radiant flux	3-50
Figure 4.1: Process used to fabricate photconductive switch, process may include growing anti-reflective coating (ARC)	4-2
Figure 4.2: Real (red) and imaginary (blue dashed) components of the refractive index for silicon at different wavelengths (at 300 K) [3].	4-3

Figure 4.3: Reflection from surfaces can either be destructive (left) or constructive (right). All light is transmitted into the silicon when both reflected waves are 180° out of phase with each other, cancelling each other out.	4-4
Figure 4.4: There is more chance to absorb incident light if the surface is textured	4-6
Figure 4.5: Left Random outward textured silicon surface [11]. Right: Scanning electron microscope photograph of a textured silicon surface with inward pyramid structure [12].	4-7
Figure 4.6: Representative Scanning electron microscope (SEM) of silicon surface for a sample which has undergone texturisation at Loughborough University's Centre for Renewable Energy Systems Technology (CREST)	4-10
Figure 4.7: Reflectivity results for silicon wafers with different fabrication processes...	4-11
Figure 4.8: Screenshots taken from QSSP results for an untreated silicon wafer. Effective carrier lifetime is computed to response from an applied pulse	4-12
Figure 4.9: QSSP results for a passivated silicon wafer. Effective carrier lifetime is computed as 36.7us using the same applied pulse as in Figure 4.8.	4-13
Figure 4.10: Transmission results in the OFF state for silicon with differing fabrication processes.....	4-14
Figure 4.11: Transmission results in the ON state for silicon with differing fabrication processes.....	4-15
Figure 4.12: CAD model of PCS using EMIRE XCcel EM Simulation software to model a 2um coating applied to the silicon to represent a pyramid surface	4-16
Figure 4.13: Simulation result of a passivated silicon die on a transmission line, with and without a representative 'textured' air gap.....	4-17
Figure 4.14 a) Band structure and Fermi level of separate semiconductor and metal materials. b) Band structure and Fermi level of semiconductor and metal in contact...	4-18
Figure 4.15: Percentage of element atoms comprising the top most surface of the passivation layer for the phosphorous doped silicon. The orbitals of the atom are also listed.	4-22
Figure 4.16: Percentage of element atoms comprising the first 300nm from the surface for the phosphorous doped silicon.....	4-22

Figure 4.17: Reflectivity of the phosphorous doped silicon wafer which incorporates a passivation layer which acts as an ARC at $\sim 1000\text{nm}$	4-23
Figure 4.19: Fabrication steps to selectively etch away passivation layer and deposit gold contacts	4-24
Figure 4.20: Diced and un-diced silicon with gold strips deposited on top of the SiO_2 passivation layer	4-25
Figure 4.21: Transmission performance in the OFF state for gold deposited silicon attached via epoxy, size of silicon die $2\text{mm} \times 1\text{mm} \times 0.3\text{mm}$	4-26
Figure 4.22: Transmission performance in the ON state (200mW of radiant flux) for gold deposited silicon attached via epoxy, size of silicon die $2\text{mm} \times 1\text{mm} \times 0.3\text{mm}$...	4-27
Figure 4.23: Transmission performance in the ON state (200mW of radiant flux) for gold deposited silicon attached via epoxy, size of silicon die $2\text{mm} \times 1\text{mm} \times 0.3\text{mm}$...	4-27
Figure 4.24: ON state S21 transmission of a $2\text{mm} \times 1.5\text{mm} \times 0.3\text{mm}$ silicon die with gold contacts (0 minute etch) attached with silver epoxy. The die is attached with the gold on the bottom of the die and in direct contact with the copper transmission line and when the contact is on top of the die. Radiant flux applied is 200mW	4-30
Figure 4.25: ON state Reflection coefficient when a gold contact (0 minute etch) silicon die of dimension $2\text{mm} \times 1.5\text{mm} \times 0.3\text{mm}$ is attached using silver epoxy either with the contact on the top or bottom of the silicon die. Radiant flux applied is 200mW	4-30
Figure 4.26: OFF state transmission coefficient when a gold contact (0 minute etch) silicon die of dimension $2\text{mm} \times 1.5\text{mm} \times 0.3\text{mm}$ is attached using silver epoxy either with the contact on the top or bottom of the silicon die. Radiant flux applied is 0mW ..	4-31
Figure 4.27: Gold contact die soldered onto transmission line. Substrate is Taconic TLC-32, $\epsilon_r = 3.2$, height = 0.79mm. In this case, silicon die is ($2\text{mm} \times 3\text{mm} \times 0.3\text{mm}$)	4-32
Figure 4.28: S21 transmission for various epoxy and solder based switches, die length is 2mm (exposed silicon surface is 1mm). Radiant flux applied is 200mW.	4-34
Figure 4.29: S11 reflection for various epoxy and solder based switches, die length is 2mm (exposed silicon surface is 1mm). Radiant flux applied is 200mW	4-34

Figure 4.29: S-Parameter transmission results for soldered silicon die in ON state (200mW of radiant flux); comparing illumination from above and below die.....	4-35
Figure 4.30: S-parameter transmission results in OFF state for soldered silicon die; comparing an optical fibre fed from above and below the die	4-36
Figure 4.32: Soldering between silicon die and transmission line	4-37
Figure 4.33: Wire bonding to gold contact on silicon die on a recessed transmission line design	4-39
Figure 5.1: Intermodulation products generated when measuring two tone linearity using the Agilent vector signal analyser E4406A at the University of Westminster.	5-5
Figure 5.2: Measurement platform for single tone linearity measurements on a photoconductive switch	5-9
Figure 5.3: AWR Microwave Office design of a 2GHz coupler	5-10
Figure 5.4: Final design in EMPIRE XCcel of the 20dB directional coupler.....	5-11
Figure 5.5: Measured s-parameters for the directional coupler design	5-11
Figure 5.6 : Wilkinson Divider Theory.....	5-12
Figure 5.7: Fabricated Wilkinson divider/combiner including MMIC amplifier chips	5-13
Figure 5.8: Measured transmission performance of Wilkinson divider and amplifier chip.....	5-13
Figure 5.9: Cascaded low pass filter designed in Microwave Office.....	5-14
Figure 5.10: Layout of planar filter.....	5-15
Figure 5.11: Simulated and measured transmission response of the low pass filter	5-15
Figure 5.12: Switch topology on TLY-5 substrate (not to scale)	5-17
Figure 5.13: OFF state S-Parameter performance for TLY-5 substrate PCS	5-18
Figure 5.14: Various ON state S-Parameter performances for TLY-5 substrate PCS	5-18
Figure 5.15: Extrapolated second and third order intercept result for a single tone linearity measurement. Silicon topology type 1 under 200mW of radiant flux.	5-19
Figure 5.16: Extrapolated TOI values for differing illumination intensities (10, 30, 50 and 200mW of radiant flux)	5-20
Figure 5.17: Switch topology on R3003 Substrate (0.53mm thick). The end of the transmission lines has been slightly chamfered to facilitate signal coupling into the silicon die – these values have been measured after fabrication	5-21

Figure 5.18: Extrapolated second and third order intercept result for a single tone linearity measurement. Optimised switch topology under 200mW of radiant flux..	5-22
Figure 5.19 : Two-tone IM Distortion measurement platform	5-23
Figure 5.20: two-tone IM Distortion measurement setup in the process of capturing data. Equipment was setup to allow minimum noise floor	5-24
Figure 5.21: Two tone intermodulation results and fundamental input tone at 1.9995GHz	5-25
Figure 5.22: Extrapolated IP3 value from fundamental signal at 1.9995GHz and corresponding intermodulation distortion at 1.9985GHz	5-26
Figure 5.23: Third intermodulation products at 30, 50 and 200mW of radiant flux	5-26
Figure 5.24: Measurement platform for two tone linearity using two separate sources	5-30
Figure 5.25: Extrapolated IP3 value for an alternative experimental setup involving separate sources. The graph also displays the equation for the line of best fit for the fundamental and third order intermodulation products.	5-31
Figure 5.26: Measurement platform for 1dB compression and power handling test.....	5-32
Figure 5.27: Power handling up to 44dBm. Fundamental power deviating away from small signal	5-33
Figure 5.28: Power handling of the switch, visual results	5-35
Figure 5.29: Experimental setup for measuring the rise and fall time of the photoconductive switch	5-40
Figure 5.30: S-parameter performance of switch types A and B under 850nm LED illumination (10kHz pulse cycle)	5-41
Figure 5.31: S-parameter performance of switch types A and B under 0mW of radiant flux.....	5-41
Figure 5.32: ON-OFF amplitude for a 2GHz signal passing through silicon type A (0.27mm gap, radiant flux is 55mW).....	5-42
Figure 5.33: OFF-ON amplitude for a 2GHz signal passing through silicon type A (0.27mm gap, radiant flux of 55mW)	5-43
Figure 5.34: Rise and fall times for switches which have either a 0.27mm or 1mm gap. Two radiant flux values are investigated, 55mW and 80mW.....	5-44
Figure 5.35: Rise and fall times for switches incorporating silicon which has been passivated in different ways and under radiant flux of 80mW.	5-45

List of Tables

Table 1.1: Potential applications for the photoconductive switch and corresponding criteria for switch performance	1-9
Table 1.2: Different microwave switch types and their attributes.....	1-13
Table 2.1: Dopant types with associated mobility values from best fit data.....	2-7
Table 2.2: Parameters which affect photoconductivity	2-13
Table 2.3: Properties of different semiconductors [18]	2-18
Table 2.4: Phosphorous doped silicon properties used in this study as listed by manufacturer (note orientation relates to the crystal structure)	2-24
Table 2.5: Boron doped silicon properties used in this study as listed by manufacturer	2-24
Table 3.1: Optimisation parameters for the top 6 switch contenders at 2GHz.....	3-8
Table 3.2: Six layer values for conductivity and permittivity for 10mW of radiant flux (valid at 2GHz)	3-17
Table 3.3: Six layer values for imaginary permittivity for 10mW of radiant flux at 1, 2, 4, 8 and 10GHz	3-18
Table 3.4: Six layer conductivity and permittivity values for silicon under 200mW of radiant flux, for 2GHz input signal. Dispersion value is also presented at 10GHz for reference	3-21
Table 3.5: Six layer conductivity and permittivity values for silicon under 50mW of radiant flux, for 2GHz input signal. Dispersion value is also presented at 10GHz for reference	3-22
Table 4.1: Silicon properties for the three samples in this study	4-8
Table 5.1: Comparison of Heterostructure photoconductive switch and microwave switches used in reconfigurable applications	5-6
Table 5.2: Sources of error in measurement and steps taken to prevent their occurrence	5-16
Table 5.3: Typical linearity and power handling results for various microwave switches	5-27
Table 5.4: Comparison of switching times for various microwave switches	5-37
Table 5.5: Rising and falling times along with ON-OFF voltage values. Rising and falling speeds are presented by taking into account the voltage difference.....	5-47

Glossary of Acronyms and Symbols

Acronym	Term	Additional Comments
6H SiC	Silicon carbide	
ARC	Anti-Reflective Coating	
B	Boron	
CdS	Cadmium sulphide	
CdSe	Cadmium selenide	
CPW	Coplanar Waveguide	
CREST	Centre for Renewable Energy Systems and Technology	
CZ	Czochralski	Relates to manufacture technique for semiconductor wafer
FDTD	Finite difference Time Domain (Technique)	Numerical analysis technique for solving Maxwell's Equations to simulate Electromagnetic performance
FET	Field Effect Transistor	
FIT	Finite integration Technique	Numerical analysis technique for solving Maxwell's Equations to simulate Electromagnetic performance
FSS	Frequency Selective Surface	Possible application where reconfiguration is desirable
FZ	Float-Zone	Relates to manufacture technique for semiconductor wafer
GaAs	Gallium Arsenide	
GPS	Global Positioning System	
GPU	Graphical Processing Unit	
GSM	Global System for Mobile Communications	
HF	Hydrofluoric	
IC	Integrated Circuit	
InP	Indium Phosphide	

IP3	Third order Intermodulation Product	Extrapolated value of main tone signal and intermodulation products generated using a two-tone input
IPA	Isopropyl Alcohol	
LED	Light Emitting Diode	
MEMS	Microelectromechanical Systems	
MMIC	Integrated circuit	
PCB	Printed Circuit Board	
PCS	Photoconductive Switch	
PEC	Perfect Electric Conductor	
PECVD	Chemical vapour deposition process	
QSSP	Quasi Steady State Photoconductance	Method for analysing carrier lifetime in silicon by applying a long light pulse and evaluating the response time
SDA	Signal Network Analyser	
SEM	Scanning Electron Microscope	
Si	Silicon	
SOI	Second Order intercept	Extrapolated value of fundamental signal and second order harmonics
SRH	Shockley Read Hall	Relates to recombination due to traps in the semiconductor
TOI	Third Order Intercept	Extrapolated value of fundamental signal and third order harmonics
VNA	Vector Network Analyser	
WiMax	Worldwide Interoperability for Microwave Access	
WLAN	Wireless Local Area Networking	
XPS	X-ray photoelectron spectroscopy	Method for analysing the elemental composition of a structure

Symbols	Definition
α_{FIT}	Fitting parameter for mobility
α_c	Absorption coefficient
ϵ_0	Permittivity of free space
ϵ_r	Relative permittivity
ϵ_L	Dark state permittivity
λ_l	Wavelength of illumination source
$\mu_e \mu_h$	Mobility (electrons and holes)
$\mu_{min, max}$	Fitting constants for mobility
σ	Conductivity
τ_{aug}	Carrier lifetime - Auger
τ_{bulk}	Carrier lifetime - Bulk
τ_{eff}	Carrier lifetime - Effective
τ_{rad}	Carrier lifetime - Radiative
τ_{SRH}	Carrier lifetime – Shockley Read Hall
τ_{surf}	Carrier lifetime - Surface
$\tau_{e,h.}$	Collision time for electrons and holes
ω_p	Plasma Frequency
ω	RF signal angular frequency
φ	Radiant Flux
ϕ_B	Barrier Height
φ_m	Work function of metal
χ	Affinity
A	Area of Illumination
c	Speed of light
C_A	Auger coefficient
d	Thickness of semiconductor
E	Electric field
E_B	Band gap energy
$E_{C,V}$	Conduction and valence band energy
E_{photon}	Energy of a photon

h_c	Plank's constant 1.054×10^{-34}
J	Current
La	Diffusion Length
La_{aug}	Diffusion Length (Auger effect)
I	Transmitted light intensity
I_0	Incident light intensity
k_b	Boltzmann constant 1.38×10^{-23}
m_e	mass of the carriers generated
n	Concentration of carriers
N_{dope}	Doping concentration of a semiconductor sample
N_{ref}	Fitting constant for mobility
P	Power of illumination source
q	Electron charge 1.66×10^{-19}
R	Surface reflection
S	Spectral Efficiency
T_a	Temperature
$\tan\delta$	Loss tangent
v_d	Speed of carriers
v_s	Surface recombination velocity
y	Distance from illuminated surface into silicon

1 Microwave Switches and their Applications

1.1 Introduction

Microwave switches are components widely used in wireless communications systems to control the flow of RF signal in high frequency circuits. In order to select a microwave switch to use in an application, the important criteria in terms of performance must be understood and characterised.

There are a variety of commercially available microwave switches, each with their strengths and weaknesses for particular applications. However, at the centre of this research is the photoconductive microwave switch. Unlike other microwave switches, the photoconductive switch is optically controlled. This is an important benefit of this type of switch, as the integration of these switches into RF systems does not require the additional design of metallic biasing lines.

RF signal can couple to these metallic biasing lines and hence change the radiation pattern of the antenna in an unintended way. They can also be challenging to design when multiple switching elements are required, such as in a reconfigurable antenna array. Indeed, this is one of the primary motivations behind understanding, developing and characterising the photoconductive switch.

In particular, this technology can benefit reconfigurable antennas and circuits – however if this is to be the case the RF system designer must understand the potential conductivity, the most accurate way to simulate the switch and the

performance in terms of loss, linearity and switching time. The switch must also be packaged appropriately for easy integration with minimum degradation to overall system performance.

The chapter introduces the photoconductive switch and comments on alternative microwave switches. In order to understand the value of this switch, the main applications are presented. Focus is on the motivation and novel contributions within this work and finishes with a thesis outline.

1.2 Photoconductive Switches

Microwave switches are used in circuits in order to block or redirect RF signals. In the OFF state, there are two main methods that can be used to block or redirect signal. The first is absorption of the incoming RF signal, where the power is usually dissipated as heat. The second is reflection of the incoming RF signal. Ideally, in the ON state, the switch should transmit maximum power. However, in reality a combination of the above is true, as no microwave switch is ideal. The insertion loss is a measure of this. This is essentially transmission loss in the switch due to absorption or radiation of the signal and is an important figure of merit for microwave switches.

This thesis is concerned with reflective switches, as these can be used to reconfigure antennas. The absorbing switch would not be suitable for most reconfigurable antennas as it absorbs the incoming signal and hence the antenna cannot resonate. There are two main categories of photoconductive switch that reflect the incoming signal as opposed to absorbing it – illumination of a silicon substrate and illumination of a silicon die. Under the right circumstances, illumination of semiconductors increases conductivity within the body of the semiconductor which in turn changes the impedance of the switch, turning it ON and OFF. The theory behind this process is described in Chapter 2.

The first category of photoconductive switch involves designing the switch on a semiconductor substrate, first demonstrated by Auston *et al.* [28]. Auston designed a transmission line including a gap on a silicon substrate. To allow an RF signal to propagate the gap was illuminated with a 530 nm laser, allowing conductivity in the

upper silicon substrate. To open the switch a higher wavelength of light of 1060nm was used to increase the depth of conductivity in the silicon substrate. This results in a conductive path to the ground plane, and hence RF signal is reflected due to the short circuit created.

Since Auston, other examples based on silicon substrates have been investigated, such as those demonstrate by Flemish *et al.* [3]. A filter like design allows signal to propagate down a transmission line whilst the silicon is not illuminated, with an insertion loss of 2dB at 2GHz, Figure 1.1.

Under illumination from a 808nm LED a short is created through the silicon substrate to ground, and creates an isolation of 27dB at 2GHz. It is difficult to establish a globally accepted value for what a sufficient insertion loss or isolation, as these qualities are very much application specific. However, to give some context, commercial types of microwave switch, typically have insertion loss in the region of 0.3-1dB and isolation in the region of 17-30dB [4].

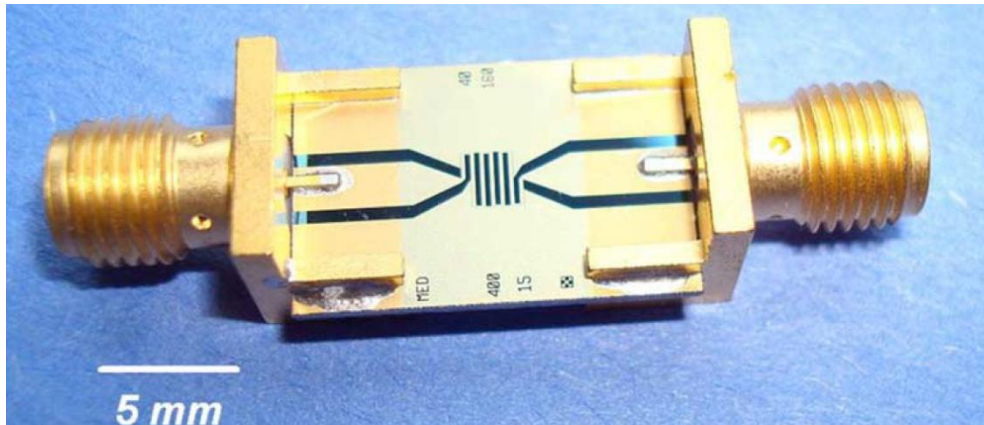


Figure 1.1: Optically controlled attenuator designed on silicon substrate, Flemish *et al.* [3]

Alternatively, it is possible to avoid having metal traces or elements all together if the antenna pattern is constructed from an area which is illuminated. Such a concept has been demonstrated by Liu *et al.* [5] where a structurally embedded photoconductive silicon bowtie antenna is implemented. In this case when the laser source is on, a bowtie shape is illuminated on the silicon substrate. When the laser is

OFF, the elements do not interfere with other nearby circuitry and the structure is also immune to EM detection. This is beneficial for stealth applications where reducing radar cross section is important, but also allows stacked 3D geometries of antennas to be implemented. Of course the drawback of such an approach is that implementation of this system is expensive. Cost-efficiency is another characteristic which is application specific – it's also the case that if a technology proves itself to solve a particular problem, the cost of manufacture can often be reduced through process refinement.

The second type of photoconductive switch consists of a die of silicon placed over a gap in transmission line, demonstrated by Panagamuwa et al. [6], see Figure 1.2. When illuminated via a 980nm laser diode the silicon die becomes conductive and bridges the gap in transmission line turning the switch ON. Under these conditions an insertion loss of 0.6dB is achieved. Whilst under no illumination, the silicon is non-conductive, and produces an isolation of 16dB between the two ports. Clearly this is less than stated above, however insertion loss is reduced – this highlights the trade-offs of different switch characteristics that need to be carefully considered.

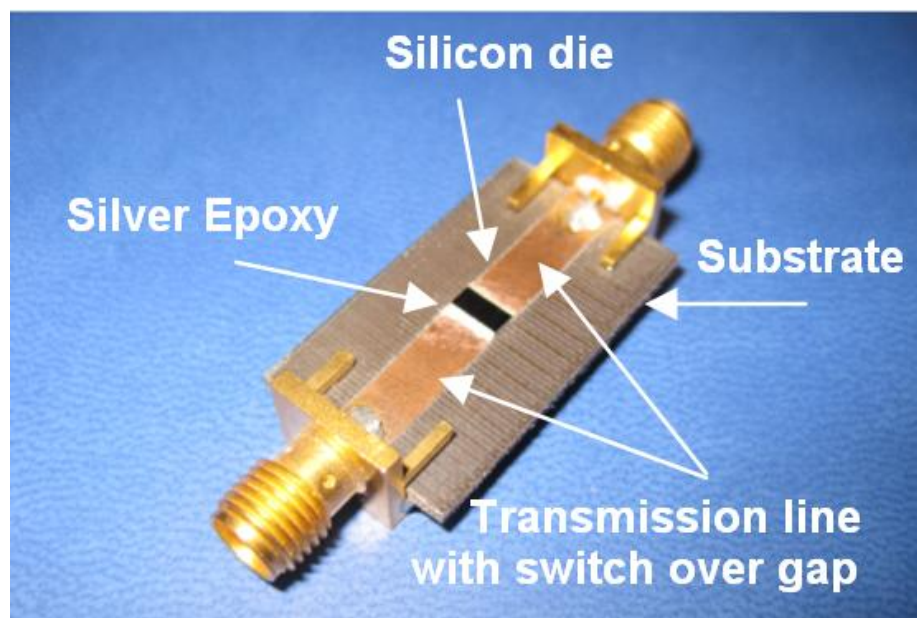


Figure 1.2: Optically controlled microwave switch incorporating silicon die [7]

Similar designs have been demonstrated on transmission lines and reconfigurable antenna by Tawk *et al.* [8] and Liu *et al.* [9]. In the former case, Tawk *et al.* presents a circular patch antenna. When the two silicon switches are not illuminated by a laser light (OFF state), only the circular ring is fed.

This results in an antenna resonance between 18 GHz and 19 GHz. Upon activation of the silicon switches, a new resonance begins to appear at 12 GHz. Research by Liu *et al.* [9] presents a switch incorporating two square open loop resonators, simulation results at 11.65GHz, reports isolation in the OFF state is reported at 56dB, and insertion loss in the ON state is 0.59dB.

The effect of switch performance on antenna efficiency is also an important factor. The switch insertion loss directly affects antenna efficiency and gain. This is reported by Tawk *et al.* [8]. For both frequency configurations of the circular patch antenna, simulated boresight gain is higher than measured boresight gain.

Specifically, at 11.8GHz, measured boresight gain is 5.42dB whereas simulated gain is 5.75dB. There is an overall increase in the antenna material losses introduced by the silicon switches – this manifests itself as reduced radiation efficiency and gain. Impedance mismatch caused by the switch can also impact antenna efficiency. The mismatch can be reduced by increasing the radiant flux supplied to the switch hence making it more conductive and improving efficiency.

1.3 Desirable qualities in a microwave switch

The concept of a microwave switch is to use a variable impedance circuit element to direct the flow of signal. In an ideal scenario the ON state impedance would be 50Ω and OFF state impedance would be infinite meaning all signal is reflected or absorbed by the switch. Non-ideal impedance of the microwave switch causes insertion losses in the ON state. Unwanted RF signal leakage when the switch is in the open state is referred to as isolation and both these quantities are two of the main figures of merit for microwave switches.

However, transmission of the switch is not the only consideration when choosing a type of microwave switch for a particular application. Other notable criteria include:

1. Bandwidth
2. Footprint
3. Cost
4. Power handling
5. Distortion of the RF signal.
6. Switching
7. Integration
8. Control power consumption

The relative importance of various criteria is very much application specific. Hence the design and fabrication of the switch, the focus of Chapters 3 and 4, also needs to be tailored towards achieving high performance and integration into the desired communication systems.

There are a number of commercially available microwave switches, including PIN and varactor diodes, Field Effect Transistors (FET) and Micro Electro-Mechanical Systems (MEMS) switches which are utilised to block RF signals when desired.

These existing switches are all controlled via a DC signal to set their state, and hence rely on metallic biasing lines to operate. There is an alternative to this control method – optical control via a fibre optic cable which pertains to the photoconductive switch. The unique benefit of the photoconductive switch is that metallic biasing lines are not required in the vicinity of RF signals

1.4 Motivation

By fully characterising the switch and exploring packaging solutions, the potential of the photoconductive switch to provide a better performance in certain aspects is to become clear.

If the aim is to prove the benefit of the photoconductive switch, particularly for reconfigurable antennas and RF circuits, the motivation behind this falls into three categories:

1. The growing number of applications which can benefit from an optically controlled switch
2. The current drawbacks of other switches
3. Potential improvement of usability and performance that having a packaged switch can provide

In particular, investigating packaging techniques allows proof of feasibility of this component for use in industry instead of the conventional types of switch such as PIN and varactor diodes which have certain disadvantages which are discussed in the upcoming section. EM simulation can be used to investigate this effect, so long as the photoconductivity within the silicon is understood.

1.4.1 Applications

Wireless systems are increasingly being designed to be multi-functional. Such a trend can be observed in the design of laptops and mobiles, where a variety of different wireless services are being covered in one platform. Where reconfigurable antennas can become advantageous is that the overall form factor of the system can be kept small if geometry of antennas is reused to cover different wireless services. A high degree of isolation may also be maintained between different services as antennas are not placed in close proximity to each other. Hence there is a drive to design reconfigurable circuits and antennas to such an end.

In the application of reconfigurable antennas and circuitry, the silicon die is placed over a gap in a signal path to alter the dimensions of the antenna or circuitry – changing the frequency of operation, polarisation or directivity. Photoconductive switches are widely being researched to reconfigure wireless communications systems such as a range of antennas [10] and circuitry including filters [11], amplifier matching circuits and couplers [12].

Figure 1.3 demonstrates a reconfigurable dipole antenna which includes two photoconductive switches [13]. Since the illumination is delivered by glass fibre optic cables, there is no effect on radiation pattern and no need to design complex DC biasing networks. In this case the resonant frequency of the antenna can be altered and the beam pattern can be changed to provide four different configurations dependent on the ON and OFF state of the two switches.

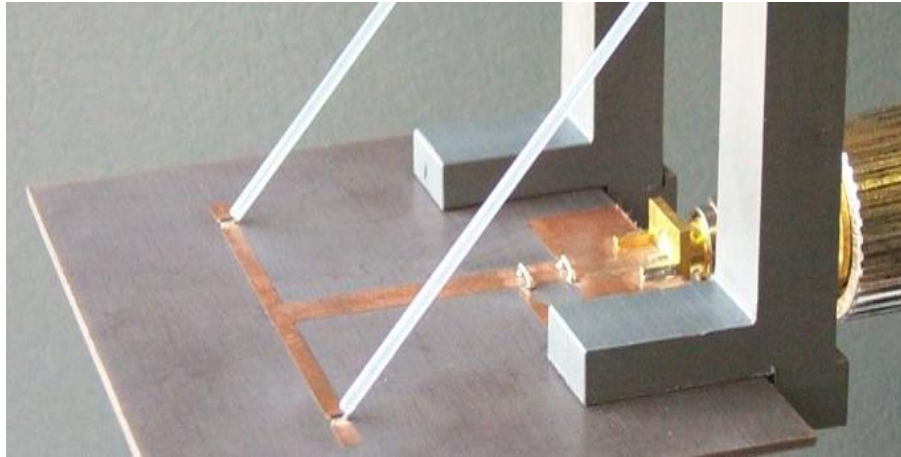


Figure 1.3: Silicon switches incorporated into a dipole to enable frequency and beam reconfiguration from Panagaumwa *et al.* [13]

Other applications include tuneable terminations and general path selection. For example a switch can be used to switch between transmit and receive paths for an antenna system as opposed to creating alternative antenna geometries. Blocking signals using photoconductive switches has been demonstrated by Flemish *et al.*[14]. In this instance the switches are used to control elements in an antenna array. Clearly, the need to develop photoconductive microwave switch technology is largely dependent on the need for these reconfigurable circuits and antennas.

Chauraya *et al.* [15] present a metallodielectric photonic band gap resonator based on photoconductive silicon switches. The application aims to filter harmonic suppression and hence increase antenna efficiency.

A real world application in which photoconductive switches may excel is that of a software defined antenna [16]. Switch criteria in terms of switching time is not critical here as once tuned the antenna remains in this state for long periods of time, 1ms is deemed sufficient. A typical transmitter for this application outputs 25-50W and hence voltage breakdown and current handling are important criteria for the switching element. These figures were collected from the author of the paper, Cole. Research into this particular helix antenna is considered in the defence industry in order to reduce the form factor of multiple antenna systems. There is also the consideration of effect that the switching mechanism may have on the performance of the antenna.

Cognitive radio which includes wideband scanning, where a single frequency is only dwelt on for a matter of ms requires a faster switching response-e.g. in the region of 10 μ s or lower is desirable. Power handling, of at least 1W is required for such an application as this is typically the transmit power of a cognitive radio system [17] .

In the past photoconductive switches have been utilised to create pulsed power, such is suggested by Mourou *et al.* [18]. Although employing a similar concept to the photoconductive switch described above, an applied bias must be employed to help the switch create the pulsed power and hence this application is not discussed further in this thesis. A number of applications are listed in Table 1.1 along with important criteria and qualities which are desired in these areas.

Criteria	Applications				
	Small Signal antenna	High Power antenna	Coaxial cable	Other circuitry (e.g. Filter)	Pulsed Power
Insertion loss	Lower Importance	Minimise	Minimise	Minimise	Minimise
Isolation	Maximise	Maximise	Maximise	Maximise	Low importance
ON-OFF transmission range	Maximise	Maximise	Maximise	Maximise	Low Importance
Power handling/ linearity	Low Importance	Maximise	Maximise	Maximise	Maximise
Switch rise/fall time	Minimise	Minimise	Minimise	Minimise	Minimise (high importance)
Switch control power	Minimise	Minimise	Minimise	Minimise	Low Importance
Effect on radiation pattern	Minimise	Minimise	Not applicable	Not applicable	Not applicable
Form factor	Application dependent	Application dependent	Application dependent	Minimise	Low importance

Table 1.1: Potential applications for the photoconductive switch and corresponding level of importance for different switch criteria

1.4.2 Types of Microwave switch

Commercial microwave switches currently used to control RF signals include Field Effect Transistors (FETs), MEMS, PIN diodes and varactor diodes. These devices serve as a direct comparison to the performance of photoconductive switches. Certain drawbacks of using these switches emphasise the need to investigate alternative methods such as photoconductive switches.

PIN diodes incorporate doped and intrinsic regions within the semiconductor structure. This means that electrical bias can control the conductivity of the switch. A PIN diode operating in the forward bias mode is in the ON state, whereas if the PIN diode is reversed biased the switch is OFF. PIN diodes have a number of applications including reconfigurable microstrip antennas [20] and active frequency selective surface (FSS) control [21].

Varactor diodes are similarly made up of a P-N junction. By applying a DC bias, the capacitance of the diode is altered. PIN and varactor diodes are inexpensive and present fair isolation and low insertion loss values. This means they are ideal in low power wireless applications such as reconfigurable wireless sensor networks [22][23]. It is possible to tune the varactor by altering the control voltage – a tuning range of $\pm 30\%$ is achievable [24].

MEMS switches are mechanical switches, which involve metal cantilever movement in order to create either an open or a closed circuit. The control of the switch is supplied by electrical bias which exerts an electrostatic force on the cantilever. MEMS are used in a wide range of applications and industries such as the medical and aerospace markets [25]. Capacitive MEMS and varactor diodes both have the capability of continuous tuning, which is important advantage for use in multiband systems [9].

FETs are three port devices, where the source-drain channel forms the conduction path for the RF signal [26]. A DC voltage is applied at the gate port to control ON and OFF state. The drawback is that they usually have a high ON state resistance [10]. FETs have been used in applications ranging from DC to THz [27]-[29].

FETs, PIN diodes and varactor diodes all incorporate some form of junction and hence the linearity response of such devices is less impressive, resulting in signal

distortion [30]. Generally the signal handling capability is also limited. Hence there can be interaction of the signal and control, in high power applications. In the case of the FET for example, the main signal level is limited to a level which will not modulate the gate-source control voltage. In addition the FET is also viewed as having high power consumption in the ON state.

MEMS demonstrate excellent isolation in the OFF state and low insertion loss in the ON state. They also have an extremely linear behaviour [31]. However the fastest tuning speeds are around a microsecond, which is slow compared to other microwave switches which demonstrate nanosecond switching [36]. They are also low power handling and can be less reliable than other switches due to their delicate mechanical membrane – these switches are much more expensive for this reason as the packaging requirements to maintain a hermetic environment inside the package are strict [37].

Lastly, FETs, MEMS, PIN and varactor diodes all require electrical bias lines to control the ON and OFF state of the switch. In particular, for reconfigurable circuit applications this is not desirable as isolation of the RF path is important [38]. The design of these biasing networks can sometimes be complex and must be considered at the simulation stage of the RF circuitry. The RF signal can couple to the DC biasing lines and hence cause additional resonance effects in the circuit. This can affect efficiency and radiation pattern of the antenna. This must be particularly addressed when multiple switches are used – such as the case for antenna arrays. Here, a complete biasing network must be designed – optimisation of each individual line and its affect on surrounding antennas is a time consuming process.

In some cases, it is simply not practical to include metallic lines – this is the case for systems that require a small form factor and include traces which are in close proximity – for example miniature filters [11].

DC controlled switches often require high voltages in order to achieve switching, and have the disadvantage that the switch is no longer electrically or thermally isolated. This has the consequence that any potential spike in control power can propagate down the DC bias line to the reconfigurable circuit. Similarly, should the power source produce large amounts of heat, the biasing lines will conduct this to the switch.

There are techniques to minimise the effect that biasing lines have on performance. These include using vias to take the signal from the RF plane to a level below the ground plane. This can be a useful approach if the circuit contains a large ground plane which can shield the presence of the biasing line. However, holes in the substrate and ground plane could still change the performance of the antenna by changing the current distribution in the structure. A popular technique is to include a quarter wavelength transmission line which is grounded and appears as an open circuit at the antenna [33]. However this is only a narrowband solution. Alternative approaches include using wideband radial open stubs [34]; however the drawback here is that these designs may be too large to implement.

In contrast the photoconductive switch can be controlled via illumination which can be delivered via a non-conductive fibre optic cable. The advantage to this method is three fold:

1. No metallic lines which could interfere with the RF performance of the circuit through unwanted coupling, potentially changing the desired radiation pattern.
2. Electrical and thermal isolation of the switching circuit. When using DC biasing lines it is possible for DC spikes to interfere with the switch and RF performance.
3. No need to produce high voltages for use in DC control circuitry

Table 1.2 presents a generalised high level view of the different types of microwave switch along with their capabilities. The above mentioned qualities merit the continued research and improvement into the photoconductive switch, and its advancement as a commercial microwave component for reconfigurable applications. Chapter 5 concentrates on reporting such switch qualities as linearity, power handling and switching speed, which have not been previously presented.

In terms of up and coming technology, research has been conducted into nano electromechanical systems (NEMS) [40]. Instead of employing a metal cantilever to bridge the gap in signal path, graphene sheets are used which allow a faster switching speed.

Attribute	PCS	PIN	Varactor	MEMS	FET
Continuous tuning	✓	✗	✓	✓	✓
Free from metallic Biasing lines	✓	✗	✗	✗	✗
Linearity	Medium	Low	Low	High	Low
Switch speed	ps - us	ns	ns	us	ns
Low Insertion loss to isolation ratio	✓	✓	✓	✓	✗

Table 1.2: Different microwave switch types and their attributes

Graphene is carbon arranged in a hexagonal distribution, similar to graphite, however it is only 1 atom thick which allows it to be lightweight and flexible. Switches made using graphene sheets consist of a coplanar waveguide (CPW) bridged by graphene sheets which when an electrical field is applied lock down and allow a short circuit of the CPW, Figure 1.4.

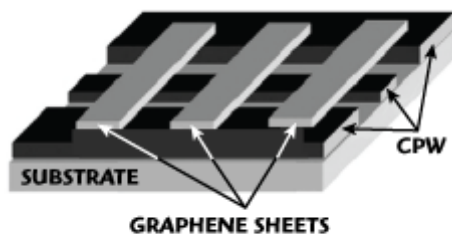


Figure 1.4: Top view of the graphene NEMS switch configuration, from Hindle [41]

These switches are a promising emerging technology which may overcome some of the disadvantages of the MEMS switch. However currently, there are manufacturing challenges to be overcome with the large scale production of graphene.

1.4.3 Why is Packaging Important?

The purpose of packaging any electrical component is to allow easy reuse of the functionality, provide electrical connection, protect the circuitry from shock, offer a support structure and handle any heat dissipation issues whilst maintaining signal

quality. Packaging requirements are largely dependent on system level requirements such as frequency, power output, low system noise, functionality, reliability, efficiency, and for radio frequency (RF) components, there are additional issues that affect performance due to the short wavelengths involved in high frequency signals. Furthermore circuit application drives packaging design decisions such as manufacturing technique and material selection which affect component operation in different ways when compared to low frequency equivalent circuits.

The photoconductive switch in its current state is not a useful component to industries. The switch requires specialist silver epoxy to attach to the circuit in question, which is not as established as solder, the fibre optic requires precise alignment, hence in its current state the system would be non-manoeuvrable, the laser light is potentially harmful, hence further measures need to be taken to ensure human safety and lastly the switch has no protection from the environment it is being used in, leading to shorter time to failure. Clearly the switch could be greatly enhanced via its packaging into a component.

However packaging of such an RF switch is not trivial. Microwave frequency circuits (typically above 300MHz) behave differently to similar circuits at lower frequencies because the wavelength of the electromagnetic (EM) waves involved are short enough to be comparable to the dimensions of the components being employed. At these higher frequencies components must be treated as distributed elements and not lumped, as is standard. Introducing packaging to encapsulate circuits affects signal performance as signals carried in the conductor and surrounding dielectrics are strongly influenced by the electrical properties of the dielectric at high frequencies, suggesting dimensions and material choice are important factors when considering packaging of high frequency components.

Packaging conventionally encompasses features, specifications and performance of the components, interconnect media material, processes to encapsulate the circuit and testing [42], with each area offering separate issue for examination. The unique challenge of optical control must also be addressed with respect to the photoconductive switch. In terms of these criteria, this thesis particularly focuses on the silicon processing and maintaining signal planarity through choice of interconnect and position of the optical control feed.

1.5 Primary Contributions

The major contributions contained in this thesis can be summarised as follows:

- Consideration of the Auger effect on the photoconductivity of the treated silicon die and its effect on silicon permittivity and loss tangent.
- Possible strategies and considerations when packaging the switch. These include calculated material models for simulation, ideal transmission line designs and studies on signal planarity.
- Effect of various fabrication techniques on the photoconductive / microwave performance of the switch. Specifically, texturing the silicon and the addition of gold contacts.
- Characterisation in terms of single-tone and two-tone linearity of the photoconductive switch (harmonic and intermodulation performance)
- Investigation of RF power handling up to 25W
- Switch rise and fall time characterisation for different variations of the photoconductive switch.

1.6 Thesis Structure

Basic semiconductor theory is introduced in Chapter 2, particularly focussing on calculating the change in conductivity and dielectric permittivity of the silicon. These two quantities are key in describing the RF performance of the switch. Recombination mechanisms will also be discussed, and in particular Auger recombination is examined and its effect is added into Platte's [1] original equation to account for some of the discrepancy seen between calculated conductivity and experimental conductivity. The chapter also reviews how fabrication of the silicon, (particularly the quality and the doping) affect conductivity. The silicon studied in this thesis is presented and a wavelength study is performed for this silicon type in order to better understand the conductivity profile created in the semiconductor.

Chapter 3 focuses on the simulation of the switch using the conductivity profile (including the Auger term) that is generated in Chapter 2. The simulated performance is compared to the measured performance in terms of transmission performance. Firstly, a short optimisation study is presented on the ideal microstrip

dimensions. This ensures that insertion loss is minimised in the ON state but isolation is maximised in the OFF state. A layered dielectric material simulation model for the illuminated silicon is presented in order to validate the conductivity profiles generated in Chapter 2. All physical geometries are modelled in detail in order to explore potential packaging techniques. In particular an in depth study on maintaining signal planarity is presented.

The fabrication processing of the silicon is investigated in Chapter 4. Mainly this is to improve efficiency of the switch in the ON state and to explore packaging interconnect solutions. Three techniques which are currently employed in the photovoltaic industry, passivation, anti-reflection coating and texturing, are investigated and analysed in terms of effect on microwave performance for the photoconductive switch. The addition of gold contacts is also presented alongside connection methods such as surface mounting and wire bonding.

Chapter 5 concentrates on the characterisation of the switch in terms of linearity, power handling and switching rise and fall time. A comparison is made between commercially available microwave switches and the photoconductive switch in order to give some overview of the current state of the art. Linearity is characterised in terms of single tone and two-tone measurements, where high power testing is presented up to 25W of RF input power (at 2GHz). Lastly, the switch rise and fall time is presented at 2GHz when the switch is illuminated by a pulsed LED.

Finally, Chapter 6 draws conclusions on the strengths of the photoconductive switch and specific packaging techniques which can be employed to package the switch for potential use in industry. Future work is also discussed in terms of fabrication processes and considerations in terms of current packaging constraints.

1.7 References

- [1] D. H. Auston, "Picosend optoelectronic switching and gating in silicon", Applied Physics Letters No. 26, pp. 101–103, 1975.
- [2] S. P. Benham, D. P. Atkins, E. J. Totten, G. A. Pettitt and P. Cushnaghan, "Software Defined Antenna", IEEE Loughborough Antennas and Propagation conference, pp 489-492, November 2009
- [3] J. R. Flemish, H. W. Kwan, R. L. Haupt and M. Lanagan, "A new silicon-based photoconductive microwave switch," Microwave and Optical technology letters, Vol. 51, No.1, January 2009
- [4] Infineon datasheet "Silicon PIN Diode bar 64" available online <http://www.infineon.com>, published June 2013, last accessed April 2014.
- [5] D. Liu, D. Charette, M. Bergeron, H. Karwacki, S. Adams, B. Lanning and F. Kustas, "Structurally embedded photoconductive silicon bowtie antenna." Photonics Technology Letters, IEEE Vol. 10, no. 5, pp. 716-718, 1998
- [6] C. J. Panagamuwa, A. Chauraya and J. C. Vardaxoglou, "Frequency and beam reconfigurable antenna using photoconducting switches" IEEE Trans. Antennas Propagat., vol. 54, no.2, pp. 449-454, 2006.
- [7] E. K. Kowalczyk, C. J. Panagamuwa, R. D. Seager, and J. C. Vardaxoglou. "Characterising the linearity of an optically controlled photoconductive microwave switch." In Antennas and Propagation Conference (LAPC), 2010 Loughborough, pp. 597-600. IEEE, 2010.
- [8] Y. Tawk, A. R. Albrecht, S. Hemmady, G. Balakrishnan and C. G. Christodoulou, "Optically Pumped Frequency Reconfigurable Antenna Design", IEEE Antennas and Wireless Propagation Letters, vol. 9, pp. 280-283
- [9] P. J. Liu, D. S. Zhao, and B. Z. Wang "Design of Optically Controlled Microwave Switch for Reconfigurable Antenna Systems", Microwave and Millimeter Wave Technology, 2007. ICMMT , pp. 1-4, April 2007

- [10] J. L. Freeman, B. J. Lamberty, and G. S. Andrews. "Optoelectronically reconfigurable monopole antenna." *Electronics letters* Vol. 28, no. 16, pp. 1502-1503, 1992.
- [11] K. Rabbi, L. Athukorala, C. Panagamuwa, J. C. Vardaxoglou, and D. Budimir. "Highly linear microstrip wideband bandpass filter with switchable notched band for wireless applications." *Microwave and Optical Technology Letters* 55, no. 6 (2013): 1331-1335.
- [12] D. Draskovic, C. Christodoulou, and D. Budimir. "Optically reconfigurable RF circuits." In *Antennas and Propagation (EuCAP), 2010 Proceedings of the Fourth European Conference on*, pp. 1-3. IEEE, 2010.
- [13] C. J. Panagamuwa "An investigation of transmission line switching and frequency shifting in dipole antennas using optically activated silicon switches", Doctoral Thesis (Ph.D.) Loughborough University, 2004
- [14] J. R. Flemish, and R. L. Haupt, "Optimisation of a photonicly controlled microwave switch and attenuator," *IEEE transactions on microwave theory and techniques*, vol. 58, No. 10, 2010
- [15] A. Chauraya, D. S. Lockyer, Y. L. R. Lee and J. C. Vardaxoglou, "A study of optically tuned metallodielectric photonic band gap array and patch antenna," *11th International Conference on Antennas and Propagation (ICAP)*, pp. 492-496, 2001
- [16] S. P. Benham, D. P. Atkins, E. J. Totten, G.A. Pettitt and P. Cushnaghan, "Software Defined Antenna", *IEEE Loughborough Antennas and Propagation conference*, pp 489-492, November 2009
- [17] P.S Hall, P. Gardner, J. Kelly, E. Ebrahimi, M. R. Hamid, F. Ghanem, F. J. Herraiz-Martinez, and D. Segovia-Vargas. "Reconfigurable antenna challenges for future radio systems," *3rd IEEE European Conference on Antennas and Propagation, EuCAP*, pp. 949-955, 2009.
- [18] G. Mourou, C. V. Stancampiano, and D. Blumenthal, "Picosecond microwave pulse generation," *Applied Physics Letters* Vol. 38, no. 6, pp. 470-472, 1981.

- [19] P. Gardner, M. R. Hamid, P. S. Hall, J. Kelly, F. Ghanem, and E. Ebrahimi. "Reconfigurable antennas for cognitive radio: requirements and potential design approaches," Institution of Engineering and Technology Seminar on Wideband, Multiband Antennas and Arrays for Defence or Civil Applications, pp. 89-94, 2008.
- [20] F. Yang, and Y. Rahmat-Samii, "A reconfigurable patch antenna using switchable slots for circular polarization diversity," IEEE Microwave and Wireless Components Letters, Vol. 12, no. 3, pp. 96-98, 2002.
- [21] A. Tennant and B. Chambers. "Adaptive radar absorbing structure with PIN diode controlled active frequency selective surface," Smart materials and structures Vol. 13, no. 1 pp. 122, 2004.
- [22] A. S. Porret, T. Melly, C. C. Enz, and E. A. Vittoz. "Design of high-Q varactors for low-power wireless applications using a standard CMOS process," IEEE Journal of Solid-State Circuits, Vol. 35, no. 3, pp. 337-345, 2000.
- [23] F. Viani, L. Lizzi, M. Donelli, D. Pregnotato, G. Oliveri, and A. Massa. "Exploitation of parasitic smart antennas in wireless sensor networks." Journal of Electromagnetic Waves and Applications Vol. 24, no. 7, pp.993-1003, 2010.
- [24] S. V. Shynu, G. Augustin, C. K. Aanandan, P. Mohanan, and K. Vasudevan. "Design of compact reconfigurable dual frequency microstrip antennas using varactor diodes." Progress In Electromagnetics Research No. 60, pp. 197-205, 2006.
- [25] R. M. Osiander, M. Ann, G. Darrin, and J. L. Champion, eds. "MEMS and microstructures in aerospace applications," CRC Press, 2005.
- [26] R. Cory and D. Fryklund "Solid State RF/Microwave Switch Technology: Part 2" www.mpdigest.com, p.p. 34, June 2009
- [27] F. Schwierz and J. J. Liou, "RF transistors: Recent developments and roadmap toward terahertz applications." Solid-State Electronics Vol. 51, no. 8 pp. 1079-1091, 2007.

- [28] Y. Ota, C. Adachi, H. Takehara, M. Yanagihara, H. Fujimoto, H. Hiasato, and K. Inoue, "Application of heterojunction FET to power amplifier for cellular telephone," *Electronics Letters* Vol. 30, no. 11, pp. 906-907, 1994.
- [29] T. Aboufoul, A. Alomainy, and C. Parini, "Reconfiguring UWB monopole antenna for cognitive radio applications using GaAs FET switches," *IEEE Antennas and Wireless Propagation Letters*, Vol. 11 pp. 392-394, 2012.
- [30] R. Caverly and G. Hiller, "Distortion in p-i-n Diode Control Circuits" *IEEE Trans. Microwave Theory Tech.*, vol. MTT-35, p. 492, May, 1987.
- [31] Radant MEMS "RMSW100HP High Power MEMS," datasheet, www.radant.com
- [32] Y. Ohno, and M. Kuzuhara "Application of GaN-based heterojunction FETs for advanced wireless communication," *IEEE Transactions on Electron Devices*, Vol. 48, no. 3, pp. 517-523, 2001.
- [33] I. Kim and Y. Rahmat-Samii. "RF MEMS switchable slot patch antenna integrated with bias network." *IEEE Transactions on Antennas and Propagation*, Vol. 59, no. 12, pp. 4811-4815, 2011
- [34] J. R. De Luis and F. De Flaviis. "Frequency agile switched beam antenna array system." *IEEE transactions on antennas and propagation* Vol. 58, no. 10 pp. 3196-3204, 2010.
- [35] J. M. Kovitz, H. Rajagopalan and Y. Rahmat-Samii. "Practical and Cost-Effective Bias Line Implementations for Reconfigurable Antennas." *Antennas and Wireless Propagation Letters*, IEEE 11 (2012): 1552-1555.
- [36] Macom Solution Technologies "Packaged PIN Diodes"
<http://www.macomtech.com/datasheets/packagedpindiodes.pdf>, last accessed 12th October 2013
- [37] R. Ramesham and R. Ghaffarian, "Challenges in interconnection and packaging of microelectromechanical systems (MEMS)." 50th IEEE Proceedings In Electronic Components & Technology Conference, pp. 666-675, 2000.

- [38] A. M. Yadav, C. J. Panagamuwa, and R.D. Seager, "Investigating the effects of control lines on a frequency reconfigurable patch antenna," Loughborough Antennas & Propagation Conference, 2010
- [39] G. Breed "A Review of RF/Microwave Switching Technologies" 2010 Summit Technical Media, LLC May 2010 High Frequency Electronics
- [40] M. Dragoman, D. Dragoman, F. Coccetti, R. Plana and A.A. Muller, "Microwave Switches Based on Graphene," Journal of Applied Physics, Vol. 105, 054309, 2009.
- [41] Pat Hindle "The State of RF and Microwave Switches" Microwave Journal, November 2010 available online
<http://www.microwavejournal.com/articles/10269-the-state-of-rf-and-microwave-switches?v=preview> last accessed 12th June 2014
- [42] S. G. Konsowski and A.R. Helland "Electronic Packaging of High Speed Circuitry", McGraw-Hill, 1997
- [43] W. Platte, and B. Sauerer, "Optically CW-induced losses in semiconductor coplanar waveguides" IEEE Trans. Microwave theory and Techniques, Vol. 37 pp. 139, Jan 1989

2 Silicon Behaviour

Key terms in semiconductor theory are introduced at the start of this chapter in order to understand the aspects which effect photoconductivity generated within semiconductors. Photoconductivity equations are presented and Auger recombination is considered as an addition to these equations at high values of radiant flux.

The processing of silicon will also be described with a view to highlighting the key attributes which affect silicon photoconductivity. The quality and processing of silicon very much determines the carrier lifetime of the silicon which is a key quantity that affects the conductivity.

Lastly, the effect of the light source is also considered as a factor which affects switch performance. In particular, the wavelength of the light affects the distribution of the carriers in the silicon. Hence, a study is conducted using newly formed conductivity profile equations which include an Auger recombination term. The aim is to demonstrate the most efficient wavelength of light to use to promote conductivity within silicon used in this thesis.

2.1 Introduction

Photoconductivity is the change in the electrical conductivity of a substance as a result of absorbing electromagnetic radiation. The potential for a material to be

photoconductive depends on the atomic structure of the material and the photon energy of the supplied radiation.

In particular, semiconductors are widely used to produce photoconductive devices. Hence an understanding of fundamental semiconductor physics is essential to grasp the concept behind photoconductive switches. The photoconductivity profile in semiconductors will be introduced in this chapter in terms of three mechanisms; carrier generation, carrier recombination and diffusion rate of carriers. These three processes, described by a formula introduced by Platte *et al.* [1], can be used to calculate the photoconductivity of a semiconductor. Further formulas introduced by Lee *et al.* [2] can also predict the dielectric changes within the semiconductor as it becomes more conductive, which is essential for RF simulation of the switch.

In general silicon is a good candidate to be used in photoconductive microwave switches. It is a material which is well researched and already used widely in both the semiconductor chip industry and the photovoltaic industry. This means that a mature technology and processing techniques of the silicon are already established.

2.2 Semiconductor Theory

The choice of semiconductor for the task of optically controlled RF switching in reconfigurable circuits is dependent on the structure and attributes of the semiconductor. These include bandgap energy and type, doping and the effect this has on mobility and collision time which are discussed in this section further.

2.2.1 Bandgap

Energy band theory allows solids to be classified as metals, semiconductors or insulators and describes the energy of electrons in atoms as shown in Figure 2.1. The band structure, or energy – momentum relationship is usually obtained by solving the Schrödinger equation for a single atom [2][3]. When these atoms are brought together to form a solid, certain modifications occur to the energy states of individual atoms that leads to unique energy band structures. The electrons in the outermost shell of the atom are called the valence electrons – the state of these electrons are altered the most [2] as they are furthest from the nucleus. Since these

electrons are most likely to be freed from their parent atom, these are of prime concern. These determine whether there will be conduction in a material.

The two bands of real interest are the valence and conduction bands. The valence band is the lowest energy band, typically filled with electrons. The conduction band is the upper band, which may be empty or partially filled. The separation between the lowest conduction band and highest valence band is called the bandgap and is an important figure in semiconductor physics [4].

The bandgap, E_{BG} , is an energy range in which no electron states (or energy levels) can exist, a forbidden band. It is defined as the energy value which is required to free an outer shell electron from its orbit around an atom's nucleus. Once free, the electron and the vacant bond (or hole) left behind are able to move about and contribute to the flow of current [1][4]. It is possible for electrons in the valence band to be excited to the conduction band, if they gain sufficient energy through photon absorption or heating. When an electron leaves the valence band it leaves behind a hole, this empty state allows the electrons some degree of freedom – and hence charge transport is possible [4].

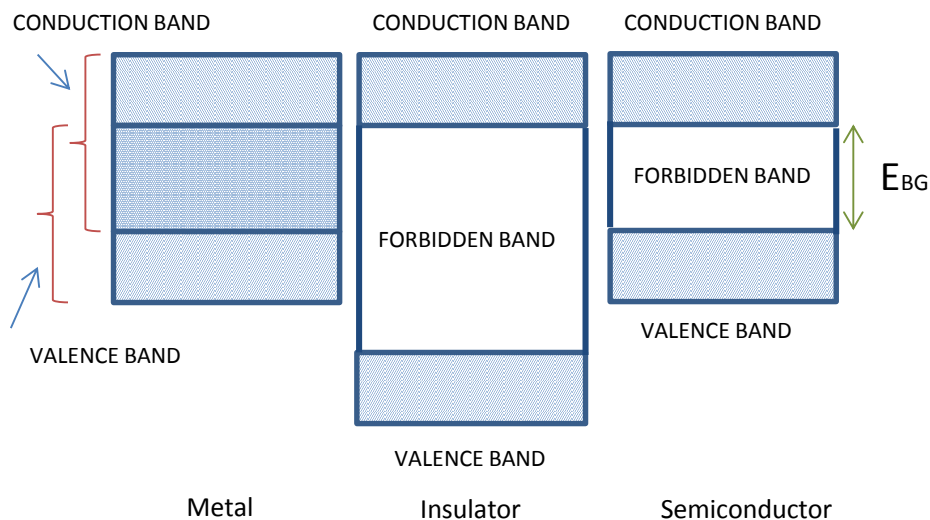


Figure 2.1: Simplified energy band diagram for a metal, insulator and semiconductor [2]

The regular crystalline structure of semiconductors means there are periodic ranges of allowed and disallowed energy states for electrons. Semiconductors have a relatively small bandgap between the conduction and valence bands - for silicon the

value is 1.1eV. The small bandgap means that the covalent bonds holding electrons at atomic sites in the semiconductor lattice can be broken by incident photons, if the photon energy is greater than the bandgap energy [5]. The energy of a photon (E_{photon}) is dependent on its wavelength (λ), the speed of light (c) and Planck's constant (h) by Eq. (2.1) as detailed in [6]

$$E_{photon} = \frac{hc}{\lambda} \quad \text{Eq. (2.1)}$$

Energy of 1.1eV is equivalent to photons which have a wavelength of $\sim 1.1 \mu\text{m}$. Hence an electron can be promoted from the valence to the conduction band using illumination with a wavelength of $1.1 \mu\text{m}$ or below.

2.2.2 Direct or Indirect

Semiconductors can be classed with either a direct or indirect bandgap, depending on the electronic band structure and momentum of the electrons in the valence and conduction band. If the momentum of the electrons in the valence and conduction band is identical, the material is a direct bandgap semiconductor such as gallium arsenide (GaAs) and indium phosphide (InP). Semiconductors with indirect band gaps include silicon (Si), germanium (Ge) and aluminium arsenide (AlAs). For indirect band gap materials, the momentum of electrons and holes in the conduction and valence band is different. This momentum can be described in terms of a k-vector in a set volume around one element of the lattice – also defined as the Brillouin zone [7].

Since a difference in momentum is apparent for indirect bandgap materials, this means that electrons require both energy and momentum to move between conduction and valence bands. Thus the likelihood of promoting free charge carriers and hence increasing conductivity in indirect bandgap materials is lower than in direct bandgap materials; essentially a simultaneous vertical and horizontal transition is required to 'free' an electron. The electron is scattered by the energy from a photon to the direct band and then scattered again to the indirect band by a phonon, conserving momentum, Figure 2.2.

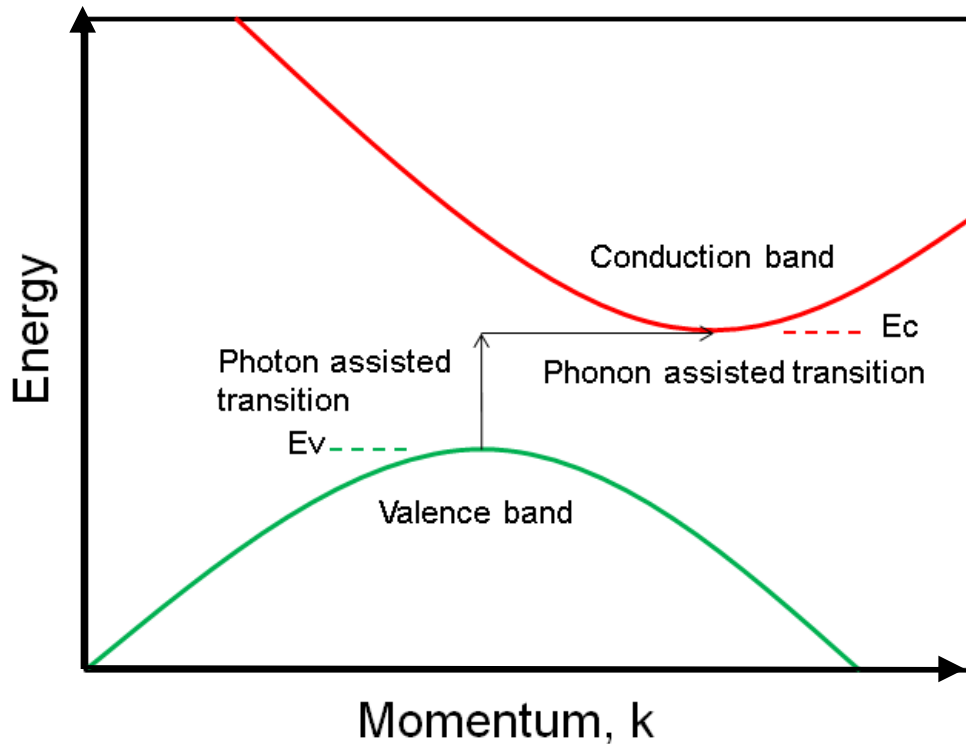


Figure 2.2: Energy vs. momentum for a semiconductor with an indirect band gap

2.2.3 Doping

It is possible to reduce the effective bandgap in the semiconductor by introducing an impurity into the semiconductor material. A pure semiconductor is referred to as intrinsic. An extrinsic semiconductor has been grown to include a dopant such as boron or phosphorus. The methods of introduction and its effect on electrical properties will be discussed further in section 2.7.2 and in Chapter 4.

Doping a semiconductor crystal introduces allowed energy states within the forbidden bandgap of the semiconductor- these states are very close to the energy band that corresponds to the dopant type. Doping comes in two variants, N-type and P-type. N-type doping can be achieved by diffusing phosphorus or arsenic (which have five outer electrons) into the silicon. Since silicon only has four outer electrons, the doping atom makes four bonds in the silicon lattice. One electron from the dopant atom is left unbounded and so can be easily promoted to the conduction band. Hence by including doping impurities the conductivity of the silicon can be increased.

Similarly, P-type doping can be achieved using boron, which has only three electrons in the outer shell of the atom. When introduced to the silicon a bond to an electron is missing, which creates an extra hole.

2.2.4 Mobility and Collision Time

Sze [5] outlines the fundamentals on semiconductor mobility which are presented in this section. When an electric field (E) is applied across the semiconductor, the free carriers will tend to drift in the direction of the field. Combined with conductivity (σ) a current density, J is created, as is described by Eq.(2.2):

Eq. (2.2)

$$\vec{J} = \sigma \vec{E}$$

Overall, the magnitude of the current generated, is dependent on the density of the free carriers, n and their average velocity in the direction of the field, v_d (q is the elementary charge), Eq.(2.3):

Eq. (2.3)

$$J = -nqv_d$$

Electric field has no influence on the density of carriers, but does influence speed of the carriers. This can be described by the term mobility, μ , which is the ratio of carriers speed to electric field, Eq.(2.4):

Eq. (2.4)

$$v_d = \mu E$$

This value is different for different semiconductors due to differing effective masses of each type of particle – note that electrons and holes have differing mobilities. A more in-depth discussion on mobility and the effect that impurities impose on performance is presented later in this chapter in Section 2.7.4. Using the above equations, conductivity within the semiconductor can be described in terms of mobility, elementary charge q and density of free carriers, Eq.(2.5):

Eq. (2.5)

$$\sigma = nq\mu$$

The density of charge carriers is formulated in Section 2.5.1.

Scattering of carriers affects mobility which in turn affects conductivity and permittivity of the semiconductor. There are two main sources of scattering; lattice scattering and ionised impurity scattering. In a perfectly periodic lattice, carriers do

not interchange their energy with the atoms which form the lattice. At temperatures above 0K, the lattice starts to vibrate, which causes carriers to collide and give up energy. This interaction with the lattice is seen as collisions with particles called phonons. As temperature increases, mobility decreases as collisions between carriers and phonons become more common and more energy is transferred.

Ionised impurity scattering refers to scattering due to doping or other unintentional impurities in the silicon. These local distortions scatter carriers which results in a transfer of energy from the carrier. Unlike lattice scattering, ion impurity scattering becomes less pronounced at higher temperatures as carriers are travelling faster and do not remain in the vicinity of the impurity for long.

For an intrinsic or lightly doped silicon, lattice scattering dominates and has the largest effect on mobility, however if the doping concentration is above 10^{15}cm^{-3} then ionised impurity scattering will be dominant. The mobility can be worked out based on the doping density of the silicon, N_{dope} , using Eq.(2.6).

$$\mu_e = \mu_{min} + \frac{(\mu_{max} - \mu_{min})}{1 + \left(\frac{N_{dope}}{N_{ref}}\right)^{\alpha_{FIT}}} \quad \text{Eq.(2.6)}$$

The equation includes fit parameters $\mu_{min,max}$, N_{ref} and α_{FIT} which have been determined from measurements [8]. The fit parameters for three different dopant types are listed in Table 2.1

Parameter	Arsenic	Phosphorus	Boron
$\mu_{min} (\text{cm}^2\text{V}^{-1}\text{s}^{-1})$	52.2	68.5	44.9
$\mu_{max} (\text{cm}^2\text{V}^{-1}\text{s}^{-1})$	1417	1414	470.5
$N_{ref} (\text{cm}^{-3})$	9.68×10^{16}	9.20×10^{16}	2.23×10^{17}
α_{FIT}	0.680	0.711	0.719

Table 2.1: Dopant types with associated mobility values from best fit data

2.3 Carrier Lifetime

Generally, carrier lifetime is the average amount of time that a carrier, such as an electron, remains in the conduction band before recombining with a hole. In a silicon wafer (a thin disc of silicon), effective carrier lifetime (τ_{eff}) includes bulk (τ_{bulk}) and surface (τ_{surf}) carrier lifetimes [9], Eq.(2.7)

$$\frac{1}{\tau_{eff}} = \frac{1}{\tau_{bulk}} + \frac{1}{\tau_{surf}} \quad \text{Eq.(2.7)}$$

At low carrier densities, bulk lifetime in single crystalline silicon is large (>1ms), hence effective lifetime is dominated by surface carrier lifetime. At the surface of the silicon, carrier lifetime is affected by defects which occur during the silicon manufacturing process, particularly the slicing of the silicon ingot into wafers. Mainly these defects consist of an increased number of dangling silicon bonds which can be considered trap sites which carriers fall into, allowing electrons to fall into the valence band and recombine with holes.

There are three main mechanisms for recombination, namely Shockley Read Hall (SRH relating to τ_{SRH}), radiative (relating to τ_{rad}) and auger (relating to τ_{aug}) recombination. Each can be expressed in terms of effect on carrier lifetime to estimate the bulk carrier lifetime, Eq.(2.8):

$$\frac{1}{\tau_{bulk}} = \frac{1}{\tau_{SRH}} + \frac{1}{\tau_{rad}} + \frac{1}{\tau_{aug}} \quad \text{Eq.(2.8)}$$

2.3.1 Shockley Read Hall (SRH) Recombination

SRH recombination refers to recombination of carriers that are a direct result of defect trap sites. A trap is located in the forbidden region of the energy band, between the valence and conduction band. Once an electron falls into a trap, it is unavailable to carry charge – it will remain in the trap until it loses energy and falls back to the valence band and recombines, there is also the option that it may gain energy and be promoted back to the conduction band (particularly if the trap is located at an energy level just below the conduction band).

Since only one carrier can reside in a trap in a given period this type of recombination is usually dominant at lower carrier densities, when the ratio between number of traps and carriers is closer. At higher carrier densities, traps become full and hence other forms of recombination become more significant.

2.3.2 Radiative Recombination

Radiative recombination refers to a band-to-band interaction between an electron and hole. This type of recombination is dominant in direct band gap materials such as GaAs, but is less common in indirect band gap materials such as silicon. If an electron and hole recombine across the band gap, then a photon is released. The energy has a similar energy to that of the band gap and hence instead of being absorbed is radiated [10]. For silicon, the radiative recombination component is usually ignored as it is very small, namely because the presence of a phonon is required for recombination to occur.

2.3.3 Auger Recombination

Auger recombination becomes significant at carrier concentrations above 10^{16} cm^{-3} . This phenomenon occurs when an electron and a hole directly interact; however instead of generating heat or a photon the energy released is absorbed by a third carrier. This type of recombination only occurs at high carrier densities as the probability of carriers directly interacting is greatly increased. This mechanism limits carrier lifetime and efficiency.

The relationship between carrier concentration n , and Auger carrier lifetime τ_{aug} can be expressed using the Auger coefficient, C_A , Eq.(2.9). Through experimentation this value has been determined to be between 10^{-29} and $10^{-32} \text{ cm}^6 \text{ s}^{-1}$ [11].

$$\tau_{aug} = \frac{1}{n^2 C_A} \quad \text{Eq.(2.9)}$$

Where n is the concentration of carriers and a typical value for C_A is $1.4 \times 10^{-30} \text{ cm}^6 \text{ s}^{-1}$ [12]. In this study, C_A is taken to be a value close to this; $1.6 \times 10^{-30} \text{ cm}^6 \text{ s}^{-1}$. This value is chosen after a fitting study, as it yields better analytical results that correlate to measured data that is presented in Chapter 3.

2.4 Modelling Silicon

Equation Eq. (2.5) introduced conductivity in terms of mobility and density of carriers. Thus, to calculate a photoconductivity profile two aspects must be considered. Firstly, the number of free carriers available to allow photoconductivity and secondly the distribution of these free carriers in the silicon.

The density of free carriers in a semiconductor is determined by three factors:

1. Generation Rate (affected by photon flux and absorption)
2. Recombination Rate (affected by silicon quality)
3. Diffusion Rate (affected by silicon quality and absorption)

2.4.1 Number of Carriers

Generation refers to the process whereby a photon entering the silicon transfers its energy to an electron in the valence band, and promotes it to the conduction band. This creates a free carrier which is then able to conduct a current. Photon flux (φ) measured in $\text{m}^{-2}\text{s}^{-1}$ is usually used to describe this phenomenon, which is the rate at which photons strike a unit area.

Generation depends on the photon flux and the photon energy. The energy of the photons can be related to wavelength of light (λ_l), the speed of light (c) and Planck's constant (h), as previously described in Eq. (2.1).

The power of the light source (P) and the effective area of silicon it strikes (A) yields the power density. Reflection of the incoming photons on the surface of the silicon is accounted for by the R term. S is the spectral efficiency term and is the percentage of photons that will actually free an electron (this is assumed to be 1). Determining the flux, Eq.(2.10), allows an estimate on the number of carriers generated given a particular power density and photon energy.

$$\varphi = \frac{P\lambda_l}{A h c} (1 - R)S \quad \text{Eq.(2.10)}$$

Recombination is the process whereby an electron no longer has enough energy to remain in the conduction band and falls back to the valence band, recombining with

a hole. Electrons lose energy by coming into contact with defect sites and other carriers in the silicon.

Recombination rate is mainly affected by the effective carrier lifetime of the material, τ_{eff} which is largely dependent on the number of defects in the silicon.

Diffusion rate does not have a large effect on the number of carriers available to conduct in the silicon; this effect is mainly concerned with the distribution profile of the carriers.

2.4.2 Distribution of Carriers

Carriers are continuously being generated as long as illumination is applied. The location they are generated depends on where the incoming photon is absorbed. They do not remain in the location they are generated, but tend to move from areas of high concentration to low concentration. Eventually the free electrons lose energy either through collisions or through traps or defect sites in the silicon. They transfer from the conduction band to the valence band and no longer contribute to conductivity.

2.4.2.1 Beer Lambert Absorption

The location which carriers are generated in the silicon can be calculated using the Beer Lambert law [9], Eq.(2.11):

$$I = I_0 e^{-\alpha d} \quad \text{Eq.(2.11)}$$

Where the transmitted light intensity, I , is dependent on the incident radiant flux, I_0 , the absorption coefficient α and the thickness of the semiconductor, d . The absorption coefficient is determined by the wavelength of light. Note that shorter wavelengths have a smaller absorption coefficient.

2.4.2.2 Recombination

In terms of recombination sites the exact location of defects in the silicon is difficult to model generically. However, it is possible to use probability distributions such as the Fermi-Dirac probability distribution function to describe electron energy states [3], but this is beyond the scope of this thesis.

Instead, it is generally correct to consider that recombination at the surface of the silicon is much greater than in the bulk; hence recombination is often referred to in terms of surface recombination velocity. Recombination velocity, v_s , is related to the depth of the silicon d and carrier lifetime at the surface of the silicon, τ_{surf} , by Eq.(2.12). The factor of 2 accounts for the top and bottom surfaces of the silicon.

$$v_s = \frac{d}{2\tau_{surf}} \quad \text{Eq.(2.12)}$$

2.4.2.3 Diffusion

Diffusion rate relates to the movement of free carriers into areas of the silicon which have a lower concentration of carriers. This may result in the carriers diffusing to areas in the silicon which have higher number of defects, affecting the conductivity of the silicon, but mainly the diffusion constant affects the conductivity profile.

Diffusion rate is greatly influenced by the diffusion distance, La . This is dependent on the electron and hole mobilities $\mu_{e,h}$, effective carrier lifetime τ_{eff} , Boltzmann constant, k_b , and temperature T_a , Eq.(2.13)

$$La = \sqrt{\frac{2\mu_e\mu_h\tau_{eff}k_bT_a}{q(\mu_e+\mu_h)}} \quad \text{Eq.(2.13)}$$

Essentially, if carriers remain in the conduction band for longer and are travelling at a faster velocity either due to mobility or temperature then they will diffuse into areas where fewer carriers exist before recombining, affecting conductivity distribution.

2.5 Photoconduction and material properties

In order to understand the potential RF behaviour of a silicon die, certain properties must be considered. Namely, these include conductivity and permittivity. These quantities dictate wave propagation through the silicon and are of key concern when understanding how such a silicon die could be used in an RF circuit.

2.5.1 Photoconductivity

Platte used the generation, recombination and diffusion rates described in section 2.4 and in various publications [13][14] to estimate the number of carriers, n , generated at a particular depths into the silicon, y , Eq.(2.14), parameters and typical values are presented in Table 2.2:

$$n(y) = \frac{P\lambda_l}{A h_c c} (1 - R) S \alpha_c \left\{ e^{(-\alpha_c y)} - \left[\frac{\alpha_c L a^2 + v_s \tau_{eff}}{L a + v_s \tau_{eff}} e^{\left(\frac{-y}{L a}\right)} \right] \right\} \left(\frac{\tau_{eff}}{1 - \alpha_c^2 L a^2} \right) \quad \text{Eq.(2.14)}$$

Constant	Description	Unit	Typical Value
La	Diffusion Length	m	2.2×10^{-2}
$\mu_e \mu_h$	Electron and hole mobilities	$\text{cm}^2(\text{V}^{-1} \cdot \text{s}^{-1})$	1414 478
τ_{eff}	Effective carrier lifetime	s	7×10^{-6}
k_b	Boltzmann constant		1.38×10^{-23}
T_a	Temperature	K	294
q	Electron charge	C	1.66×10^{-19}
n	Concentration of carriers	m^{-3}	$10^{-21} - 10^{-23}$
P	Power of illumination source	W	0.01-0.2
λ_l	Wavelength of illumination source	m	$500-1000 \times 10^{-9}$ (980nm)
A	Area of illumination source	m^2	7.85×10^{-7}
h_c	Plank's constant		1.054×10^{-34}
c	Speed of light	ms^{-1}	3×10^8
R	Surface reflection		0.15-0.35
S	Spectral Efficiency		1
α_c	Absorption coefficient	m^{-1}	6200 @980nm
y	Distance from illuminated surface into silicon	m^{-1}	$0 - 530 \times 10^{-6}$
v_s	Surface recombination velocity	ms^{-1}	0.25-20

Table 2.2: Parameters which affect photoconductivity

The number of carriers and mobilities of the electrons and holes can be used to calculate the DC photoconductivity σ as is described in Eq.(2.15):

$$\sigma = q (\mu_e + \mu_h)n \quad \text{Eq.(2.15)}$$

2.5.2 Factoring in Auger Recombination

Since Platte's formula only includes a surface term for recombination and does not include a bulk recombination, the formula is only valid for carrier densities below 10^{16}cm^{-3} . Above this level, Auger recombination limits the carrier lifetime and should be accounted for in the formula to reflect the change in conductivity profile. An attempt to include this term and analyse the effect is now presented.

The Auger term can be factored into the conductivity equation by recalculating the carrier lifetime of the silicon based on the initial number of carriers generated. Once calculated the new value of carrier lifetime can be substituted into the original equation.

Assuming that Auger recombination dominates over other recombination mechanisms at high carrier concentration then $\tau_{bulk} = \tau_{aug}$. Effective carrier lifetime comprises of both bulk and surface carrier lifetimes, Eq.(2.7). Hence the new effective carrier lifetime can be expressed as Eq.(2.16):

$$\frac{1}{\tau_{eff_aug}} = \frac{1}{\tau_{aug}} + \frac{1}{\tau_{eff}} \quad \text{Eq.(2.16)}$$

Compensated carrier concentration, n_{aug} is computed by replacing τ_{eff} in Eq.(2.13) and Eq.(2.14) with τ_{eff_aug} , indicated in Eq. (2.17) and Eq. (2.18):

$$La_{eff} = \sqrt{\frac{2\mu_e\mu_h \tau_{eff_aug} k_b T_a}{q(\mu_e + \mu_h)}} \quad \text{Eq.(2.17)}$$

$$n_{aug}(y) = \frac{P\lambda_l}{A h_c c} (1 - R) S \alpha_c \left\{ e^{(-\alpha_c y)} - \left[\frac{\alpha_c La_{eff}^2 + v_s \tau_{eff_aug}}{La_{eff}^2 + v_s \tau_{eff_aug}} e^{\left(\frac{-y}{La_{eff}}\right)} \right] \right\} \left(\frac{\tau_{eff_aug}}{1 - \alpha_c^2 La_{eff}^2} \right) \quad \text{Eq.(2.18)}$$

Conductivity then becomes, Eq.(2.19)

$$\sigma = q (\mu_e + \mu_h)n_{aug} \quad \text{Eq.(2.19)}$$

2.5.3 Dielectric Permittivity

Dielectric permittivity is affected by the injection of carriers which increase loss in the semiconductor, in this case silicon. The real part of the dielectric constant decreases as the concentration of carriers increases whereas the imaginary part increases.

Lee et al. [2] present these changes using the equations below. Change in the permittivity is dependent on the original value of dark state silicon ε_L , number of carriers injected, $n_{e,h}$, mass of the carriers generated $m_{e,h}$, plasma frequency ω_p , applied RF signal angular frequency, ω , and collision times for both electrons and holes in silicon $\tau_{e,h}$, Eq.(2.23):

$$\omega_p = \frac{nq^2}{\varepsilon_0 m_e} \quad \text{Eq.(2.20)}$$

$$\tau_e = \frac{\mu_e m_e}{q} \quad \text{Eq.(2.21)}$$

$$\tau_h = \frac{\mu_h m_h}{q} \quad \text{Eq.(2.22)}$$

$$\varepsilon_r = \varepsilon_L + \frac{n_{e,h} q^2}{m_{e,h} \varepsilon_0 \left[-\omega^2 + j \left(\frac{\omega}{\tau_{e,h}} \right) \right]} \quad \text{Eq.(2.23)}$$

The imaginary part of the permittivity relates directly to the phase difference between the constantly alternating electric field and the dipoles in the structure that try to align themselves to the E-field. Normally, the dipoles are randomly arranged in a dielectric. However when an external electric field is applied, they align with this alternating field. Dipoles exist as each atom in the dielectric consists of a cloud of orbiting electrons which react faster than the positively charged nucleus they surround. As the electrons have less mass they align to the alternating electric field faster and hence create a charge imbalance.

2.5.4 Loss Tangent

Loss can be described as in, Eq.(2.24):

$$\tan \delta = \frac{\varepsilon_r'' \varepsilon_0}{\varepsilon_r' \varepsilon_0} \quad \text{Eq.(2.24)}$$

The conductivity, σ , can be described by the imaginary part of the dielectric constant, ϵ_r'' , and is frequency dependent, f , as is presented in Eq.(2.25). Hence it can be used interchangeably with the loss tangent:

$$\sigma = 2\pi f \epsilon_0 \epsilon_r''$$

As conductivity increases, the electric field in the material tends to 0 according to Eq.(2.26) – hence if conductivity is large then loss is also large:

$$\bar{E} = \frac{J_c}{\sigma} \quad \text{Eq.(2.26)}$$

Loss arises due to motion and heat. The loss is attributed to the imaginary component of the permittivity ϵ_r'' which is a function of frequency – this is described as dispersion. The energy supplied by the external electric field is dissipated in the system due to the constant rotation of the dipoles' polarity. Loss is induced by the acceleration and deceleration of motion and friction incurred from this process. Hence as frequency of the applied electric field increases, loss tangent also increases. Alternatively, this effect can also be described directly by representing the permittivity with a real part and an imaginary component, which describes the loss incurred through applying an alternating electric field.

Hence, silicon can be described by the definitions of varying permittivity and conductivity as a function of frequency. This behaviour can be modelled in 3D Electromagnetic Simulation software and is investigated further in Chapter 3. The following sections will outline how the choice and fabrication processes affect the quality and photoconductivity of silicon. This allows values to be assigned to the above formulae for the silicon chosen in this research.

2.6 Photoconductive Material Choice

Classically, the majority of photoconductive devices will have an atomic composition which falls into the following categories; elemental semiconductors (e.g. silicon, Si), Group III-V compounds (e.g. gallium arsenide, GaAs) and Group II-VI Compounds (e.g. cadmium sulphide, CdS) [5]. However more recently, other variants are being

investigated for their potential, such as compounds in the same elemental group (silicon carbide, SiC).

Given the discussion in the section 2.2.2, one might assume that the best choice of semiconductor for photoconductive devices would be a direct bandgap material. However silicon has also proven it is a good candidate for use in photoconductive devices, as its properties (such as mobility) can readily be altered to more efficiently promote conductivity. A short review of different intrinsic semiconductor materials highlights why silicon is chosen for investigation in this thesis.

2.6.1 Elemental Semiconductors: Si

It has been widely demonstrated that silicon can be used as an effective photoconductive RF switch material in applications such as antennas [16] and other microwave circuits [17]. There are four valence electrons per atom in silicon. A covalent bond is shared by two electrons from different atoms at room temperature, under no illumination, Figure 2.3.

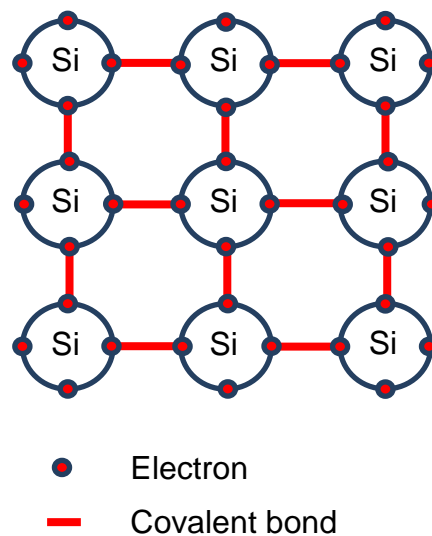


Figure 2.3: Atomic structure of silicon

The photon energy needed to break these bonds is relatively low (Band gap energy, $E_{BG} = 1.1\text{eV}$), making it an ideal contender for photoconductive devices. Once free, the electron leaves the valence band to the conduction band, leaving a hole in the valence band and hence a movement of charge is possible.

2.6.2 Group III-V compounds: GaAs and InP

Karabegovic *et al.* [18] demonstrate gallium arsenide as photoconductive switch material. Gallium arsenide's short carrier lifetime is utilised to produce fast switching speeds for use in producing pulsed microwaves. More generally, the use of GaAs in place of Si has both advantages and disadvantages.

On one hand, the wavelength of light needed to create electron hole pairs is lower than Si. A wavelength closer to visible light increases the number of light sources that are available. At lower wavelengths the signal attenuation is reduced in glass fibres, hence it is more common that fibre optic cables at these lower wavelengths are made from plastic. Hence a more flexible plastic fibre optic could be used to carry the optical signal as opposed to the standard glass fibre optics which usually carry near infra-red signals.

On the other hand, the thermal conductivity of GaAs is a third of Si; $0.5 \text{ Wcm}^{-1}\text{K}^{-1}$ compared to $1.5 \text{ Wcm}^{-1}\text{K}^{-1}$ Table 2.3 (limiting its ability to conduct away heat and increasing the likelihood of failure. From a manufacturing point of view, Si wafer processing for large volume applications is less expensive when compared to GaAs, as wafer size is smaller and material cost is higher [19]. Possible restrictions may also need to be addressed due to gallium arsenide's toxicity.

Properties	Si	GaAs	CdS	6H SiC
Band gap (eV)	1.1	1.42	2.42	3.05
Electron Mobility ($\text{cm}^2\text{V}^{-1}\text{s}^{-1}$) @ 10^{16}	1100	6000	350	950
Thermal Conductivity $\text{W}\cdot\text{cm}^{-1}\cdot\text{K}^{-1}$	1.5	0.5	0.4	4.9
Carrier Lifetime (s)	10^{-6}	10^{-8}	10^{-9}	10^{-8}
Direct /Indirect	Indirect	Direct	Direct	Indirect

Table 2.3: Properties of different semiconductors [19]

Other semiconductors such as indium phosphide InP [21] and variations such as Iron doped indium phosphide, InP: Fe [22] have also been investigated for microwave switching applications. In the latter research, Andersson *et al.* comment on InP: Fe's suitability for use in systems requiring high speed amplitude modulation. Like GaAs, InP has a shorter carrier lifetime (~10ns), making it less suitable when compared to Si for use in a system where a continuous ON or OFF state needs to be maintained. Carrier lifetime describes the length of time an average carrier remains 'free' to conduct current.

2.6.3 Group II-VI compounds: CdS and CdSe

The use of cadmium sulphide (CdS) and cadmium selenide (CdSe) as a photoconductive mechanism in metamorphic antennas is described by Tuffin *et al.* [23]. Photoconductive layers are fabricated using a thick film deposition technique, and the semiconductor powder is mixed with dopants and flux. This technique was particularly researched as a less expensive method to produce photoconductive capability. However, drawbacks to using this compound include relatively low carrier mobility. This value is further decreased after the material undergoes the necessary fabrication processes for proper use as a switch.

2.6.4 Group II compounds: 6H SiC

Other semiconductors such as silicon carbide, 6H SiC [24] have also been utilised as photoconductive switches [24]. The 6H component describes the crystalline structure of the compound which is a hexagonal unit cell in this case. It has particularly high thermal conductivity and high maximum current density, which make it attractive for use in high powered devices [25].

However 6H SiC has a band gap of 3.05eV compared to silicon's 1.1eV, hence much higher photon energy is needed to promote electrons to the conduction band. For this reason these materials usually require an electrical bias to stimulate conductivity. SiC is not optically active at the near IR wavelengths where communications grade light sources are readily available.

2.6.5 Composite Polymers

The advantages and disadvantages of commercially available MEMS (Micro Mechanical Membrane Switches), PIN and varactor diodes have been briefly discussed in Chapter 1. Recent research has also focused on materials that react to the application of a biasing electric field as opposed to illumination. This category comprises phase change chalcogenides or polymer electrolyte-silver-polyaniline composites, where reversible changes in conductivity are achievable. Haupt *et al.* [26] reports that rapid changes are achievable of nearly three orders of magnitude by methods involving laser heating and controlled cooling. Minimum conductivity of these materials is 10^{-7} S/cm, compared to silicon's 10^{-5} S/cm, and the maximum conductivity is limited to 10^3 S/cm. However, these materials still require the addition of DC electrical supply lines to change their conductivity, which can affect performance in reconfigurable antenna applications.

2.7 Silicon Processing

Having briefly discussed a variety of semiconductor materials, the rest of this Chapter focuses on the most viable technology in this field to date, silicon. Silicon can typically be purchased in a disc shape, referred to as a wafer. There are a number of criteria to consider when selecting a semiconductor material which will impact on the performance of the final device. Important factors include: resistivity, carrier lifetime, dopant type and density, wafer thickness and wafer finish. These will be discussed in the following sections in terms of manufacturing process Figure 2.4. Other qualities can also be specified such as wafer diameter, which will determine how many devices can be made from a single wafer and wafer orientation which refer to the orientation of the silicon crystals.

Silicon wafers can be formed in two types, polycrystalline and single crystal. For high quality applications such as integrated circuits and this photoconductive microwave switch, the single crystal approach is required. Polycrystalline silicon is less expensive to grow, but has many crystalline defects, such as grain boundaries, and dislocations.

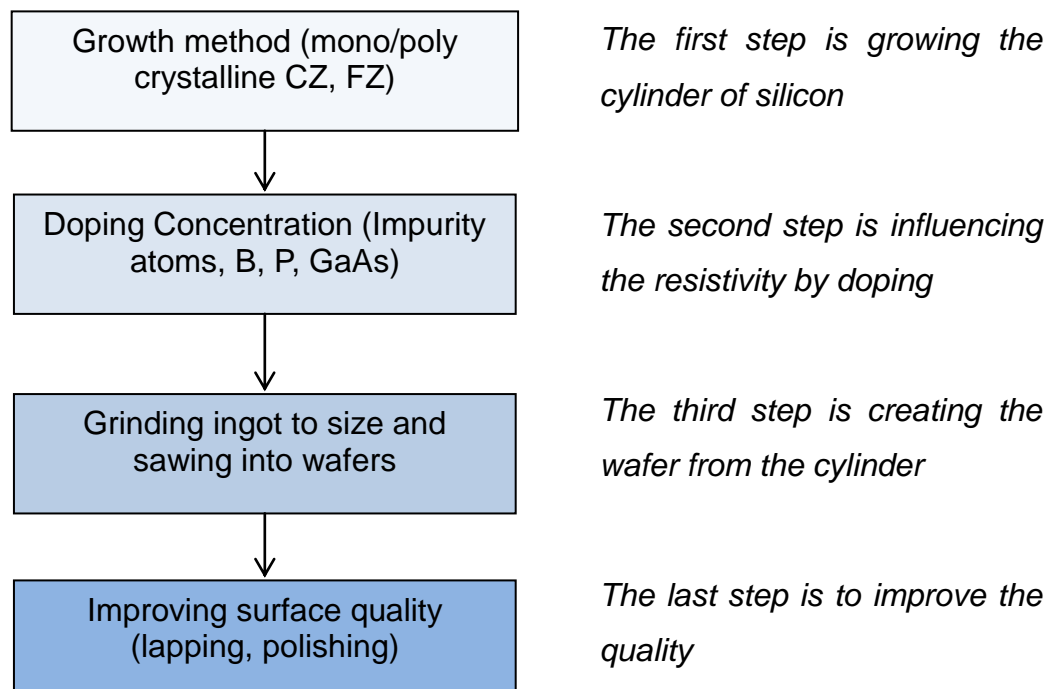


Figure 2.4: Fabrication process of silicon wafers

The two main techniques for growing single crystal silicon are Czochralski (CZ) and Float-Zone (FZ) methods. Both methods are briefly discussed along with other fabrication choices of silicon wafers, which ultimately dictate how photoconductive the silicon will become.

2.7.1 Silicon Growth method: Czochralski (CZ) vs. Float-Zone (FZ)

The Czochralski process involves high purity molten silicon, which may have dopant impurity atoms added such as phosphorus or boron to change the silicon's properties. A pure silicon seed crystal is placed in the molten sand (SiO_2) and pulled out slowly as it is rotated. The SiO_2 gradually dissolves, releasing oxygen. The majority of this oxygen is lost as gas, however some remains in the silicon and is essentially an impurity. The result is a silicon rod that is called an ingot. The diameter of the silicon ingot is determined by the temperature and rate at which the rod is removed and rotated.

The Float-Zone process starts with a high-purity polycrystalline rod and a monocrystalline silicon seed crystal that is held face to face in a vertical position and is rotated. Both elements are partially melted and allowed to make contact. As the molten zone moves along the polycrystalline rod, the silicon solidifies as a single crystal [27].

The FZ Silicon has lower levels of oxygen and carbon impurities due to the fact the process is carried out in a gaseous chamber, where silicon is not in contact with the chamber walls. This method of growth can therefore produce very pure, high resistivity silicon with long carrier lifetimes.

The CZ technique has the benefits of better resistance of the wafers to thermal stress, faster production speed and lower cost. However, in this research a Float-Zone grown wafer is used to manufacture the switches. The important qualities of this method of growth include high resistivity and long carrier lifetimes which can be achieved due to the reduced impurities in the silicon.

2.7.2 Resistivity and Doping

The resistivity is controlled by the impurity level of the silicon. Unwanted impurities are introduced to the silicon depending on the silicon growing process, which will be discussed in the upcoming section. However, impurities in terms of doping atoms are sometimes intentionally introduced to the silicon in order to change its conductivity and mobility.

High levels of doping introduce atoms of different sizes and increase the occurrence of local areas of charge. This increases atom scattering hence reducing mobility of the carriers. The presence of these foreign atoms also increases the defect sites within the silicon crystalline lattice, which increases the recombination of carriers. Hence a compromise between acceptable resistivity, recombination and mobility which affect conductivity in both the ON and OFF state of the switch is required

2.7.3 Thickness of wafer

After the ingot has been grown and any dopant impurities introduced, the ingot is ground to the exact diameter required and cut into wafers using a diamond saw.

Thickness of the wafer should be chosen according to wavelength of illumination used to control the photoconductive switch. This is directly related to the absorption coefficient, α_c ; if the photons pass through the silicon they will not contribute to conductivity. Robustness of the wafer may also need to be considered.

2.7.4 Processing the Ingot Polished Surfaces

In order to remove damaged surface silicon, a technique called lapping is performed, which ensures a flat wafer surface. Wafers are then etched in a chemically active reagent to remove any crystal damage remaining from the previous process step. Finally, the surface may be polished to ensure an ultra-smooth finish.

When purchasing silicon wafers, the finish is offered as either unpolished, polished one side or polished both sides. The main bulk of this research concentrates on silicon which has been polished on both sides and which provides a superior performance due to increased contact between the silicon and copper transmission line.

2.8 Silicon Properties

The fabrication process dictates the physical properties of the silicon which in turn affect the potential for photoconductivity. This section introduces the physical properties of the silicon used in this thesis. These values can then be used in the Equations introduced in section 2.4 in order to calculate the photoconductivity profile. The effect of using different wavelengths of light to illuminate the silicon can be investigated for different thickness of silicon.

2.8.1 Properties and fabrication of the Silicon in this thesis

Photoconductive microwave switches were first investigated by Auston in 1975 [28]. Here photoconductivity was produced by the absorption of picoseconds optical pulses in a silicon substrate. In contrast the current photoconductive switch being investigated in this research consists of a die of phosphorous doped silicon, resistivity $>14000\Omega$, attached between two lengths of copper microstrip line.

Silicon wafer with the properties listed in Table 2.4 was used in this thesis and has previously demonstrated good performance in Panagamuwa [29] and Chauraya's [30] studies:

Criteria	Value
Type	Float Zone
Doping	N-Type (P)
Resistivity	$\sim 1.4 \times 10^6 \Omega \cdot \text{cm}^{-1}$
Thickness	300um
Finish	Polished both sides
Bulk carrier lifetime	>1ms
Orientation	1-0-0

Table 2.4: Phosphorous doped silicon properties used in this study as listed by manufacturer (note orientation relates to the crystal structure)

A second type of silicon wafer is also investigated in this work, with slightly lower grade quality, and has qualities presented in Table 2.5:

Criteria	Value
Type	Float Zone
Doping	P-Type (B)
Resistivity	$\sim 1 \times 10^6 \Omega \cdot \text{cm}^{-1}$
Thickness	530um
Finish	Polished one side only
Bulk Carrier lifetime	Not stated
Orientation	1-0-0

Table 2.5: Boron doped silicon properties used in this study as listed by manufacturer

For the purpose of identification, these two silicon types are identified either as phosphorous or boron doped in future chapters.

In order to reduce the radiant flux needed to control the photoconductive switch, N-type phosphorus is introduced to the silicon, with a concentration of $\sim 3 \times 10^{11} \text{cm}^{-3}$. This helps facilitate conduction in the ON state, yet maintains a high resistivity of $\sim 1.4 \times 10^6 \Omega \cdot \text{cm}^{-1}$ in the OFF state so isolation is not compromised. As doping concentration is increased, these impurities cause the carrier lifetime of the photo-

generated carriers to decrease and hence limits the effectiveness of conductivity generated through illumination.

Further silicon processing to produce an effective RF switch in die form will be investigated in more detail in Chapter 4.

2.9 Conductivity Profile (with Auger Recombination)

Figure 2.5 demonstrates the effect that the Auger recombination term has on conductivity profile for 10mW, 50mW and 200mW of radiant flux at 980nm wavelength of illumination. The values relate to the phosphorous doped silicon and have been listed previously in Table 2.2. Note that reflection from the surface is 0.15. The traces are generated using Eq.(2.14) no Auger term and Eq.(2.18) with Auger term, to calculate the number of carrier generated at different depths into the silicon.

The effect that the Auger recombination term has on conductivity is much greater for the 200mW of radiant flux. At a distance of $1\mu\text{m}$ into the silicon the conductivity without Auger term is 5114S/m compared to 1892S/m with the inclusion of the Auger recombination term. This is due to the fact that as the applied radiant flux increases the number of carriers produced increases. Auger recombination becomes more influential at high carrier densities, as the carriers are more likely to interact. The Auger recombination is dependent on the square of the number of carriers, so as recombination is increased the carrier lifetime is drastically reduced – the term becomes dominant over other types of recombination as number of carriers increases above $\sim 10^{16} \text{ cm}^{-3}$ (depending on the quality of the silicon).

The Auger term has little effect when 10mW of radiant flux is assumed. The maximum conductivity in the die occurs near the surface and is $\sim 260\text{S/m}$ without the Auger term applied. The corresponding carrier concentration that produces a conductivity of $\sim 260\text{S/m}$ is $8.68 \times 10^{15} \text{ cm}^{-3}$; at this level of carrier concentration the Auger term is not dominant. The small reduction in conductivity when the Auger term for a 10mW of radiant flux is applied can be seen more clearly in Figure 2.6. If 50mW of radiant flux is applied, the Auger term reduces the conductivity at the surface by 110S/m when compared to not including the term.

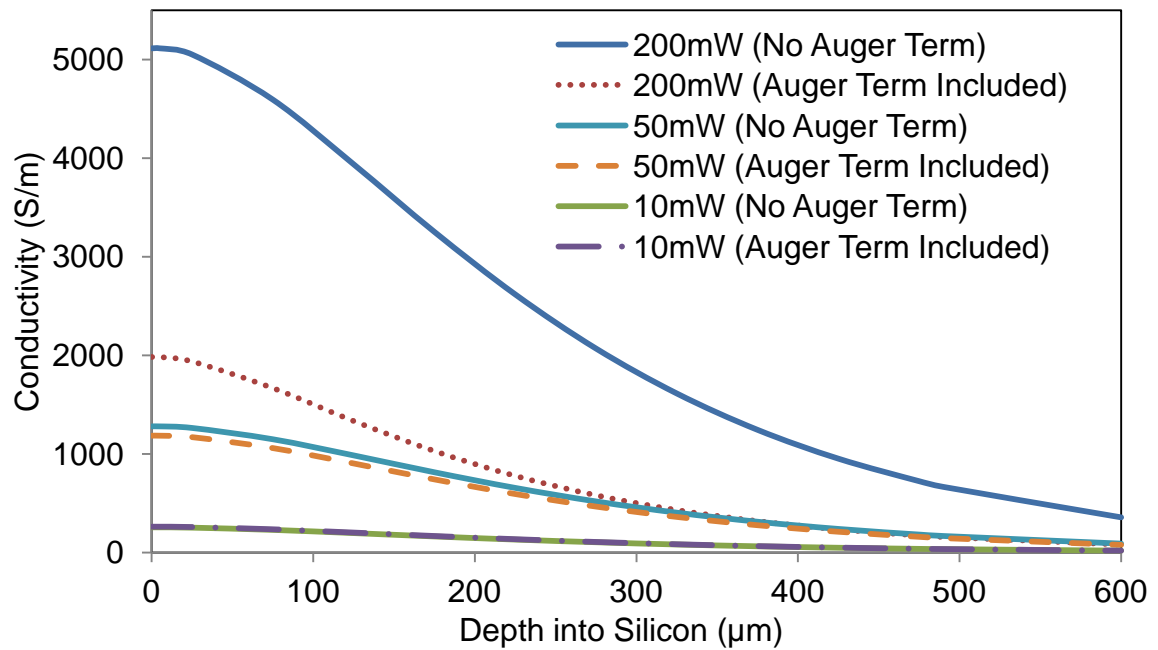


Figure 2.5: Conductivity profile for 10mW, 50mW and 200mW of radiant flux at 980nm. The graph demonstrates the effect the Auger term has on the conductivity profile

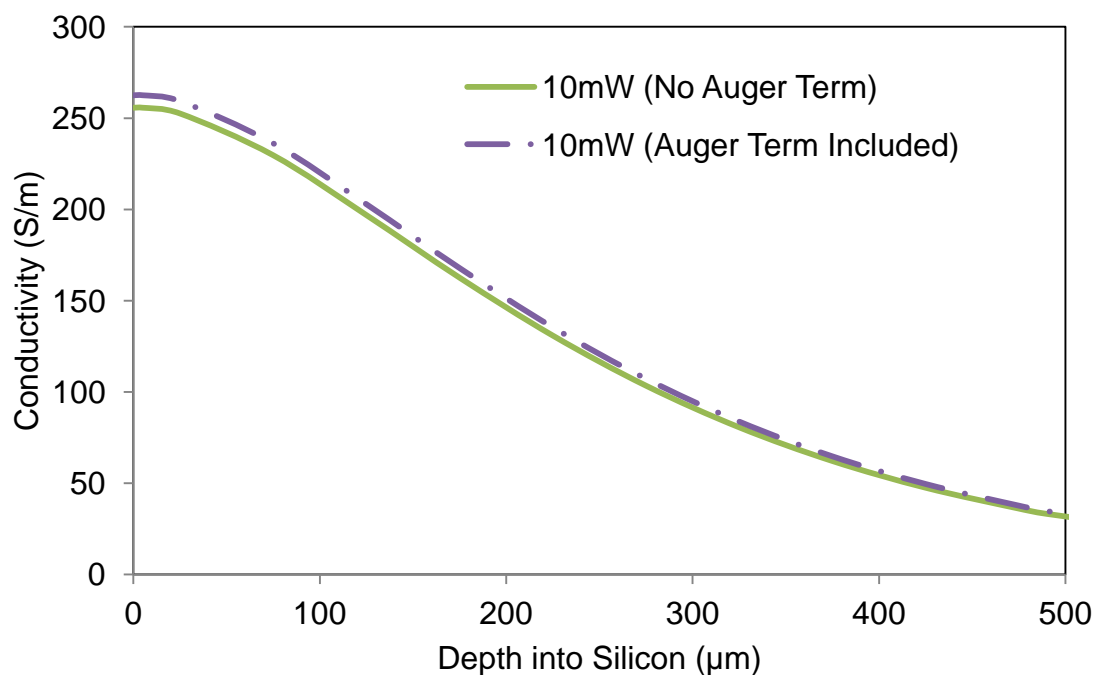


Figure 2.6: Conductivity profile for 10mW of radiant flux at 980nm. The graph demonstrates that the effect the Auger term is only small with relation to the conductivity profile at this radiant flux

In Chapter 3, the conductivity profiles generated here are investigated further through EM simulation and comparison with measured results. Both conductivity profiles with and without Auger term are simulated and compared to measured results to analyse the profiles.

The permittivity is dependent on the carrier concentration. As carrier concentration increases, the real part of the permittivity decreases from the dark state permittivity of 11.8, as is demonstrated in Figure 2.7. As the number of carrier increases in the silicon, the permittivity approaches the value for metals. A characteristic frequency at which the material changes from a dielectric to a metallic response is defined as the plasma frequency, ω_p . This is when the real part of the permittivity approaches 0 [31]. The imaginary part of the permittivity is very important in describing conductors, as it describes the conductivity and is responsible for the loss in the silicon. As number of carriers increases the imaginary part of permittivity decreases (resulting in large negative values), as is shown in Figure 2.8. This gives an idea of how the silicon reacts at different optical illumination intensities, using the Auger term to account for higher recombination at larger carrier densities.

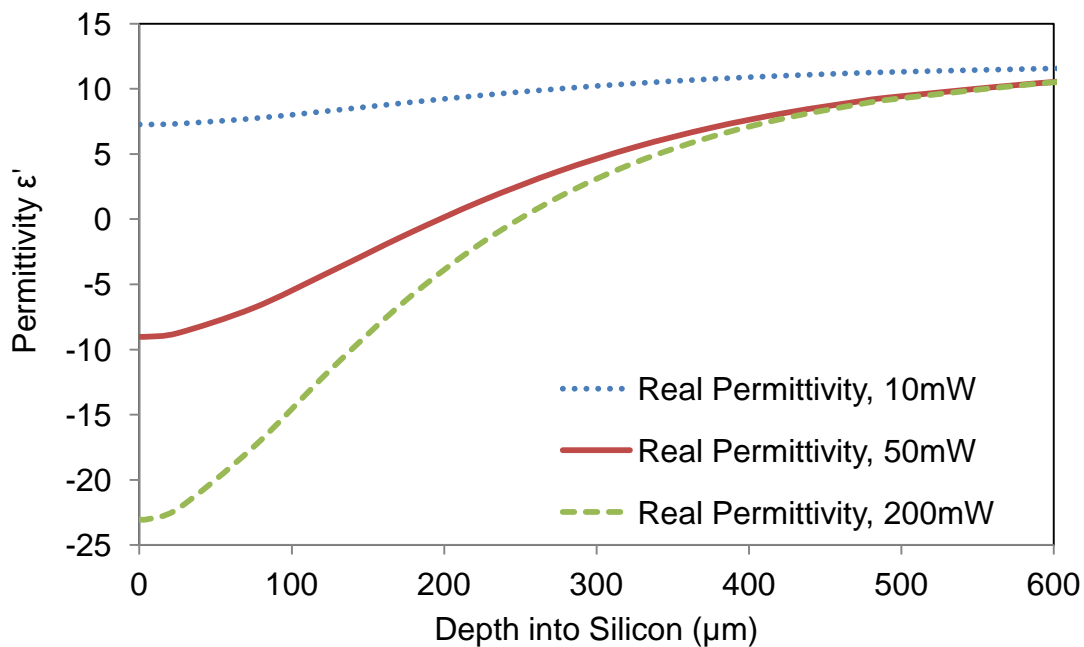


Figure 2.7: Real part of the permittivity for Phosphorous doped silicon - carrier density is calculated including the Auger Term

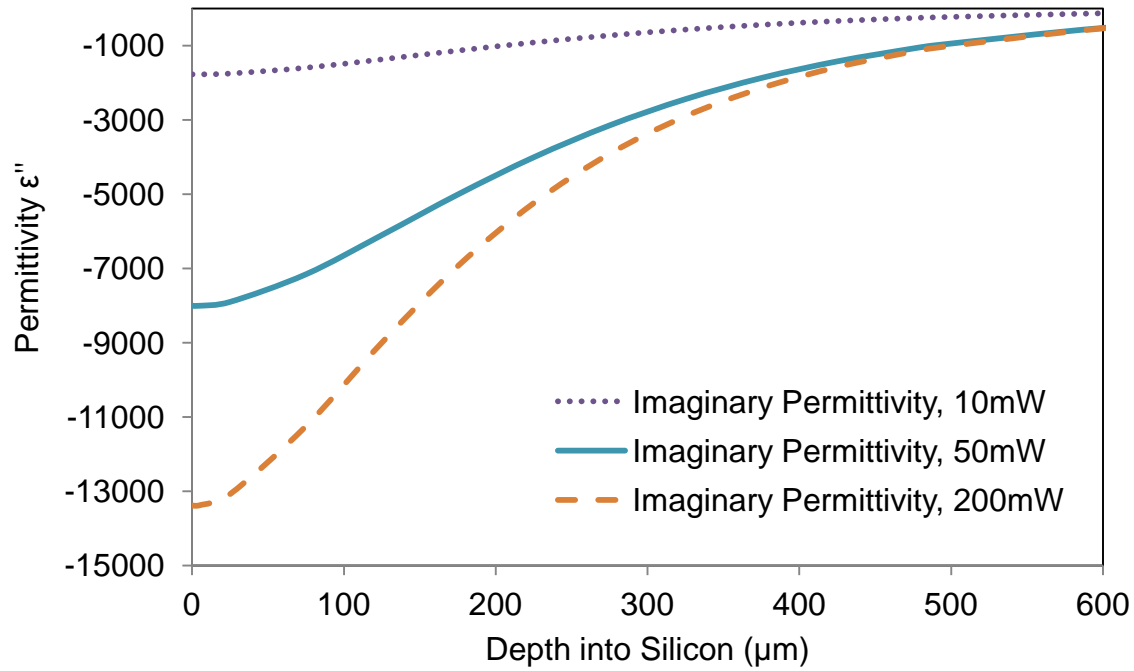


Figure 2.8: Imaginary part of the permittivity for Phosphorous doped silicon - carrier density is calculated including the Auger Term

2.10 Optimum Wavelength

It has been demonstrated that conductivity profile differs with radiant flux. However, conductivity profile also varies with wavelength of illumination, hence it is expected that there will be an optimum wavelength of light which produces the most favourable conductivity profile. This is investigated for two depths of silicon and by considering the average conductivity in the silicon die. A radiant flux of 10mW is chosen to conduct this investigation. The Phosphorous doped silicon is examined.

2.10.1 Absorption depth and diffusion constant

Lan *et al.* experimentally demonstrate that wavelength of light affects insertion loss of an optically controlled microwave switch [31]. When comparing 635nm, 808nm and 980nm of laser illumination as a light source at the same radiant flux, 980nm yielded the least insertion loss for a 2GHz RF signal.

Estimating the best wavelength of light for the generation of free carriers depends on the depth and quality of the silicon. The absorption depth has a large impact on the photoconductivity profile and is dictated by the wavelength of light. Higher wavelengths mean that photons are absorbed deeper in the silicon – if the wavelength is too high, a significant number of photons are likely to be transmitted through the wafer. Figure 2.9 depicts typical absorption depths with varying wavelength of light. To be clear, absorption depth is the inverse of the absorption coefficient. It is the distance into the material at which light drops by a factor of $1/e$ (~36%) of its original intensity.

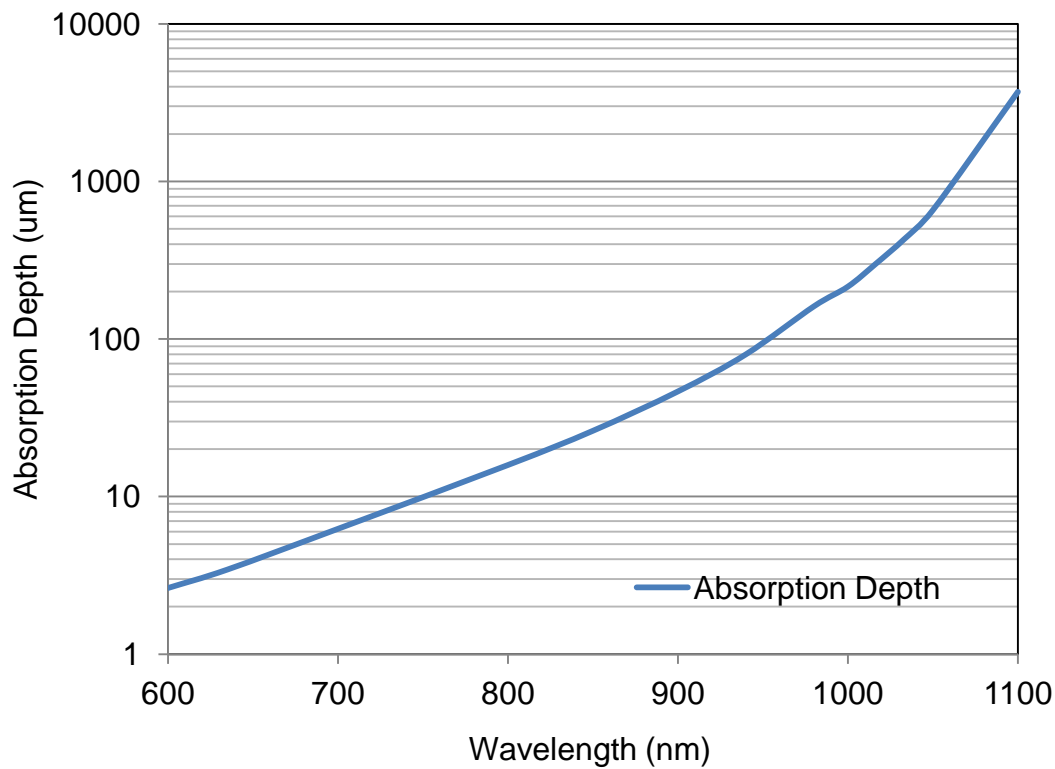


Figure 2.9: Measured data of photon absorption depth in silicon [34].

In this section on optimum wavelength, silicon with a depth of 0.3mm and 0.53mm is studied as these are the two depths of silicon that will be investigated in terms of RF switch performance and measured in subsequent chapters. These two silicon types are investigated as they are pre-purchased from previous studies by Panagamuwa [29] and Chauraya [30] at Loughborough University. For a 0.3mm silicon, ~3.5% of the light is transmitted typically using a wavelength of light of 980nm to illuminate.

Thinner silicon dice may require lower wavelengths in order not to incur optical losses through non-absorption.

Silicon quality must also be considered when choosing a wavelength of light. If there is high surface recombination then a low wavelength of light would result in carriers recombining as soon as they are created as photons are absorbed close to the surface at lower wavelengths. Diffusion coefficient should be considered in this instance. In order to observe both absorption and diffusion effects Eq. (2.18) will be used to generate conductivity profiles based on the wavelength of light. Values relate to the phosphorous doped silicon wafer outlined in Table 2.4. Figure 2.10 depicts change in conductivity with regards to depth into the silicon from the light source.

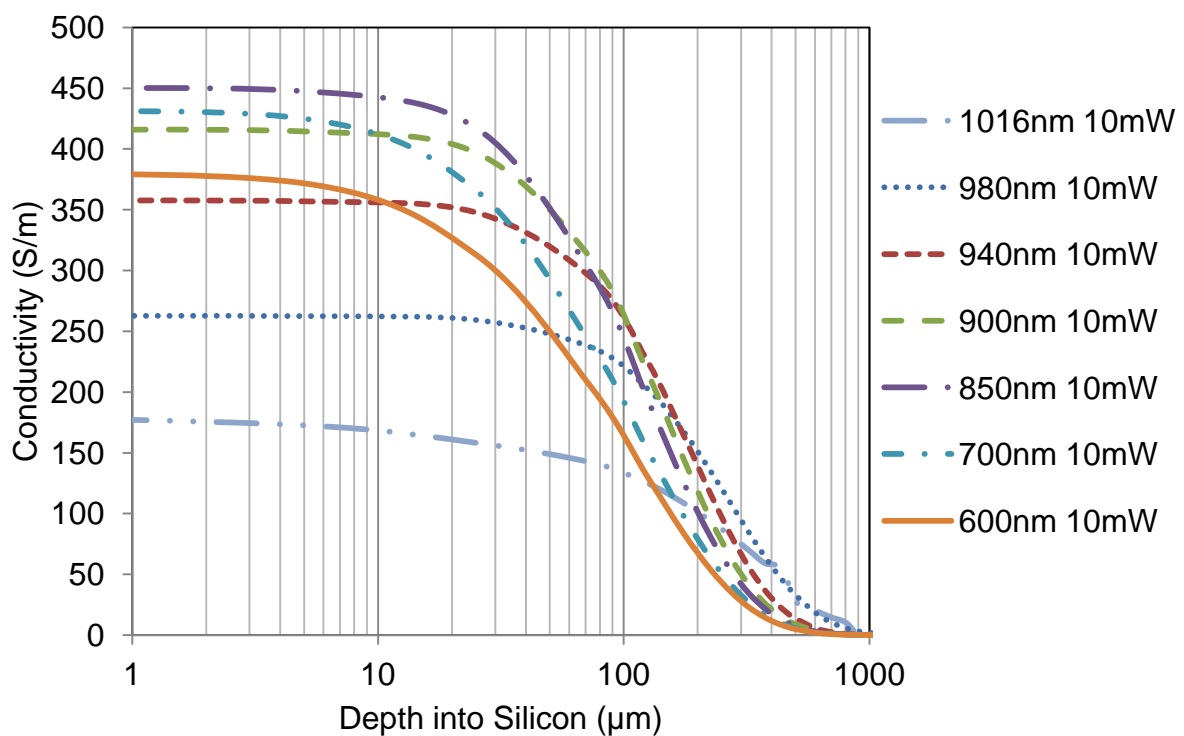


Figure 2.10: Conductivity in silicon material at 10mW of radiant flux for varying depths into the silicon

The first thing to note here is that the conductivity behaviour at different silicon depths can be separated into two profiles – pre 100μm depth and post 100μm depth. Considering the conductivity results at small silicon depths (<100μm), it is clear that the higher wavelengths of light 940nm and 980nm results in reduced conductivities.

From an absorption point of view, this is expected as a larger majority of the incoming photons are being absorbed deeper (i.e. $>100\text{ }\mu\text{m}$) in the silicon.

Following this logic the lowest wavelengths of light 600nm should produce the highest conductivity in the silicon at these smaller silicon depths, however this is clearly not the case. One limiting factor for conductivity is the recombination rate at the surface of the silicon, which is high due to the defects introduced in the manufacture stage. Hence, if electrons are created near the surface, they will recombine faster than if they are generated in the bulk. This is why the 'mid' wavelengths of light such 850nm and 900nm produce the most conductivity in the pre-100 μm depths within the silicon.

Post 100 μm depth conductivity behaviour is displayed in more detail in Figure 2.11. At the depth of 300 μm , the higher wavelength of light produce the highest conductivity within the sample, and as wavelength reduces so does the conductivity at that depth.

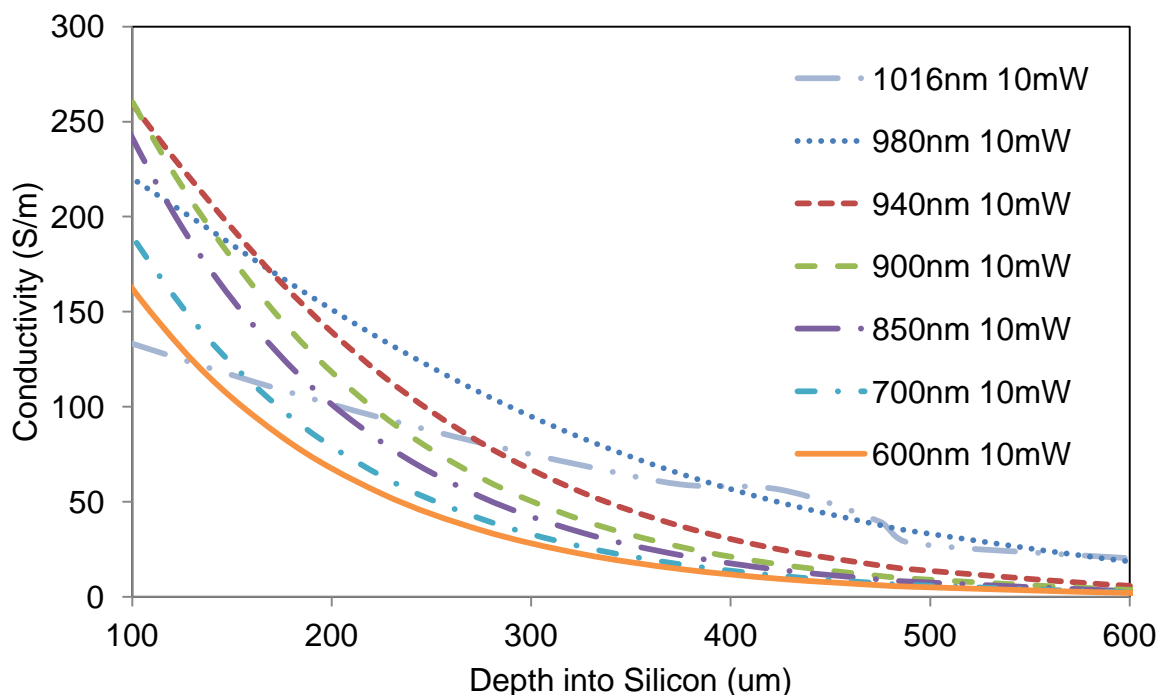


Figure 2.11: Conductivity in silicon material at 10mW of radiant flux at a wavelength of 980nm

The main point to consider here is that the wavelength of light chosen to illuminate the silicon has a large effect on conductivity of the sample at different depths – it

should be chosen carefully to reflect the depth of the silicon. The second point is that diffusion of the carriers generated should also be considered along with quality of the silicon being used.

To put the above results into context, the average conductivity of the silicon samples has been computed for both a 0.3mm silicon die and a 0.53mm silicon die, Figure 2.12. Here, the results clearly show there is a peak in the average conductivity at a specific wavelength. For the 0.3mm silicon this value is 930nm and for the 0.53mm sample the value is higher, 960nm. If it is assumed for the moment that a higher average conductivity will allow higher transmission through the switch, then it benefits to use the wavelength of light which generates the highest average value.

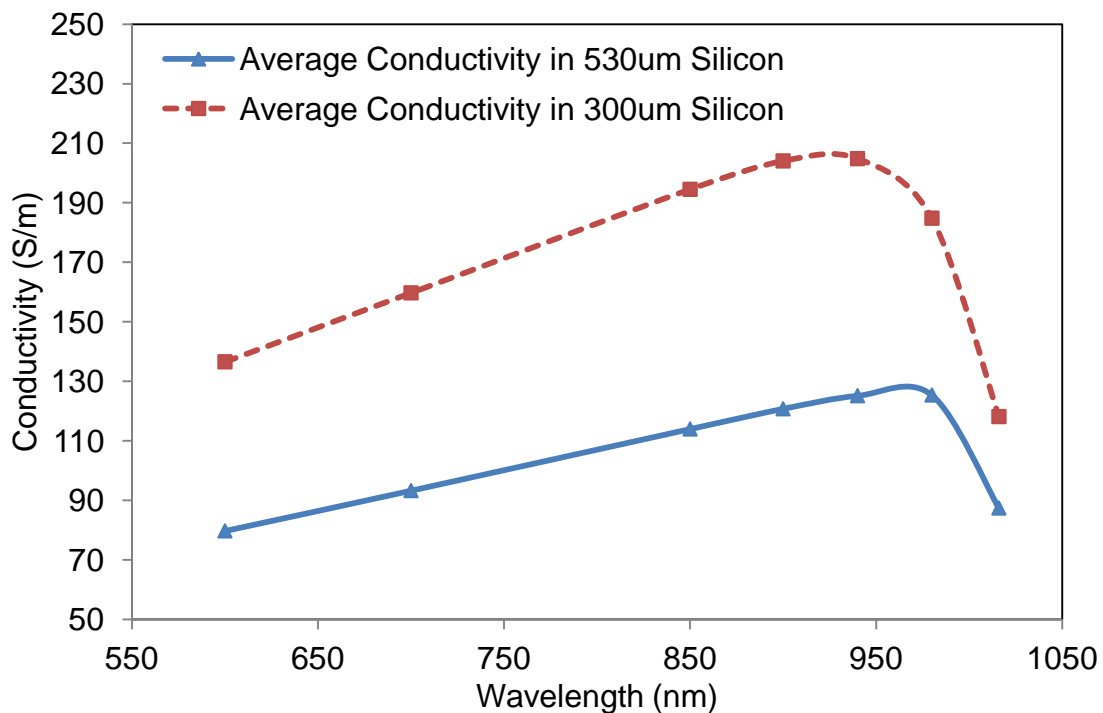


Figure 2.12: Average conductivity in silicon material for depths of 0.3 and 0.53mm at 10mW of radiant flux at a wavelength of 980nm

At high conductivities the RF signal travels at the edge of the conductor, due to the skin depth effect. When the conductivity is $<1000\text{S/m}$, the skin depth is over $160\mu\text{m}$. Since the skin depth is in the same order as the die thickness (between 0-10GHz) it is assumed the RF signal will likely travel through the entirety of the switch. To this end a high average conductivity is advantageous. The effect is further investigated in Chapter 3, where simulations on signal planarity are investigated. The conclusion is

that thicker switches require higher wavelengths of light to improve average conductivity. The absorption depth is greater at these wavelengths and the carriers generated have a greater depth in which to further diffuse.

2.10.2 Beam Profile

Having discussed the appropriate wavelength of light to use for the silicon investigated in this research, a 980nm light source is used for most of the following studies. Photoconduction in the silicon is induced by laser light delivered via a fibre optic cable. The system consists of a 980nm 1W laser housed in a metal enclosure. The laser is coupled to a 1mm diameter fused silica fibre optic cable through a lens. Through varying the current to the laser the radiant flux delivered can be varied between 0 – 200mW. The radiant flux was measured using a radiant flux meter.

Using a beam profiler, WinCamD from DataRay [35], the light source was characterised in terms of power distribution, Figure 2.13.

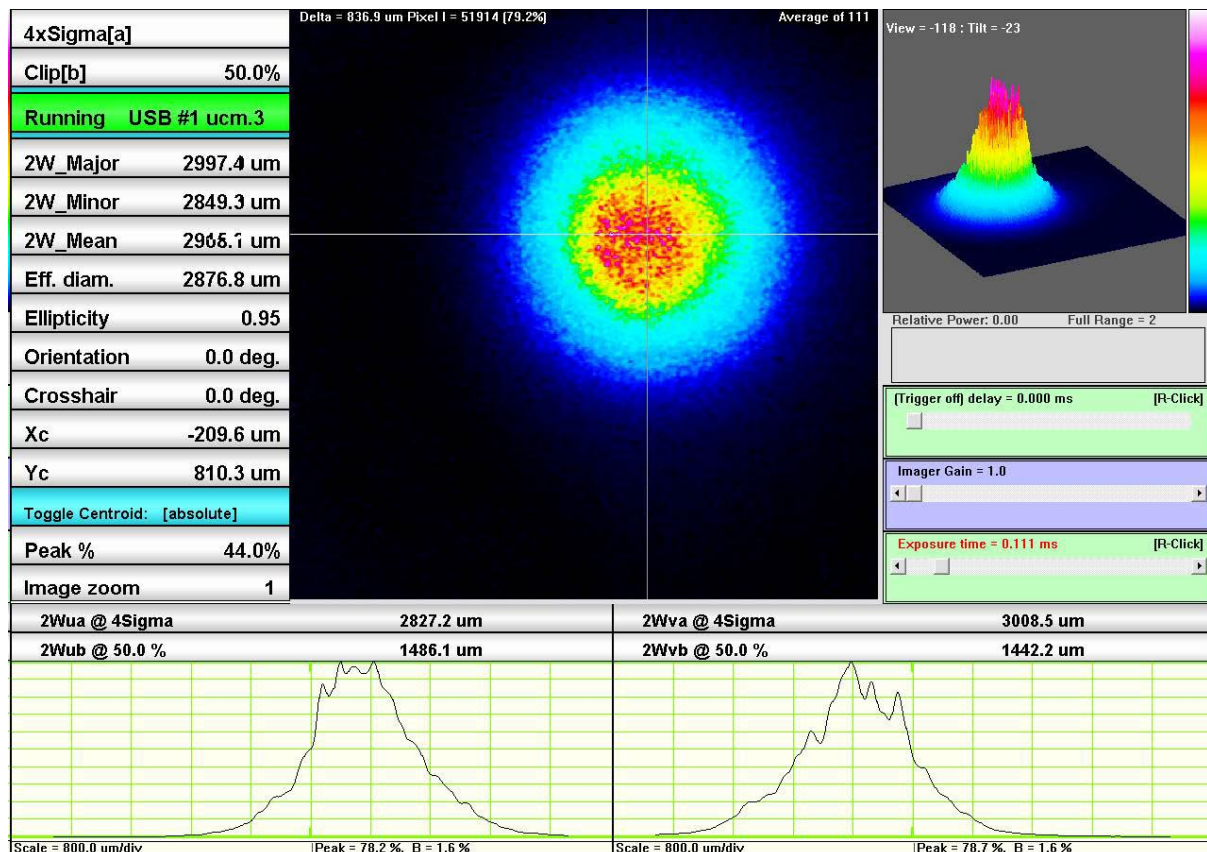


Figure 2.13: Beam profile for the fibre-optic coupled laser source which illuminates the silicon in this study

The camera captures the power density of the incident beam, and the DataRay software allows analysis of the beam in terms of wavelength, distribution and power. This is presented for the chosen laser source, incorporating the fibre optic cable for delivery, there is a Gaussian distribution and the wavelength of light is confirmed to be 980nm.

Since both silicon and light source have been defined, it is possible to model the switch on a transmission line in the following chapter.

2.11 Conclusions

One of the most important concepts that allows photoconduction within semiconductors is the band gap structure, which exhibits a small band gap energy separating valence and conduction band. Within silicon, this allows photons with a wavelength less than 1100nm to break the covalent bonds between silicon atoms and creates a free electron in the conduction band. Since silicon is an indirect bandgap material, a phonon is also required to promote conductivity within the material.

Doping of the silicon increases its conductivity and also has an effect on both mobility and carrier lifetime. These qualities have a direct effect on the photoconductivity profile created by illumination of the silicon.

Formulae are presented to calculate the change in carrier density, dielectric constant and loss tangent which occur when the silicon is illuminated. This data is required in order to run electromagnetic simulations of the microwave switch to determine RF performance. An extra term is added to Platte's formula to compensate for the Auger recombination which occurs at carrier concentrations above 10^{16} cm^{-3} .

Choice of fabrication process of the silicon wafer impacts the potential photoconductive performance of the silicon switch in terms of recombination centres and ON and OFF state conductivity.

The fabrication process and photoconductivity profile for silicon used in this thesis has been presented. It can be shown that there is an ideal wavelength of light which should be utilised in order to efficiently promote conductivity within this silicon. This

wavelength is dictated by the silicon depth, because absorption is dependent on the Beer Lambert Law. For a 300 μ m thick switch, the optimum wavelength was calculated as 930nm. For a switch with 530 μ m thickness, the ideal wavelength is 960nm. The actual wavelength chosen for use in this thesis conforms to a 980nm laser. This is the closest commercially available wavelength that can be produced via a laser diode. Although LEDs are available for a range of wavelengths they do not produce coherent light – this means they are more difficult to focus into a high intensity spot.

The conductivity profile calculated in this chapter will be used in the following chapter in order to investigate possible packaging strategies through numerical modelling.

2.12 References

- [1] W. Platte, and B. Sauerer, “Optically CW-induced losses in semiconductor coplanar waveguides” IEEE Trans. Microwave theory and Techniques, Vol. 37 pp. 139, Jan 1989
- [2] C. H. Lee, P.S. Mak, and A.P. DeFonzo,” Optical control of Millimeter-wave propagation in dielectric waveguides,” IEEE Journal of quantum electronics, Vol. 16, No. 3, March 1980
- [3] F. J. Hyde “Semiconductors” Macdonald & Co., First published 1965, pp.35
- [4] C. Kittel, “Introduction to solid state physics,” John Wiley & Sons, Seventh Edition 1996.
- [5] S. M. Sze, “Physics of semiconductor devices,” John Wiley & Sons, Second Edition, 1981 (first published 1969).
- [6] J. Singh “Electronic and Optoelectronic Properties of Semiconductor Structures” Cambridge University Press, 2003 pp 345
- [7] R. S. Muller and T. I. Kamins “Device electronics for integrated circuits” John Wiley and Sons, 3rd ed. 2003

- [8] R. C. Jaeger and T. N. Blalock, "Microelectronic Circuit Design", Fourth Edition, McGraw-Hill, 2011, Originally first published 1997
- [9] R. H. Bube, "Photoelectronic properties of semiconductors" Cambridge University Press, 1992.
- [10] C. Honsberg and S. Bowden, "PVCDROM Bulk Lifetime"
<http://pveducation.org/pvcdrom/characterisation/bulk-lifetime>, last accessed 4th April 2014
- [11] R. A. Sinton and R. M. Swanson, "Recombination in highly injected silicon (solar cells)," IEEE Trans. Electron Devices, vol. 34, no. 6, pp. 1380-9, Jun 1987
- [12] Ioffe Physical Technical Institute "Electrical Properties of Silicon," available online <http://www.ioffe.ru/SVA/NSM/Semicond/Si/electric.html> last accessed 17th June 2014
- [13] W. Platte "Effective photoconductivity and plasma depth in optically quasi-CW controlled microwave switching devices" IEE Proceedings, Vol. 135, Pt. J , No. 3, pp. 251-253, Jun. 1988
- [14] W. Platte "Visual indication of locally varying photoconductivity" IEE Proceedings, Vol. 131, Pt. I, No. 3, pp. 77-81, Jun. 1984
- [15] C. Balanis "Advanced engineering electromagnetics", John Wiley & sons, Inc. pp. 78, 1989.
- [16] Y. Tawk, M. Al-Husseini, S. Hemmady, A. R. Albrecht, G. Balakrishnan, and C. G. Christodoulou. "Implementation of a cognitive radio front-end using optically reconfigurable antennas." In Electromagnetics in Advanced Applications (ICEAA), 2010 International Conference on, pp. 294-297. IEEE, 2010.
- [17] K. Rabbi, L. Athukorala, C. J. Panagamuwa, J. C. Vardaxoglou, and D. Budimir. "High-linearity reconfigurable microstrip UWB bandpass filters." In Microwave Integrated Circuits Conference (EuMIC), 2011 European, pp. 172-175. IEEE, 2011.

- [18] A. Karabegovic, R. M. O'Connell, and W. C. Nunnally, "Photoconductive switch design for microwave applications," IEEE Trans. Dielectrics and Electrical Insulation, vol. 16, No. 4, 2009
- [19] P. Hindle "The state of RF microwave switches"
<http://www.microwavejournal.com/articles/10269-the-state-of-rf-and-microwave-switches>, November 2010
- [20] J. Crowder "Packaging options expand in RF power" EE Times, August 2010
[website:http://www.eetimes.com/design/microwave-rf-design/4206015/Packaging-options-expand-in-RF-power](http://www.eetimes.com/design/microwave-rf-design/4206015/Packaging-options-expand-in-RF-power) Last accessed 13th August 2010
- [21] F. J. Leonberger and P. F. Moulton, "High-speed InP optoelectronic switch," Applied Physics Letters, vol. 40, pp. 447-449, Nov. 1979.
- [22] R. Andersson and S. T. Eng, "Phase and amplitude characteristics of InP : Fe modified interdigitated gap photoconductive microwave switches," IEEE Trans. on microwave theory and techniques, Vol. 37, No.4, pp. 729, Apr 1989
- [23] R. P. Tuffin, I. C. Sage, B. J. Hughes and G. J. Ball, "Electronically Controlled Metamorphic Antenna," EMRS DTC 4th Annual Technical Conference, Edinburgh, Jul. 2007.
- [24] K. S. Kelkar, N. E. Islam, C. M. Fessler and W. C. Nunnally, "Design and characterisation of silicon carbide photoconductive switches for high field applications" Journal of Applied Physics, Vol. 100 , Issue 12, pp. 124905-124905-5, 2006
- [25] M. Bhatnagar, and B. Jayant Baliga. "Comparison of 6H-SiC, 3C-SiC, and Si for power devices." Electron Devices, IEEE Transactions on 40, no. 3 (1993): 645-655.
- [26] R. L. Haupt and J. R. Flemish, "Reconfigurable and Adaptive Antennas Using Materials with Variable Conductivity", IEEE Second NASA/ESA Conference on Adaptive Hardware and Systems, 2007

- [27] S. Meroli "Two growth techniques for mono-crystalline silicon: Czochralski vs Float Zone" Website http://meroli.web.cern.ch/meroli/Lecture_silicon_floatzone_czochralski.html last accessed 22/08/2013
- [28] D. H. Auston, "Picosend optoelectronic switching and gating in silicon", Appl. Phys. Lett. 26 pp. 101–103, 1975.
- [29] C. J. Panagamuwa "An investigation of transmission line switching and frequency shifting in dipole antennas using optically activated silicon switches", Doctoral Thesis (Ph.D.) Loughborough University, 2004
- [30] A. Chauraya "Photoconductive switching using silicon and its applications in antennas and reconfigurable metallodielectric electromagnetic band gap (EBG) structures" Doctoral Thesis (Ph.D.) Loughborough University, 2006
- [31] M. S Dresselhaus, "Optical properties of solids." Proceedings of the International School of Physics, Academic Press NY, 1966
- [32] L. Lan, Z. Deshuang, L. Feng, Z. Qiaoli, and W. Bing Zhong., "Influence of laser wavelength on insertion loss of silicon based optically controlled microwave switch." Microwave and Optical Technology Letters 55, no. 1, pp. 187-190, 2013.
- [33] C. Honsberg and S. Bowden, "PVCDROM : optical properties of silicon" <http://pveducation.org/pvcdrom/materials/optical-properties-of-silicon>, last accessed 7th March 2014
- [34] Virginia Semiconductor, Inc., "Optical Properties of Silicon" <http://www.virginiasemi.com/> last accessed November 2011
- [35] DataRay "WinCamD S-WCD-UCD23" <http://www.dataray.com/> last accessed 12th June 2014

3 Numerical Modelling and Packaging Design

3.1 Introduction

In order to investigate packaging techniques and optimise switch performance, a number of different silicon die models are considered in terms of their conductivity profile. The transmission line topology is also an important aspect which dictates insertion loss and isolation. This must be designed in relation to the light source and silicon size. The chapter opens with a brief introduction into the current state of the art in terms of designing and simulating photoconductive microwave switches in terms of numerical modelling.

A simulation study is presented in order to design an optimised transmission line through numerical modelling. Optimisation is particularly based on transmission performance in both the ON and OFF state of the switch. The latter section of the chapter focuses on comparing various simulation models i.e. the conductivity profiles generated in Chapter 2 will now be used to produce a 3D EM simulation model for the silicon. These are then used to explore the concept of signal planarity within the switch and the associated optical feed technique.

3.1.1 Electromagnetic Simulation of Silicon

When designing reconfigurable circuits or antennas, it is fairly common to simulate the switching element as an 'ideal' component [1]. In the ON state, this means simulating the antenna with a piece of Perfect Electrical Conductor (PEC), which has infinite conductivity across the gap. In the OFF state this means simulating the design with an open gap (with no bridging material). Modelling the switch in such a

way in an antenna system reduces simulation time and complexity, whilst still allowing a proof of concept for the antenna.

This method does not represent the losses in the switch and how it may affect the performance of the antenna. This has led to a more in depth simulation of microwave switches in general. For example, a PIN diode is inserted into a reconfigurable antenna by modelling the switch as a transmission line with the same transmission properties [2]. The photoconductive switch loss may be modelled using equivalent circuits or physical representation of the conductivity profile in the silicon. Avanish *et al.* [3] represent optical control of a microstrip load on silicon substrate as an equivalent circuit. The equivalent circuit consists of a capacitance and resistance generated by the laser spot at the end of the transmission line – simulations and measurements agree when investigating the level of reflection from the load.

Equivalent 3D representations of the photoconductive switch have also been suggested to account for loss in the device. For example Panagamuwa *et al.* [4] model the silicon as a dielectric material with an effective conductivity and permittivity based on a mixture of measurement results and Platte's formula [5]. Rene *et al.* [6] add further complexity by considering the current density caused by the generation of carriers under illumination. Rene *et al.* model the photo-induced load in the semiconductor substrate using the generation, diffusion, and recombination equations. The solution of the ambipolar diffusion equation with a Gaussian excitation is determined from Hankel functions [7]. The conductivity profile is then modelled as a 6 layered hemispherical structure of varying conductivities.

3.1.2 Switch Topology

Switch insertion loss is not only dependent on the conductivity profile within the silicon, but also on the adjoining structure or interconnect method. The radiant flux focused on the silicon die can be easily be adjusted during switch operation to increase conductivity. This can be achieved by simply increasing or decreasing the current supplied to the laser. The intensity of illumination required is dependent on what level of loss is acceptable in the application the switch is employed in. On the other hand, the transmission line topology cannot be modified during operation and so has to be optimised before fabrication.

Switch topology can be described as the physical geometry of the optically controlled switch, –transmission line, interconnect, substrate and silicon die. For example, this may be the gap between the transmission line or the width of the transmission line; this can be categorised as the transmission line topology. Switch topology could also incorporate any additional circuitry or microstrip traces used to operate the switch. It could also relate to the size of the silicon die or the type of substrate used – these aspects cannot be changed once the switch is fabricated, unlike radiant flux.

Switch isolation is dependent on the OFF state conductivity of the silicon and gap width between the transmission lines. Considering both ON and OFF performance are dependent on switch topology, this aspect has been the focus of previous studies to improve photoconductive switch performance.

Chauraya *et al.* [8] present alternate topologies to improve switch performance. In this study, three switch topologies are compared, chamfered, notch and interleaved, as in Figure 3.1. Chamfering the microstrip at the gap was found to decrease capacitance across the gap, hence increasing the isolation in the OFF state.

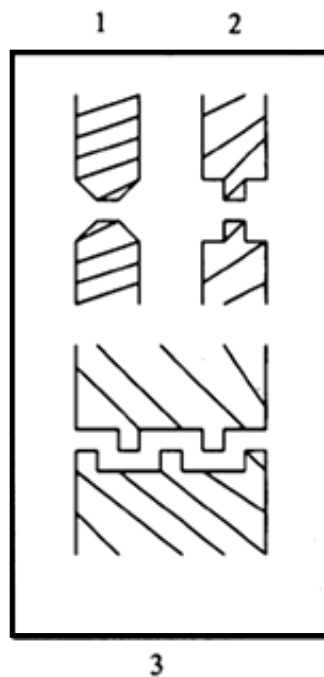


Figure 3.1: Three switch topologies, (1) chamfered, (2) notch, and (3) interleaved designs investigated by Chauraya *et al.* [8]

Flemish *et al.* [9] improve the performance of their optically controlled attenuator by optimising the dimensions of their component's layout. In this case, the trace width and gap between traces of the attenuator were varied in order to optimise for maximum isolation and minimum insertion loss.

An alternative approach to employing a simple silicon die across a gap is to etch a more elaborate pattern. Research by Liu *et al.* [10] present a switch incorporating two square open loop resonators. Simulation results at 11.65GHz, report an isolation in the OFF state of 56dB, and insertion loss in the ON state of 0.59dB. Xue *et al.* [11] present a switch based on a bridge structure which improves the isolation of the switch. The drawback is that insertion loss is relatively high, and hence the design is only useful when handling low power signals.

This chapter first looks to use a simple one layer equivalent model to optimise the transmission line topology through a simulation study. More complex models such as six layer (cuboid) models are then investigated using 3D EM simulation software packages EMPIRE XCcel v5.3 - v5.51 which uses Finite Difference Time Domain Technique (FDTD) [12] and CST Microwave Studio 2013 [13] using the Finite Integration Technique (FIT). Both are time domain techniques which involves discretising the model into cuboids and then performing a Fourier transform on the time signals in order to calculate frequency response. Differences in approach will be briefly discussed in section 3.3.3. The equations computed in Chapter 2 serve to provide the conductivity and permittivity values for the six layer profile of the silicon. Other factors are also included when modelling the switch such as signal planarity (interconnection method) and optical feed technique with a particular focus on effect on transmission performance.

3.2 Transmission Line Topology

Switch topology values such as transmission line width and gap width influence both insertion loss in the ON state and isolation of the switch in the OFF state. As described in Chapter 1, the switch comprises of a die of silicon attached over a gap in transmission line. In this thesis, the focus is on optimisation of the transmission line topology which forms part of the switch topology as a whole. The case study involving optimisation of the transmission line topology has been based around a

1mm die of silicon, as the physical diameter of the optical fibre delivering the illumination has a 1mm diameter. For this particular size of silicon it is expected that there will be an optimum combination of substrate thickness, permittivity and gap width between the two lengths of transmission line that cause the best impedance match.

This study aims to optimise transmission line topology by considering the use of different substrate materials. A 50Ω transmission line with a gap was designed using commercially available substrate materials of different permittivity and thicknesses. The substrate thickness and permittivity naturally determines the line width of a 50Ω transmission line. A parameter study was then conducted varying the gap width to optimise both insertion loss and isolation in ON and OFF states respectively.

3.2.1 Transmission Line Parameter Simulation

The switch was simulated in IMST EMPIRE XCcel version 5.3 as a $1\text{mm} \times 1\text{mm} \times 0.53\text{mm}$ die of silicon. For this early study, the conductivity was estimated based on the measured performance of the boron doped silicon. This technique was previously utilised by Panagamuwa *et al.* [4] in order to use a conductivity value which represents the loss of the photoconductive switch. The conductivity was estimated to be 45S/m ; Eq. (2.18), Eq. (2.22) and Eq. (2.23) from Chapter 2 are used to calculate the corresponding $\epsilon_r = 11.1$ and $\tan\delta = 9.2$ in the ON state. In the OFF state the die has a conductivity of 0.035S/m , $\epsilon_r=11.8$ and $\tan\delta = 0.02$. The die is attached with silver loaded epoxy between two lengths of transmission line. It is assumed that the silicon has one bulk conductivity; this is a valid assumption to make during this investigation as silicon performance is not being optimised in this part of the study and the same model for silicon is used in each transmission line topology.

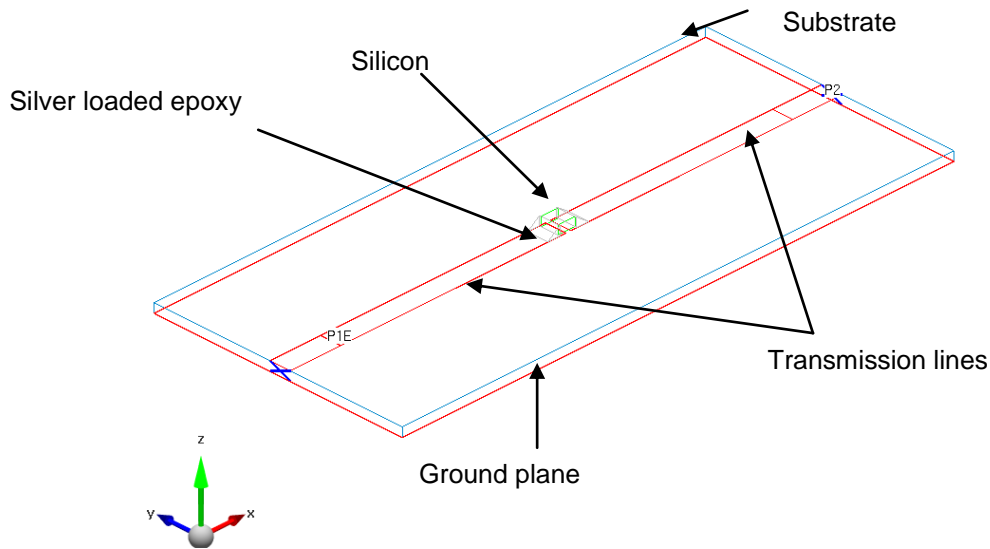


Figure 3.2: Basic simulation model of an ideal switch placed between two transmission lines.

Three substrates were investigated in this research:

- Rogers 3003 (R3003), $\epsilon_r = 3$, $\tan\delta = 0.0031$
- Rogers RT Duroid 6006 (R6006), $\epsilon_r = 6.12$, $\tan\delta = 0.0027$
- Taconic TLY-5 (TLY5), $\epsilon_r = 2.2$, $\tan\delta = 0.0009$

The effect that varying line width has on switch performance was considered by simulating different commercially available substrate thicknesses, 0.25-1.52mm. Line width is dictated by a 50 Ω impedance match, varying between 0.74 - 3.8mm.

The effect that gap width between the two transmission lines has on insertion loss and isolation was also considered. For this parameter in particular there will always be a trade-off between insertion loss and isolation – gap widths between 0.2-0.4mm were investigated. This range was chosen based on previous experience, where a typical gap width of 0.25mm produces insertion loss of 0.6dB and isolation of 16dB [4]. The lower limit of 0.2mm is the minimum gap width that can accurately be achieved using the chemical etching process at Loughborough University.

3.2.2 Results

Simulation results for 27 different switch dimensions were collected, and S21 results in both the ON and OFF states are presented in Figure 3.3. The circle highlights data points with low insertion loss and high isolation – these cases have been investigated in more detail. It is believed that for this initial study, 27 samples is

sufficient in determining trends in behaviour, but further variations could be investigated in future work. Thinner substrates with a corresponding thinner line width produce superior results as unwanted capacitive coupling across the gap in the OFF state is reduced.

Line widths that closely match the dimensions of the silicon produce better results. The currents on the transmission line are mainly on the outer edges and hence maintaining line width improves results.

The impedance of these transmission lines are more closely matched to 50Ω . Coupling across the gap is facilitated by the presence of conductive silicon. Hence silicon which is the same width or slightly larger than the line width encompasses the fringing electric field at the gap discontinuity.

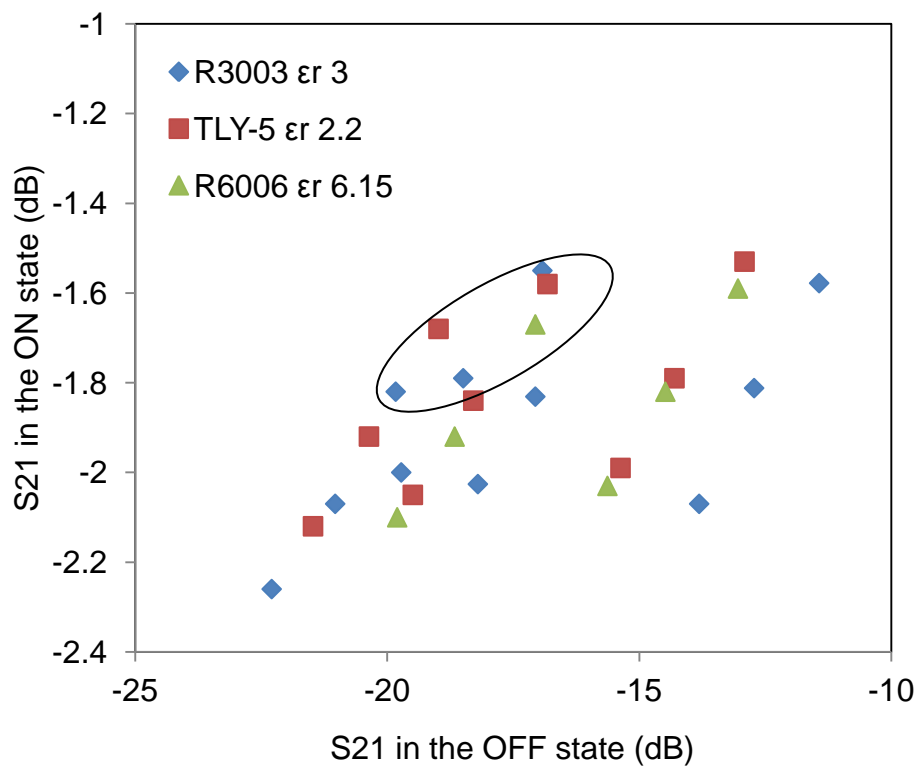


Figure 3.3: Switch variations and their respective insertion loss and isolation values at 2GHz; markers represent different line and gap widths, particular values of interest are circled as having optimum S21 in ON and OFF states. Details are viewable in Table 3.1.

Substrate type	Substrate height (mm)	Track width (mm)	Gap width (mm)	S21 OFF (dB)	S11 ON (dB)	S21 ON (dB)	Impedance (Ω)
R3003	0.25	0.6	0.2	-19.8	-14.0	-1.8	36
TLY-5	0.25	0.74	0.2	-19.0	-14.9	-1.7	42
R3003	0.5	1.22	0.3	-18.5	-14.7	-1.8	44
R6006	0.64	0.9	0.2	-17.1	-15.1	-1.7	37
R3003	0.5	1.22	0.2	-16.9	-15.9	-1.6	45
TLY-5	0.5	1.53	0.2	-16.8	-14.4	-1.6	48

Table 3.1: Optimisation parameters for the top 6 switch contenders at 2GHz

The design incorporating Rogers 3003 substrate, height 0.5mm, gap width 0.3mm was used to continue the silicon optimisation process. This topology was chosen as this design presents an ON state insertion loss of 1.8dB and an OFF state isolation of 18.5dB with an input impedance to the transmission line of 44 Ω . The impedance is affected by not only the line impedance but also the presence of the silicon. The substrate thickness is also double that of some alternate switch designs, leaving more scope for achieving these results during fabrication accounting for manufacturing tolerances. In later studies the transmission line has also been tapered slightly at the gap, as is presented by Chauraya [8] in order to further increase coupling across the gap and improve input impedance.

One aspect which is not focussed on in this study is optimisation of bandwidth of operation. The switch is optimised for use at ~2GHz which is close to the GPS (Global Positioning system), L-Band Satellites communications, WLAN (Wireless area network), GSM (Global System for Mobile Communications) and other commercially used frequency bands. At higher frequencies, the isolation of the switch may be the limiting factor of use. As frequency increases, the coupling across the gap is increased and hence isolation is reduced. This effect can be seen

in measured results later in this chapter in section 3.3.1. If high isolation is a key requirement in terms of switch operation, then further optimisation studies can be conducted where isolation can be increased by increasing the gap in transmission line.

3.3 Silicon Conductivity Simulations

The previous section has proposed a transmission line topology which maximises transmission in the ON state, and minimises transmission in the OFF state. This transmission line is now used to explore the effect that silicon conductivity has on transmission performance. The investigation starts by considering the effect of conductivity profile. Firstly, the simplest representation of the switch is presented that draws attention to why more realistic models must be considered.

For the more complex six layer conductivity model, EMPIRE results are compared to CST generated results – where the conductivities in both models have been defined using different methods – both results are compared to measured data.

3.3.1 Measurements compared to an Ideal Switch

In reality, no switch is perfect or ideal – each will have an associated insertion loss and isolation and these have an effect on the overall antenna or microwave circuit performance. An ideal switch has 50Ω impedance in the ON state and infinite impedance in the OFF state.

Firstly, an ideal switch is simulated and compared to measured data of the silicon switch. Figure 3.4 and Figure 3.5 depicts the simulation model which comprises two segments of transmission line with a $1\text{mm} \times 1\text{mm} \times 0.3\text{mm}$ block of perfect electric conductor (PEC) centred over the gap between transmission lines to act as the ideal ON state. Silver epoxy is also included in the simulation model and is modelled as having a conductivity of 20000 S/m . The connectors are not modelled in this simple setup; instead ports are added to excite the structure. Results presented here are for Rogers 3003 0.5mm thick substrate, $\epsilon_r = 3$, $\tan\delta = 0.0031$. Transmission line width is 1.2mm , the length of the line is 30mm and the gap between transmission lines is 0.3mm . The OFF state results are produced by changing the block of PEC to be a block of vacuum.

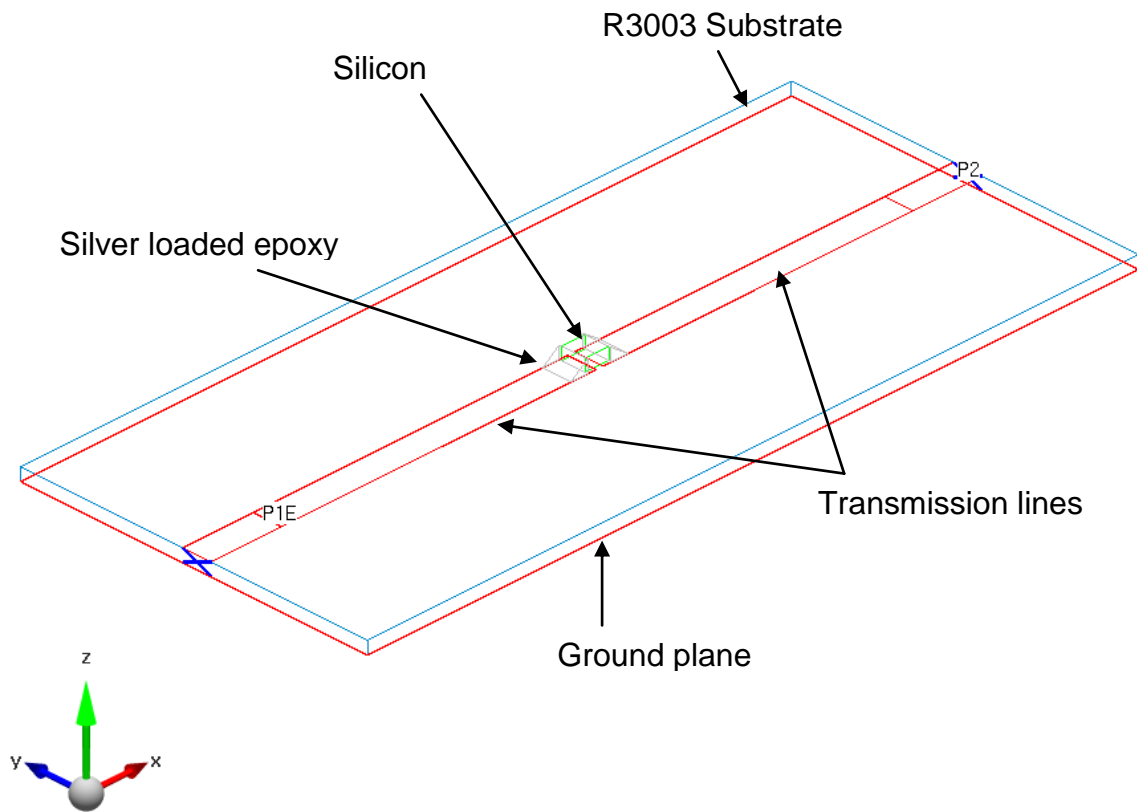


Figure 3.4: Basic simulation model of an ideal switch placed between two transmission lines.

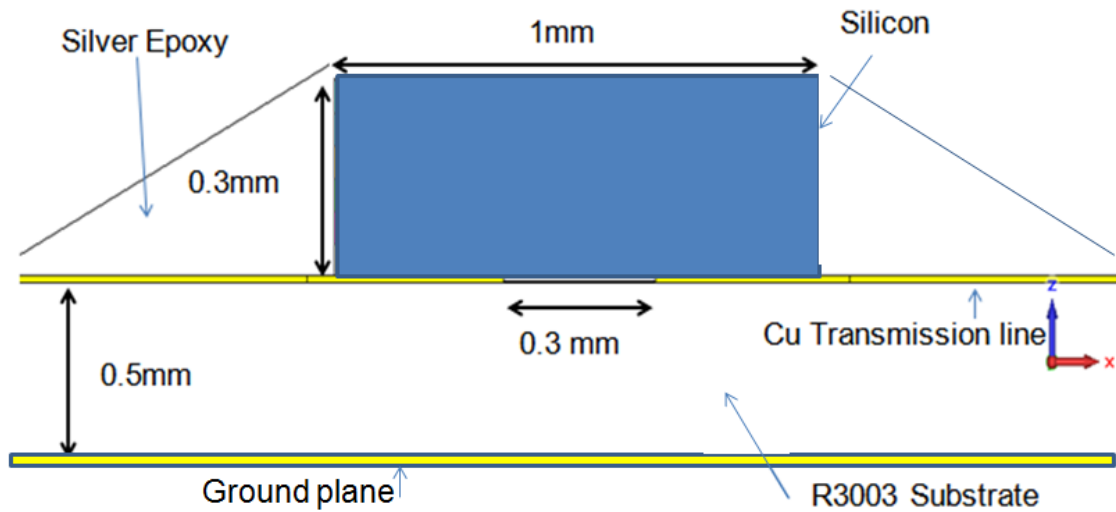


Figure 3.5: Simulation model of silicon including silver loaded epoxy on a Rogers 3003 substrate with dimensions

Figure 3.6 demonstrates that depending on radiant flux, the transmission through the silicon differs. For the maximum radiant flux used of 200mW, the ideal switch

simulation and measured results differ, demonstrating an extra 8.6% power loss. The radiant flux of 200mW is not exceeded in this thesis as increasing the illumination above this value shows little improvement to the insertion loss of the switch, but drastically increases the input control current needed to power the laser.

The measured results in Figure 3.6 also demonstrates that the switched transmission line has a bandwidth of optimum use in the ON state. Insertion loss using 200mW of radiant flux, remains lower than 0.7dB between 0.65GHz-4.5GHz. The switch can still be used outside of this bandwidth depending on the application requirements. The frequency range between 0-6GHz has mainly been concentrated on in this thesis as it includes some typical frequency bands such as WLAN, WiMax and GSM.

The most limiting factor on bandwidth is the OFF state isolation. As isolation is dependent on the gap width between the transmission lines, as frequency increases the coupling in the OFF state also increases, reducing the isolation to 11.6dB at 6GHz, as is demonstrated from measured data in Figure 3.7. The isolation between 0.65GHz-4.5GHz ranges between 28.4dB – 12.2dB. As previously mentioned, the switch topology has been optimised for use ~2GHz. For use at higher frequencies, it's possible that the gap width could be made larger to improve isolation.

There is also a discrepancy between simulated ideal switch and measured data, as can be observed in Figure 3.7, where S_{21} of the simulated switch is -30.2dB, and S_{21} of the measured switch is -19.4dB. This is because, in its OFF state, the silicon still has a small value of conductivity due to the doping. The dielectric loading better confines the field and so improves coupling from one transmission line to the other. In contrast, the simulated vacuum is a perfect insulator and hence field coupling is not easily facilitated.

The S_{11} result is presented in Figure 3.8. There is a greater level of reflection for the measured switch when compared to the simulated ideal switch. The simulated value of S_{11} at 2GHz is -0.005dB compared to the measured value of -0.25dB. The ratio of returned signal is greater for the simulated case as the vacuum acts as an insulator to reduce coupling across the transmission line gap.

Clearly, an ideal switch does not represent what is seen in practise and so a more accurate model is required. As mentioned in section 3.1.1, it is common to simulate the switches used in reconfigurable antennas as ideal, to prove the concept of reconfiguration. However, simulation of an ideal switch will not give comparable results in terms of measured data for transmission in the ON and OFF state.

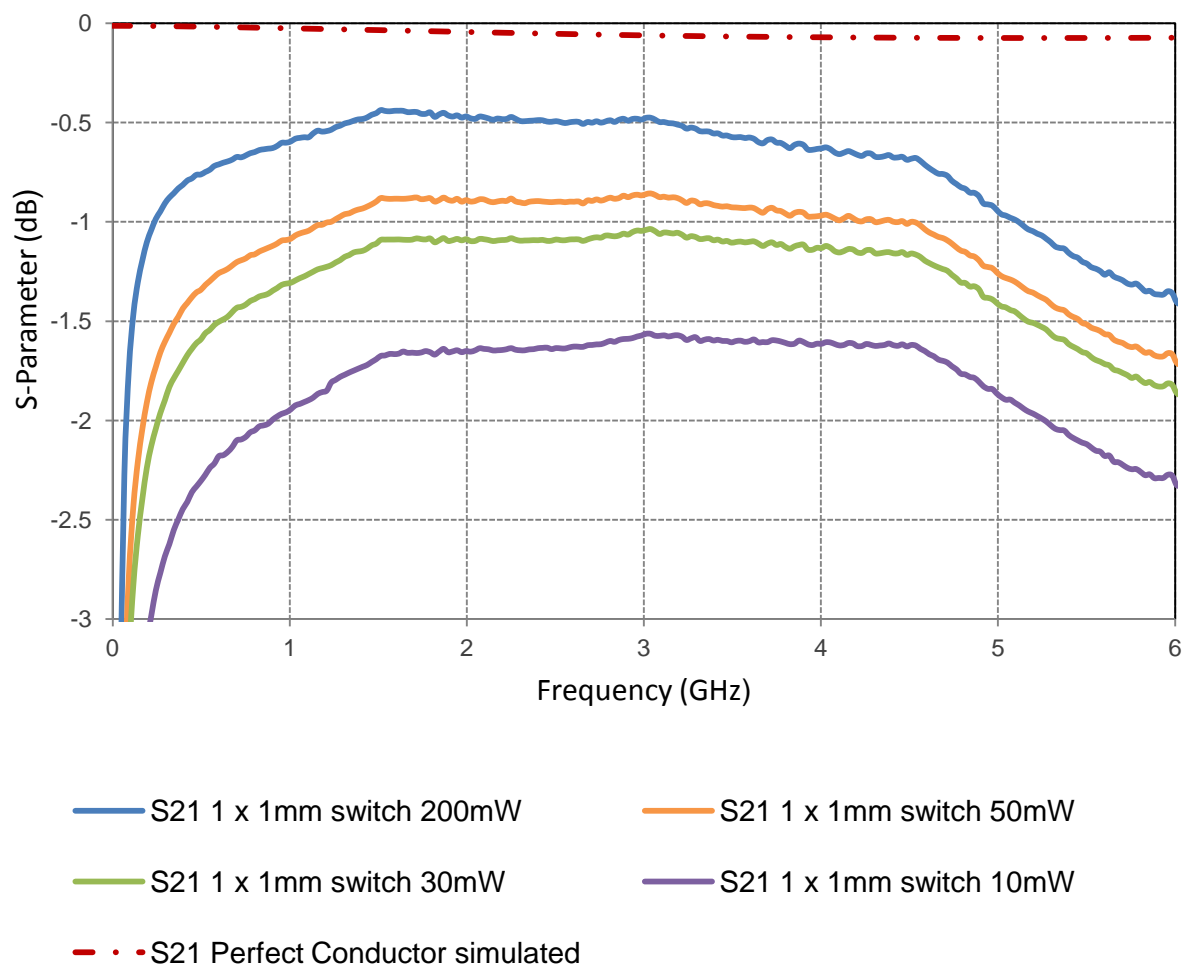


Figure 3.6: Ideal switch simulation results in terms of transmission alongside measured S21 results for various values of radiant flux

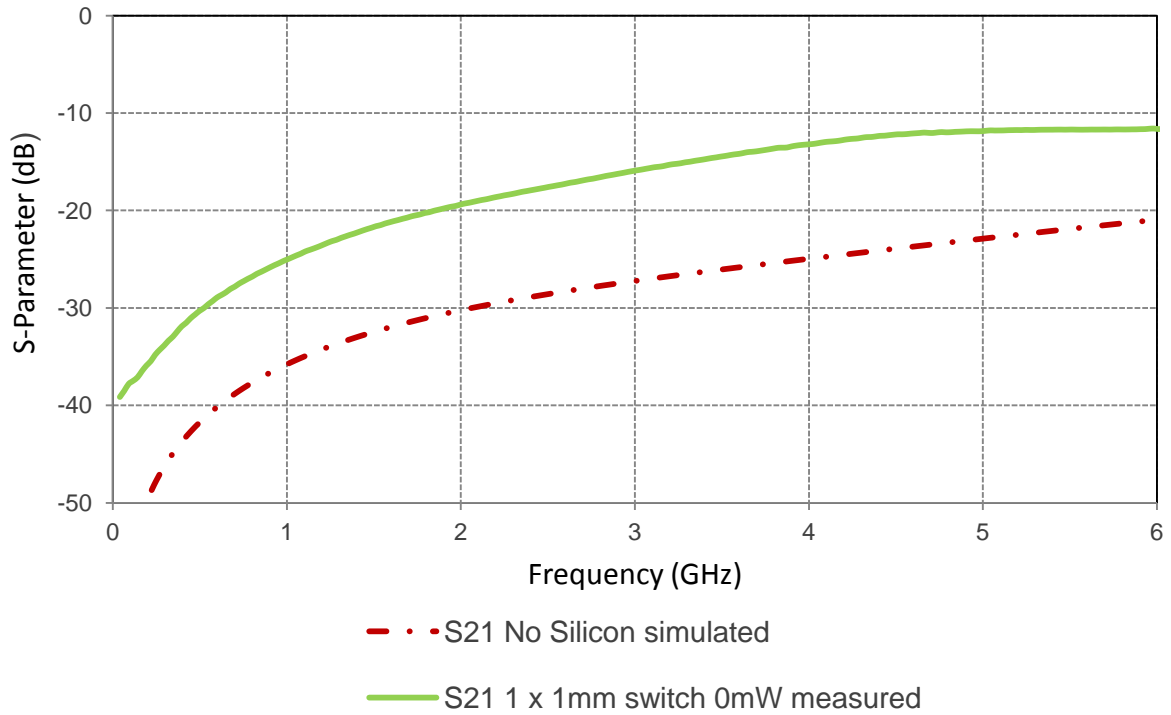


Figure 3.7: Transmission results in the OFF state, comparing simulated ideal switch case and comparing to corresponding measured result for the same topology

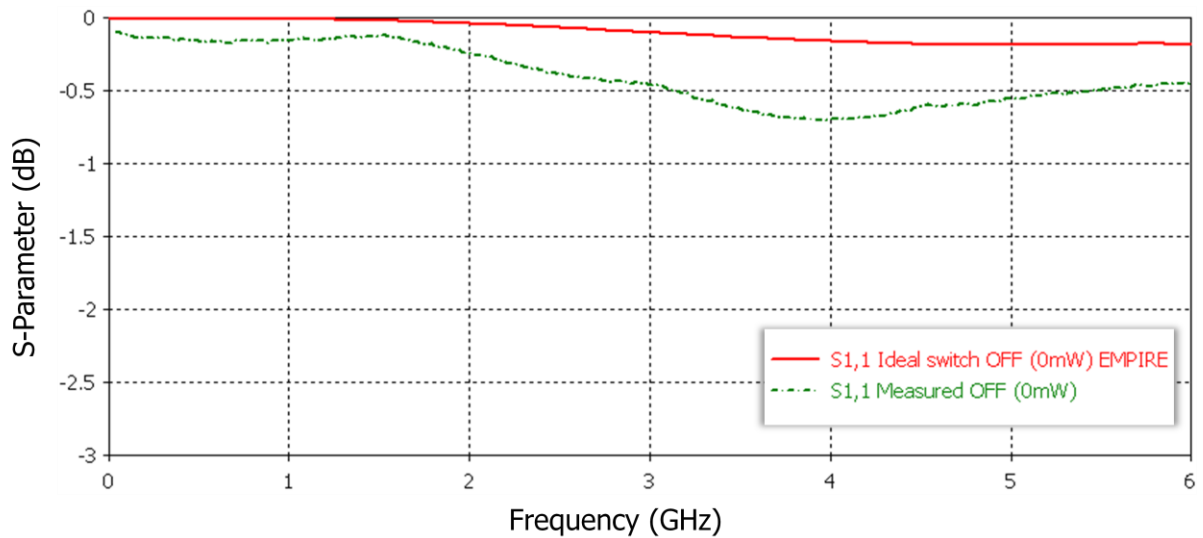


Figure 3.8: Ideal switch simulation results in terms of S11 alongside measured S11 results for 0mW of radiant flux (OFF state)

3.3.2 Equivalent one layer model

A second approach that is commonly used is to assign an equivalent conductivity to the block representing the silicon switch [14][15]. An average conductivity and loss tangent can be assigned by considering the equations introduced in Chapter 2, with the associated permittivity. This approach is similar to the initial simulation study of transmission line topology presented in section 3.2. In that study, a lower conductivity was used to calculate the relative permittivity, as it was assumed that the silicon had a low carrier lifetime.

In this instance, the number of carriers generated is calculated using Eq. (2.17) which includes a term for Auger recombination. Here, a radiant flux of 10mW and a wavelength of 980nm is assumed, a conductivity profile with an average value of 185S/m is calculated. A loss tangent of 145 (at 2GHz) is used to represent the loss which is based on a calculated permittivity of 8.6.

The S-parameter results are presented in Figure 3.9. Reducing the conductivity clearly impacts on the S21 result, there is a drop of approximately 0.9dB across the frequency range when compared to the ideal (PEC) switch model which was shown previous in Figure 3.6. The difference in S21 at 2GHz between measured and simulated equivalent conductivity model is 0.63dB. The corresponding difference in S11 between the measured and simulated result is 5.607dB, as is also shown in Figure 3.9. The measured result still demonstrates a higher return loss; reasons for this will in turn be investigated in the upcoming sections as the simulation model is improved.

There is a discrepancy between the OFF state S21 measured and simulated values using EMPIRE with conductivity in the die of 0.017S/m as is demonstrated in Figure 3.10. The difference is 11dB at 2GHz, which equates to a decrease in isolation of 92%. The initial doping affects the conductivity of the wafer, which is commonly quoted on silicon datasheets.

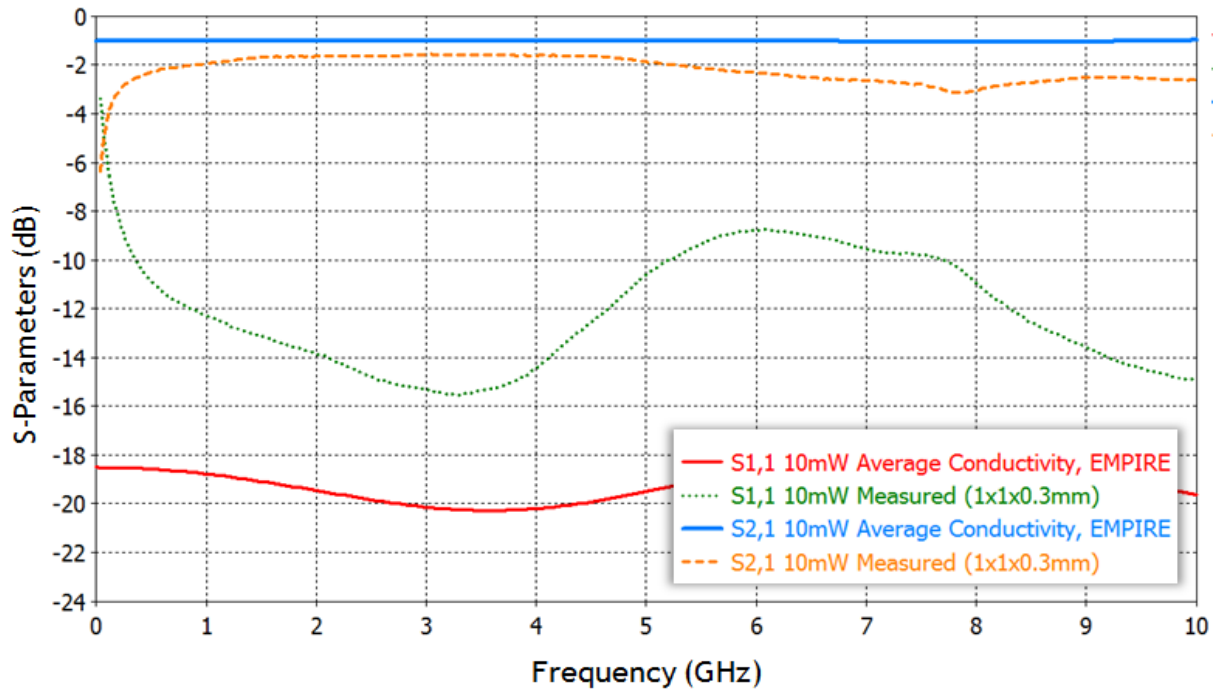


Figure 3.9: S-parameter results for an equivalent one layer conductivity simulation model in EMPIRE - based on the average conductivity in the silicon. This is compared to measured results for a 10mW radiant flux.

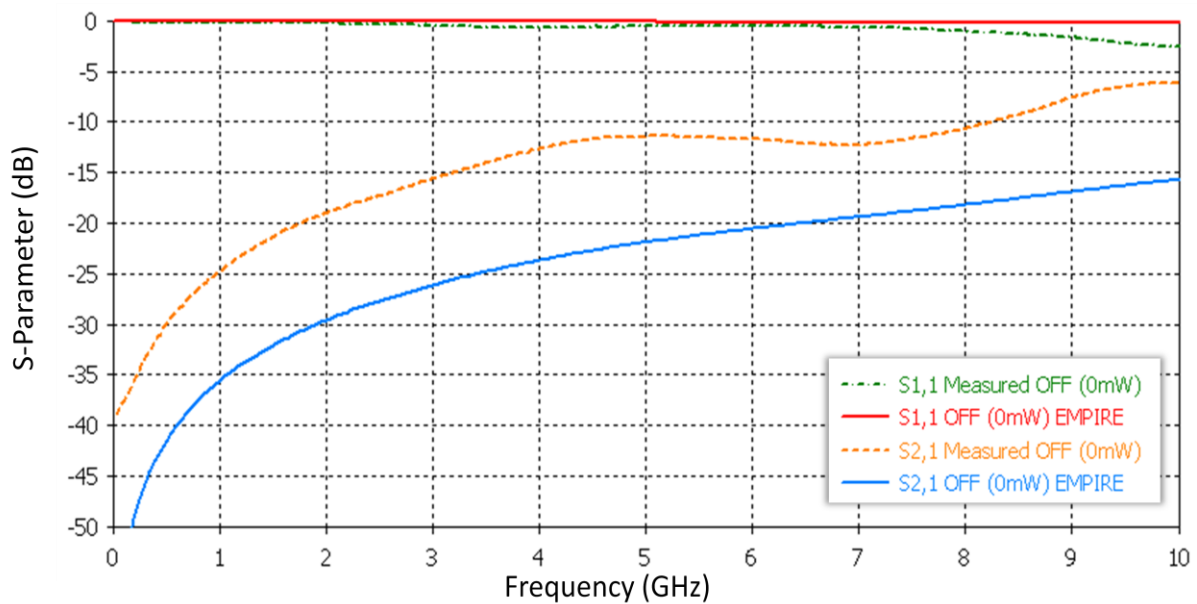


Figure 3.10: S-parameter results in OFF state with an OFF state conductivity value of 0.017S/m

This value is not tested for each wafer so in reality this doping concentration might be slightly greater than reported. This could go some way to explaining why there

appears to be greater isolation in simulation as compared to measured results. It can be accounted for by increasing the conductivity value entered for the OFF state silicon material in the simulation model to 0.035S/m. This was established by running a parameter sweep on the conductivity value to match simulated and measured results.

3.3.3 Six layer model

The conductivity profile can be described as a layered model with varying conductivity and permittivity. This is more accurate than the one layer model as it captures the absorption of the photons more accurately within the silicon. This in turn highlights that highest conductivity is present closest to the surface of the silicon which is illuminated. It is hypothesised that this profile can perhaps be exploited to enhance the performance of the switch.

The layered material properties of the silicon can be calculated using the Eq. (2.17) introduced in Chapter 2. A representative model of the six layer silicon, along with a reminder of the dimensions is presented in Figure 3.11, each layer is 50 μ m thick. The corresponding values for conductivity, permittivity and loss tangent at 2GHz are presented in Table 3.2 for a radiant flux value of 10mW (wavelength 980nm).

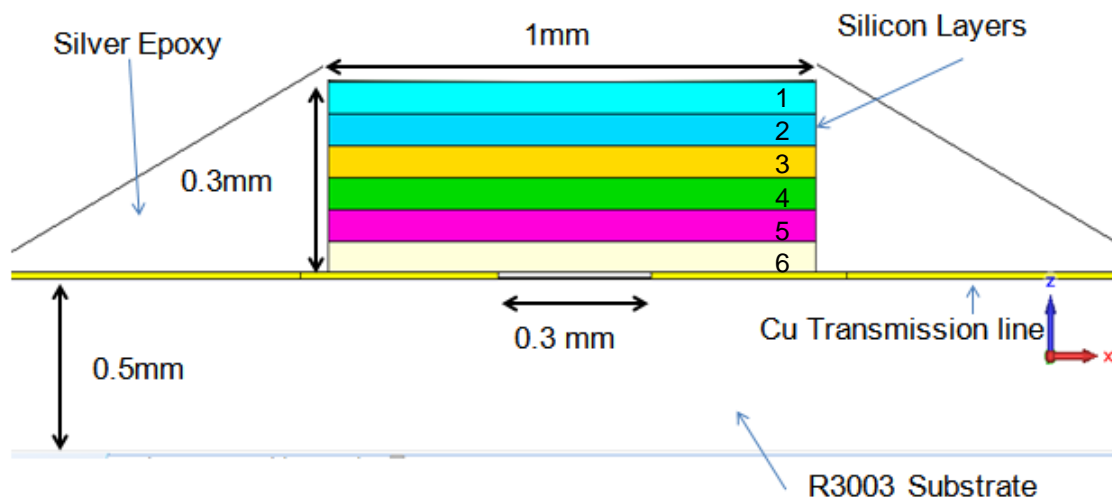


Figure 3.11: Layered silicon model including silver epoxy on a Rogers 3003 substrate with dimensions – illumination is from above, applying 10mW of radiant flux.

Layer no.	σ (S/m)	ϵ_r'	ϵ_r''	$\tan\delta$
1	259	7.33	1749	238
2	236	7.74	1593	205
3	203	8.33	1368	164
4	168	8.94	1132	126
5	135	9.51	913	96
6	107	10.01	723	72

Table 3.2: Six layer values for conductivity and permittivity for 10mW of radiant flux (valid at 2GHz)

Using EMPIRE's simulation software, the best way to describe such a material is to define six layers with varying real permittivity and a corresponding loss tangent or conductivity valid at a defined frequency. Within CST, it is possible to define the dispersion of such materials by entering the real and imaginary parts of the permittivity of the material at different frequencies. Note that the imaginary permittivity listed in Table 3.2 corresponds to the single frequency of 2GHz, but values corresponding to 1, 2, 4, 8 and 10GHz are input into the dispersion table for the photoconductive silicon model within CST.

The CST model is excited via waveguide ports using the inhomogeneous port accuracy enhancement that essentially accounts for the fact that the port covers both substrate and vacuum areas and is inhomogeneously filled. The enhancement ensures that the correct mode is injected into the structure across the entire frequency range. These ports can be visualised in Figure 3.12.

Layer no.	ϵ_r'' 1GHz	ϵ_r'' 2GHz	ϵ_r'' 4GHz	ϵ_r'' 8GHz	ϵ_r'' 10GHz
1	3498	1749	874	437	350
2	3186	1593	796	398	318
3	2736	1368	684	342	274
4	2264	1132	566	283	226
5	1824	913	457	228	183
6	1447	723	366	181	145

Table 3.3: Six layer values for imaginary permittivity for 10mW of radiant flux at 1, 2, 4, 8 and 10GHz

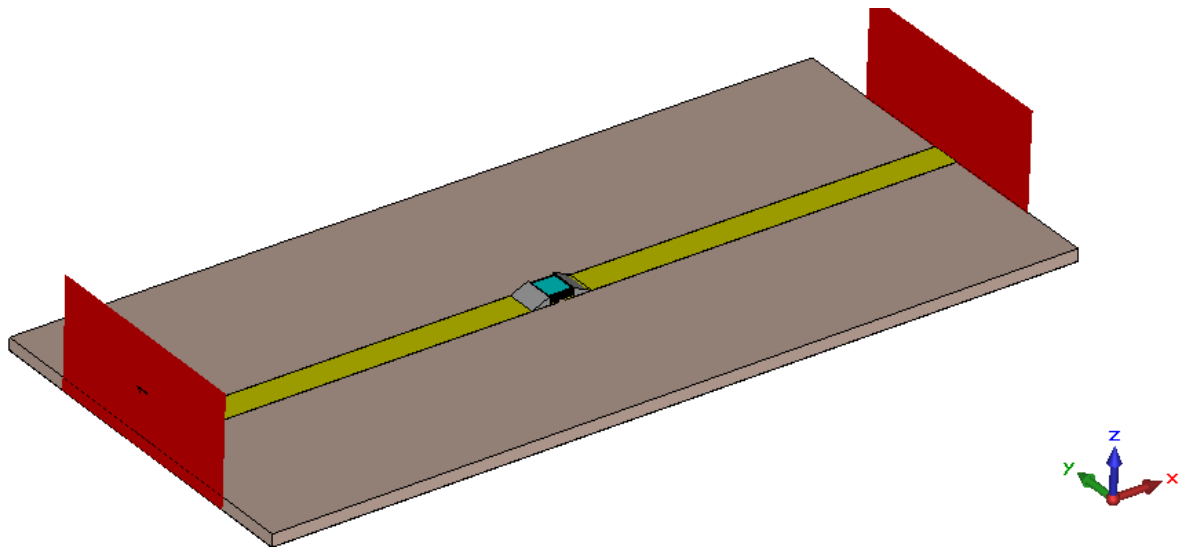


Figure 3.12: CAD model in CST 2013, 6 layer silicon attached over a 0.3mm gap in transmission line (excited by waveguide port: Quasi-TEM mode)

The two approaches are compared in terms of S21 and S11 in Figure 3.13 and Figure 3.14. It is worth noting that these two EM simulation software use different techniques in order to solve Maxwell's Equations. Both are based on time domain techniques; EMPIRE uses a Finite Difference Time Domain (FDTD) approach

whereas CST uses a Finite Integration Technique (FIT) approach. The FDTD method solves Maxwell's equation in the partial differential form. A solution is achieved in a leap frog manner, where E-Field vectors are solved at an instance of time followed by H-field vectors at the next instance in time for each mesh cell [16].

FIT approach solves Maxwell's equations in their integral form [17]. However, for Cartesian grids the FIT can be rewritten as a FDTD method. Both techniques provide a full wave solution, so good correlation between results is expected.

In terms of discretisation, both software use a hexahedral mesh. EMPIRE automatically generates a mesh – extra mesh lines have been added to the model in areas which require a dense mesh such as the silicon layers. CST also automatically generates a mesh, where user has control over wavelength based refinement and in this model, local mesh settings were applied to the silicon to ensure adequate discretisation to capture field behaviour accurately.

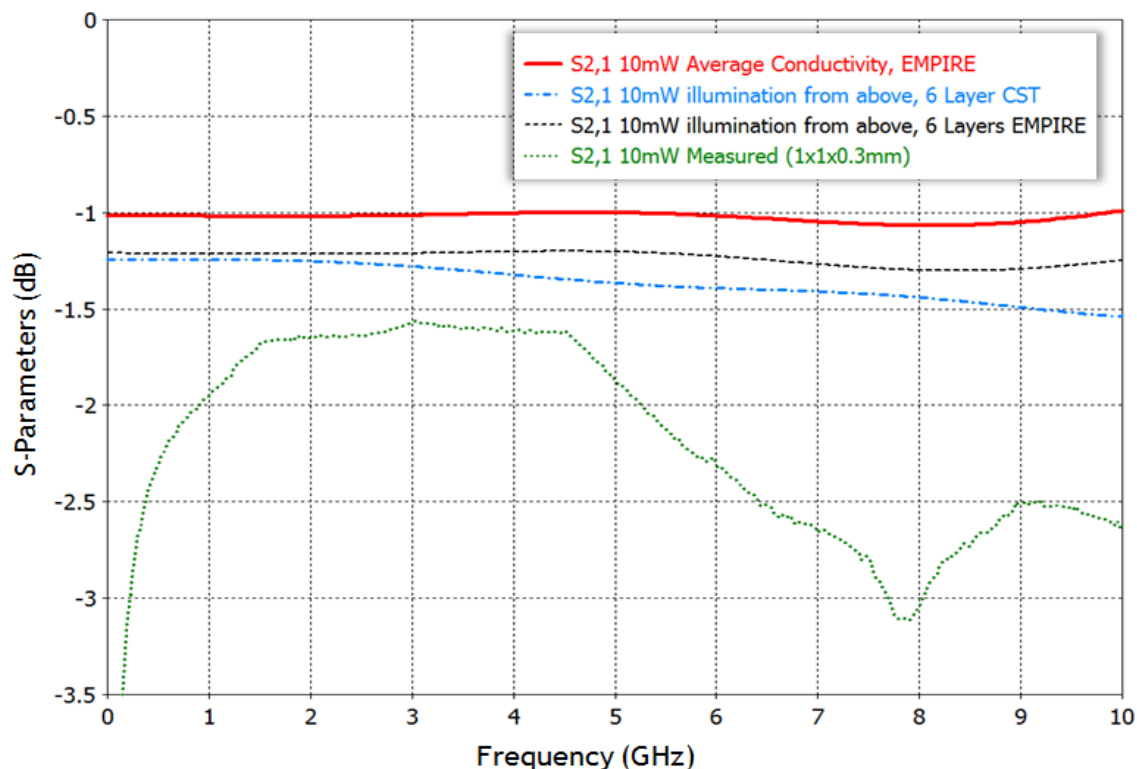


Figure 3.13: S21 results comparing 6 layer photoconductive silicon model in EMPIRE (FDTD) and CST (FIT) with measured data under 10mW of radiant flux

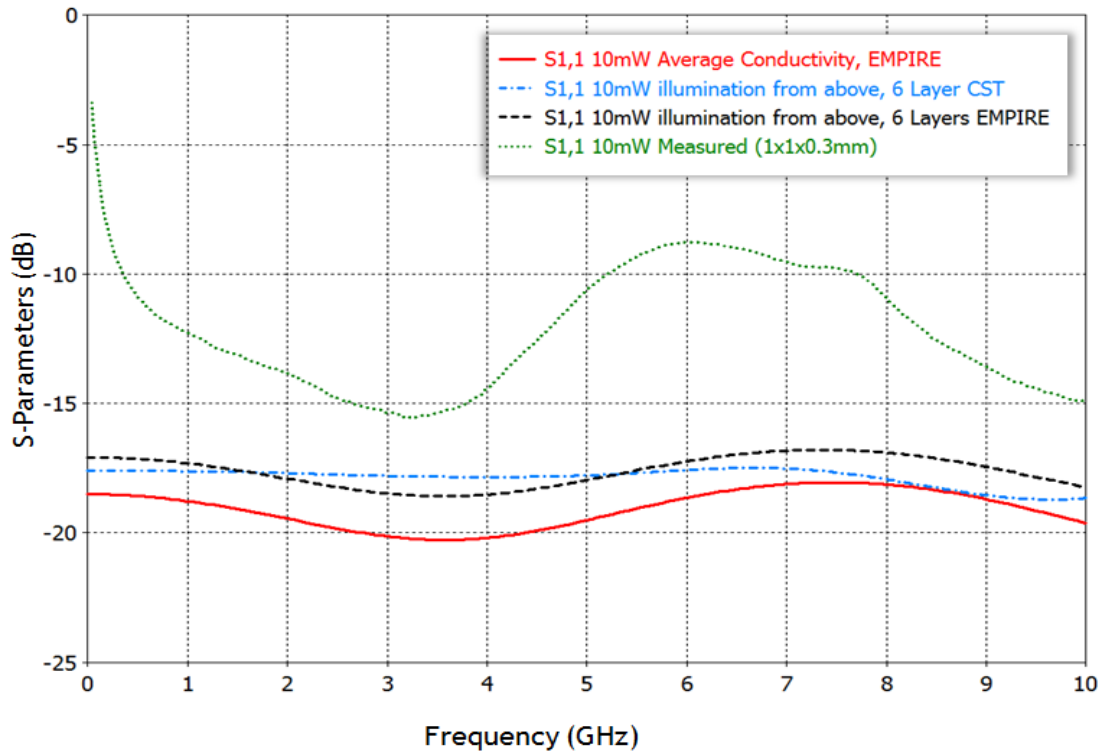


Figure 3.14: S11 results comparing 6 layer photoconductive silicon model in EMPIRE (FDTD) and CST (FIT) with measured data under 10mW of radiant flux

CST employs Perfect Boundary Approximation technique, meaning that multiple dielectrics in a mesh cell can be handled accurately so that stair casing effects due to a cuboid mesh are not apparent. This allows a coarser mesh in the structure which means a reduced simulation time without compromising accuracy.

The CST simulated result shows a greater level of dispersion as frequency increases when compared to the EMPIRE result. Between 1-10 GHz the S21 decreases by 0.3dB when the six layer structure is simulated using CST. When the same structure is simulated in EMPIRE there is no decrease in S21 between 1 and 10GHz. This is most likely due to the fact that the imaginary part of the permittivity (which dictates the loss in the material) is listed for a number of frequencies. A curve of best fit is then plotted with respect to these imaginary permittivity values in CST.

The loss tangent value which is derived from real and imaginary permittivity is specified in EMPIRE for only one frequency but is used for the full 0-10GHz frequency range.

At 2GHz, the measured S21 value is -1.65dB. The simulated value at 2GHz for EMPIRE is -1.18dB. The corresponding simulated value for CST is -1.25dB. As frequency increases the S21 results for CST and EMPIRE generated plots diverge slightly. There are still some discrepancies between the simulated and measured transmission performance. This is also evident in the S11 plot, where the CST simulated 6 layer result has a reduced value of 4dB compared to the measured result at 2GHz.

CST produces results that have a closer correlation to the insertion loss measured in a fabricated photoconductive switch. Since the real and imaginary part of the permittivity can be specified at given frequencies, this model should predict the dispersion at higher frequencies more accurately. CST also affords the use of perfect boundary approximation (particularly advantageous for curved structures) and the ability to run simulations on GPU (Graphics Processing Unit) cards as a hardware acceleration method and hence, further effects and simulations will be performed using CST.

3.3.4 Effect of radiant flux on profile

Before moving onto other factors that may affect the transmission performance of an optically switched transmission line, first we briefly investigate the effect of radiant flux on S-parameter performance. Table 3.4 demonstrates the conductivity profile, calculated via Eq. (2.18), under 200mW of radiant flux.

Layer no.	σ @2GHz(S/m)	ϵ_r'	ϵ_r'' 2GHz	ϵ_r'' 10GHz
1	1940	-22.2	13100	2613
2	1670	-17.4	11200	2246
3	1330	-11.6	8990	1798
4	1030	-6.2	6930	1386
5	776	-1.78	5240	1047
6	579	1.68	3910	782

Table 3.4: Six layer conductivity and permittivity values for silicon under 200mW of radiant flux, for 2GHz input signal. Dispersion value is also presented at 10GHz for reference

Table 3.5 presents the six layer material values for 50mW of radiant flux. These tables show the silicon conductivity at 2GHz and the imaginary permittivity at 2GHz and 10GHz, although the simulation includes dispersion calculated for 1, 2, 4, 8 and 10GHz. CST requires only the definition of real and imaginary permittivity in order to model dispersive materials.

Layer no.	σ @2GHz(S/m)	ϵ_r'	ϵ_r'' 2GHz	ϵ_r'' 10GHz
1	1170	-8.75	7897	1579
2	1060	-6.72	7153	1430
3	904	-4.03	6098	1219
4	742	-1.18	5006	1001
5	593	1.43	4005	801
6	466	3.68	3146	629

Table 3.5: Six layer conductivity and permittivity values for silicon under 50mW of radiant flux, for 2GHz input signal. Dispersion value is also presented at 10GHz for reference

The permittivity is negative as according to the Drude equation, as plasma frequency is large enough so that there is a change from dielectric to metal type material. Plasma frequency is related to the oscillations which occur of electron density in conducting media (e.g. plasmas or metals).

It is clear that as radiant flux increases, the conductivity increases when compared to Table 3.2. This increase is due to the increased photon flux which occurs at higher levels of radiant flux.

This translates to an increase in transmission as is described in Figure 3.15. Increasing radiant flux from 10mW to 200mW increases transmission across the frequency range by approximately 1dB. The trend is fairly similar if we compare to the measured result. At higher values of radiant flux the transmission is increased across the frequency range by approximately 1.2dB. An intermediate value of illumination is also included, 50mW. With regards to simulated results, the 50mW

result is only 0.1dB below the 200mW result. However in measurements the difference between 50mW and 200mW result is 0.35dB. Clearly there is a discrepancy still present. However, the six layer model is an improvement on the one layer model and closer to reality.

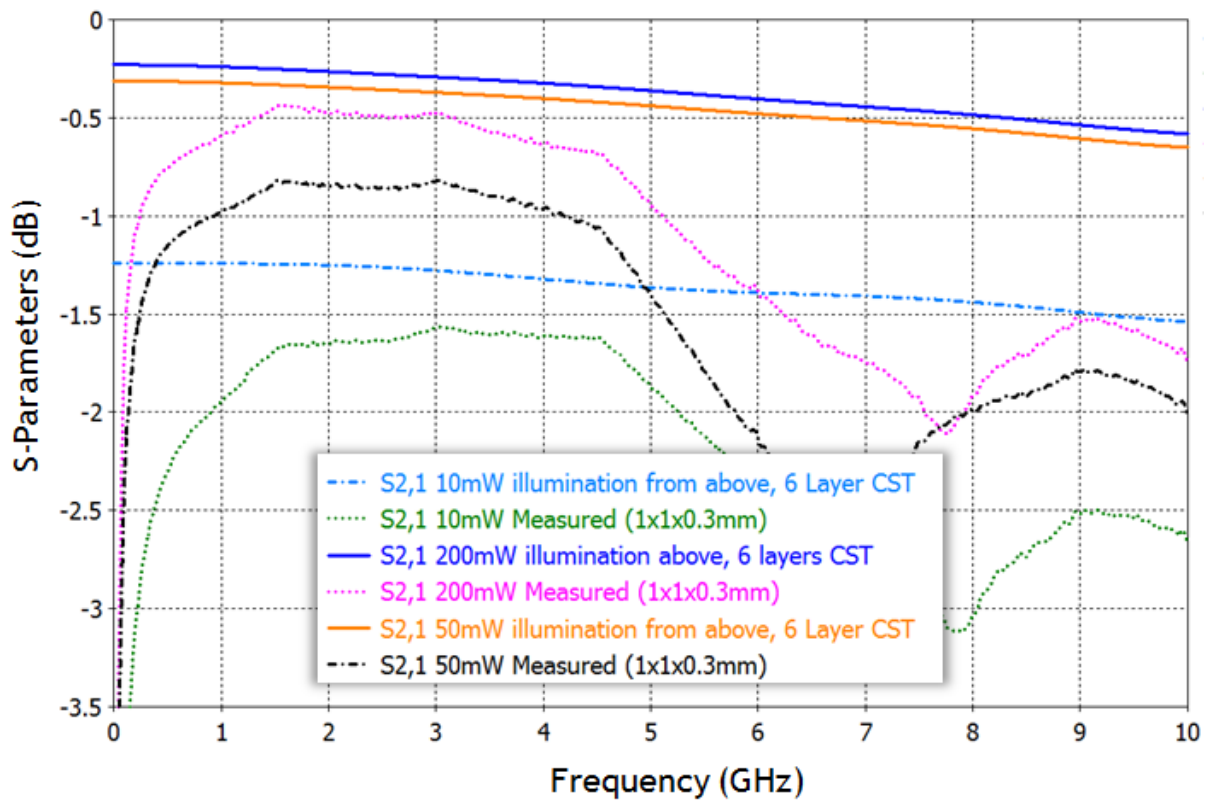


Figure 3.15: S21 results comparing 6 layer photoconductive silicon model under 10mW, 50mW and 200mW of radiant flux

The S11 results are shown in Figure 3.16. The measured result shows a different trend to that seen from the S21 results. In particular in the region of 5-10GHz, the measured results for both 10 and 200mW of radiant flux show similar values. The simulated results do not predict such behaviour; they maintain a constant difference across the frequency range. Since a corresponding behaviour is not seen in the S21 result, it is assumed that in this region the loss in the optically controlled transmission line must increase.

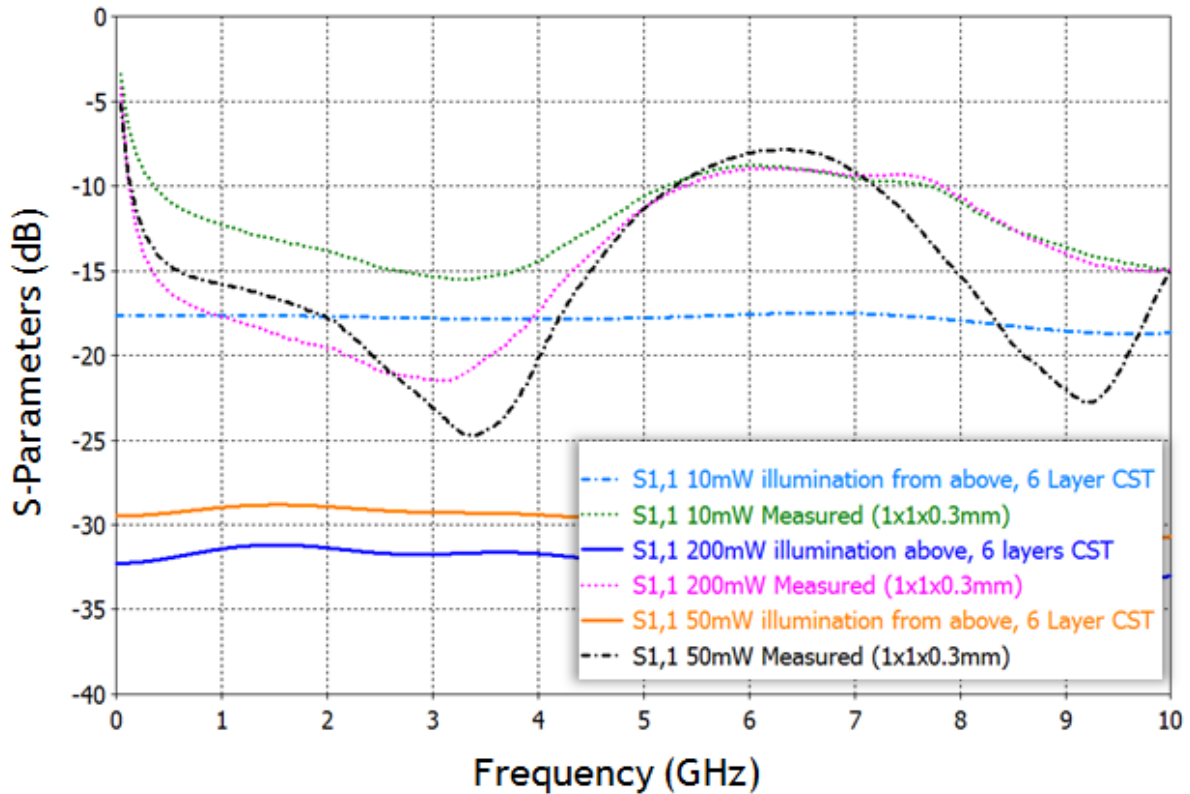


Figure 3.16: S11 results comparing 6 layer photoconductive silicon model under 10mW, 50mW and 200mW of radiant flux

3.3.5 Silicon Model Limitations

There are a number of limitations to the silicon conductivity model. These could explain the discrepancy between measured and simulated results:

- It is assumed that the carrier lifetime is a constant value. In reality, the carrier lifetime is a changing value with carrier density
- Mobility changes as carrier density increases (charge scattering) [18]
- Traps at the edges of the silicon are filled at high carrier densities, leading to increased carrier lifetime / conductivity at the edges at higher optical control powers
- Six layers are assumed when in reality the change in conductivity is not discrete. Other conductivity profiles were also investigated, for example a 7 layer profile with a 5 μ m highly conductive layer on the surface and a 10 layer conductivity model. Adding additional layers leads to increase in mesh cell number, which lengthens simulation time. In particular, the addition of the 5 μ m

layer also dictates the minimum time step of the simulation. Hence, a six layer model was chosen as the effect on transmission performance is small when compared to a ten layer model.

3.4 Geometry of the Switch and Transmission Line Simulations

In the previous section, the conductivity profile of the silicon was considered. This was done in isolation to modelling the exact fabricated transmission line to ascertain the effect that silicon conductivity profile has on transmission and compare to measured results.

In order to compare simulated and measured results better, the proper geometry of the full transmission line and switch must be modelled. This includes simulation of the passivation layer (or insulating oxide layer) on the surface of the silicon and the SMA connectors. CST is used to perform these subsequent simulations, including the frequency dependent dispersion model of the 6 layer silicon. This level of detail does increase simulation time, but allows a complete comparison and validation of the conductivity profile generated via Eq. 2.17 and 2.18 to measured results which include the SMA connectors and a silicon die which has an oxide passivation layer coating the surface.

3.4.1 Passivation layer model

To improve the carrier lifetime of the silicon, a passivation layer is often grown in order to repair dangling bonds on the surface. These dangling bonds are created during the fabrication process, and are sites of high recombination in the silicon, hence limiting the conductivity of the silicon die. The process of passivation and its effects are discussed further in Chapter 4. The passivation layer is a layer of insulating silicon dioxide, which is typically 200nm thick. The layer has been modelled as a 200nm thick layer of vacuum around the whole silicon die.

The simplification of a vacuum material reduces simulation time, but has the same effect on the S-parameter response as is present in measurements. S₂₁ results for illumination under 10mW radiant flux are presented in Figure 3.17 and are compared to the 10mW measured results. It can be observed that the decrease in transmission towards DC can be attributed to the presence of the passivation layer. The

passivation interferes with the Si-Cu contact, leading to a poor connection between the die and transmission line. Contamination of the silicon die could also contribute.

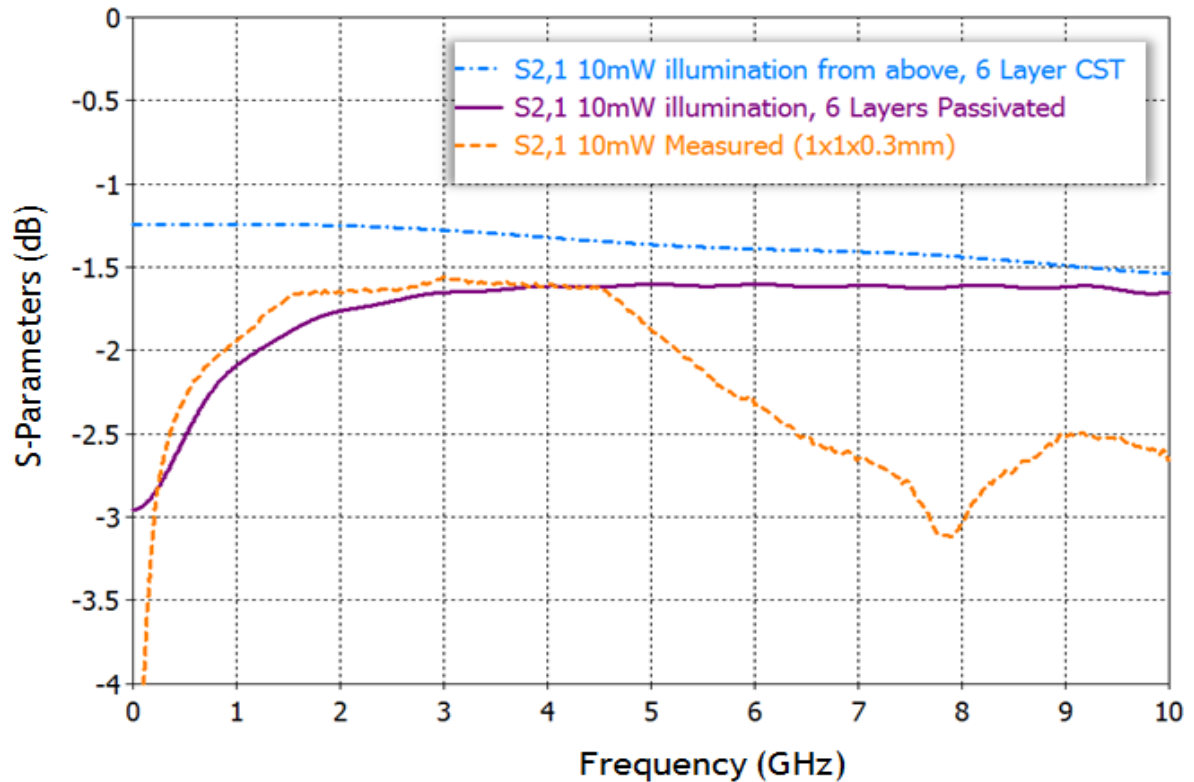


Figure 3.17: S21 performance of the six layer silicon model with passivation later

The addition of the passivation layer has the effect of decreasing the transmission over the entire frequency range, but is most notable at the lower frequencies. At these frequencies, the coupling from transmission line to silicon die over the 200nm vacuum is reduced and at DC there is no conduction path from one transmission line to the other. The transmission is reduced by 0.55dB at 2GHz when compared to the 6 layer silicon model simulated in CST without this layer of insulation. The value of S21 at 2GHz for the passivated model is -1.8dB -this is closer to the measured S21 at 2GHz, -1.67dB. The S11 result presented in Figure 3.18 shows fair agreement between simulated and measured result up to 4GHz.

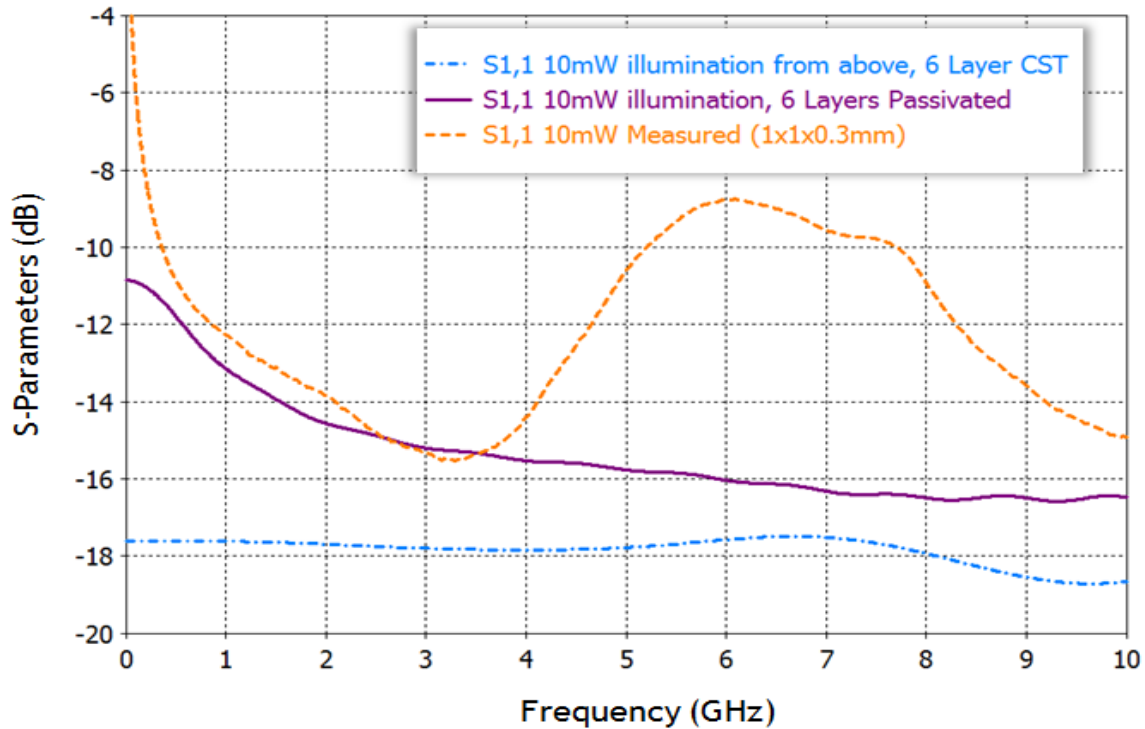


Figure 3.18: S11 performance of the six layer silicon model with passivation layer

Adding the passivation layer has increased the S11 by 3.2dB in terms of simulated results. This would be expected, as this insulating oxide layer creates a discontinuity in the circuit – the impedance at this point is not matched to 50Ω. The result is an increased level of reflection and reduced signal coupling to the conductive silicon. Above 4GHz there is still some discrepancy in the results as reflection increases in the case of the measured result. Hence finally, the last point of investigation is the connector geometry effect on S-parameter results.

3.4.2 Effects of connector

Lastly the effect of the SMA connector is modelled by including the SMA geometry, which is generated by Antenna Magus [13] and imported into the CST project, Figure 3.19. A waveguide port is used to excite the SMA aperture directly, ensuring the correct mode is injected into the structure. It can be seen that the connectors themselves contribute to the insertion loss parameters. Typically connectors are designed to be low loss components, however in reality there will always be some loss of signal and interaction of the connector housing and signal propagating along

the cable from the test set. The loss from cables and adaptors can be removed using calibration techniques, however it is more difficult to ascertain the effect of the connector on PCB board. When looking at small differences in insertion loss, the connector may contribute to this value, as is documented in a study performed by CST comparing simulations to measurements [20].

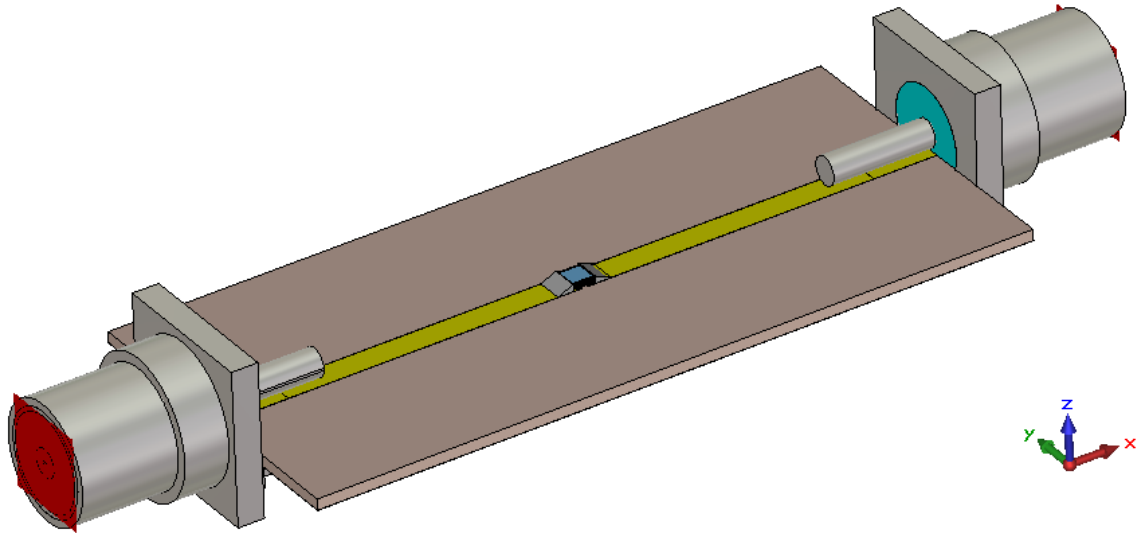


Figure 3.19: Full optically switched transmission line model in CST including 6 layer silicon, passivation layer and SMA connectors

The effect at 2GHz is small, 0.1dB when comparing the CST simulation with and without connectors, Figure 3.20. However at 10GHz the difference in S21 is 0.6dB. The effect of the connectors on the results is more noticeable as frequency increases; the peak transmission is at 5GHz for the simulated result. The peak in transmission for the measured 10mW result occurs at 4.58GHz.

There is also a discernible dip at 8.44GHz for the simulated 10mW result, the corresponding dip in the measured result occurs at 7.73GHz. The corresponding S11 results are presented in Figure 3.21. Similarly to the S21 analysis, the effect of adding the connectors into the simulation has a small effect on S11 up to ~4GHz. Above this frequency, the connectors impact more on the S11 results – the trend is more similar to the measured results.

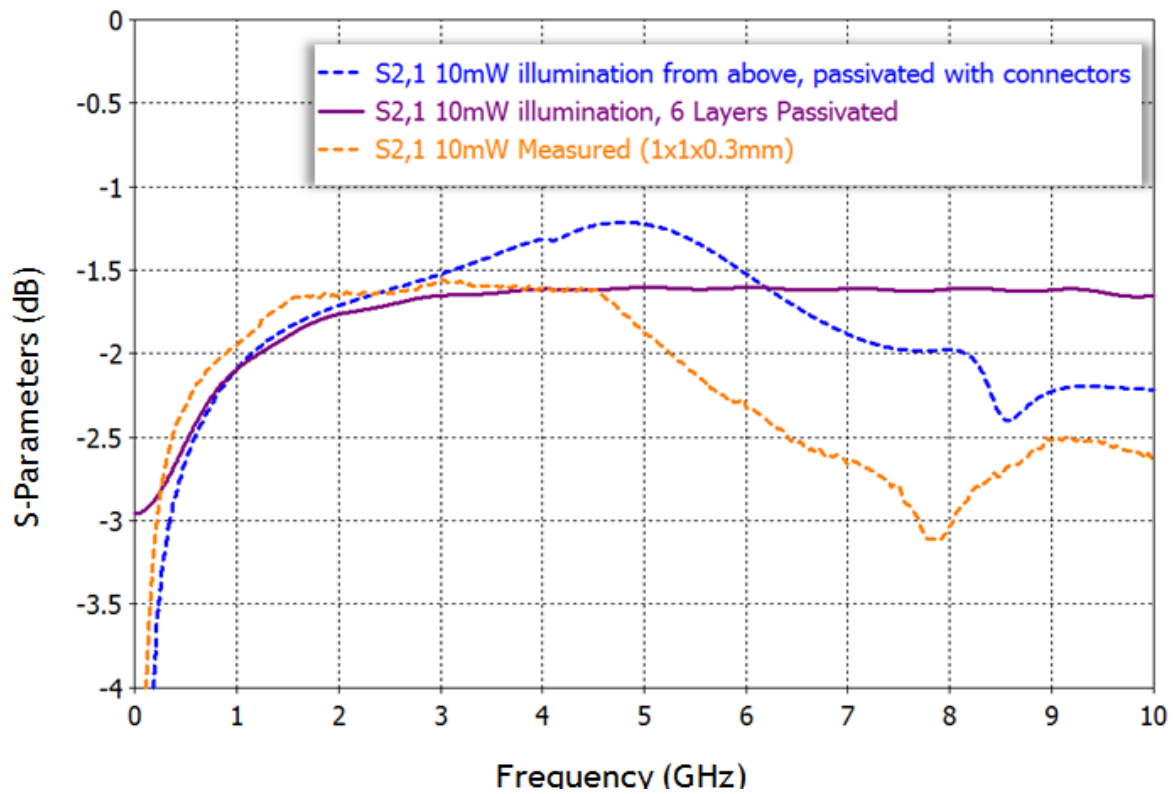


Figure 3.20: S_{21} parameters relating to simulated results for an optically switched transmission line model in CST including six layer silicon, passivation layer and SMA connectors

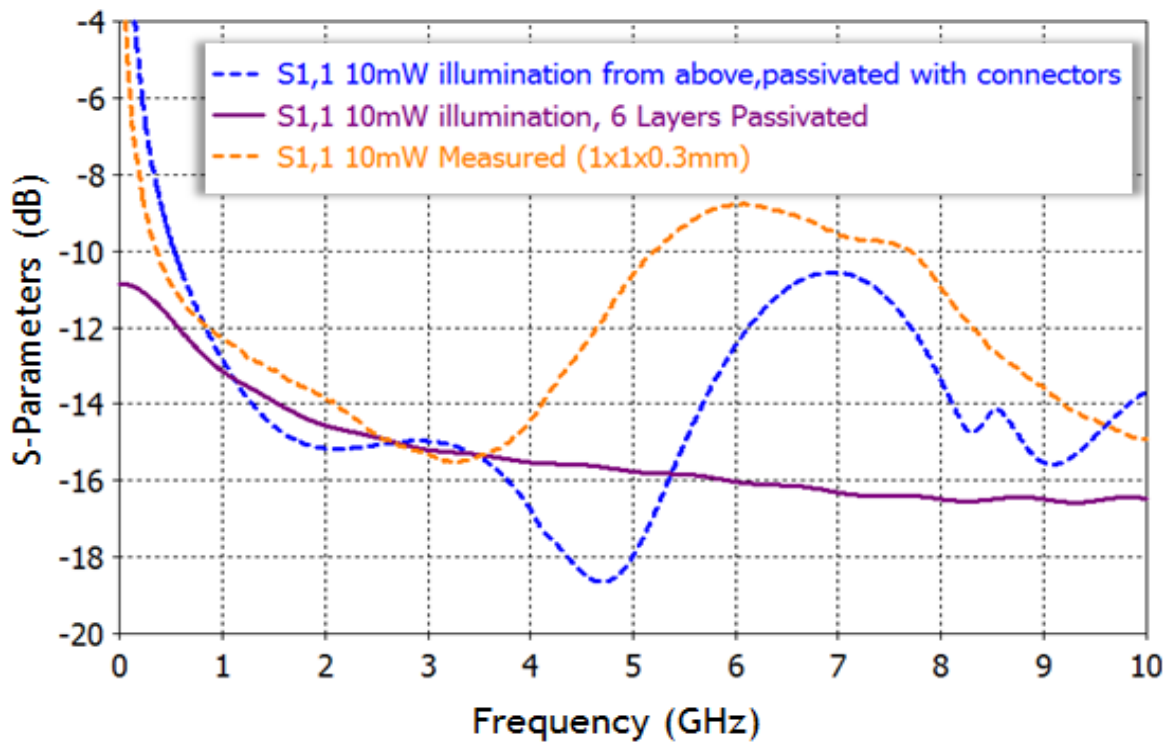


Figure 3.21: S_{11} parameters relating to simulated results for an optically switched transmission line model in CST including six layer silicon, passivation layer and SMA connectors

The OFF state S21 results are presented in Figure 3.22 and corresponding S11 results are presented in Figure 3.23 for the optically controlled transmission line with passivated silicon and SMA connectors. The conductivity of the die has been increased from the original estimation based on approximate doping density from 0.017S/m to 0.035S/m. At 2GHz, the measured result is -19.3dB and the simulated result is -21.8dB.

In terms of the S11, the measured result is 0.2dB less than the simulated result. As described previously, these slight discrepancies could be due to the doping concentration. This could be confirmed by running secondary ion mass spectrometry analysis on the silicon sample to determine the exact doping concentration, however this was not performed in this study.

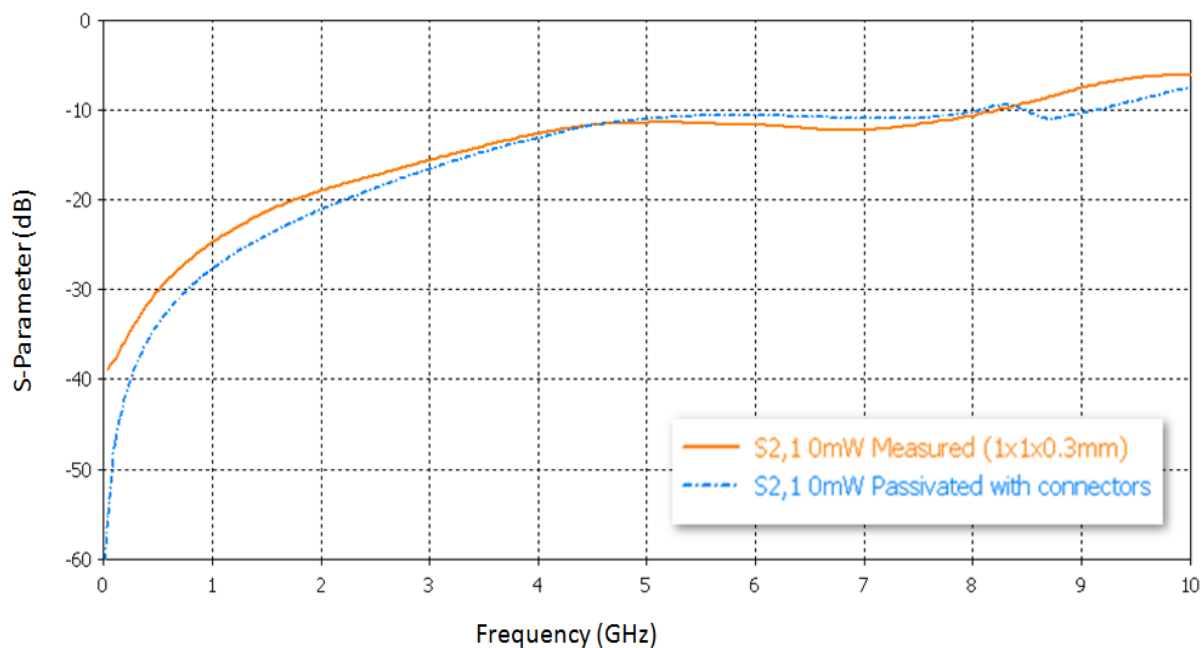


Figure 3.22: S21 relating to simulated results for an optically switched transmission line model in CST including passivation layer and SMA connectors in the OFF state (0mW radiant flux)

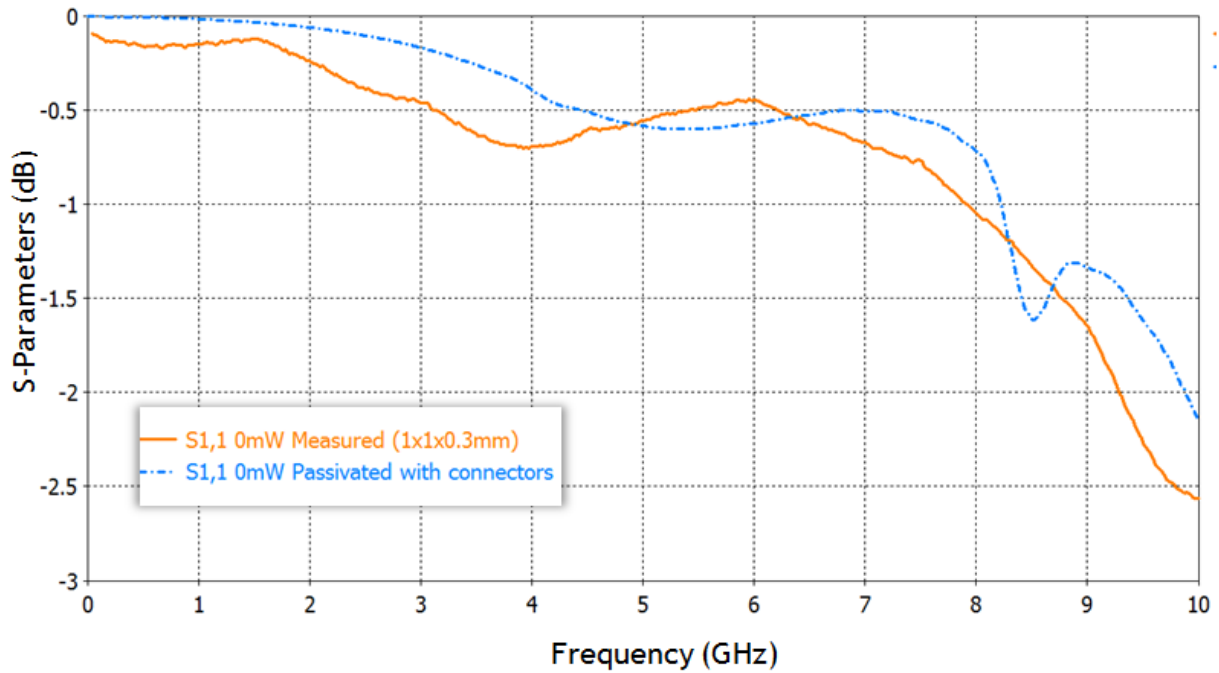


Figure 3.23: S11 relating to simulated results for an optically switched transmission line model in CST including passivation layer and SMA connectors in the OFF state (0mW radiant flux)

3.5 Maintaining Signal Planarity

The conductivity profile of the silicon depends on the illumination direction – in theory this can be applied from above or below and at any desired angle. Of particular interest and the motive behind this study is to investigate the concept of fibre optic control of the switch from below, delivered through the substrate. The benefits of such a control method are clear; it would allow the silicon die to be attached by a flip chip method. Directly connecting the die to the board shortens the signal path while reducing the interconnect inductance and capacitance, improving electrical performance.

A flip chip assembly also eliminates the need for wire bonds, potentially reducing package size [22]. Due to the nature of silicon's photoconductivity, the majority of charge carriers form at the surface of the silicon, with conductivity decreasing with further penetration into the silicon die. Illumination from beneath the silicon allows the microwave signal to benefit from the increased conductivity as it travels down the transmission line and through the silicon switch, maintaining planarity.

3.5.1 Wire bonding

Wire bonding involves forming metal wires between the signal path and metal pads that attach to the silicon die [22]. In the case of the photoconductive switch there is only one signal path, so one pad is required for input and a second for output, as is shown in Figure 3.24. The signal path is not planar as it tends to flow up the wire bonds into the metal pad as this provides less resistance than flowing directly into the conductive silicon. Often, multiple wire bonds are formed to reduce the parasitic inductance and also to improve reliability. Sometimes this can be applied as a ribbon bond [24] which provides the advantages of high current capability and reduced spreading resistance. Notice, that the most conductive layer of silicon is closest to the illumination source, and also closest to the metal pad where the wire bonds connect to. Wire bonding may be the ideal method of connection if illumination is from the top of the silicon die to best connect to the highest conductivity area of the silicon.

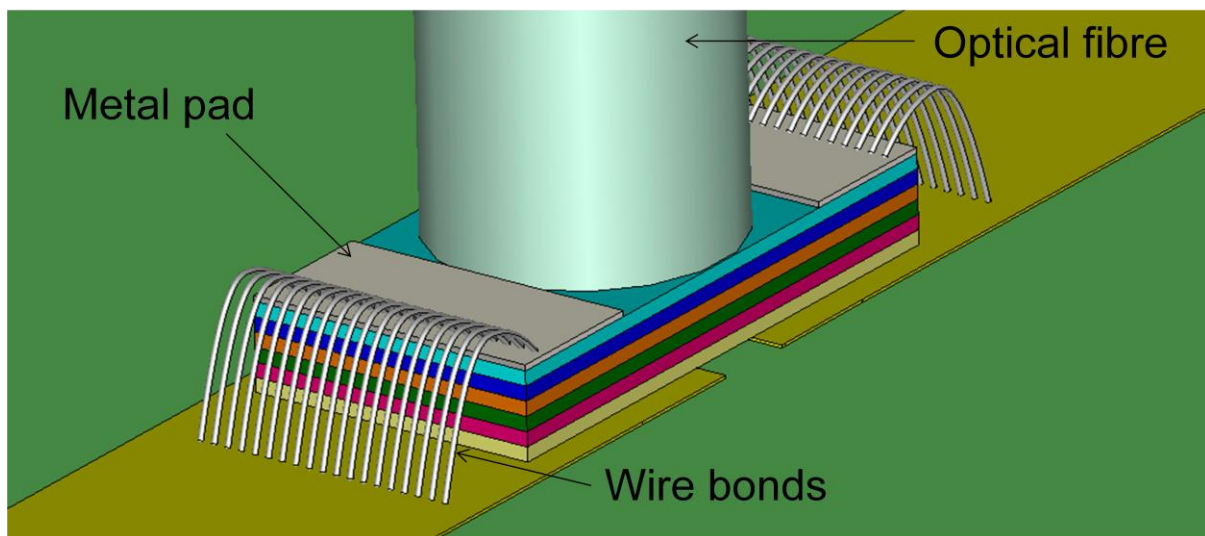


Figure 3.24: Representative model of a wire bonds connecting to a photoconductive silicon die with fibre optic cable

3.5.2 Flip Chip

Flip-chip technology was first introduced to integrated circuits (ICs) in 1964, when IBM introduced Controlled Collapse Chip Connection to interconnect ICs to their substrates [25]. The flip-chip technique is the mounting of a chip with its active side

facing the substrate. In the case of the photoconductive switch, this means the silicon surface which is illuminated.

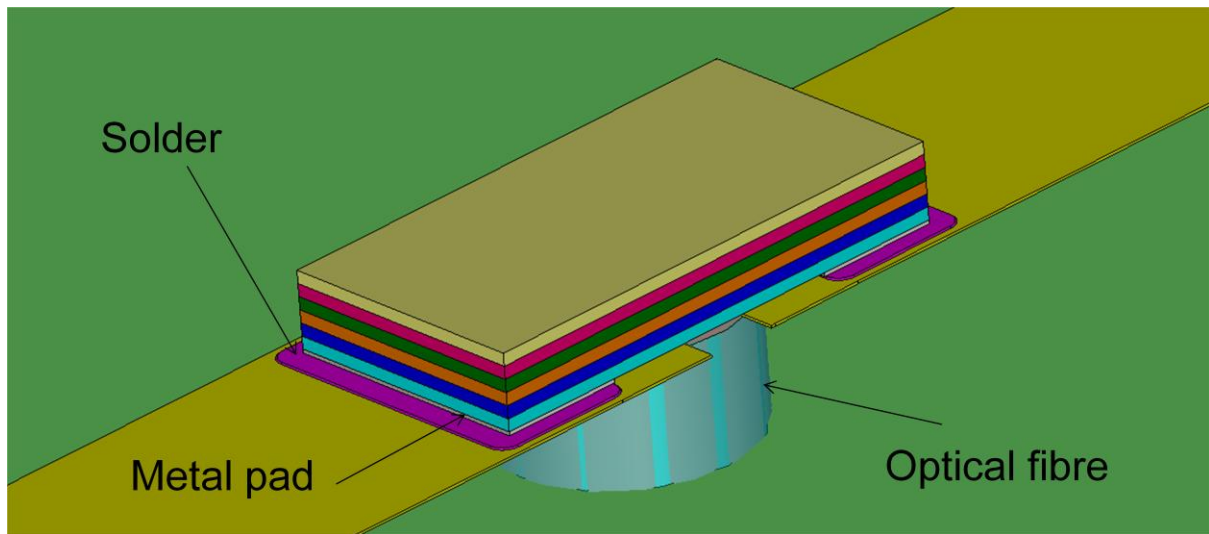


Figure 3.25: Representative simulation model of a flip-chip method of packaging for a bare silicon die photoconductive switch with fibre optic cable (substrate is made transparent so as to see the optical fibre)

The contact itself can be formed via a number of different methods – these include solder bumps, conductive polymers and pressure contacts. A representation of a flip chip type approach for the photoconductive switch is shown in Figure 3.25

There are a number of benefits this type of packaging technique can add to performance, especially when considering RF signals [26]. In particular, the shorter package-to-die path reduces inductance, hence reducing signal distortion at the interconnect. The technique also allows for thinner device profile and ease of manufacturability [27]. In the case of the photoconductive switch, only two connections are required, but in general the flip-chip technique is acknowledged to allow much finer pitch connections.

3.5.3 Planarity Study Simulations

The concept of planarity will be investigated through simulations, simply by considering the effect of applying illumination from above and below, without the associated packaging structures to establish the effects of planarity on switch performance.

In order to achieve this a photoconductive switch is modelled by attaching a silicon die between two lengths of transmission line using silver epoxy as is described in Section 3.4. To see the effect on the s-parameter and field performance, the same geometry of switch and transmission line is used but the silicon geometry is changed to reflect illumination from above (Figure 3.26 (a)) or from below (Figure 3.26 (b)).

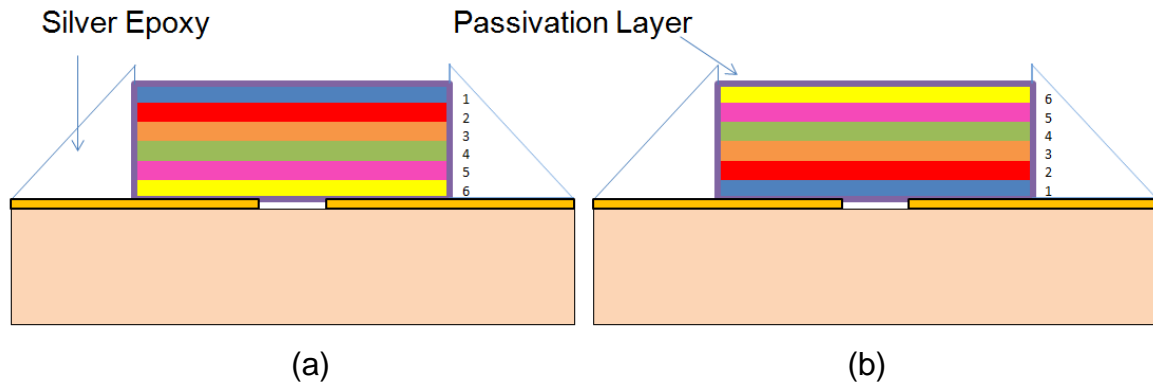


Figure 3.26: Layered silicon model including silver epoxy on a Rogers 3003 substrate with an Passivation (oxide) coating– illumination is from above (a) and below (b) – diagram is not to scale

In this preliminary study, the practicalities of illuminating the silicon die from below will be ignored. Illumination techniques will be covered in detail in the next section. The motive behind this investigation is to determine the benefit of this approach.

The silicon die has dimensions 1mm × 1mm × 0.3mm and is modelled on Rogers R3003 with a dielectric relative permittivity of 3 and a thickness of 0.5mm. The silicon is simulated as a dielectric with conductivity 0.035S/m in the OFF state. In the ON state the silicon is simulated as a dielectric material with a six layer conductivity profile, with the top layer closest to the illumination source having a conductivity of 259S/m and the bottom layer having a conductivity of 107S/m. The other conductivities and parameters are described in Section 3.4. The associated model includes SMA connectors and the 200nm passivation layer of the silicon die. The effects on insertion loss and isolation are simulated using CST Microwave Studio 2013 under the following conditions:

- Case A, Illumination is assumed from above, hence highest conductivity is present at the top of the silicon;

- Case B, Illumination is assumed from below, hence highest conductivity is present at the bottom of the silicon;

3.5.4 Planarity Study Results

Of particular interest is the transmission in the ON state. S21 results are presented in Figure 3.27. Here, it is clear that the transmission is only marginally improved by choosing to place the highest conductivity layer closest to the transmission line. At 2GHz, the improvement is 0.18dB. This corresponds to an S21 of -1.55dB for the silicon die illuminated from below and, -1.73dB for the die illuminated from above. At 10GHz the improvement is 0.25dB. The corresponding S21 at this frequency for the die illuminated from below is -1.95dB.

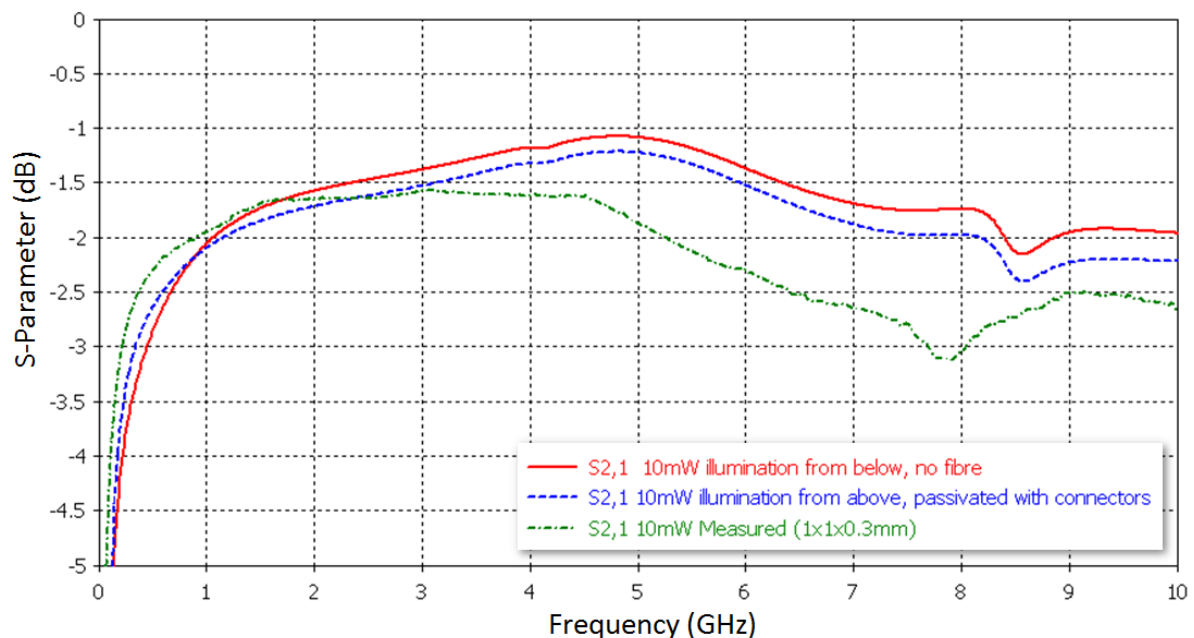


Figure 3.27: S21 performance of optically controlled transmission line with silicon illuminated from above and below. Measured result corresponds to illumination from above.

The S11 is presented in Figure 3.28. At 2GHz the S11 for the die illuminated from below is -16.5dB compared to an S11 of -15dB for the die illuminated from above. Although the physical optical feed is not considered here, it can be noted that there is some small benefit from having the most conductive area of the silicon in close proximity to the copper transmission line, hence maintaining signal planarity.

There may be two possible reasons for only a small difference in S-parameter performance. The first could be that the difference in conductivity between top and bottom layer conductivity is not particularly large for a 10mW radiant flux. There is still 107S/m conductivity on the layer furthest from the illumination, compared to the top layer of 259S/m.

If a shorter wavelength of light is used, the conductivity profile would have a much larger variation of the conductivity, where the highest conductivity is concentrated at the surface nearest to the illumination. In this case, signal planarity could be more important. This is an area of further work.

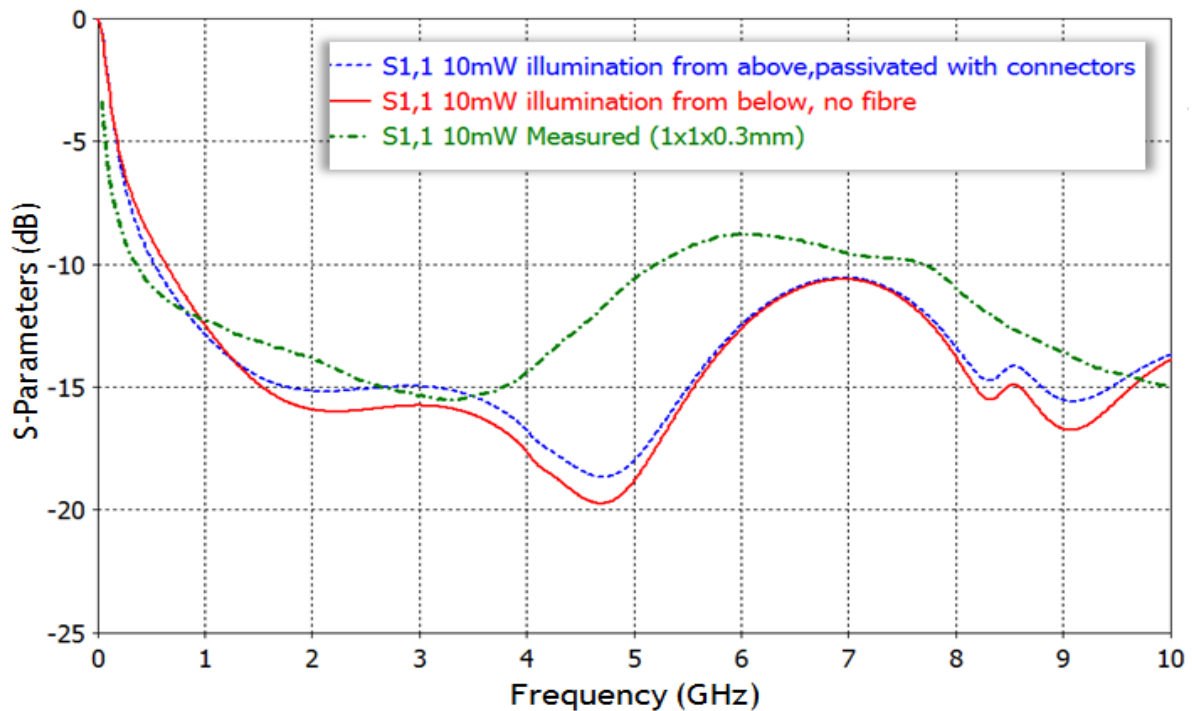


Figure 3.28: S11 performance of optically controlled transmission line with silicon illuminated from above and below. Measured result corresponds to illumination from above.

The second could be related to the large skin depth. For the maximum conductivity layer of 259S/m the skin depth is 0.70mm at 2GHz and is 0.31mm at 10GHz. The depth of the die is 0.3mm; hence the skin depth at the highest frequency being investigated and at the highest conductivity being simulated is larger than the thickness of the silicon. This means the signal travels throughout the volume of the

silicon, and is not confined to the edges as is the case for high conductivity materials such as Copper. The average conductivity of the illumination from above and below case is the same, and hence the S-parameter performance may be expected to be similar.

To investigate whether the small improvement can practically be applied, the method of light delivery will be investigated in more detail.

3.6 Optical Feed Techniques

The feasibility of the photoconductive switch as a packaged component that can be used in portable wireless systems relies on the ability to effectively deliver light accurately, efficiently and in a uniform fashion to the semiconductor switch in any situation. This section will review different optical feed techniques presented in the literature and investigate in detail the techniques needed to realise the flip-chip design in section 3.5.

3.6.1 Literature Review on Optical Feed techniques

The optically activated silicon switch for microwave applications was first demonstrated by Auston [28] in 1975 using a transmission line with a gap fabricated on silicon substrate. To allow signal to propagate light with a wavelength of $0.56\text{ }\mu\text{m}$ was allowed to illuminate the surface of the silicon. To prevent signal from propagating a higher wavelength of light was used which had the effect of increasing the absorption depth of the silicon making it conductive down to the ground plane, shorting the transmission line. The two pulses were generated using a mode locked Nd:glass laser. Both wavelengths were generated in conjunction with a crystal, and the pulses were separated in a beam splitter and focussed into a laser spot onto the gap in the silicon microstrip structure.

The drawback here is that two light sources are required to achieve fast switching speeds. More recently the illumination of silicon to define entire antenna geometries using a waveguide type system to deliver the illumination has been investigated. Such a design is demonstrated in [29]. Due to optical total reflection, it allows the laser beam delivered by the optical fibres to propagate inside the quartz waveguide – or the “light tank” - with minimal loss. When the light reaches the silicon there is a

change in refractive index which allows the light to leak out of the waveguide into the silicon and hence the bowtie antenna is created. In this case many fibres are needed to ensure flexibility of the switching mechanism. The reconfiguration is essentially making the antenna appear and disappear, which is proof of concept for more complex stacked geometries of antennas.

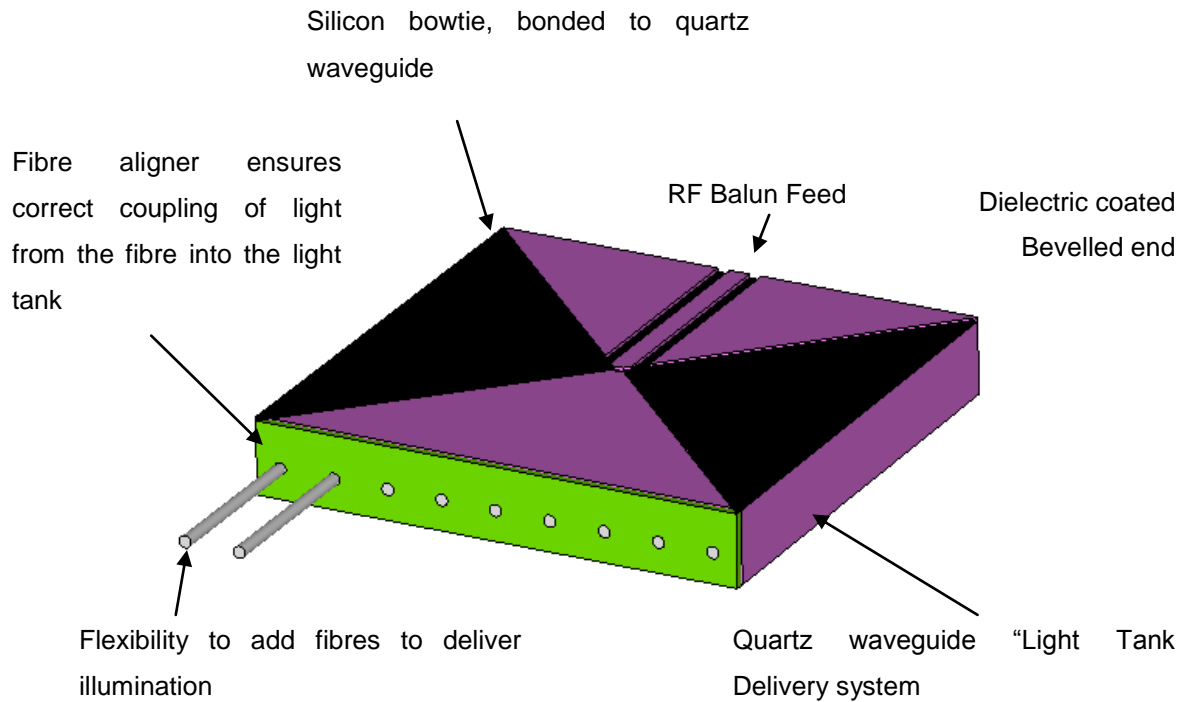


Figure 3.29: Waveguide light delivery system for reconfigurable bowtie antenna [29]

Fibre optic cable is an attractive medium of delivering illumination, as this light delivery method will not create EM interference with the RF circuitry. Due to the wavelength of light and high illumination power needed to achieve conductivity in silicon, coherent laser light produced by a laser diode and coupled into a fibre optic cable has been a popular choice in delivering the controlling illumination to the silicon material. Such a method is applied by Panagamuwa *et al.* [30] where a fibre is aligned manually at an angle of 45° to the surface of a silicon die of dimension $1\text{mm} \times 2\text{mm} \times 0.3\text{mm}$.

An insertion loss of 0.6dB is achieved when switched ON and an isolation of 16dB when OFF at 2GHz. The advantage of this method is that switch topology need not be altered to accommodate the optical control method. The study by Panagamuwa *et al.* acknowledged that to maximise light coupling the laser footprint must ideally uniformly illuminate the entire silicon die. However, the practicalities of implementing such a design in a portable wireless system were beyond the scope of Panagamuwa's research.

Similarly, the authors of [31] describe a light coupling method from above using LED light sources delivering a radiant flux of 22mW. A phase shifter is implemented using an array of LEDs to excite silicon switches. Respectively, Kaneko *et al.* [32] describe a photoconductive switch which is activated by a Vertical Cavity Surface Emitting Laser which has been flip chipped directly over the silicon switching element. The downside to both these approaches is that the light source is not remote, so power leads carrying DC current are in close proximity to the RF signal and directly in the antenna radiation plane, negating the perceived advantages of the optical switching trigger.

Tawk *et al.* [33] report on a light coupling method from beneath the antenna through the ground plane and substrate. In this instance a 1mm hole is drilled through the substrate and a fibre optic is butted against the bottom surface of the silicon switch and held in place using a plastic fixture. An insertion loss of 2dB in the ON state and an isolation of 7.5dB in the OFF state at 8.4GHz are reported. The authors later go on to utilise the new coupling geometry in a circular patch antenna. The advantage to this approach is that it allows for easier integration of antennas utilising this switch into microwave systems, particularly as the fibre can be aligned via a hole in the substrate and the switch can be packaged as a flip chip design with a view to maintaining signal path planarity. Potential drawbacks include the consequences associated with drilling holes into the substrate which may have an impact on the performance of the intended design. Performance degradation in terms of insertion loss and isolation may be observed, which will be investigated later in this paper.

Haupt *et al.* [34] also demonstrate optical control by allowing an LED to illuminate a photoconductive attenuator designed on a silicon substrate. The CPW with filter like design is printed on a silicon substrate. It is then incorporated into a monopole

antenna using a flip chip design, where the switch is turned over and the CPW is soldered onto the feed path of the antenna. A 3.5mm hole is drilled into the ground plane and substrate and a 40mW IR LED positioned underneath the hole is allowed to illuminate the flip chipped switch, Figure 3.30.

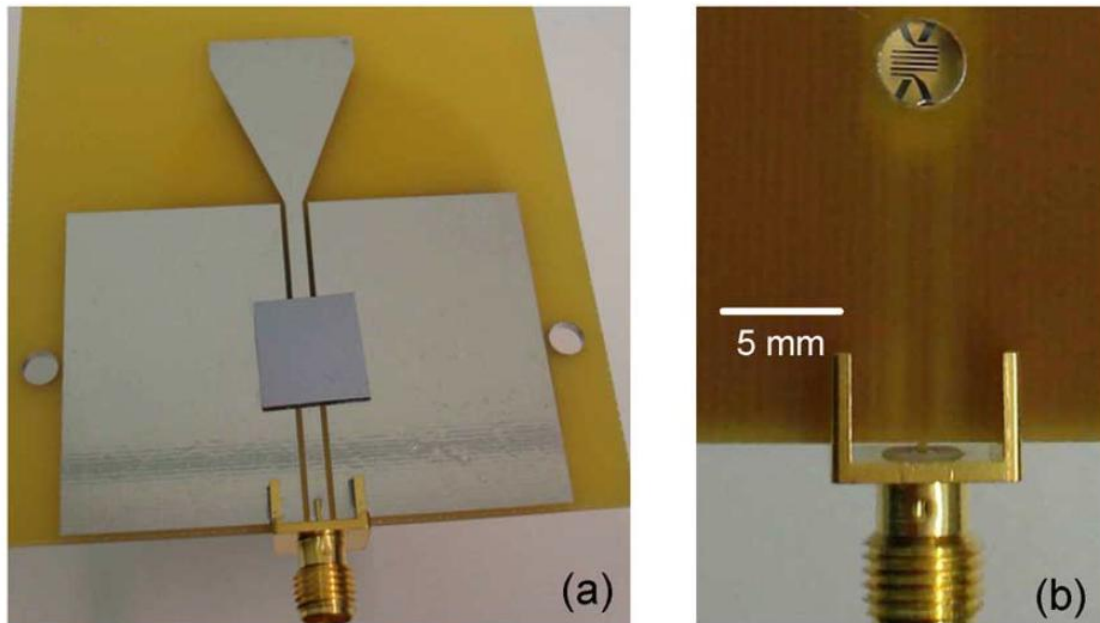


Figure 3.30: (a) Front and (b) back views of antenna element integrated with the photoconductive attenuator [34]

As an un-integrated switch, an isolation of 20dB is reported whilst under illumination of 40mW of radiant flux – e.g. illumination creates a short to the ground plane of the switch. An insertion loss of 0.6dB is recorded without illumination.

Lockyer *et al.* [35] describe a concept using a Xenon strobe lamp in conjunction with an optical mask on silicon to produce an FSS array. Similarly, the authors of [36] investigate the potential of directly illuminating a thick film of semiconductor CdS using a pixilated array of light sources from beneath a transparent ground plane to produce a metamorphic antenna. The quantity of high power illumination sources needed and the difficulty in confining conductivity of the semiconductor to the required antenna geometry without leakage are seen as major barriers to the practicality of this research.

Young *et al.* [37] look to address the issue of uniformity as well as efficiency by implementing a prismatic waveguide output coupler to distribute the light. Fibre

optics are still required to couple light into the waveguide, where an overall efficiency of 50% is reported. The silicon die is of a larger dimension in this research, 1mm × 5mm × 0.4mm; hence a greater radiant flux is required to create the desired level of illumination in the silicon. Under illumination of 470mW of radiant flux, the insertion loss at 2.4GHz is 30dB and the isolation under 0mW of radiant flux is 46dB. Clearly, this approach provides poorer transmission in the ON state and has the drawback of difficult integration into small systems.

3.6.2 Through the Substrate Feed Technique

Section 3.5 introduced the concept of signal planarity by ensuring the most conductive surface of the silicon die is in direct contact with the transmission line. This section will investigate the practicalities and consequences of delivering light to the silicon die from a fibre optic cable inserted from below the substrate, highlighted in Figure 3.31. This model includes 6 layer silicon with a passivation layer and SMA connectors on Rogers 3003 (0.5mm) substrate.

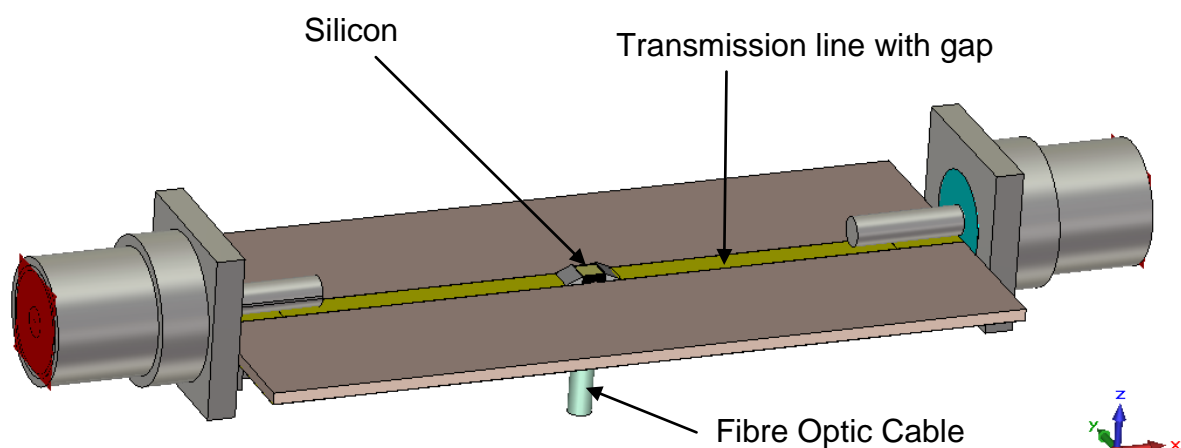


Figure 3.31: CAD model of optically switched transmission line with an optical fibre providing illumination to the silicon from below

The fibre was simulated as a dielectric with permittivity of 4.82 and corresponding loss tangent = 0.0054, these values are taken from the pre-loaded CST material

library. The effects on insertion loss and isolation are simulated using CST Microwave Studio 2013 under the following conditions:

- Case A, no fibre : reference model (illumination is assumed from below, without the fibre being present. Note that the hole in the substrate is not simulated either
- Case B, fibre inserted directly below the silicon die through the substrate with a fibre optic cable with a diameter of 1mm;
- Case C, fibre inserted directly below the silicon die through the substrate with a fibre optic cable with a diameter of 2mm;
- Case D, hole in the substrate to accommodate an LED which is permitted to shine onto the silicon. High power LEDS can typically have a diameter of 3.5mm

From these simulations the direct effect of coupling light into the silicon using a fibre optic or LED can be ascertained. Whilst modelling, it is assumed that light coupling to the silicon is 100% efficient. This study concentrates on the effect that fibre and LED position have on performance and not the coupling efficiency.

Simulated S-parameter results for case A, B and C are presented in Figure 3.32 and Figure 3.33

Case A: No Fibre (Reference)

This case is included so as to investigate the effect that a fibre, or hole in the ground plane might have on the microwave performance of the optically controlled microwave switch. Ideally, losses that are incurred by the optical feed structure should be minimised.

This case could be realistically accomplished by the use of transparent substrate such as polyethersulphone, a transparent plastic which has been researched in the photovoltaic industry [38]. Transparent conductors such as indium tin oxide could also enable feeding from below the substrate a feasible option as reported in [39].

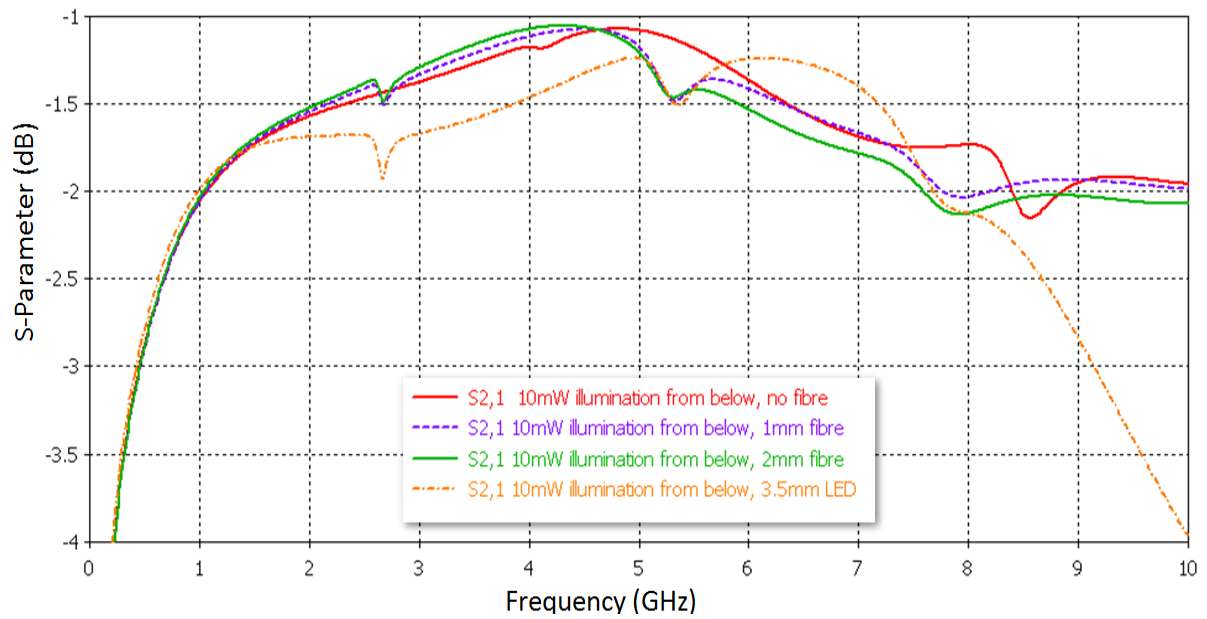


Figure 3.32: S21 performance of an optically controlled transmission line with varying diameter of fibre optic cable

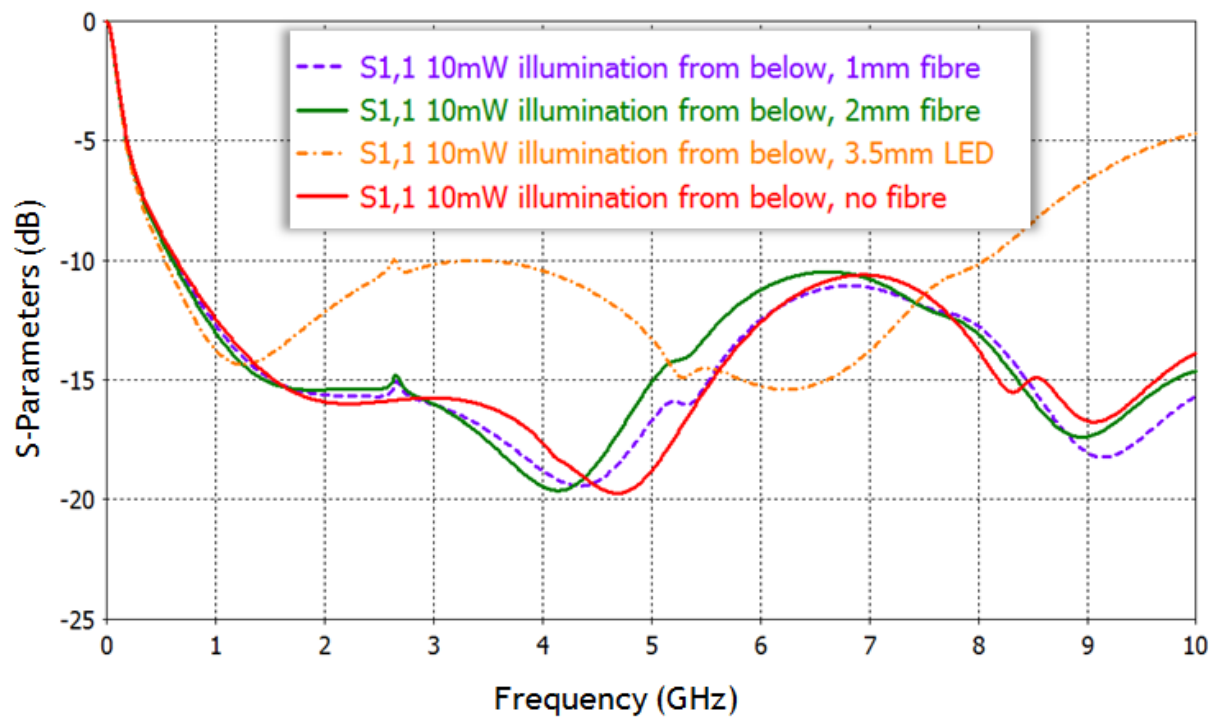


Figure 3.33: S11 performance of the optically switched transmission line under different fibre optic cable diameters

Case B: 1mm Fibre

Overall, inserting a 1mm fibre from below the substrate has little effect on S-parameter performance, when comparing the reference case (no fibre). However, there is a loss in transmission introduced at 2.65GHz, between 4.8- 5.8GHz and around 8GHz caused by the presence of a hole in the ground plane and substrate. In terms of S11 result, a similar trend can be observed. However, if the values are taken for 10GHz, the 1mm fibre case B demonstrates a smaller S11 of -16dB, where as the reference case A exhibits an S11 of -14dB. At this frequency there must be some radiation or loss occurring from the presence of the fibre which reduces both the reflected signal at port 1 and transmitted signal seen at port 2.

Case C: 2mm Fibre

The same discrepancies are also present for the simulations of the 2mm fibre through the substrate. There is a small dip in transmission at 2.65GHz and ~5GHz between the 2mm fibre (Case C) and the reference model (Case A). Up to 5.8GHz there is no discernible different in S21 between the scenario of a 1mm fibre and a 2mm fibre. The S21 performance above 5.8GHz between Case B and C shows a reduction in transmission of 0.15dB. The increase in fibre diameter has a negative effect on transmission performance for higher frequencies.

The surface currents for the 2mm optical fibre case C and no fibre case A are detailed in Figure 3.34 for a 2GHz input signal. The distribution between the two plots is fairly similar; however there are higher surface currents on the SMA connectors for the scenario where the fibre is present.

The maximum peak surface current for the case without the fibre is 280A/m, where as the maximum peak for the 2mm fibre optic case is 307A/m (1W peak input). The electric field for a 10GHz input signal is detailed in Figure 3.35 and Figure 3.36.

This shows the electric field distribution in the dielectric of the fibre and also how the signal is disturbed as it travels through the switch and fibre. In the case of the 2mm

fibre, there is slightly more field coupling towards the edges of the substrate when compared to the no fibre case.

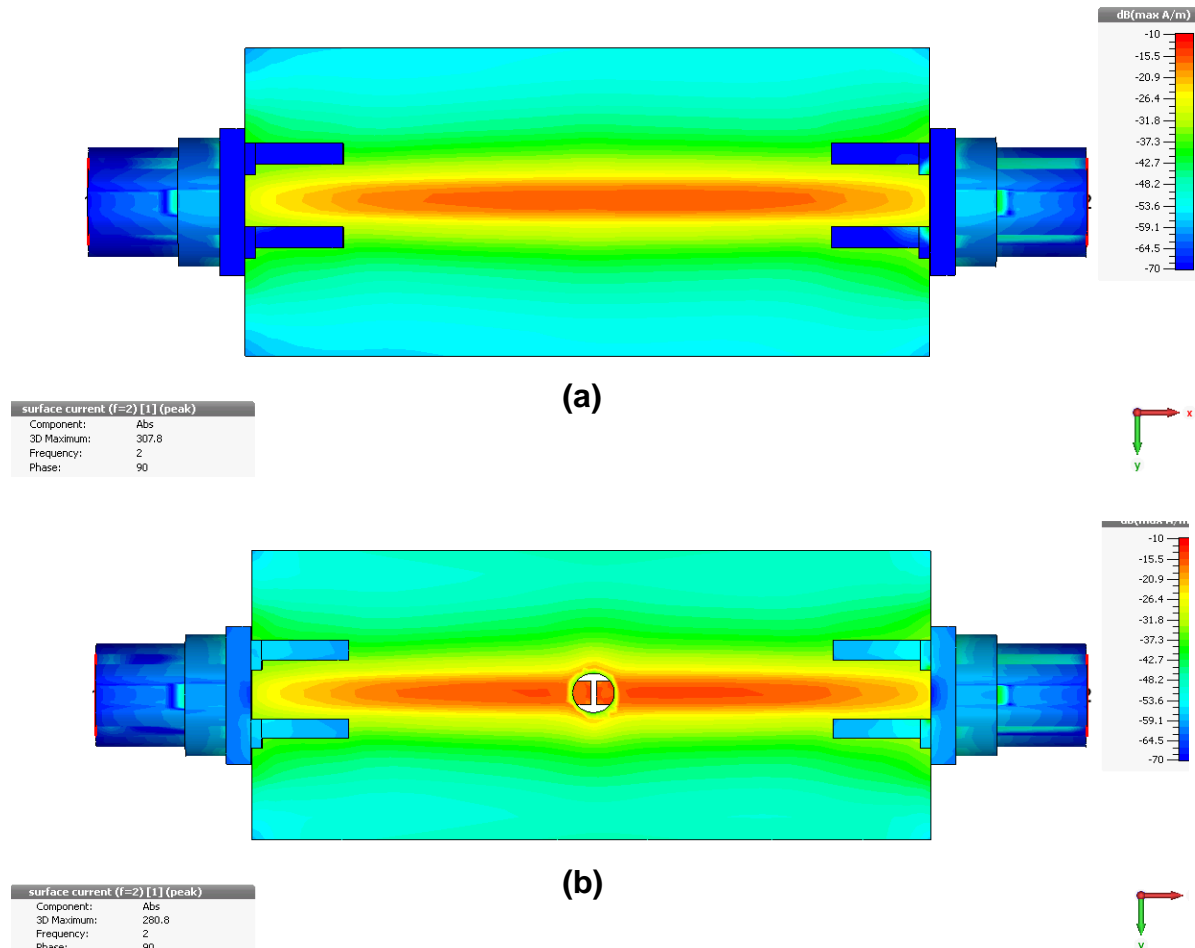


Figure 3.34: Surface currents on the topside of the ground plane and metallisation at 2GHz. Plot (a) shows the switch without a fibre. Plot (b) shows a switch with fibre inserted through ground plane and substrate. There is a higher level of surface current in the case where a fibre is inserted – noticeable on the SMA connectors and towards the corners of the board.

The differences in field distribution are small which correlates to the small changes seen in the S-parameter analysis. The plots show there are higher fields in the dielectrics and surrounding metal for the fibre case, which manifest as higher degrees of loss and reduced transmission through the structure.

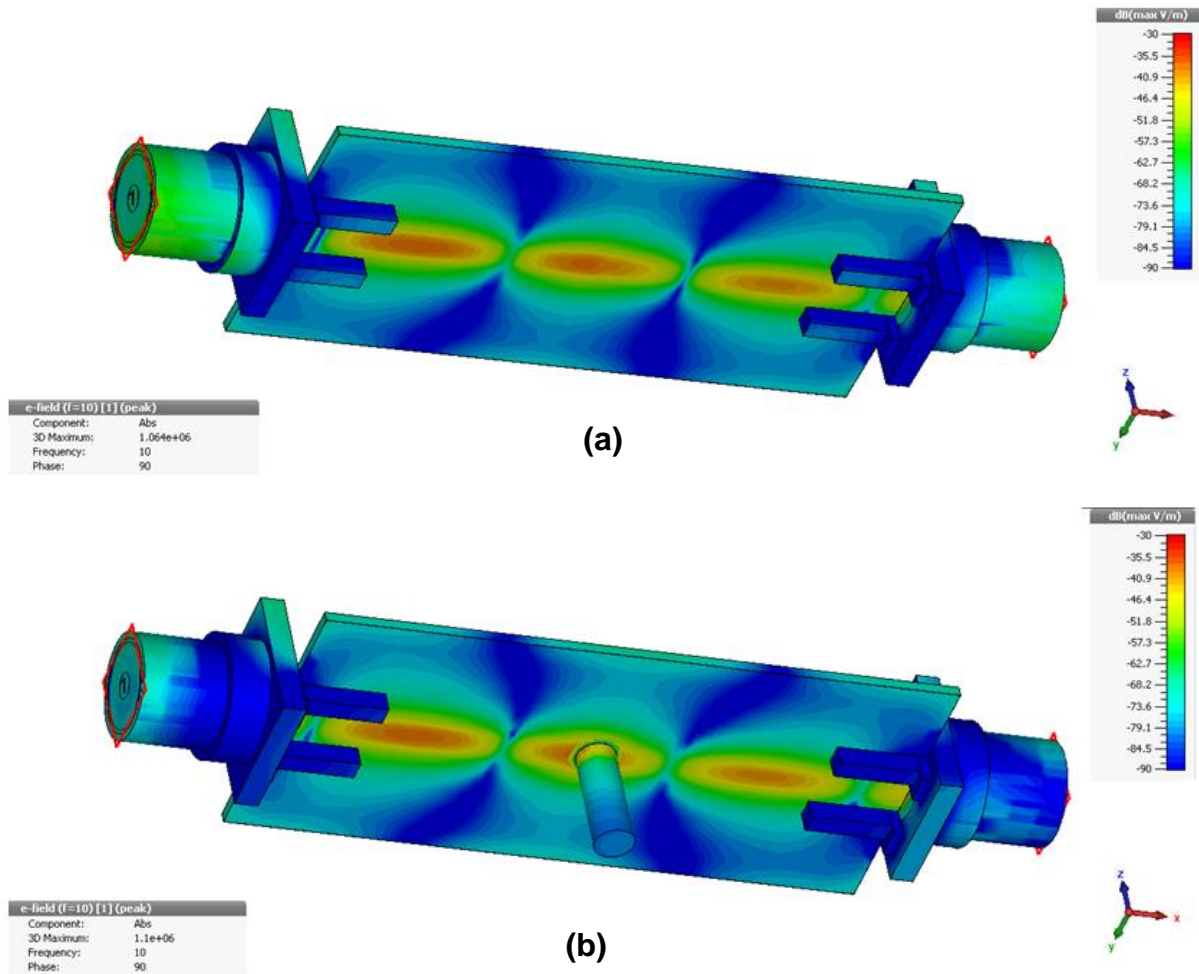


Figure 3.35: E-Field distribution on the underside of the switch at 10GHz. Plot (a) shows the switch without a fibre. Plot (b) shows a switch with fibre inserted through ground plane and substrate. There is a higher level of electric field coupling to the edge of the board in the case where a fibre is inserted.

Case D: 3.5mm Hole

There are notable advantages to using an LED over a laser source [40]. The laser diode is more efficient, however, it is more sensitive to electrostatic discharge and is more expensive. Generally, LEDs are potentially easier to integrate in terms of the additional components that are needed to operate the LED. Hence, it is worth investigating the scenario where the silicon is illuminated by an LED. Typically high power LEDs have a diameter in the region of 3.5mm [41].

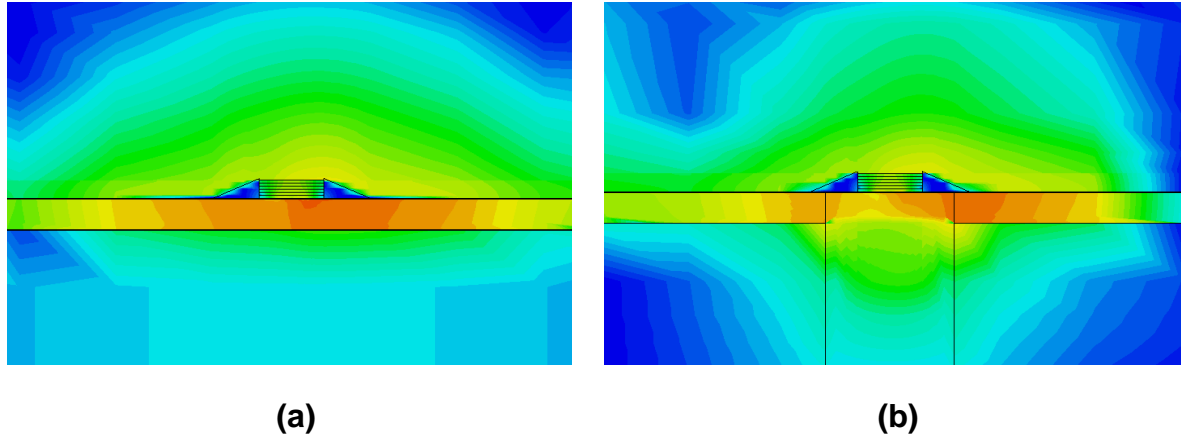


Figure 3.36: E-Field distribution for a cross section of the switch with (a) and without (b) fibre at 2GHz with the same scaling as in Figure 3.35

For the case where a 3.5mm hole is simulated in the substrate and ground plane under the switch, there is a more noticeable increase in insertion loss, particularly as frequency increases. At 2GHz the transmission is reduced by 0.2dB when compared to cases A B and C. Leading up to 10GHz, the transmission reduces to -4dB, this is 2dB below the scenarios where a 1mm and 2mm fibre are considered.

As wavelength decreases, the effects of the gap discontinuity become more pronounced. It is important to note that in this scenario there is no fibre in the substrate; instead there is a vacuum material which has a relative permittivity of 1. The relative permittivity of the substrate is 3. The greater the variance in permittivity the greater the potential discontinuity in the signal path. This could be the source for the reduced transmission performance. The fibre has a similar permittivity to that of the substrate, in the region of 4.82, and hence the reduction in transmission is not so great. It is also true that in the scenario of the larger hole, there is less ground plane. Since the fields are strongest between the transmission line and ground plane, the lack of ground plane in this region could potentially cause a greater degree of loss.

3.6.3 Fabrication

Since the ideal transmission line properties are based on a very thin substrate and simulated as such, a transmission line was fabricated on TLY-5 substrate, with a thickness of 1.15mm to ensure structural stability and ease of manufacture. Although

dimensions of the optically switched transmission line are different, the trend between illumination from above and below can still be explored, but not directly compared to the simulated results generated.

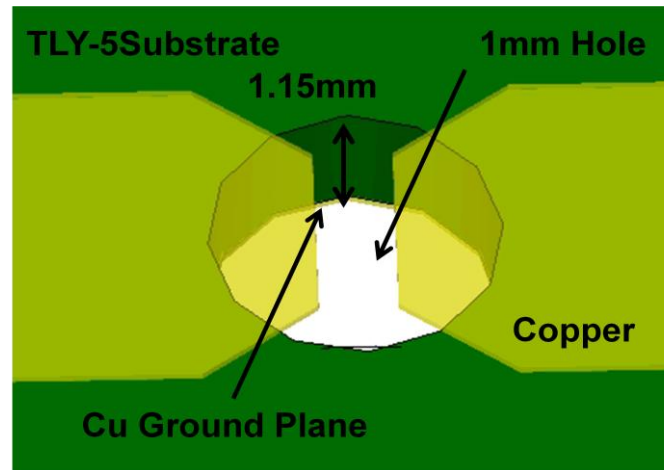


Figure 3.37: Transmission line topology including a hole in the substrate, copper has been given a slight transparency so as to demonstrate that the hole is in the ground plane and substrate only.

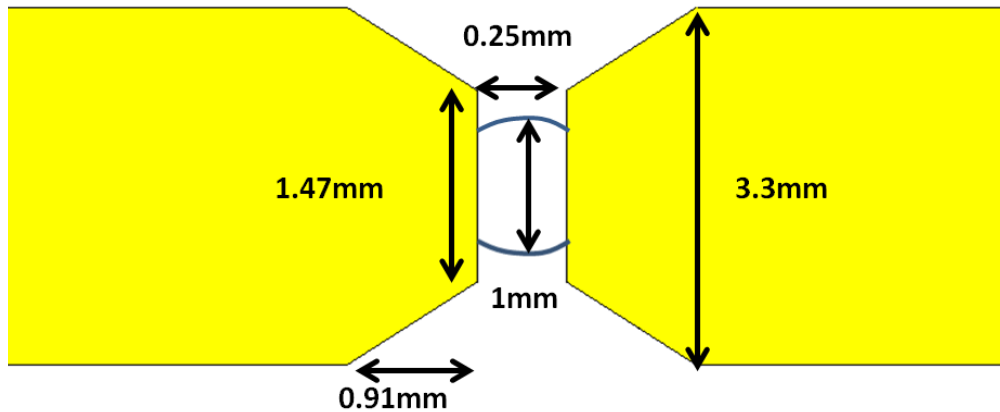


Figure 3.38: Transmission line dimensions including hole in substrate, the diagram is not to scale

When fabricating, a 1mm hole was drilled in the substrate leaving the copper transmission line and 0.25mm gap intact, with the silicon die bridging the gap. This is the same scenario as described in the previous simulation studies. Results are

presented in Figure 3.39 and Figure 3.40. Fabrication of the switch on the transmission line has revealed a larger insertion loss increase than predicted in simulation.

There is a decrease of 3.5dB in the transmission when light is delivered through the hole, however when light with a radiant flux of 200mW is delivered from above at an angle of 45° , the transmission is -1dB; some of this difference can be attributed to the difference in irradiation of the silicon die. Isolation in the OFF state is unaffected by the presence of the fibre through the substrate, as is observed in the simulation, and is 15.6dB at 2GHz.

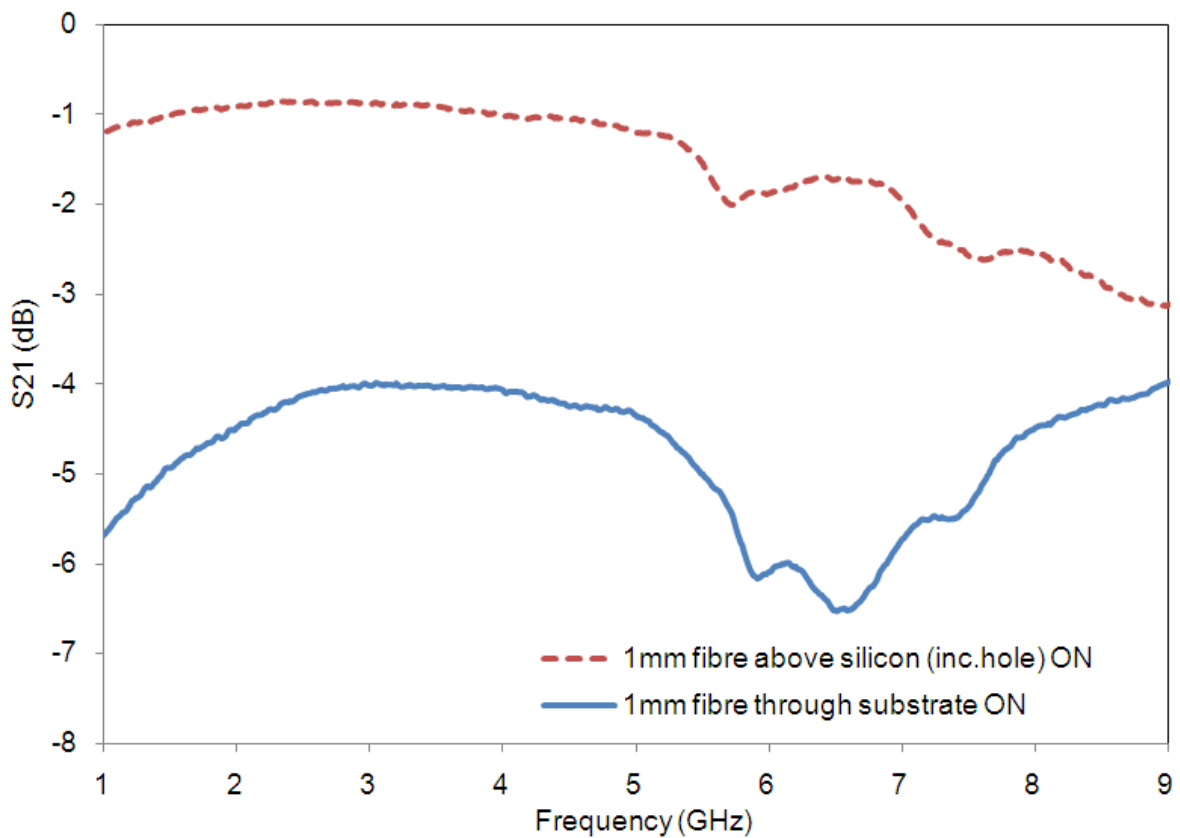


Figure 3.39: Measured S21 result of an optically switched transmission line controlled from above and below under 200mW of radiant flux

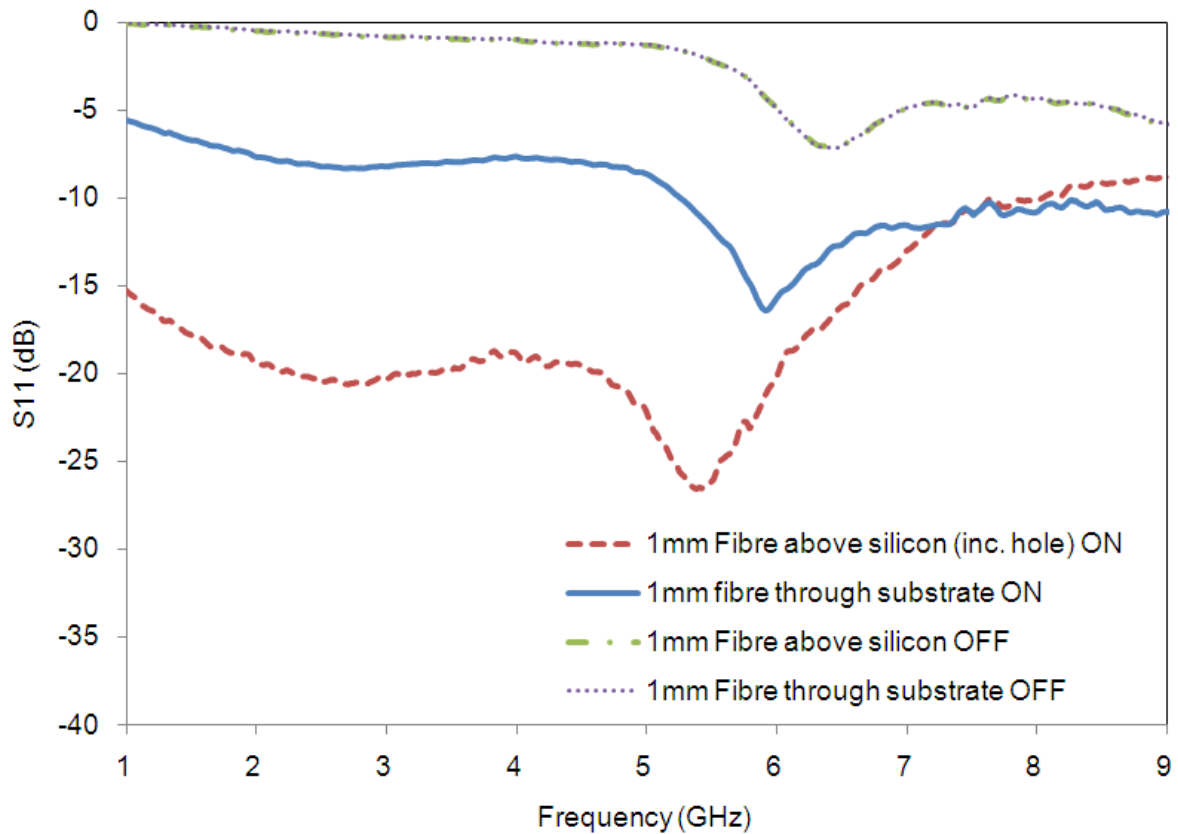


Figure 3.40: Measured S11 result of an optically switched transmission line controlled from above and below under 200mW of radiant flux

3.6.4 Discussion

The simulation results indicate that drilling a hole in the substrate and ground plane and insertion of a fibre optic cable has a small effect on the microwave performance of the switch and hence using a fibre optic or LED from beneath the ground plane is a viable optical control technique. There is some discrepancy between simulated values and measured results. Insertion loss when the fibre is fed through the substrate is increased by 3.5 dB compared to the same switch with a fibre delivering light from above. In simulation there was very little difference in insertion loss.

Differences can be attributed to the simplification of the simulation model for silicon conductivity. It is assumed that light coupling efficiency is 100% between fibre and silicon die. For the fabricated optical switch, light coupling can only occur through the 0.25mm gap between the transmission lines, this has the consequence that a proportion of the light delivered by the 1mm fibre will not irradiate the silicon die. The copper transmission lines reduce light coupling to the silicon by obstructing the

optical path. The width of the gap between the transmission lines greatly impacts the insertion loss of the switch. Hence by increasing the gap from 0.25mm to 1mm to allow unobstructed path for the light also dramatically increases switch insertion loss as there is reduced signal coupling across the transmission line gap.

Alternatives to improve light coupling and yet maintain similar levels of insertion loss could include using a smaller silicon die together with a reduced diameter of fibre optic. The possibility of using a transparent conductor, as mentioned in [39] could also provide an unobstructed path for illumination of the silicon. Limited simulation has revealed that as the substrate permittivity increases, and hence diverges from the permittivity of the glass fibre, $\epsilon_r = 4.85$, there appears to be an increased loss in transmission as a discontinuity occurs at the material boundaries. Hence choice of substrate is also a concern when choosing to use this optical control method.

The simulation model does not include the formation of an insulating silicon oxide which is present from the passivation process. Passivation prevents the formation of an ohmic contact between silicon and transmission line; hence an increase in insertion loss for the fabricated transmission line is observed. Due to this layer the full benefits of signal path planarity cannot be realised as the contact between die and transmission line is degraded.

Perfecting fibre alignment will increase light coupling and silicon treatments such as anti-reflection coating and optimisation of passivation will improve conductivity. Signal planarity could further be exploited using the fibre optic underneath the silicon die by using a lower wavelength of optical illumination. This would decrease the absorption depth, hence raising the concentration of charge carriers near the surface of the silicon which in a flip chip assembly is in close proximity to the transmission line, hence reducing signal path.

Supplying light from above the silicon die avoids having to alter switch topology to suit the optical control method. When fibre supplies illumination from above the silicon, substrate choice, transmission line width and gap between the transmission lines have no effect on optical coupling of light into the silicon die. In this instance, microwave performance due to switch topology can be optimised separately without detriment to optical coupling.

3.7 Conclusions

An optimised transmission line topology has been presented which provides maximum transmission in the ON state and minimises isolation in the OFF state. This is achieved by matching the transmission line width to the width of silicon. A transmission line which is slightly larger than the die width accommodates electric field fringing which occurs across the gap in transmission lines.

This optimised transmission line is used as the basis for exploring the simulation model of the silicon die. Equations introduced in Chapter 2 are used to model the silicon as a six layer model, with a frequency dependent conductivity profile. The effects of passivation and SMA connectors also reduced transmission of the optically controlled transmission line. This is an important step to accurately modelling the effect a photoconductive switch will have on an RF application such as a reconfigurable system.

It has been demonstrated that if the highest conductivity layer in the silicon is in closest proximity to the copper transmission line then transmission performance in the ON state can be marginally improved by 0.18dB. In order to implement this, the optical feed method is investigated.

The potential for using fibre optic cable in the control of a photoconductive microwave switch have been simulated and discussed. Simulation results suggest that insertion loss in the ON state is not adversely affected by attaching a 1mm fibre through the ground plane and substrate. If the hole in the substrate and ground plane is made larger to accommodate a LED source of diameter 3.5mm, the effects on transmission are degraded by up to 2dB at 10GHz.

The benefits of supplying the light from beneath the ground plane are clear, this method allows for a flip chip package design maintaining signal planarity and potentially improving performance. The barrier to realising such a design is the obstruction of the light path caused by switch topology. These are promising findings as there is potential to investigate other switch topologies which may include transparent materials such as transparent conductor indium tin oxide in order to improve transmission in the ON state for the photoconductive microwave switch.

3.8 References

- [1] B-Z. Wang, S. Xiao, and J. Wang. "Reconfigurable patch-antenna design for wideband wireless communication systems." *IET Microwaves, Antennas & Propagation*, Vol. 1, no. 2, pp. 414-419, 2007
- [2] D. Piazza, N. J. Kirsch, A. Forenza, R. W. Heath, and K. R. Dandekar. "Design and evaluation of a reconfigurable antenna array for MIMO systems." *IEEE Transactions on Antennas and Propagation*, Vol. 56, no. 3, pp.869-881, 2008.
- [3] A. Bhadauria, A. K. Verma, E. K. Sharma, and B. R. Singh. "Optically controlled microstrip load and stub on silicon substrate." *Microwave and Optical Technology Letters* 39, no. 4, pp. 271-276, 2003.
- [4] C. J. Panagamuwa, A. Chauraya, and J. C. Vardaxoglou, "Frequency and beam reconfigurable antenna using photoconducting switches," *IEEE Trans. Antennas Propagation*, vol. 54, no.2, pp. 449-454, 2006.
- [5] W. Platte, and B. Sauerer, "Optically CW-induced losses in semiconductor coplanar waveguides" *IEEE Trans. Microwave theory and Techniques*, Vol. 37 pp. 139, Jan 1989
- [6] G. Rene, J. D. Arnould, and A. Vilcot. "Semi-analytical computation and 3D modelling of the microwave photo-induced load in CPW technology." *Microwave and optical technology letters* 48, no. 9 pp. 1718-1721, 2006.
- [7] G. Arfken, "Hankel Functions." *Mathematical Methods for Physicists*, 3rd ed. Orlando, FL: Academic Press, Chapter 11.4, pp. 604-610, 1985
- [8] A. Chauraya, D. S. Lockyer, Y. L. R. Lee, and J. C. Vardaxoglou. "A study of optically tuned metallodielectric photonic band gap array and patch antenna," *ICAP 11th International Conference on Antennas and Propagation*, pp. 492-496, 2001.
- [9] J. R. Flemish, and R. L. Haupt, "Optimisation of a photonicallly controlled microwave switch and attenuator," *IEEE transactions on microwave theory and techniques*, vol. 58, No. 10, 2010.

- [10] D. Liu, D. Charette, M. Bergeron, and H. Karwacki, "A 1-18 GHz photonicallly-reconfigurable phased-array antenna," IEEE Proc. Aerospace Conference, vol. 3, pp. 483, 1998
- [11] X. Xue, H. Wei, and I. Shih. "Optically controlled switching in microwave bridges." In Microwave Conference, 2000. 30th European, pp. 1-4. IEEE, 2000
- [12] IMST EMPIRE XCcel version 5.3, <http://www.empire.de/>
- [13] CST STUDIO SUITE 2013, <http://www.cst.com/>
- [14] Y. Tawk, A. R. Albrecht, S. Hemmady, G. Balakrishnan and C. G. Christodoulou, "Optically Pumped Frequency Reconfigurable Antenna Design", IEEE Antennas and Wireless Propagation Letters, vol. 9, pp. 280-283
- [15] K. Rabbi, L. Athukorala, C. Panagamuwa, J. C. Vardaxoglou, and D. Budimir. "Highly linear microstrip wideband bandpass filter with switchable notched band for wireless applications." Microwave and Optical Technology Letters 55, no. 6, pp. 1331-1335, 2013.
- [16] K. S. Yee, "Numerical solution of initial boundary value problems involving Maxwell's equations in isotropic media." IEEE Trans. Antennas Propag. 14, no. 3 pp.302-307, 1966.
- [17] T. Weiland "A discretization model for the solution of Maxwell's equations for six-component fields." Archiv Elektronik und Uebertragungstechnik 31 pp. 116-120, 1977
- [18] E. Hendry, M. Koeberg, J. Pijpers, and M. Bonn, "Reduction of carrier mobility in semiconductors caused by charge-charge interactions", The American Physical Society, Physical Review B 75, 233202, 2007
- [19] Antenna Magus, version 4.3, <http://www.antennamagus.com/>
- [20] M. Rutschlin "Measurement and Simulation in Modern Device Design" Computer Simulation Technology European User Conference, session 5.1.3, 2012

- [21] A. Benninghoven, "Surface investigation of solids by the statical method of secondary ion mass spectroscopy (SIMS)." *Surface science* 35 (1973): 427-457.
- [22] R. G. Werner, D. R. Frear, J. DeRosa, and E. Sorongon. "Flip chip packaging." In *Advanced Packaging Materials: Processes, Properties and Interfaces*, 1999. Proceedings. International Symposium on, pp. 246-251. IEEE, 1999.
- [23] G. G. Harman, *Wire bonding in microelectronics*. McGraw-Hill, 2010.
- [24] S. Masahito, and N. Takeuchi. "Ribbon, bonding wire and microwave circuit package." U.S. Patent 5,936,492, issued August 10, 1999.
- [25] G. A. Riley "Challenges in Flip Chip Assembly," *Solid State Technology*, <http://electroiq.com/blog/2007/05/challenges-in-flip-chip-assembly/> website last accessed April 2014
- [26] T. Krems, W. Haydl, H. Massler, and J. Rudiger. "Millimeter-wave performance of chip interconnections using wire bonding and flip chip." In *Microwave Symposium Digest*, 1996., IEEE MTT-S International, vol. 1, pp. 247-250. IEEE, 1996.
- [27] T. Tschan "An Overview of Flip-Chip Technology," *Chip Scale Review*, June 2001, website http://www.chipscalereview.com/archives/ES/issues/0501/tutorial_01.html
- [28] D. H. Auston, "Picosecond optoelectronic switching and gating in silicon," *Applied Physics Letters*, vol. 26, pp. 101-103, 1975
- [29] D. Liu, D. Charette, M. Bergeron, H. Karwacki, S. Adams, B. Lanning, and F. Kustas. "Structurally embedded photoconductive silicon bowtie antenna." *Photonics Technology Letters*, IEEE 10, no. 5, pp. 716-718, 1998.
- [30] C. J. Panagamuwa and J. C. Vardaxoglou, "Optically reconfigurable balanced dipole antenna", *12th Int. Conf. Antennas Propagation*, vol. 1, pp.237 -240 2003
- [31] C. J. Panagamuwa, A. Chauraya, and J. C. Vardaxoglou, "Antenna frequency and beam reconfiguring using photoconducting switches," *IET Seminar on*

Wideband, Multiband Antennas and Arrays for Defence or Civil Applications, pp. 55, 2008

- [32] Y. Kaneko, T. Takenaka, T. S. Low, Y. Kondoh, D. E. Mars, D. Cook, and M. Saito, "Microwave switch: LAMPS (light activated microwave photoconductive switch)," IEEE Electronic Letters, 2003.
- [33] Y. Tawk, A. R. Albrecht, S. Hemmady, G. Balakrishnan, and C. G. Christodoulou, "Optically pumped frequency reconfigurable antenna design," IEEE Antennas and Wireless Propagation Letters, vol. 9, pp. 280-283, 2010
- [34] J. R. Flemish, and R. L. Haupt, "Optimisation of a photonically controlled microwave switch and attenuator," IEEE transactions on microwave theory and techniques, vol. 58, No. 10, 2010.
- [35] D. S. Lockyer, J. C. Vardaxoglou, and M. J. Kearney, "FSS array generation by optical means," National Conference on Antennas and Propagation, pp. 132-135, 1999
- [36] R. P. Tuffin, I. C. Sage, B. J. Hughes, and G. J. Ball, "Electronically controlled metamorphic antenna," 4th EMRS DTC Technical Conference Edinburgh, A9, 2007
- [37] P. P. Young, R. Magnusson, T. A. Maldonado, and T. R. Holzheimer, "Method for high power illumination of silicon for optically configurable microwave circuits," Proc. SPIE 4768, vol. 74, 2002
- [38] K. Woo, D. Kim, J. S. Kim, Soonkwon Lim and J. Moon. "Ink-Jet printing of Cu-Ag-based highly conductive tracks on a transparent substrate." Langmuir 25, no. 1, pp. 429-433, 2008.
- [39] R. L. Haupt "An Adaptive Rectangular Microstrip Patch Antenna Array Element Using Photonic Controls," IEEE Aerospace Conference, pp. 1-6, March 2008
- [40] M. Ott "Capabilities and Reliability of LEDs and Laser Diodes", What's New in Electronics, vol. 20, no. 6, 1997

- [41] OSRAM LED datasheet “SFH 4232, IR LED Emitter, 850nm 120deg “available online <http://uk.rs-online.com/web/p/ir-leds/6811244/> last accessed June 2013.
- [42] S. S. Gevorgian, “Design considerations for an optically excited semiconductor microstrip gap at microwave frequencies”, IEE Proc. Vol 139, No. 2, April 1992
- [43] Y. Tawk, A. R. Albrecht, S. Hemmady, G. Balakrishnan and C. G. Christodoulou, “Optically Pumped Frequency Reconfigurable Antenna Design”, IEEE Antennas and Wireless Propagation Letters, vol. 9, pp. 280-283
- [44] K. P. Kumar and R. Seager “Optically controlled microwave switch packaging” Unpublished Project report, Loughborough University, September 2006
- [45] A. M. Yadav, C. J. Panagamuwa, and R.D. Seager, “Investigating the effects of control lines on a frequency reconfigurable patch antenna,” Loughborough Antennas & Propagation Conference, 2010
- [46] E. K. Kowalczyk, C. J. Panagamuwa, R. D. Seager, and J. C. Vardaxoglou, “Characterising the linearity of an optically controlled photoconductive microwave switch,” Loughborough Antennas and Propagation Conference, 2010

4 Fabrication Techniques for Photoconductive Switches Using Silicon

There are four main components to consider whilst researching photoconductive switches (PCS); the transmission line topology, the semiconductor choice, connection methods and also the light source selection. Light source selection and transmission line topology has already been covered in Chapters 2 and 3. In this chapter, the fabrication of the switch will be considered with regards to the silicon treatment and the connection method between transmission line and silicon die.

4.1 Introduction

In terms of silicon choice, the first decision when making a device incorporating silicon is which type of wafer to select. Initial factors such as surface quality and doping will affect the conductive properties of the silicon as is described in Chapter 2. However, it is also common to apply post-processing on the wafers to enhance their quality. These processes such as passivation and texturing are described and tested in the context of the photoconductive microwave switch in the following sections.

Lastly, further variations of switch design are investigated. These include depositing gold pads onto the silicon in order to make a better electrical connection to the silicon die. Figure 4.1 shows a top level fabrication workflow starting from a silicon wafer and describing the steps required to process the silicon into a photoconductive switch.

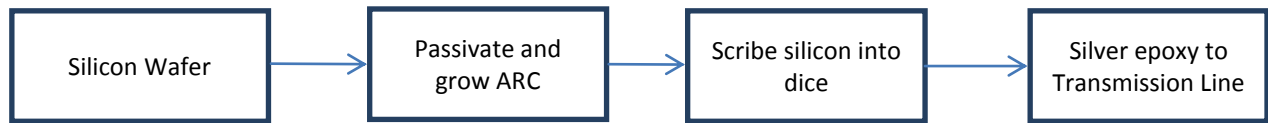


Figure 4.1: Process used to fabricate photconductive switch, process may include growing anti-reflective coating (ARC)

The initial processing of the silicon into wafer form has already been covered in Chapter 2 - two different wafers of silicon with differing properties are studied in this chapter. One high quality phosphorus doped silicon wafer which is 300 μ m thick and one boron doped 530 μ m thick wafer which is of lower quality. Both these wafers have been described in detail in Chapter 2. The second step once a wafer has been purchased is to try to improve performance by applying techniques such as passivation, which will be described in the following sections.

To become a useful component the silicon must be cut to the correct dimensions and then finally connected into the switching circuitry. Several methods exist to make an electrical connection such as the use of conducting polymers, solder and wire bonds; however some of these methods require further processing of the silicon. Since the transmission line topology has been optimised in Chapter 3, this chapter focuses on ways to optimise the silicon.

4.2 Overview on Silicon Processing Techniques

Once the silicon wafer is formed, it can further be refined, depending on application. In order to improve conductivity, it is possible to both maximise the amount of light that enters the silicon and maximise the carrier lifetime by improving silicon quality.

4.2.1 Anti-Reflection Coating (ARC)

With regards to developing techniques to enhance the performance of silicon in the photovoltaic industry, renewable solar energy research has focussed on reducing the amount of reflection on the surface of solar panels [1]. Anti-reflective coatings (ARC) deposited as films on semiconductor surfaces decreases the reflected light on the

premise of a thickness, d , related to the wavelength of light, λ_0 and the refractive index of the ARC, n_1 as is presented in Eq. (4.1):

$$d = \frac{\lambda_0}{4n_1} \quad \text{Eq. (4.1)}$$

n_1 should be chosen on the basis that it will act as a ‘matching’ material between the air (refractive index n_0) and silicon (refractive index n_2) as is described by Eq. (4.2).

$$n_1 = \sqrt{n_0 n_2} \quad \text{Eq. (4.2)}$$

Ideally this is around the region of 1.9 at 980nm – this corresponds to a value of $n_2 = 3.58$ as can be extracted from Figure 4.2. Silicon dioxide is commonly used as an ARC on solar cells and has a refractive index of ~ 1.5 [4].

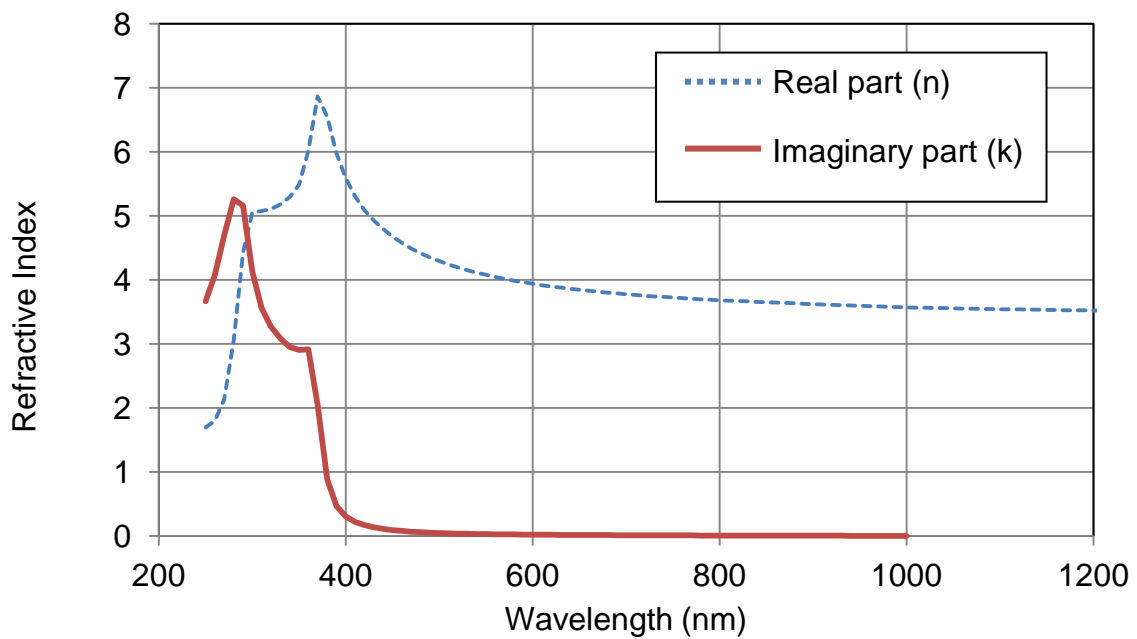


Figure 4.2: Real (red) and imaginary (blue dashed) components of the refractive index for silicon at different wavelengths (at 300 K) [3].

Other commonly used films include silicon nitride [5] and aluminium nitride [6]. This coating often has the dual purpose of also passivating the silicon – this will be discussed in more detail in section 4.2.2. The thickness of film is directly related to the wavelength of light, where the aim is to achieve destructive interference between

the two sets of reflected waves (r_1 and r_2) as the incident wave (i_1) hits the surface of the film and then hits the surface of the silicon, Figure 4.3:

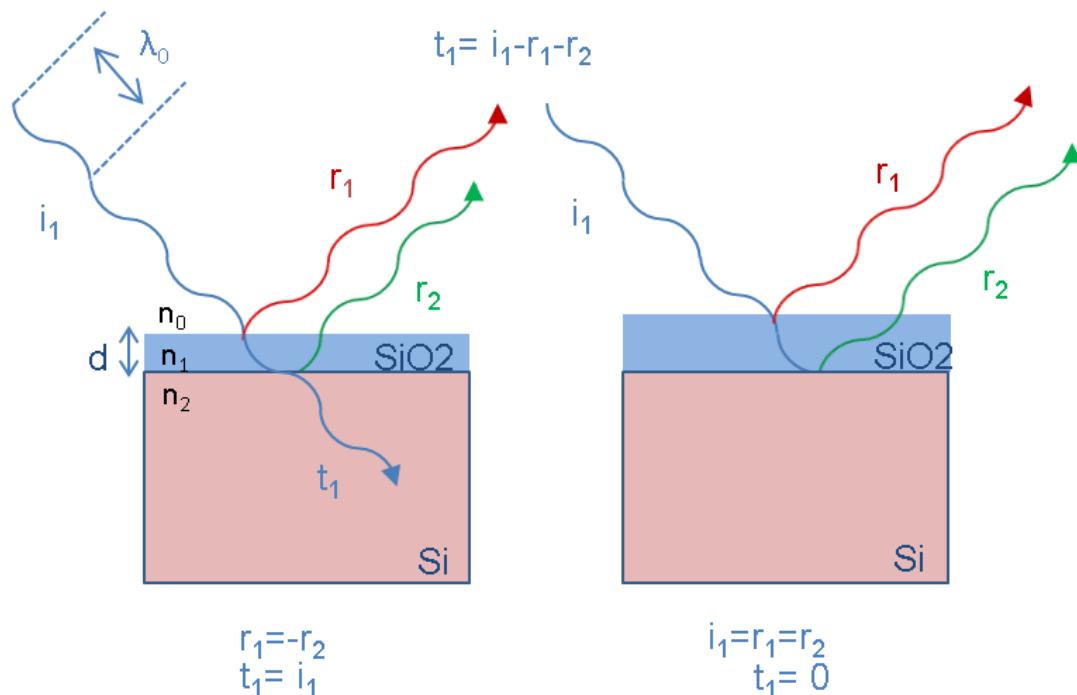


Figure 4.3: Reflection from surfaces can either be destructive (left) or constructive (right). All light is transmitted into the silicon when both reflected waves are 180° out of phase with each other, cancelling each other out.

4.2.2 Passivation

Passivation is a well-researched process which improves the surface quality of silicon wafers. Dangling silicon bonds are formed at the surface of the wafer, particularly where a diamond saw has been used to dice up the silicon. These are sites of recombination, where free electrons become trapped and are no longer able to conduct signal. In order to reduce the number of dangling silicon bonds at the surface of the silicon a passivation layer is grown.

There are a number of methods that have been developed for the purpose of passivation for both solar cells and semiconductor components. These include:

- 1) Chemical vapour deposition process (PECVD) [5]
- 2) Forming gas anneal [7]
- 3) Ion implantation, plasma processing
- 4) Valence mending passivation – depositing 1 atom layer such as sulphur and selenium [8]

Often a combination of wet and dry deposition layers make up the passivation, which forms silicon dioxide on the surface of the silicon and reduces the number of dangling silicon bonds caused by the sawing of the silicon rod into wafers.

A mixture of passivation techniques can be used to achieve a high quality passivation. Dry oxide has the disadvantage of growing very slowly, however it forms uniform layers which do not exhibit many defects at the oxide silicon boundary. Wet oxide is formed with the addition of steam. The disadvantage of this method is that hydrogen atoms are liberated by the decomposition of the water molecules and produce imperfections that may degrade the oxide quality [9]. On the other hand, this oxide forms quickly.

The number of defects near the surface of the silicon directly affects the recombination rate of carriers as trap sites enable Shockley Read Hall (SRH) recombination. If a carrier falls into a trap, it is no longer available to conduct, and hence by removing these trap centres a higher carrier lifetime can be established. Passivation is often finished via a thermal anneal step, which further improves carrier lifetime. This step is performed at a high temperature (1000°C) for 10 minutes.

Passivation layers can be as thin as 10nm. However they are often grown thicker to also act as an anti-reflection coating. When the thickness of the oxide is quarter of a wavelength thick of the illumination wavelength, maximum transmission of the light can be achieved into the silicon. For a wavelength of 980nm, silicon oxide ($n \approx 1.5$) with a thickness close to 160nm will in theory maximally reduce reflection at the silicon surface. Typically the surface reflection of untreated silicon is 35%, this can be reduced to 8.5% using an anti-reflection coating [1].

4.2.1 Texturing

Experimental techniques to alter the surface texture of the silicon are also being explored to reduce the reflection of the silicon by allowing maximum absorption. Texturing has the advantage over anti-reflection coating as it reduces reflection across all wavelengths of light. It is possible to apply both techniques to essentially minimise reflection. Texturing increases the surface area of the silicon, making it more likely that light will be absorbed into the silicon, Figure 4.4.

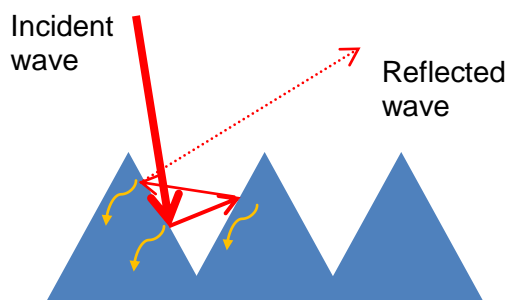


Figure 4.4: There is more chance to absorb incident light if the surface is textured

The use of surface texturing has been researched by the photovoltaic industry and has been successfully used to increase the light entering solar cells [10]. A number of techniques have been developed by creating both random pyramids on the surface [11] and by creating inverted pyramids [12]. The effect on the surface of the silicon can be seen in Figure 4.5. This is easily achieved in mono crystalline silicon as the silicon has a particular orientation at the surface that allows etching along the faces of the crystal planes.

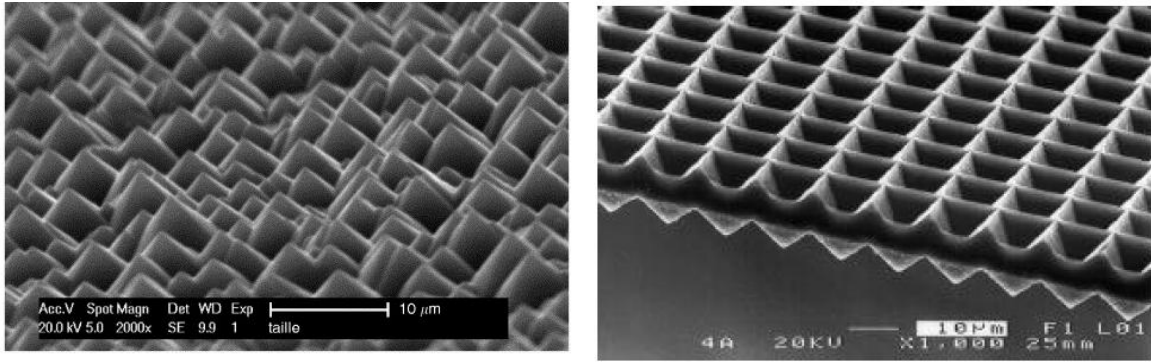


Figure 4.5: Left Random outward textured silicon surface [11]. Right: Scanning electron microscope photograph of a textured silicon surface with inward pyramid structure [12].

4.2.2 Processing techniques for enhancing PCS

Another technique also employed by the photovoltaic industry is aluminium backing to reduce the amount of light that passes straight through the silicon. However in the context of a small microstrip switch requiring a gap, a metal backing plate is not a suitable option. Largely many of the techniques employed by the solar energy industry are only just beginning to be applied to photoconductive switches.

Specifically for microwave switches Young *et al.* [37] has reported on a thermal oxidisation of the silicon providing both passivation and anti-reflection coating (ARC). The reflection of incident light was reduced from 30% to 8.2% hence improving efficiency. Anti-reflection coating was also employed by Flemish *et al.* [14], where plasma etching was employed to allow soldering to end launch SMA connectors and also utilised by Kelkar *et al.* alongside silicon surface polishing to increase the low optical absorption of the silicon die [15].

Hughes *et al.* [16] cites silicon processing as the dominant mechanism limiting the photoconductive efficiency of silicon switches. The author speculates that trapping and recombination of the photo-generated carriers at defect sites is greatly increased, mainly due to the diamond saw process used to scribe the silicon wafer into dice. Hughes *et al.* claim that defects could be reduced by 4 orders of magnitude by employing reactive ion etching and applying a number of oxidise and etch cycles to polish the surface. An improvement of carrier life time of 1-2 orders of

magnitude is estimated; however follow up work to support this hypothesis has not been published.

4.3 Variation 1: Passivation and Texturing

The previous chapter highlighted the way in which switch topology can improve microwave performance. Here, the focus is to improve the performance of the silicon by employing techniques currently used in the photovoltaic industry.

Further research to improve the silicon properties with a view to increase efficiency include combining ARC, surface alteration, polishing and addressing the way silicon is processed. These could yield a superior outcome and result in a more efficient and effective switch. In the second section of this Chapter, silicon which has been treated with these techniques is mounted onto the optimised switch topology presented in Chapter 3. The effect of these techniques is quantified in terms of improvement of RF performance for a silicon microwave switch. Table 4.1 summarises the silicon samples investigated.

	Treatment	Depth of oxide (nm)	Carrier lifetime before dicing (μs)
A	Polished (untreated)	2 (native)	13.4
B	Polished (Passivated SiO_2)	57	36.7
C	Textured $4\mu\text{m}$ pyramid base (Passivated SiO_2)	57	29.5

Table 4.1: Silicon properties for the three samples in this study

4.3.1 Fabrication

To give a brief overview, the fabrication process depends on four main steps. First is the choice of silicon which affects the number of carriers generated in the semiconductor. The doping and quality affect the maximum carrier lifetime that an

untreated silicon wafer may exhibit. Second, the surface texturing can reduce the reflection at the surface of the silicon allowing more photons to enter the silicon. Third, the passivation may also act as an intermediary material which allows more photons to enter the silicon. It can also improve the surface quality of the silicon. Lastly, the wafer must be cut into dice – this process can introduce defects into the die which affect carrier lifetime.

4.3.1.1 Silicon choice

The silicon used in this case study is the boron doped silicon. Note the measured data presented in Chapter 3 related to the higher quality phosphorus doped silicon. The boron doped silicon is the higher grade float-zone (FZ) wafer as opposed to the typical Czochralski (CZ) type wafer used to manufacture solar cells. The wafer is lightly boron doped, with a resistivity of $\sim 10\text{k}\Omega\text{m}^{-1}$. Only one side is polished. All these factors have an impact on the carrier lifetime of the silicon which ultimately affects conductivity of the switch in the ON state. The doping applied to the wafer will also affect OFF state performance, as high levels of doping degrade switch isolation. The thickness of wafer is $530\mu\text{m}$; this also influences the distribution of free carriers in the switch.

4.3.1.2 Texturing

The silicon surface was textured using an anisotropic etching process in Isopropyl Alcohol (IPA – 5% concentration) and a Sodium Hydroxide Solution (NaOH – 2%, H_2O , 93%) at 90°C for 15 minutes. This results in the creation of a random pyramid structure on the wafer's surface, where typically the pyramids have a base dimension of $4\mu\text{m}$, Figure 4.6. Note that that pyramids which are too small ($0.3\mu\text{m}$) increase reflection values as light diffraction becomes more apparent at longer wavelengths. Large pyramids ($15\mu\text{m}$) are also not desirable as the pyramids may break during handling. The uniformity of the pyramid size is dependent on the presence of IPA. The etching time also dictates the depth of the pyramid structure. This process reduces surface reflection of the die allowing more photons to enter the silicon, as shown in Table 4.1.

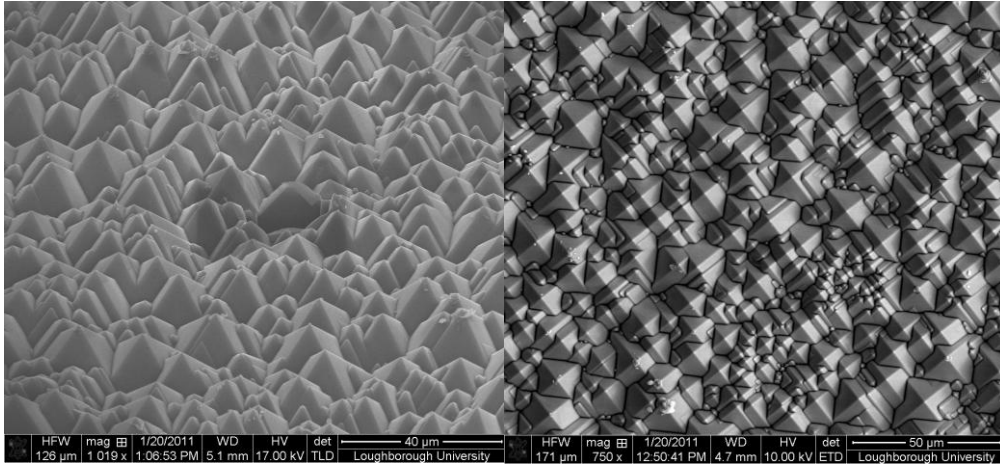


Figure 4.6: Representative Scanning electron microscope (SEM) of silicon surface for a sample which has undergone texturisation at Loughborough University's Centre for Renewable Energy Systems Technology (CREST)

4.3.1.3 Passivation

A passivation layer to reduce the number of traps on the surface of the silicon, hence increasing minority carrier lifetime, was thermally grown on both polished and textured silicon samples.

Silicon dioxide was deposited to a depth of 57nm (refractive index $n=1.45$). Optical properties such as thickness of the oxide and reflectivity of the samples were measured using spectrophotometer and ellipsometer, reflectivity is presented in Figure 4.7.

A Quasi-steady state photoconductance method was used to monitor the minority carrier lifetime. This value is affected by carrier concentration. Eq. (4.3) relates carrier concentration, n , to conductivity, σ . As the silicon is near intrinsic, the density of holes and electrons is assumed to be equal. Electron and hole mobility μ_e and μ_h are respectively $1414 \text{ cm}^2\text{V}^{-1}\text{s}^{-1}$ and $471 \text{ cm}^2\text{V}^{-1}\text{s}^{-1}$, where q is the elementary charge constant. When σ is 45S/m as assumed in the parameter simulation study in Chapter 3, the carrier concentration is $1.5 \times 10^{15} \text{ cm}^{-3}$.

$$n = \frac{\sigma}{q (\mu_e + \mu_h)} \quad \text{Eq. (4.3)}$$

The carrier lifetimes presented in Table 4.1 are based on this carrier concentration for a whole wafer.

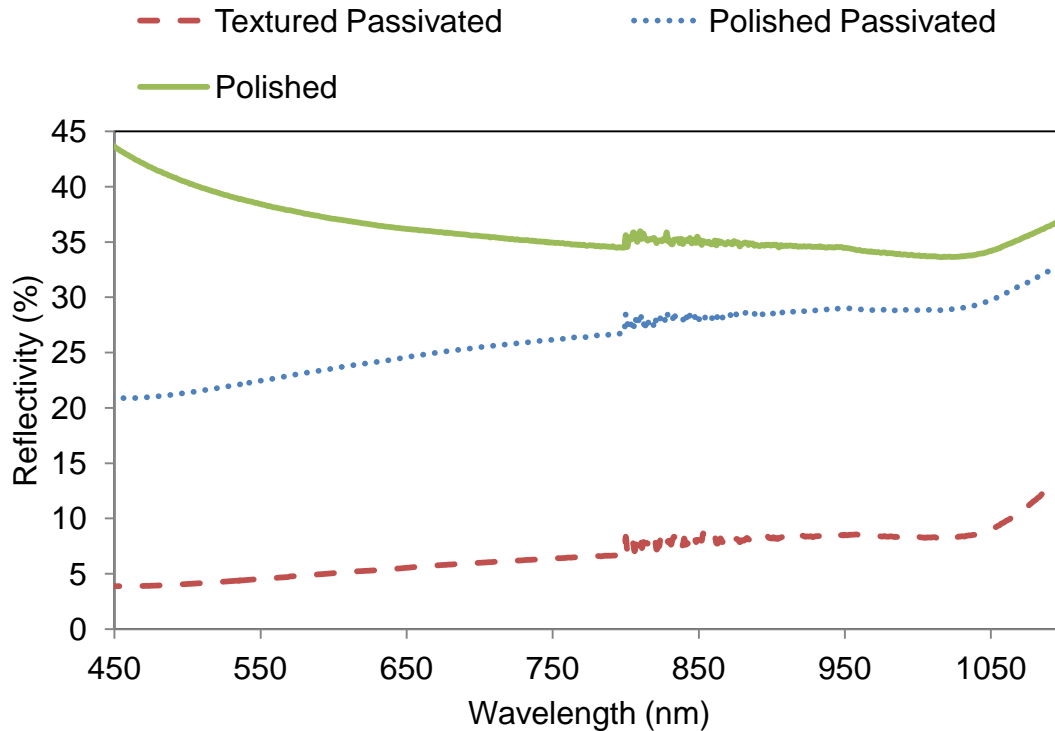


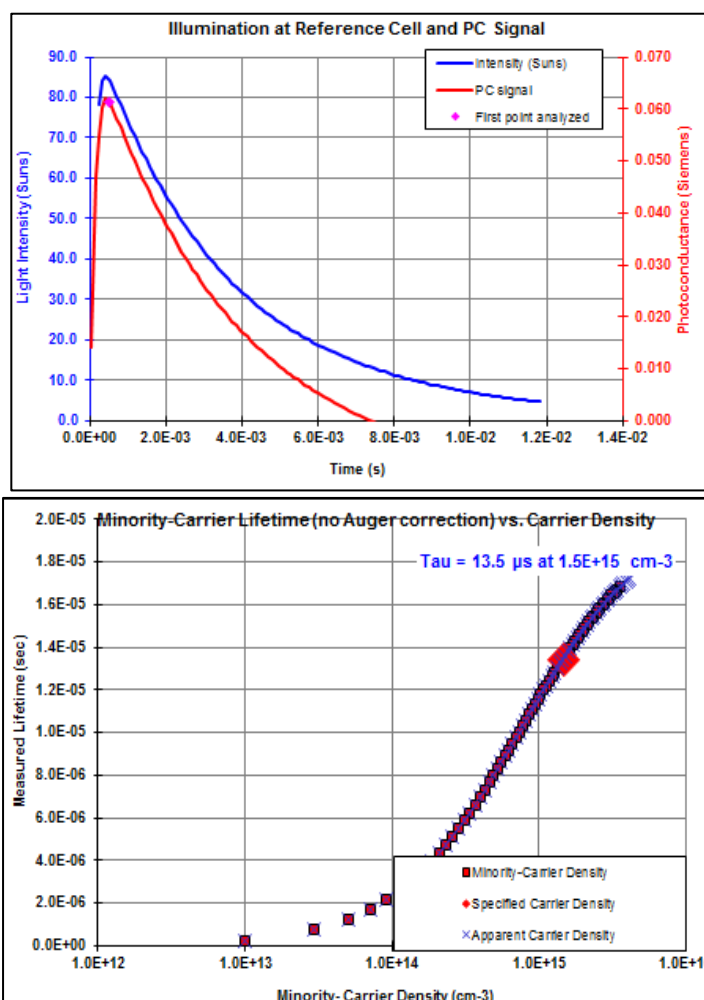
Figure 4.7: Reflectivity results for silicon wafers with different fabrication processes. Equipment changes lamps at 800nm hence disturbing the results slightly

4.3.2 Using Carrier Lifetime as a Measure of Quality of Passivation

Effective carrier lifetime is often used as a measure of quality of silicon and passivation. As mentioned in Eq. (2.7) effective carrier lifetime is a combination of bulk and surface carrier lifetimes. The bulk silicon lifetime is determined by the chemical purity of the material - if the silicon is of high quality (float-zone) the bulk lifetime will be high and hence the effective carrier lifetime is dominated by the surface carrier lifetime, which is defined by the passivation quality

A wafer lifetime measurement device, Sinton Equipment WCT-100 [17], was used to determine the recombination lifetime by members of CREST. The WCT-100 uses an Eddy-current method to measure the effective carrier lifetime. The equipment

consists of a sensor (or coil) which is placed near the silicon sample and can detect a change in conductivity. Light is pulsed onto the sample to create the excess carriers, and the coil circuit senses the increase in conductance of the sample due to the carriers. Quasi Steady State Photoconductance (QSSP) analysis [18] is used to calculate effective carrier lifetime of the silicon sample. This technique involves exposing the wafer sample to a light pulse which varies very slowly compared to the effective lifetime of the sample. The lifetime can be extracted from the slope of the decay curve. Figure 4.8 and Figure 4.9 represent carrier lifetime calculated for an untreated and passivated silicon switch respectively, based on the decay. Note that the passivated sample has a much longer carrier lifetime of 36.7 μ s as compared to the untreated sample with a carrier lifetime of 13.5 μ s.



Response of a light pulse applied to the wafer under test. This is compared to the known response of a reference sample (blue)

Carrier lifetime is computed based on the response from the pulse and a line of best fit is used to determine the carrier lifetime Tau.

Figure 4.8: Screenshots taken from QSSP results for an untreated silicon wafer. Effective carrier lifetime is computed to response from an applied pulse

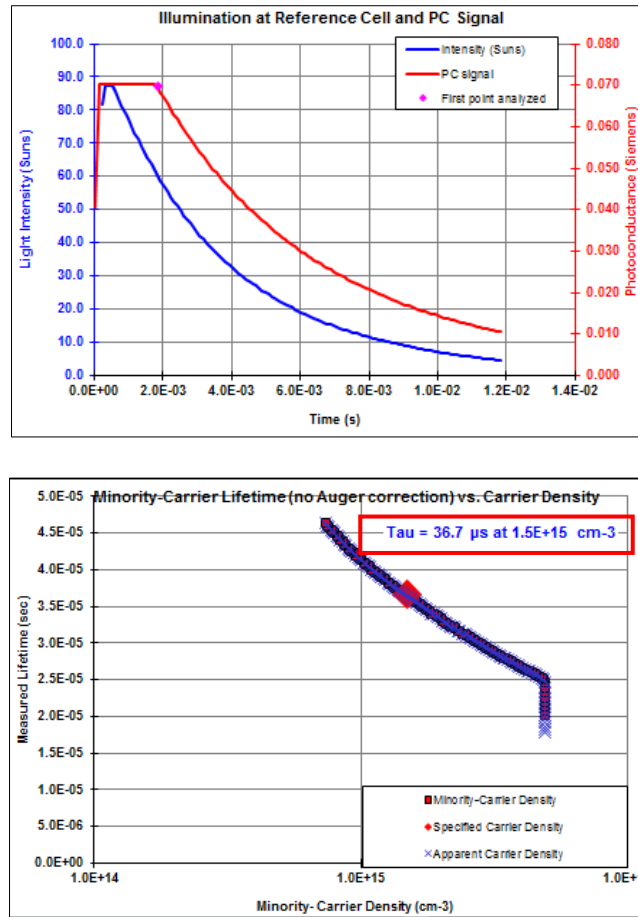


Figure 4.9: QSSP results for a passivated silicon wafer. Effective carrier lifetime is computed as 36.7us using the same applied pulse as in Figure 4.8.

4.3.2.1 Dicing

The samples were diced into 1mm × 1mm switches using a diamond wafer saw – this process reduces the carrier lifetime as the saw creates defects at the dice edges. Defects can be reduced by polishing the edges after dicing, but these facilities were not available for this initial study. The silicon was attached to the optimised transmission line design using silver loaded epoxy and mounted on a metal base to act as a ground plane and allow attachment of SMA connectors.

4.3.2.2 Measurement

A laser diode coupled to a 1mm diameter fibre optic cable delivered 200mW of radiant flux to the silicon die to allow switch control, as described by Panagaumwa *et al.* [16]. S-parameter measurements were taken using an Anritsu 37397D Lightning Vector Network Analyser. It is assumed that all light that is not reflected is absorbed

by the silicon, this is a valid assumption as the depth of the silicon is 530 μm ; using a laser with a wavelength of 980nm the absorption coefficient is $\sim 100\text{cm}^{-1}$ and hence very little light is transmitted through the silicon.

4.3.3 Results and Discussion

The results indicate that treating the silicon has minor effect on the OFF state characteristics of the switch. At 2GHz the difference between polished and passivated textured silicon samples is -19dB vs. -20dB. This does equates to a percentage change of 25%, however the power level is relatively much lower than for the switch ON state, Figure 4.10. Hence only ON state insertion loss changes will be discussed further. Reflection values throughout the optical and near IR spectrum are presented in Figure 4.7, however quoted reflection percentages refer to 980nm in the text. Insertion loss values are compared at 2GHz throughout.

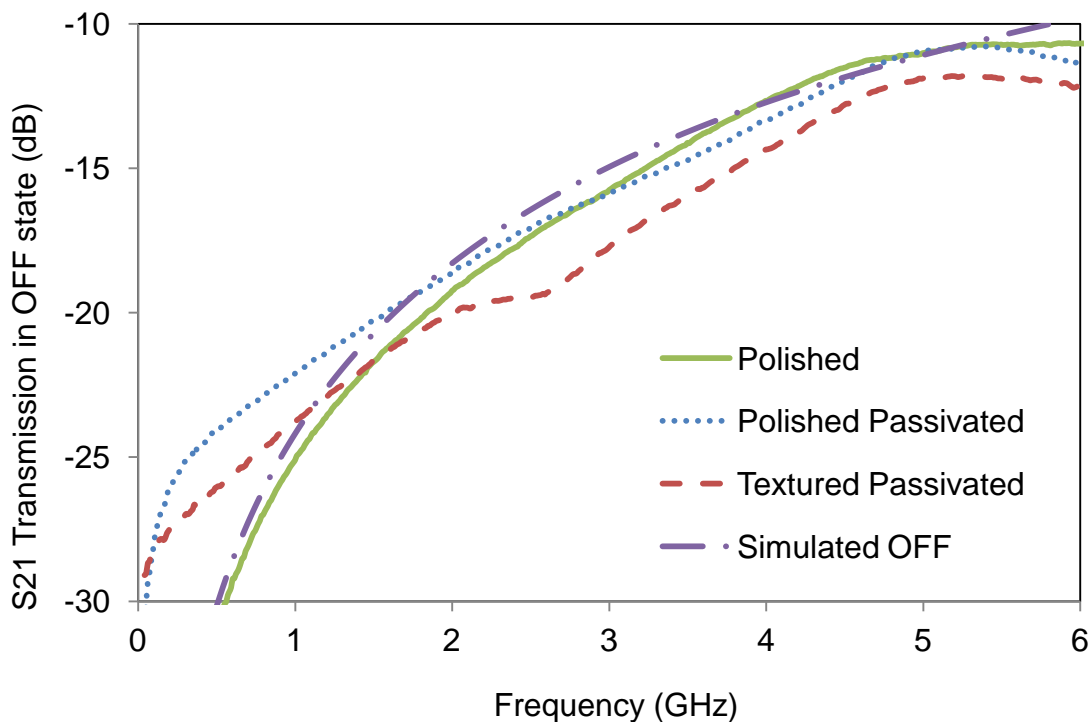


Figure 4.10: Transmission results in the OFF state for silicon with differing fabrication processes

Simply passivating the silicon sample reduces the insertion loss of the photoconductive switch by 0.5dB from 1.8dB to 1.3dB, which in terms of power ratio is a 13% improvement, Figure 4.11. A small amount of this increase can be

attributed to a reduction in reflectivity by 5.2%, however the bulk improvement in performance is due to the increased carrier lifetime of the silicon [20].

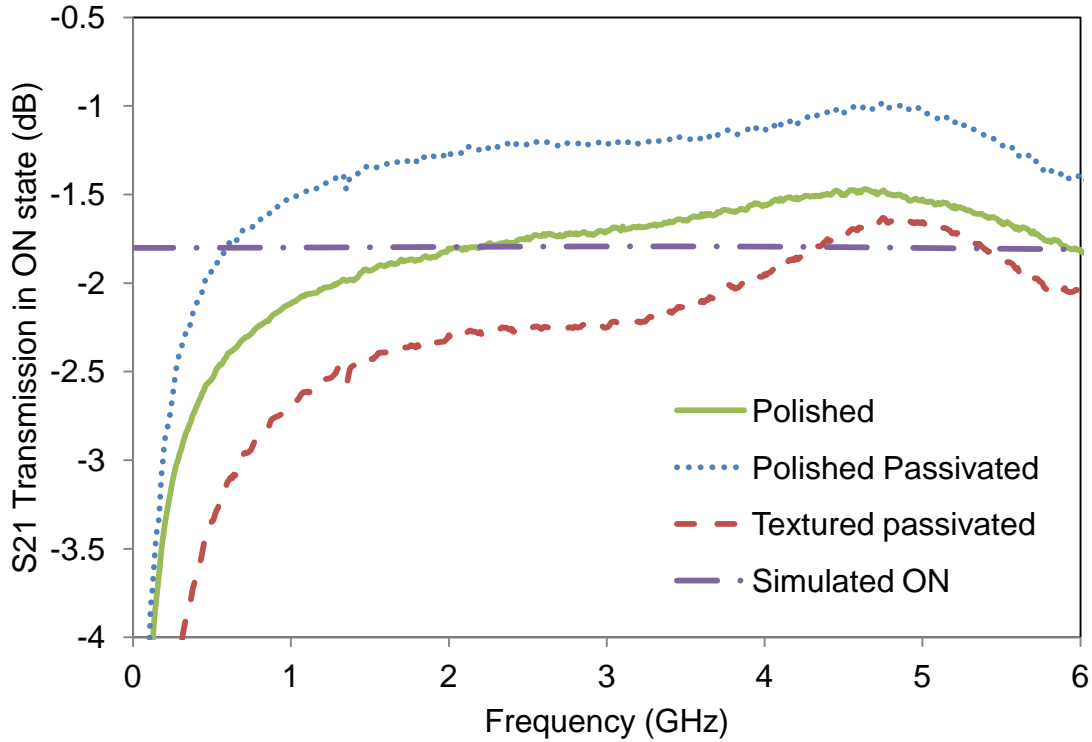


Figure 4.11: Transmission results in the ON state for silicon with differing fabrication processes

Polished silicon was measured to have a minority carrier lifetime of $13.4\mu\text{s}$, compared to passivated silicon which has a minority carrier lifetime of $36.7\mu\text{s}$. The carrier lifetime has been improved through eliminating dangling surface bonds using oxygen. Silicon atoms bond with the oxygen and hence reduce traps which cause carriers to recombine. Since carriers are available for longer, conductivity is improved and hence insertion loss is reduced.

The measurement results indicate that texturing the surface of the silicon does not improve microwave performance in terms of insertion loss. There are more photons entering the textured passivated silicon, a reduction in reflectivity of 20.4% is observed when compared to the passivated polished sample. However the insertion loss is increased by the texturing process from 1.3dB to 2.3dB, equating to 21% increase in loss.

There are a number of possible reasons for this degradation. The texturing process physically changes the flat surface of the die and creates non-uniform air gap cavities (depth $\sim 4\mu\text{m}$) between the silicon surface and the copper transmission line it is in contact with. Potentially, these cavities decrease capacitance and reduce coupling between die and transmission line, therefore increasing loss. Taking these cavities into account in the EM simulation model, Figure 4.12 as a $2\mu\text{m}$ air gap on the surface of the silicon it is clear that there is a reduction in insertion loss between the textured and non-textured switches at 2GHz, Figure 4.13. As proof of concept, only a $2\mu\text{m}$ gap is investigated through simulation, as including small details increases simulation time by slowing the energy decay out of the system and limiting the maximum time step. The $2\mu\text{m}$ coating is a compromise between the reality of some of the pyramid surface being in close proximity to the transmission line and some being up to $4\mu\text{m}$ from the copper surface.

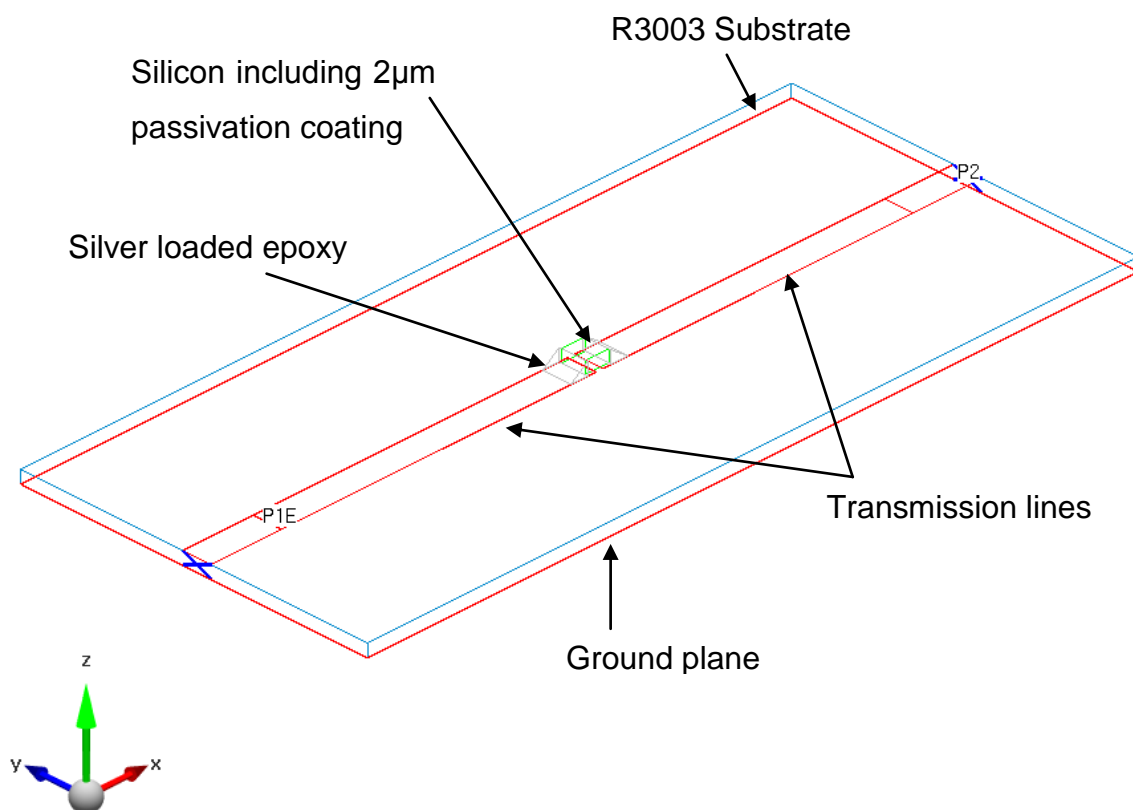


Figure 4.12: CAD model of PCS using EMIRE XCcel EM Simulation software to model a $2\mu\text{m}$ coating applied to the silicon to represent a pyramid surface

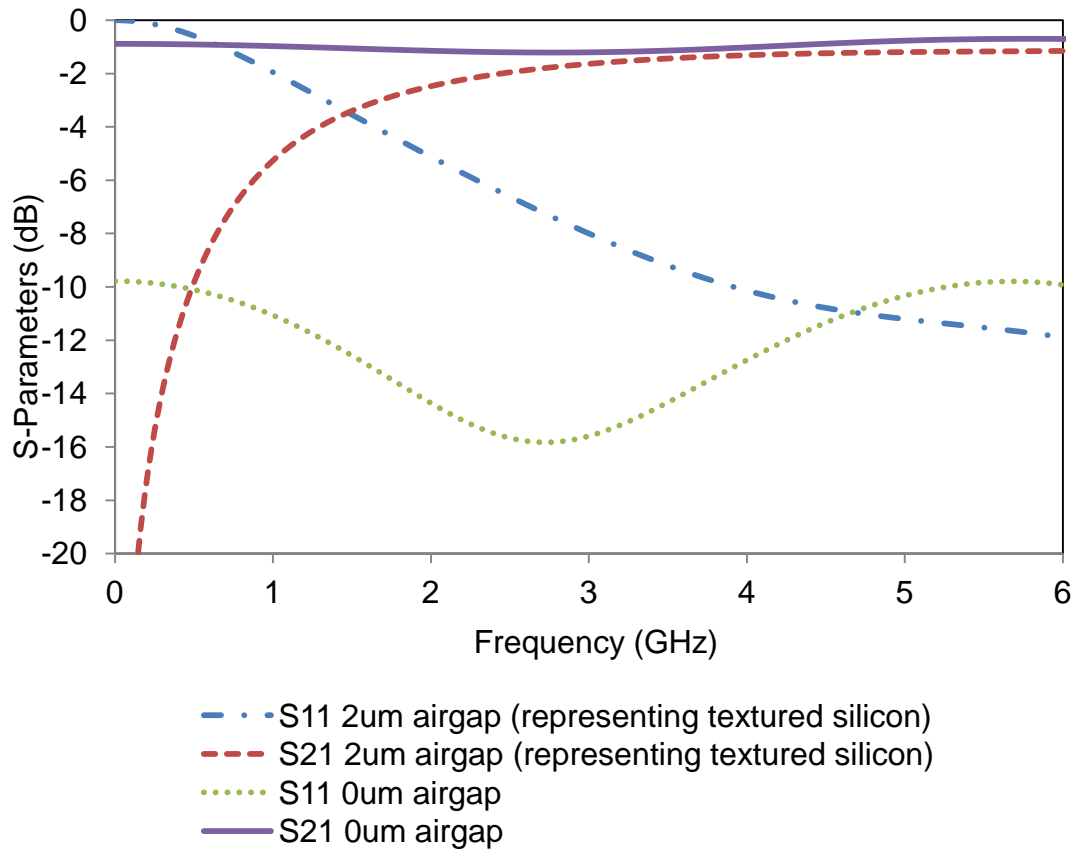


Figure 4.13: Simulation result of a passivated silicon die on a transmission line, with and without a representative ‘textured’ air gap

A second point to consider is that texturing increases the surface area of the silicon and damages the surface compared with a polished finish. Despite passivation, the surface is still an area of high carrier recombination compared to the bulk of the silicon. There is a $7.1\mu\text{s}$ reduction of carrier lifetime of the passivated textured sample compared to the passivated polished sample.

Since there is a greater area for recombination of carriers to occur at the surface, this is most likely to be the main reason why the conductivity is reduced. The wafers used in this study are high quality FZ, whereas lower grade CZ silicon is typically used in the manufacture of solar cells where this texturing technique is normally applied. The observed degradation to microwave performance may be attributed partially to this fact as the damage caused to high grade FZ compared to CZ is not outweighed by the benefit of reduced light reflectance across a broader frequency spectrum.

4.4 Overview on Contact Type

To be able to integrate the switch into RF systems, a method to connect the die to a metal interconnect is required. To facilitate this, a metal contact on the silicon die is necessary. Doping can be locally introduced to assist the transition of the RF signal between a metal and semiconductor. The level of doping can form either an ohmic or schottky contact. If a contact is formed on top of the passivation layer, without local doping then the contact can be described as capacitive.

4.4.1 Metal-Semiconductor Junctions

To understand the important concepts and challenges involved in making semiconductor-metal contacts, the band structure of these materials needs to be revisited. Figure 4.14 (a), describes the simplified band diagram of a metal and semiconductor that are not in contact. The valence and conduction energies, E_V and E_C have been previously explained in Chapter 2. There is also the addition of E_F , the Fermi energy level. This is in theory the energy level that would be half filled with electrons and half filled with holes. In intrinsic semiconductors, this exists in the forbidden band gap zone. The level is not physical, but is based on the probability of equal occurrence of electrons and holes. The Fermi energy is important in order to characterise the solid and also the work function [21].

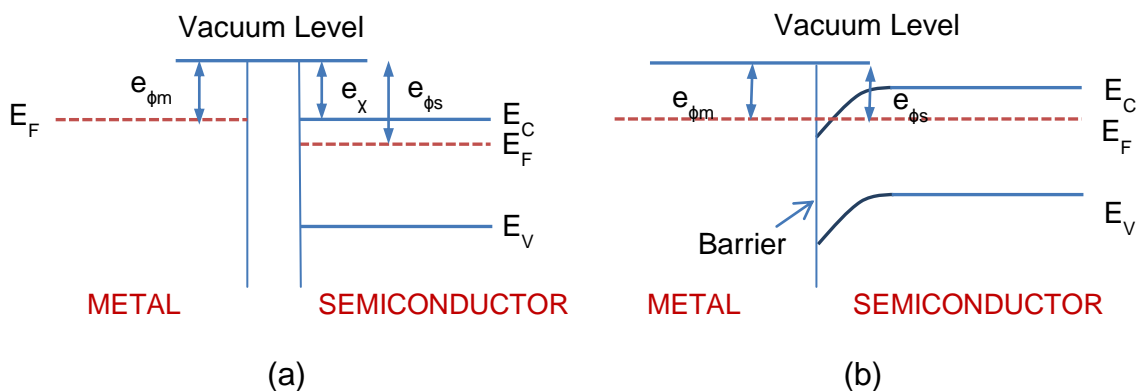


Figure 4.14 a) Band structure and Fermi level of separate semiconductor and metal materials. b) Band structure and Fermi level of semiconductor and metal in contact

The work function is the energy difference between Fermi level and vacuum level and differs between materials. The vacuum level describes the potential energy of an electron in vacuum and is taken to be 0eV. To make a good contact between a metal and semiconductors, the work functions should be closely matched. This can be achieved by doping the semiconductor, which changes the band structure as is demonstrated in Chapter 2.

This band bending allows the Fermi energy level to be equal for both metal and semiconductor, Figure 4.14 (b). The electron affinity is the difference in energy between the vacuum level and the bottom of the conduction band. For semiconductors, an electron entering the material from the outside vacuum would naturally move into the conduction band; however in metals the outside electron would on balance move to the Fermi level, hence why there is a distinction between work function and affinity [22]. Affinity is a useful value as it is independent of a material's doping concentration. It can be used to predict the Schottky barrier height, ϕ_B , which forms between a metal with work function ϕ_m and semiconductor with affinity χ , Eq. (4.4):

$$\phi_B = \phi_m - \chi \quad \text{Eq.(4.4)}$$

In Silicon, χ is $\sim 4.15\text{eV}$, so this gives an indication of the value of metal work function required in order to reduce the barrier height and most efficiently make a contact between a metal and silicon [23].

4.4.2 Ohmic Contacts

The equation above, Eq. (4.4), relates to the Schottky-Mott rule [24], however in practise creating ohmic contacts directly based solely on this rule is challenging. Some metal-silicon surface restructuring means that the barrier height cannot be easily predicted.

A contact is described as ohmic if it provides very low resistance between both materials in contact – e.g. current flow is not impeded by the contact. Ohmic contacts can be created by introducing a high level of doping to the semiconductor in the junction region. This essentially narrows the depletion area and hence allows

electrons to tunnel through the barrier. If the depletion width is 2.5nm in size, then a doping density of $\sim 10^{-19} \text{ cm}^{-3}$ is required to achieve ohmic contacts.

Other factors which also need to be considered are ease of formation and compatibility of any techniques and materials that may be introduced after the formation of the contacts. There should be no diffusion of the contact metal into the SiO_2 [25]. Flemish *et al.* [26] implement ohmic contacts on a photoconductive microwave attenuator. The contacts are made of gold whereas the photoconductive element is a silicon substrate.

4.4.3 Schottky contact

If low levels of doping are introduced, then a rectifying or Schottky contact is produced. For ohmic contacts field emission (or tunnelling) is the main method for conduction. In the case of a Schottky contact, thermionic emission is the dominant conduction mechanism. Electrons jump over the barrier between the silicon and metal. This method impedes the transfer of current.

Depending on the application, this type of contact can be used to reduce charge injection at low voltages, which affects turn-off speed. In the case of Karabegovic *et al.* [27], a photoconductive microwave switch fabricated using GaAs is investigated. The electrodes on the switch are made of silver which has a high work function, and hence the formation of rectifying contacts are ensured.

4.4.4 Capacitive Contacts

In RF circuits capacitive contacts can be realised as RF signal can couple from the transmission line through a thin insulator layer (such as naturally formed or deliberately grown silicon dioxide) into the silicon. This type of contact means there is high capacitance in the signal path, and hence the insertion loss of the component will be increased. Such contacts have been used in the work of Chauraya *et al.*, where a passivated silicon die is attached across a gap in transmission line using silver epoxy [29]. Contrary to the theory above, capacitive contacts have also been demonstrated by Flemish *et al.* to have a lower insertion loss when compared to

ohmic contacts [26]. This is mainly believed to be because it is advantageous to keep the passivation layer across the entire surface of the silicon.

4.5 Variation 2: Gold Contact Capacitive Switch

Variation 1 of the switch concentrated on the quality of the silicon. Variation 2 of the switch investigates the effect that metallised contacts have on the RF performance. The contacts are formed on top of a passivation layer; hence the switch is referred to as a capacitive switch.

In order to make a better electrical connection between the silicon and circuit, the silicon needs to be modified to include metal contacts. Currently silver loaded epoxy is used to make an electrical connection between silicon and transmission line. The addition of metal contacts allows investigation of alternative methods of connection. It is important to maintain the high quality of silicon so conductivity and lifetime are not compromised. So in the following sections a process is detailed to preserve a passivation layer while still depositing a gold contact area.

4.5.1 Passivation Analysis

In this experiment, phosphorus doped silicon is used. The switch is described as capacitive, as there is a passivation layer remaining on the switch. The composition of this surface passivation layer is detailed in Figure 4.15 and Figure 4.16. X-ray photoelectron spectroscopy (XPS) analysis [28] details the elemental composition and thickness of this passivation layer. There is an initial layer of carbon for the first 30nm indicating slight surface contamination, Figure 4.15. The switch was passivated using oxygen, and hence the majority of the passivation is made from silicon (~34%) and oxygen (~65%), Figure 4.16. The orbitals of the atoms have been included which give a complete definition of the energy level and shape of the orbital which describes the wavelike behaviour of an electron in a particular atom.

Figure 4.16 indicates the thickness of the passivation layer is ~120nm thick. The reflectivity of the sample is measured using a spectrophotometer and ellipsometer, Figure 4.17. This graph highlights that the passivation layer is also acting as an ARC at a wavelength close to the 980nm laser used in this thesis, particularly when compared to the polished boron doped sample utilised in section 4.3.

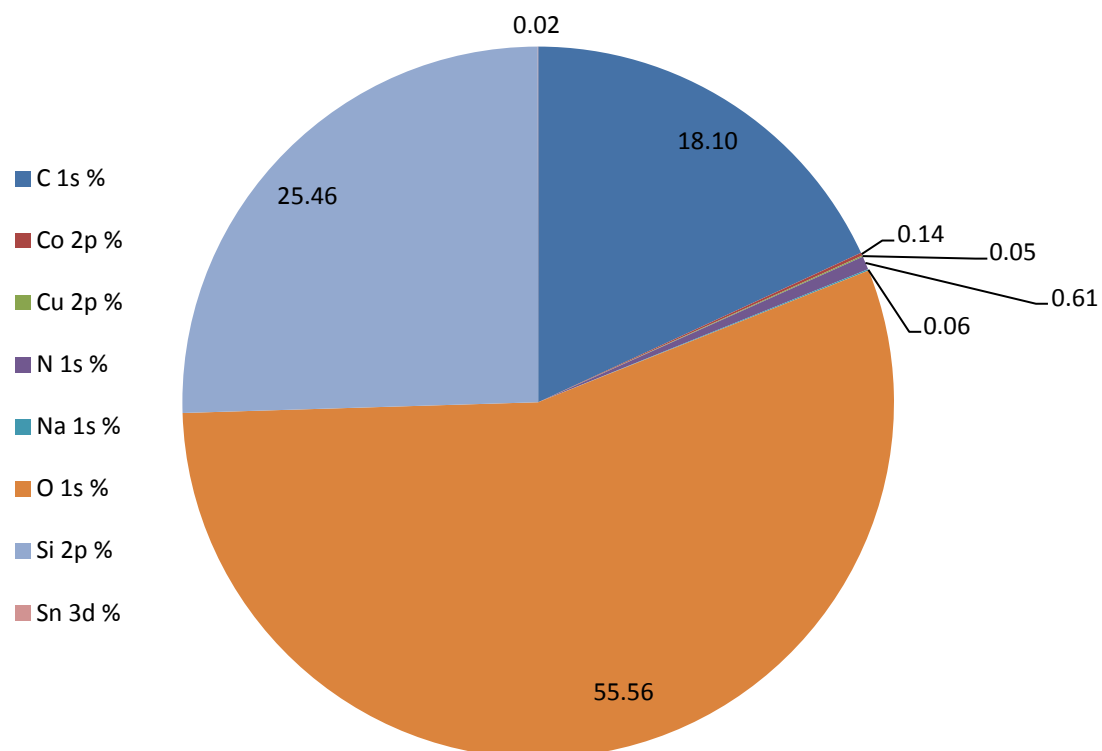


Figure 4.15: Percentage of element atoms comprising the top most surface of the passivation layer for the phosphorous doped silicon. The pie chart indicates there are very small traces of other elements where the orbitals of the atom are also listed.

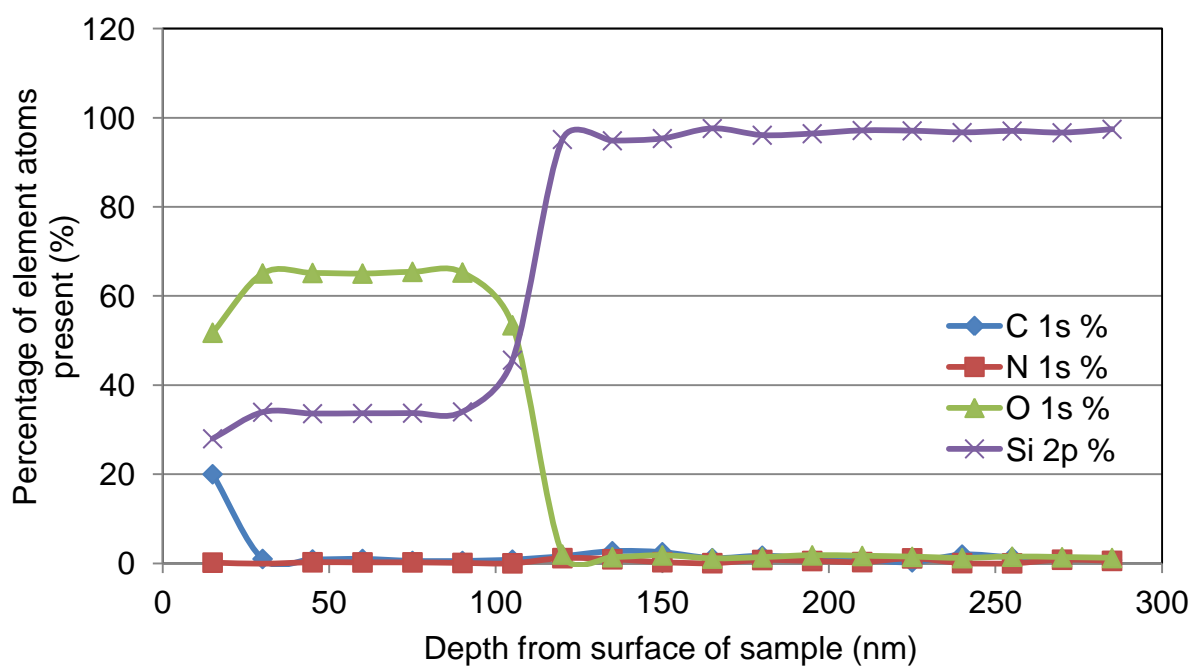


Figure 4.16: Percentage of element atoms comprising the first 300nm from the surface for the phosphorous doped silicon

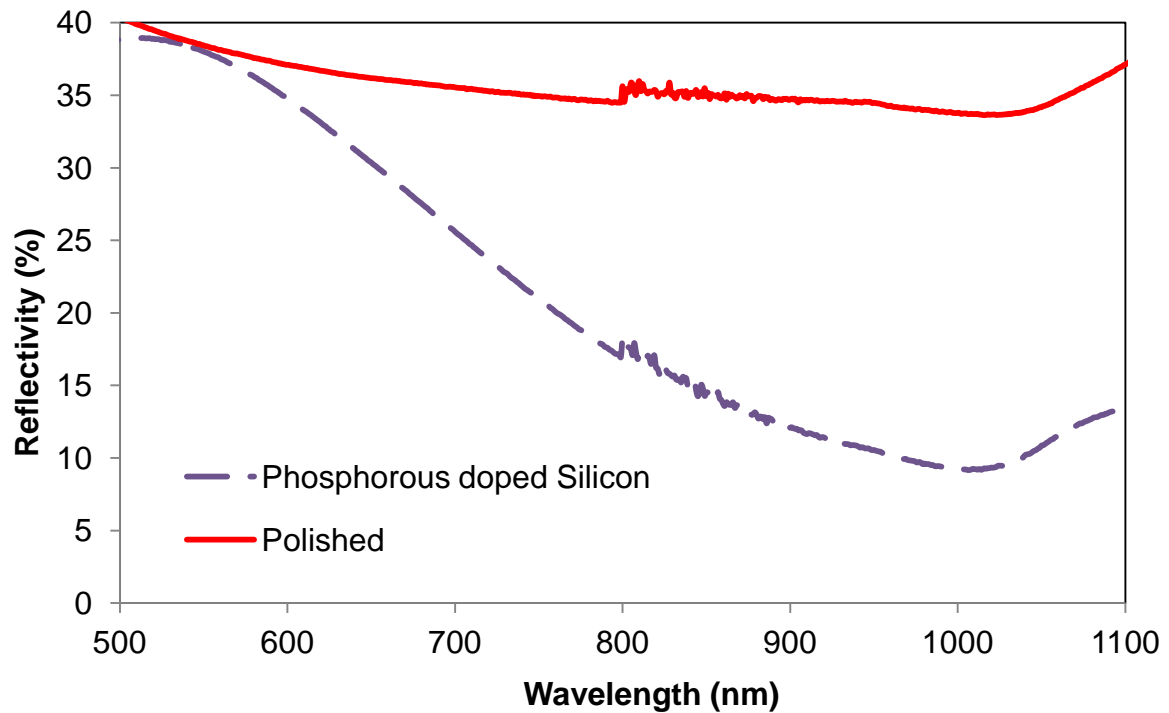


Figure 4.17: Reflectivity of the phosphorous doped silicon wafer which incorporates a passivation layer which acts as an ARC at ~1000nm

4.5.2 Fabrication Process

The fabrication process is presented in Figure 4.18. This procedure was performed at Leeds University through the Institute of Microwaves and Photonics. The wafer is first prepared by cleaning in an ultrasonic bath to remove any contamination.

To selectively etch a pattern into the silicon a photo resist (SP8) is spun onto the silicon wafer. Spinning ensures the thickness of the resist is a constant 4 μ m across the wafer. This resist is then baked on a hot plate to allow drying.

An acetate mask is used to cover the areas in which resist should remain in order to pattern the wafer. A UV light is applied to the masked wafer; the exposed areas undergo a chemical change. The wafer is placed in a developer in order to remove the photo resist areas which have been exposed to light.

The photo resist remaining on the silicon is non-reactive with the hydrofluoric (HF) acid solution used to etch away silicon dioxide. Depending on the length of time left in the HF, different amounts of silicon dioxide are removed.

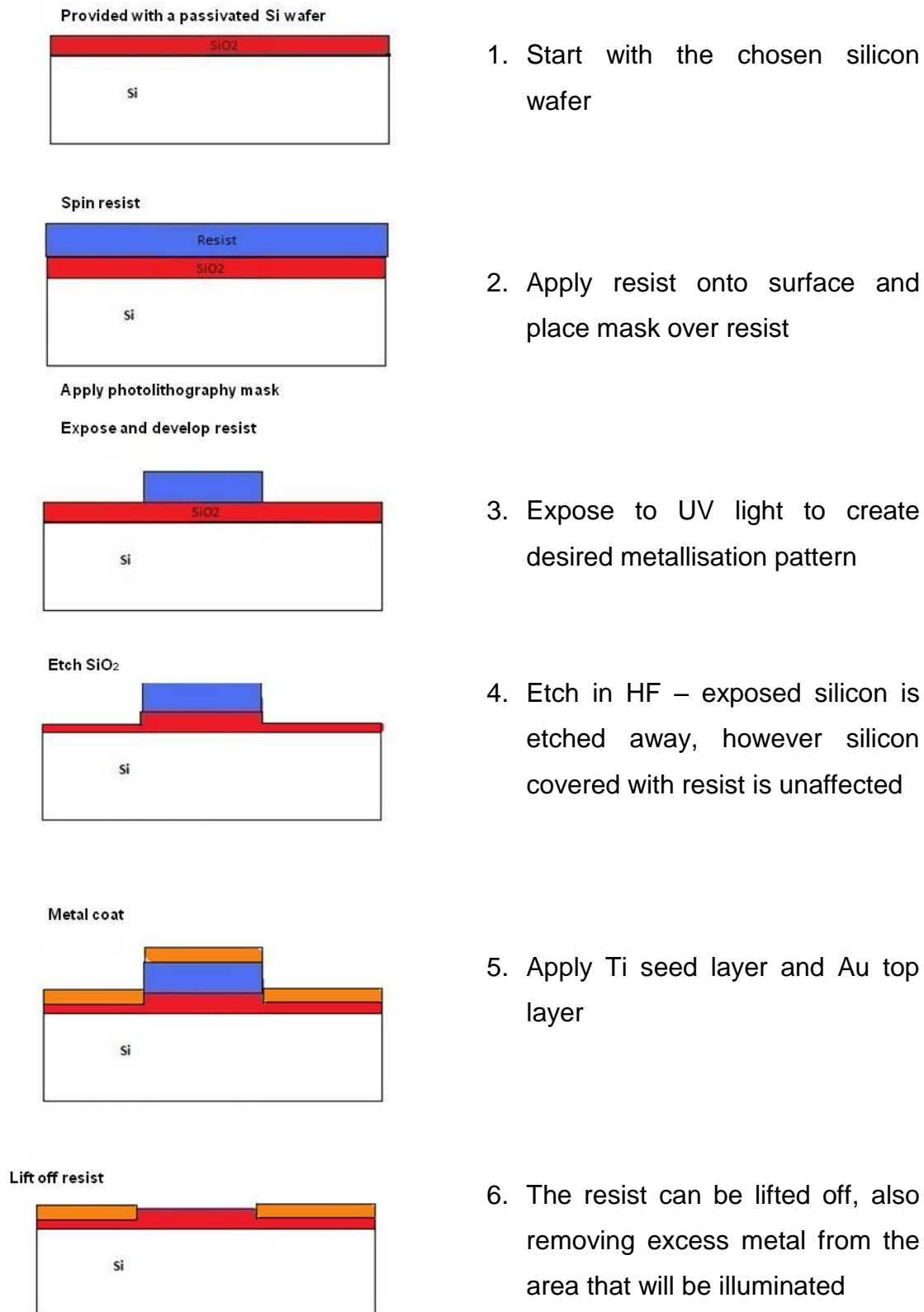


Figure 4.18: Fabrication steps to selectively etch away passivation layer and deposit gold contacts

Three different samples were produced:

- 1) No etching of SiO_2 layer
- 2) 2 minute 15 second etch of SiO_2
- 3) 3 minute etch of SiO_2

In order to achieve metal contacts, the etched wafers were put in an evaporation chamber. A 10nm layer of titanium was first evaporated onto the silicon, followed by a 100nm layer of gold. The seed layer of titanium more readily adheres to silicon dioxide and allows the gold to hold to the silicon.

Finally a lift-off process is employed to remove the gold and photoresist from selected areas of the silicon. The wafer is agitated in acetone solution which dissolves the photoresist and lifts-off the gold which sits on top of the resist.

In order to use in microwave circuits, the wafer is diced using a diamond wafer saw into dice with a length of 2mm, each with a 0.5mm gold contact at each end, Figure 4.19. A variety of widths between 0.5mm-3mm are created.

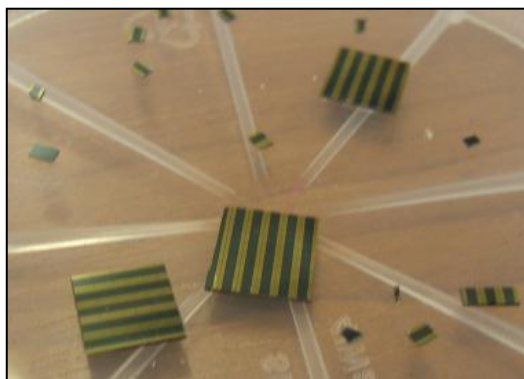


Figure 4.19: Diced and un-diced silicon with gold strips deposited on top of the SiO_2 passivation layer

4.5.3 Results

In order to determine the effect on insertion loss and isolation, the 2mm × 1mm × 0.3mm samples were connected to the optimised transmission line designed on R3003 as is described in Chapter 3. Silver loaded epoxy is used as the connection method. The transmission lines were then characterised using an Anritsu Vector Network Analyser (37397D Lightning series). Figure 4.20 represents the OFF state S21 characteristics.

Values are similar for all three samples that have had gold evaporated on top of the passivation layer. Figure 4.21 presents the ON state transmission of the switch. There is a noticeable difference in the low frequency performance of the switch between samples. The samples which have undergone passivation etching have an improved low frequency performance up to 700MHz, Figure 4.22. Whereas at higher frequencies the sample which has not been etched exhibits better transmission performance.

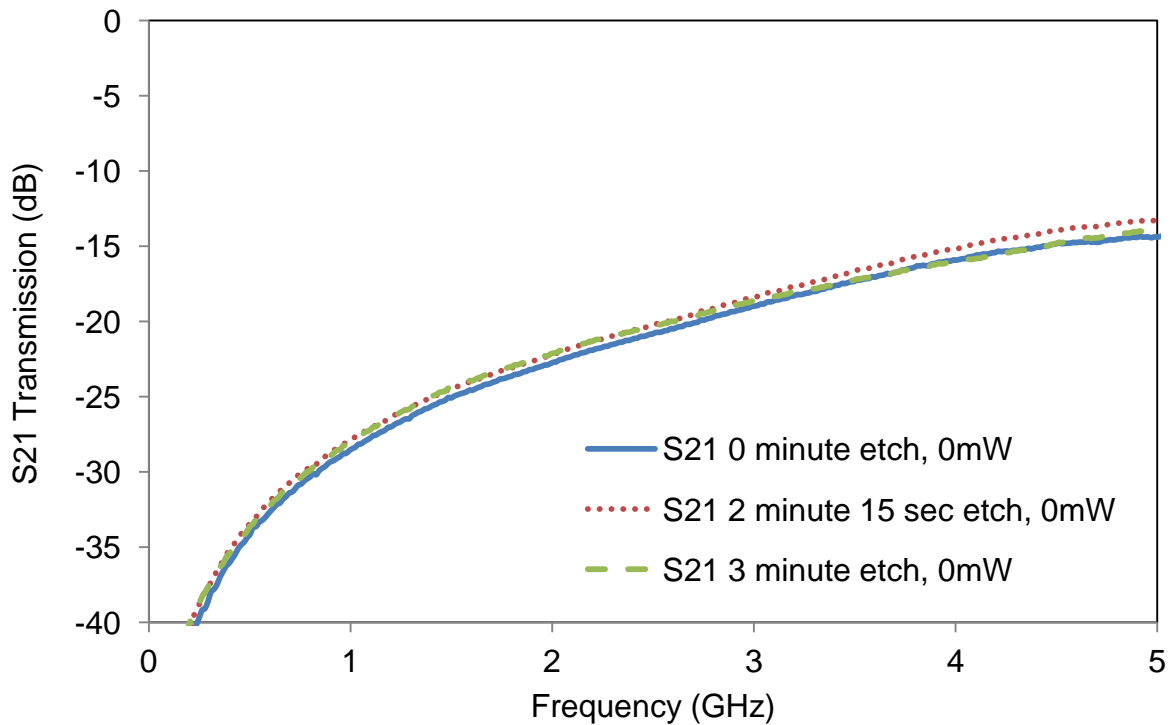


Figure 4.20: Transmission performance in the OFF state for gold deposited silicon attached via epoxy, size of silicon die 2mm × 1mm × 0.3mm

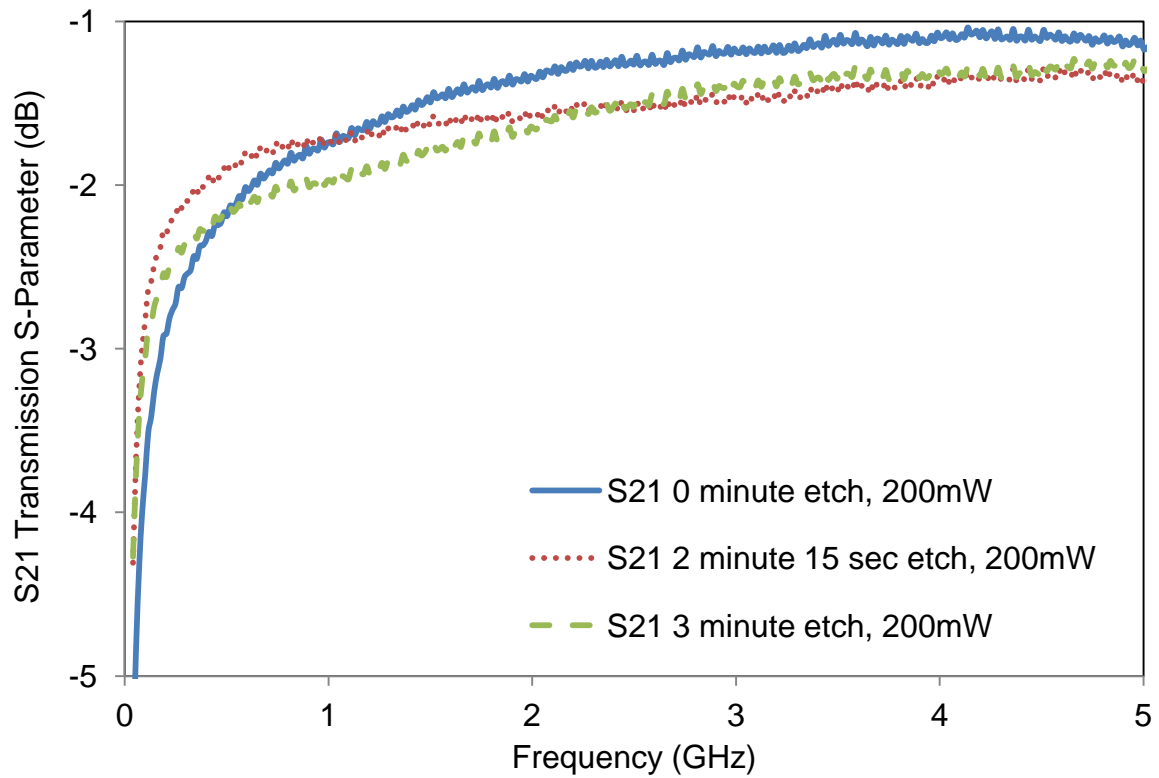


Figure 4.21:Transmission performance in the ON state (200mW of radiant flux) for gold deposited silicon attached via epoxy, size of silicon die 2mm x 1mm x 0.3mm

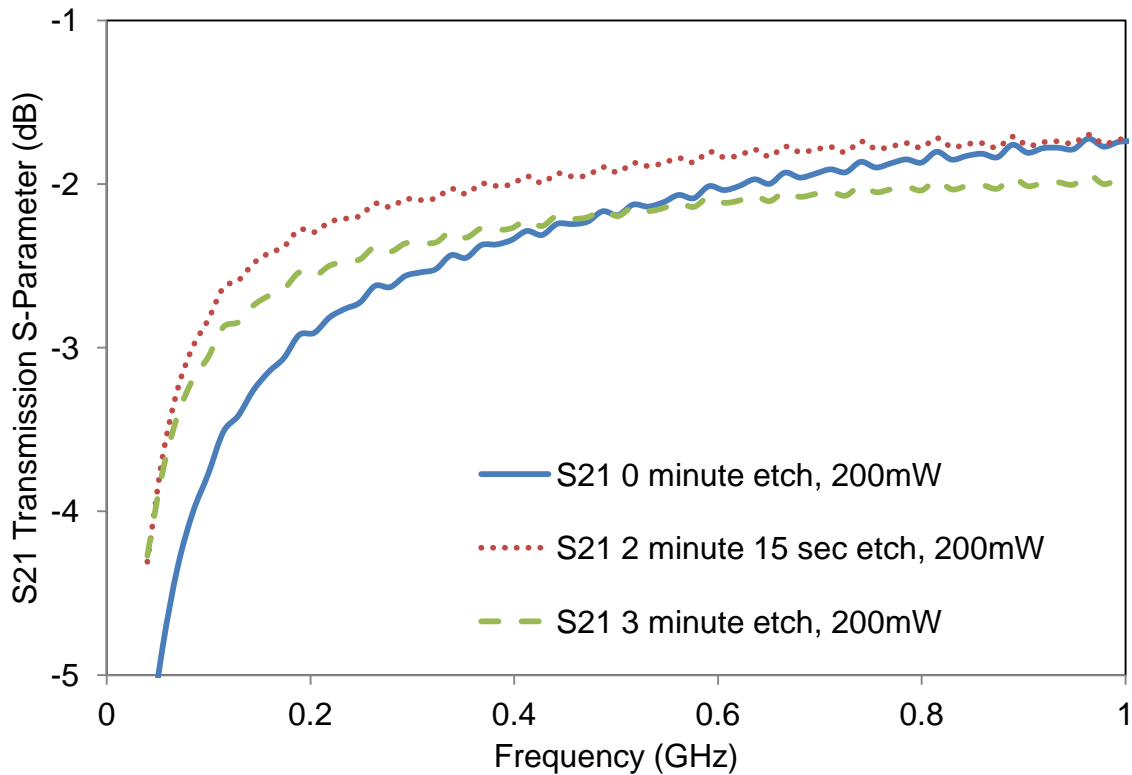


Figure 4.22:Transmission performance in the ON state (200mW of radiant flux) for gold deposited silicon attached via epoxy, size of silicon die 2mm x 1mm x 0.3mm

The process of selectively etching the passivation away has achieved the desired result up to 700MHz; the reduced air gap increases RF coupling of the input signal into the silicon. After this point, the sample which has not undergone etching exhibits a better performance. This is most likely because the extra processing step of etching the silicon has degraded the passivation and silicon quality. This is outlined by the poorer performance for the silicon sample which has been etched for 3 minutes and hence has a reduced passivation thickness underneath the metal.

4.6 Connection Methods

If contacts are formed on the silicon die, it is possible to use well established techniques such as wire bonding and surface mounting in order to connect the die into the circuit. In this case, the die can be bonded directly to the transmission line.

4.6.1 Conductive Epoxy vs. Solder

Previously, silver loaded epoxy has been used to attach the die to the copper transmission line. The composition of silver loaded epoxy is such that silver particles are suspended in a non-conductive resin. Signal is expected to propagate between silver particles, which is not ideal and may lead to higher loss within the material. The preparation requires mixing two parts which activates the adhesion process. In order to set the adhesive, the mixture can be cured $\sim 85^{\circ}\text{C}$ for 10 minutes; else the mixture will set if left at room temperature for 24 hours.

The conductivity of the silver loaded epoxy used in this thesis is estimated to be in the region of 20,000S/m [41]. However with the creation of gold contacts it is possible to explore other methods of interconnection – surface mounting and wire bonding. These methods can employ solder which is over 10 times more conductive than silver loaded epoxy [42].

On one hand, the use of silver epoxy has certain advantages when compared to lead solder. The processing temperature for epoxies is lower than the melting point for eutectic solders which is typically around 180°C [43]. On the other hand, solder has better adhesion qualities, less chance of contamination and better conductivity

compared to silver loaded epoxy [44]. The thermal conductivity and mechanical stability of solder is also superior.

In the following sections, the silicon die is fixed using both epoxy method and then solder method in an attempt to improve the RF performance of the switch further when compared to a die connected via silver epoxy.

4.6.2 Epoxy Method – Contact Position

The placement of the gold contact is first investigated. One option is that the die can be attached across the transmission line gap with the gold contact in direct contact with the copper transmission line. The other scenario involves the contact being positioned at the top most surface of the silicon closest to illumination.

The Rogers 3003 substrate, $\epsilon_r = 3$, height = 0.5mm is used, with a gap in the transmission line of 0.27mm. A 2mm x 1.5mm x 0.3mm die which has been processed with gold contacts is placed over the gap in transmission line. One transmission line has the die face down with contacts making intimate contact with the transmission line. The other has the die face up, with contacts on the surface of the silicon which is illuminated. In both cases, the die is attached using silver loaded epoxy. The die is then illuminated via a 1mm diameter optical fibre delivering 200mW of radiant flux.

The transmission performance when under the described conditions is presented in Figure 4.23. The insertion loss performance is very similar for the two variations of contact position. Up to 4GHz, the switch variation which has the gold touching the copper transmission line has better performance – at 2GHz the difference is ~0.2dB. The reflection coefficient is presented in Figure 4.24; the corresponding difference is 3.2dB at 2GHz. The OFF state performance in terms of S21 is presented in Figure 4.25. At 2GHz, the die with the contact touching the copper transmission line has a reduced transmission in the OFF state of 2.2dB when compared to the die with the contact on the top most surface of the die.

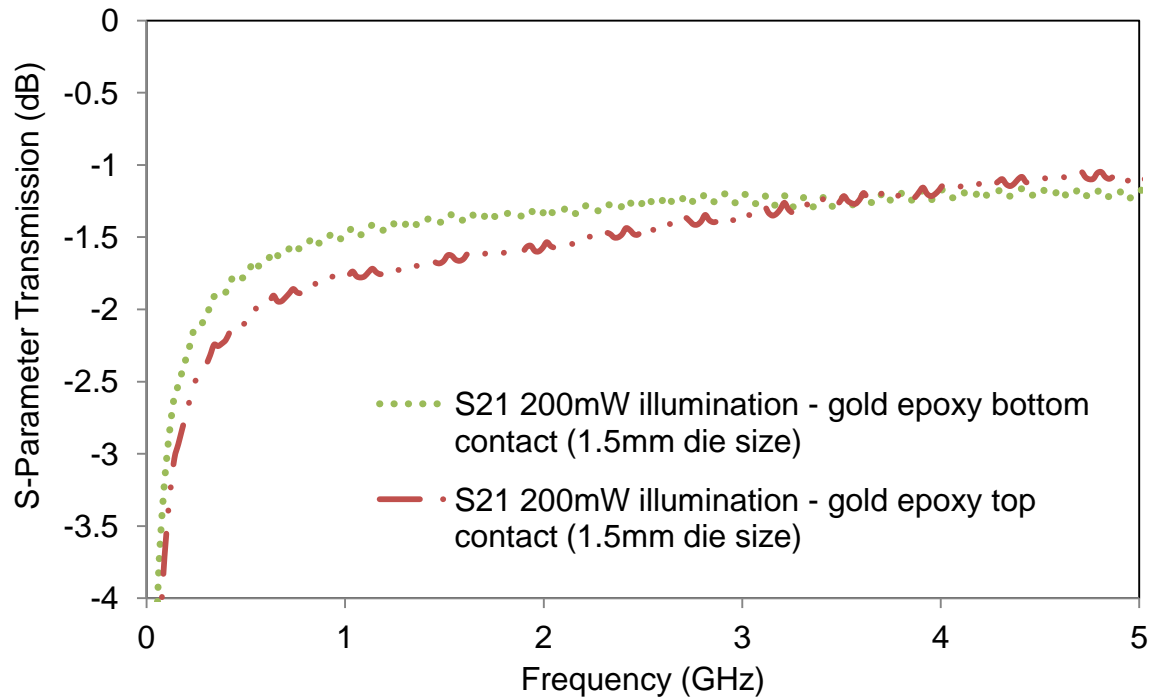


Figure 4.23: ON state S21 transmission of a 2mm x 1.5mm x 0.3mm silicon die with gold contacts (0 minute etch) attached with silver epoxy. The die is attached with the gold on the bottom of the die and in direct contact with the copper transmission line and when the contact is on top of the die. Radiant flux applied is 200mW

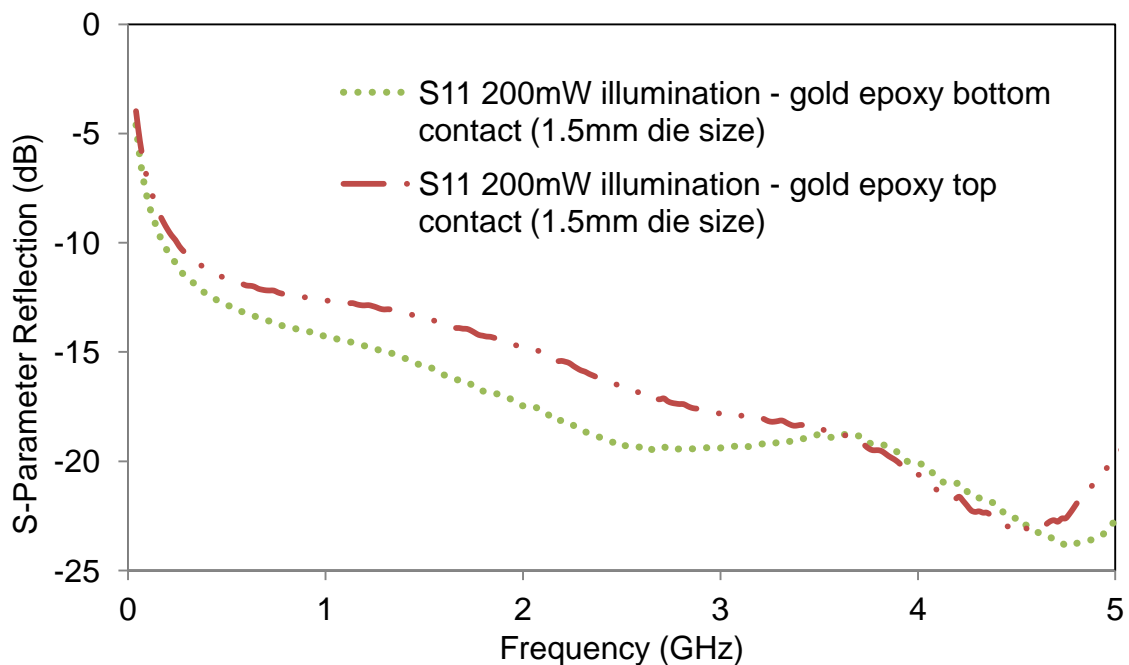


Figure 4.24: ON state Reflection coefficient when a gold contact (0 minute etch) silicon die of dimension 2mm x 1.5mm x 0.3mm is attached using silver epoxy either with the contact on the top or bottom of the silicon die. Radiant flux applied is 200mW

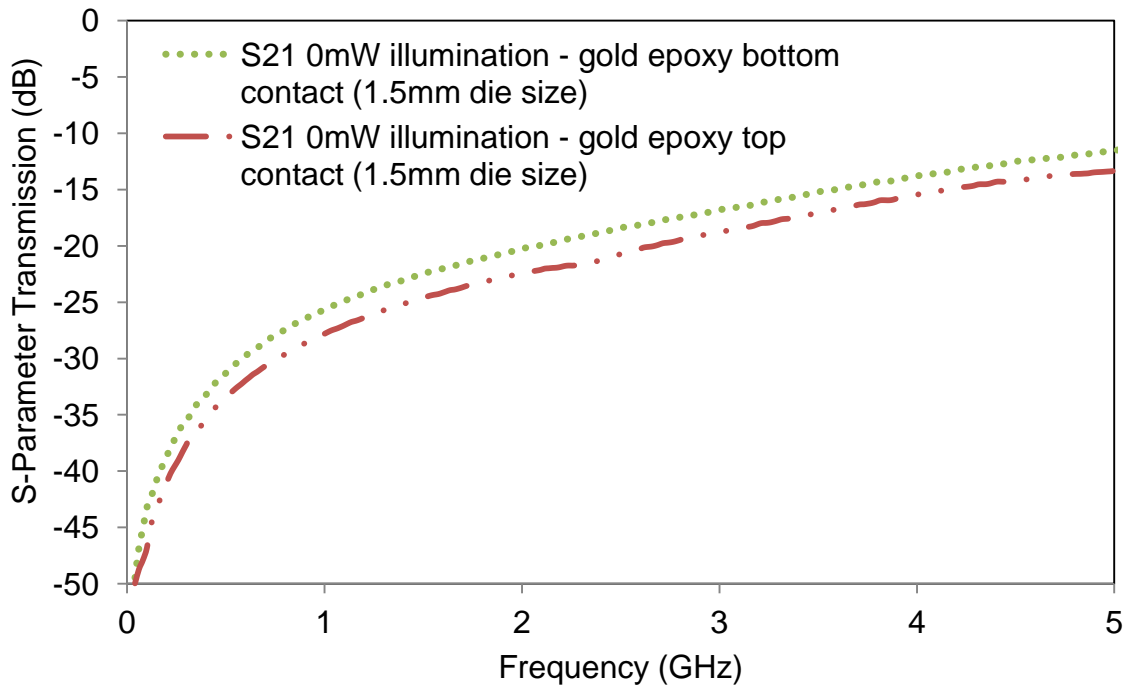


Figure 4.25: OFF state transmission coefficient when a gold contact (0 minute etch) silicon die of dimension 2mm x 1.5mm x 0.3mm is attached using silver epoxy either with the contact on the top or bottom of the silicon die. Radiant flux applied is 0mW

The signal transmission path involves a transition between copper transmission line and silicon die – the gold contact is made in an attempt to facilitate this transition. The results suggest that a better contact is made when the gold is in direct contact with the copper transmission line. Naturally, this is a more planar route for the RF signal to travel. This is perhaps why less insertion loss is incurred when compared to a die with the contacts based on the top most surface. In this scenario, if the switch is to benefit from the gold contact, the RF signal must travel to the top most surface of the silicon. This could potentially cause a discontinuity in the signal path which results in higher reflection in this case.

In the OFF state, this trend is continued. The transmission is reduced when the contact is positioned on the top most surface of the silicon. This would be expected as the silicon remains slightly conductive in the OFF state due to the phosphorous doping. This means there is still coupling of the signal from the gold contact into the silicon die. It should not be ruled out, that some of the difference in transmission performance could be due to the different application of silver loaded epoxy to each variation, as the difference seen here is relatively small. However, both transmission

lines were treated with the same formulation of the silver loaded epoxy and the transmission line gap was measured after fabrication to ensure these dimensions were equivalent for the two switches.

4.6.3 Surface Mounting using Solder

Similar to the epoxy case above where the contacts make intimate connection with the transmission line, a metalised dice was mounted over a gap in a transmission line using solder. In order to achieve this both copper transmission line and metallised area were heated simultaneously and joined with solder using flux to facilitate the process, Figure 4.26. In theory this method of interconnect provides a planar route for the high frequency signal to propagate down if the silicon is illuminated from below, as is discussed in Chapter 3. Silver loaded epoxy is not an ideal conductor, hence it is expected that performance can be improved by replacing this fixing method by solder. A better contact can be made between the copper transmission line and the gold contact formed on the silicon.

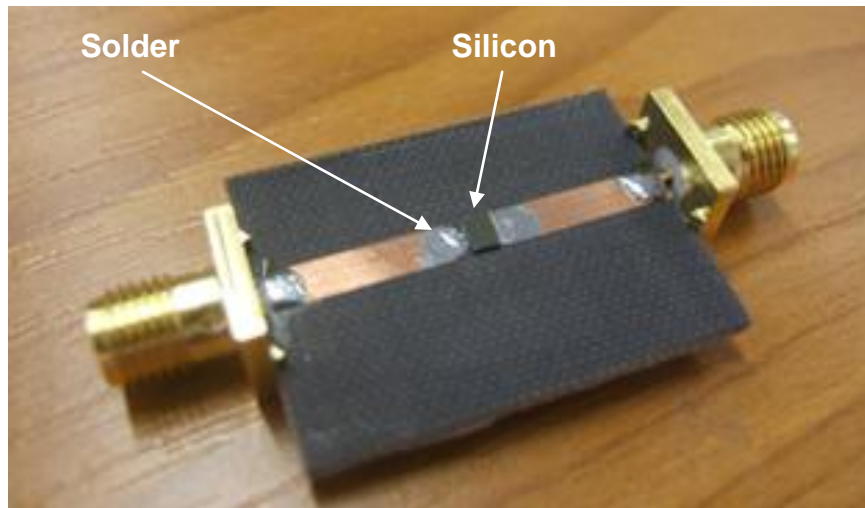


Figure 4.26: Gold contact die soldered onto transmission line. Substrate is Taconic TLC-32, $\epsilon_r = 3.2$, height=0.79mm. In this case, silicon die is (2mm \times 3mm \times 0.3mm)

4.6.3.1 R3003 Substrate

In this case, the Rogers R3003 substrate is used, $\epsilon_r = 3$, height = 0.5mm. A 2mm \times 1.5mm \times 0.3mm silicon die with gold contacts is attached over a 0.27mm gap in transmission line. Three cases are investigated. Firstly, the epoxy attached case which was described in section 4.6.2, where the gold contact makes direct contact with the copper transmission line.

Secondly, the same size die is attached using a surface mounting technique, with solder. Lastly, a smaller die with dimension 2mm \times 0.5mm \times 0.3mm is also soldered across a 0.27mm gap in transmission line. The die is illuminated with 200mW of radiant flux.

Results are presented in Figure 4.27 to Figure 4.28. Focusing on the two cases which involve the 1.5mm silicon die, it can be seen that the silver loaded epoxy method seems to have superior results in terms of insertion loss. At 2GHz the epoxy attached die, has an insertion loss of 1.33dB. The soldered die has an insertion loss of 4dB. At low frequencies the soldered die incurs more loss than at frequencies above 4GHz. The reflection is also higher for the soldered 1.5mm die, -4.2dB at 2GHz compared to the epoxied die, which has an S11 of -17dB at 2GHz. This suggests most of the signal is being reflected in the case of the soldered die.

Since the performance is particularly degraded at lower frequencies, this suggests that there may be an air gap or insulator which is degrading the capacitive coupling effect at DC. This could have been introduced during the manual soldering process, where an excess of solder was used to facilitate the soldering process. In order to try to get a better connection, another attempt at soldering was made, but this time using a smaller die of dimensions 2mm \times 0.5mm \times 0.3mm was used.

The insertion loss of this die is improved at lower frequencies. At 2GHz the S21 is -3dB and the S11 is -11dB. The epoxy based switch is still superior in performance however. The following section investigates more solder based switches which are fabricated on an alternative substrate to try to enhance performance.

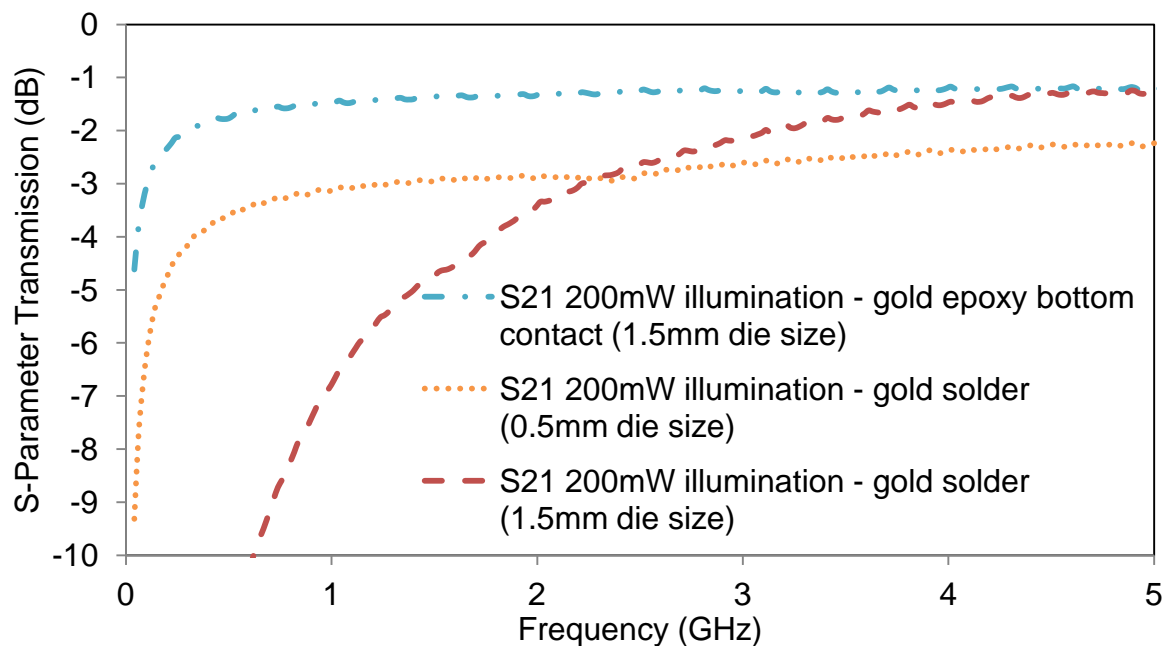


Figure 4.27: S21 transmission for various epoxy and solder based switches, die length is 2mm (exposed silicon surface is 1mm). Radiant flux applied is 200mW

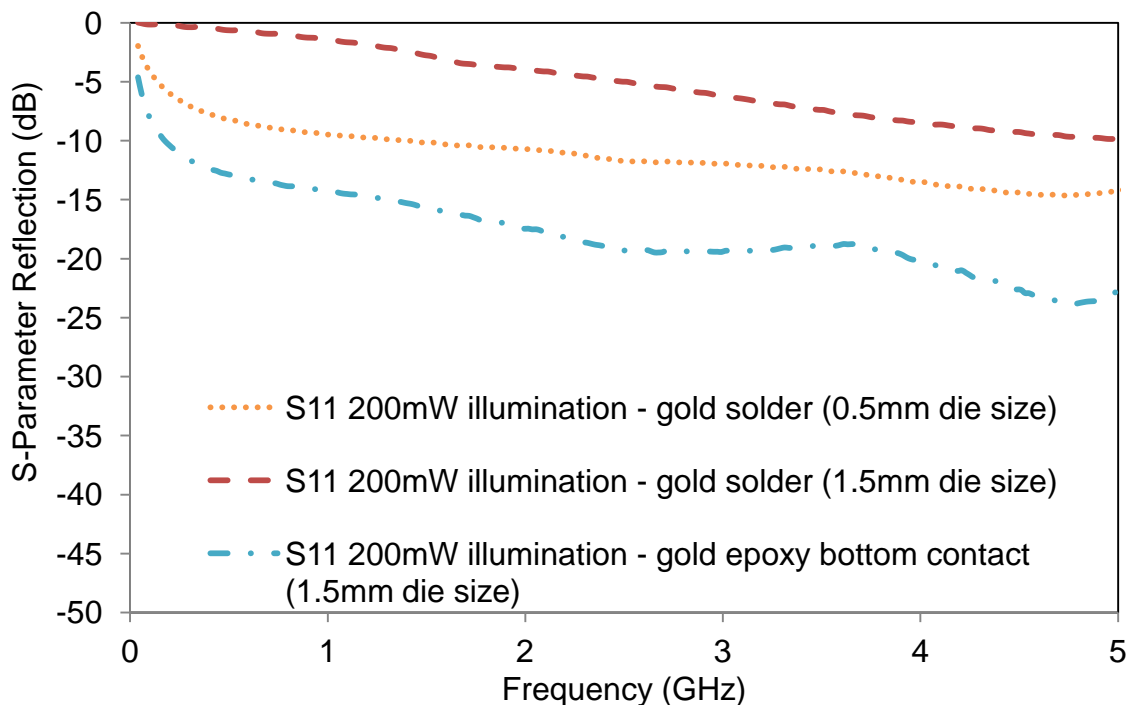


Figure 4.28: S11 reflection for various epoxy and solder based switches, die length is 2mm (exposed silicon surface is 1mm). Radiant flux applied is 200mW

4.6.3.2 TLC-32 Substrate

Two variations of the soldered silicon chip are investigated. Both are designed to have a 50Ω transmission line on Taconic TLC-32 with a permittivity $\epsilon_r = 3.2$, and a height = 0.79mm. The first is a soldered chip (2mm \times 2mm \times 0.3mm) over a 1mm gap in the transmission line. The second variation includes a 1.4mm hole which is drilled in the substrate directly beneath the soldered silicon chip. This allows the die to be illuminated from below, through the substrate, and hence improve the planarity of the signal path, as is discussed in Chapter 3. The intention is not to directly compare these variations in terms of transmission as the gap in transmission line differs between the two variations. However, some idea of performance can be gained by investigating these soldered chip results.

The transmission performance in terms of S-Parameter behaviour is measured using the Anritsu 37397D Lightning Vector Network Analyser, and are presented in Figure 4.29 and Figure 4.30. The transmission for the substrate with the hole beneath the silicon chip at 2GHz when the die is illuminated from below is -2.22dB. When the die is illuminated from above, the S21 is -1.44dB.

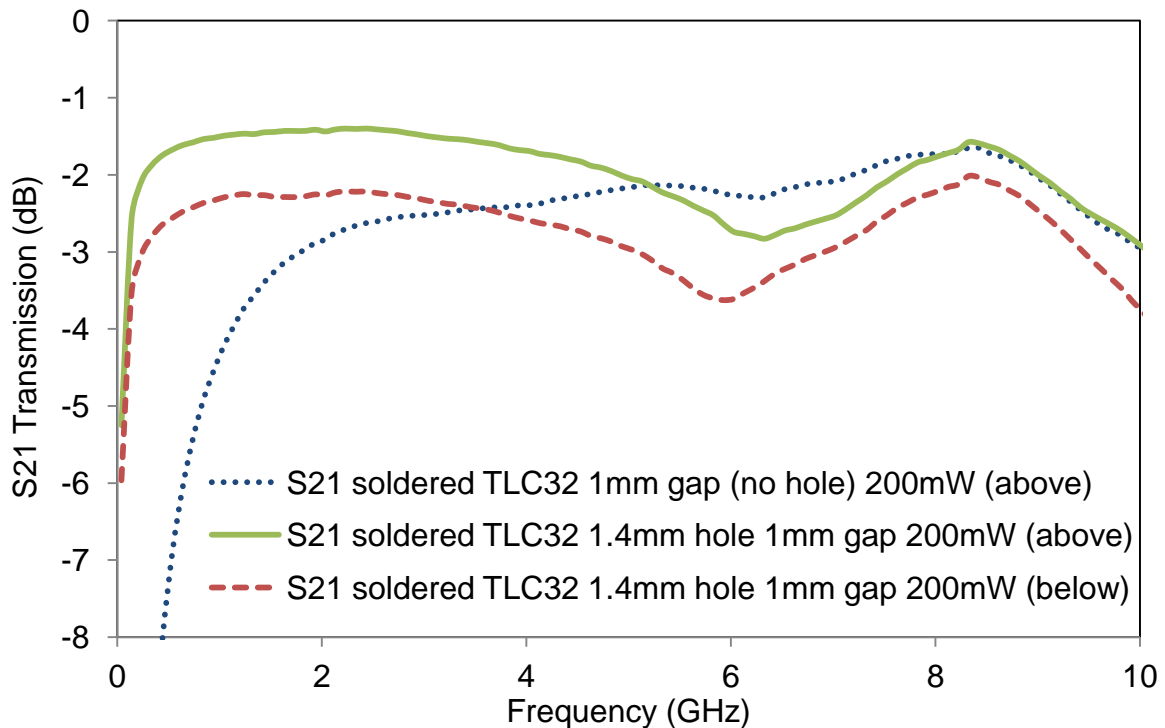


Figure 4.29: S-Parameter transmission results for soldered silicon die in ON state (200mW of radiant flux); comparing illumination from above and below die

This is in contrast to the expected performance in terms of the planar route for the RF signal. Simulation results in Chapter 3 demonstrate that a slight improvement in transmission in terms of S21 can be observed when the highest conductivity in the die is closest to the transmission line (e.g. then the die is illuminated thorough the substrate).

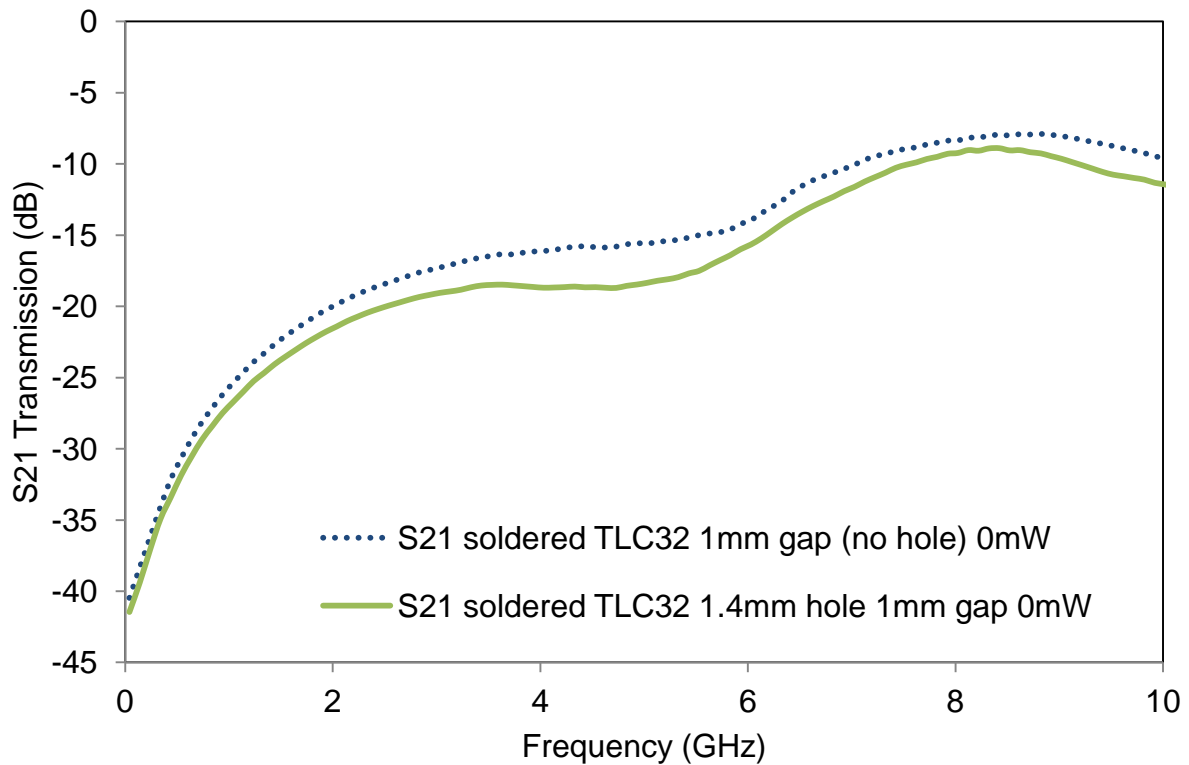


Figure 4.30: S-parameter transmission results in OFF state for soldered silicon die; comparing an optical fibre fed from above and below the die

Five attempts at soldering the die onto the transmission line were performed for the TLC-32 substrate. Twice the soldering process failed. In these cases it is likely the gold contact on the silicon became degraded due to the prolonged application of heat. When visually inspecting the successful cases it can be seen that in one case the die does not lie flush with the board – there is an air gap introduced on one side of the silicon, Figure 4.31. This die was not measured due to it obviously being of lower quality. It's possible that other dice produced by this method could also suffer from some connection failure. Since multiple switches have been fabricated and measured on different occasions, the poor performance is unlikely to be due to poor

measurement calibration. In order to facilitate the connection, solder flux was used, which can cause a layer of non-conductive material to interfere with the signal path.

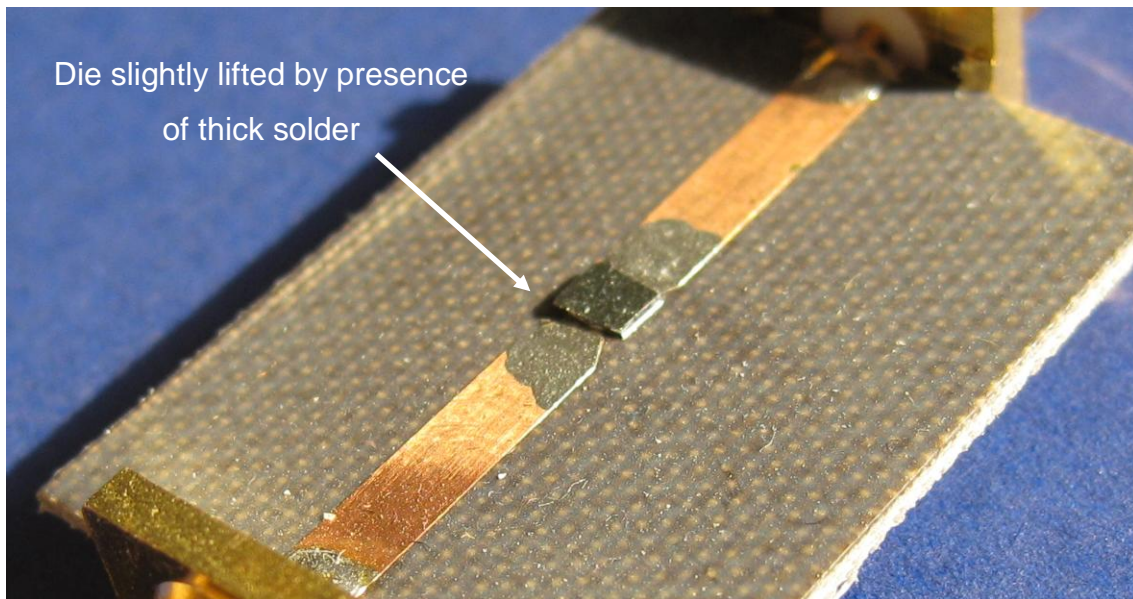


Figure 4.31: Soldering between silicon die and transmission line

One possible reason for the results could be due to the pressure exerted by the fibre. When the optical feed is above the die, the fibre pushes the silicon down, hence enhancing contact between the chip and transmission line. On the other hand, when the fibre is below the chip, it can push up on the die, decreasing direct contact between die and transmission line. Ideally if the die is properly soldered this behaviour should not be expected. In this thesis the only method available is to manually solder the die in place, however future work could include soldering the die in place via a surface mount machine, or with the help of solder masks.

In order to demonstrate that this manual method of surface mounting may be less reliable, the addition of the soldered chip on the transmission line with a gap of 1mm between copper segments is presented. At 2GHz the transmission is -2.88dB (die is illuminated from above), which is 1.44dB below the soldered version of the switch with a 1.4mm hole in the substrate illuminated from above. At 8GHz, the transmission performance of the 1mm gap transmission line is similar to the 1.4mm hole transmission line illuminated from above.

The transmission in the switch could be compromised at the lower frequencies due to there being extra space between transmission line and silicon die due to human error when soldering the silicon down. The process was repeated in order to improve the soldering technique, but the equipment in place is intended to be used to solder packaged chips and components onto circuits, not bare silicon chips. If such space was introduced when soldering the die down, the performance is degraded at frequencies where the wavelength is larger and coupling of the RF signal into the silicon is reduced.

The transmission performance of both soldered chip switch variations is presented in Figure 4.30. They both have a similar transmission in the OFF state. At 2 GHz, the S21 of the switch with a hole in the substrate is -21.8dB. Alternatively, the corresponding transmission for the switch with no hole (the 1mm gap in line) is -21.4dB.

4.6.4 Wire bonding

There are three main wire bonding processes, namely thermocompression, thermosonic or ultrasonic. The ultrasonic bonding option is chosen for investigation in this section. The concept behind ultrasonic bonding involves softening one or both of the welding surfaces with ultrasonic energy or heat [45]. The energy is absorbed into the metal and causes changes in the crystal lattice of the metal through dislocations. These changes result in most contaminants in the metal being pushed aside to expose clean areas. Rapid bonding and low temperature processing are the main advantages of this ultrasonic bonding technique [47]. The disadvantage of using this technique is that the initial setup of the equipment is much more complex in terms of defining parameters correctly.

The thermosonic bonding involves heating the tip of the wire as well as applying ultrasonic energy and pressure to form the connection to metal pad [48]. The advantages of this technique are that non directional ball bonding is possible and complex looping of the wire is also an option. The disadvantage is that it has a lower yield than ultrasonic wedge bonding, a higher chance of contamination and requires a larger bond pad area [49].

Thermocompression is the other alternative, which has the main advantage that the parameter setup for the equipment is much simpler. The three main disadvantages are the higher temperatures required and that this method is not suitable for small bond pads and that surface contamination is more likely.

The ultrasonically formed bond facilitates a high conductivity signal path which can replace the silver loaded epoxy. If the silicon is illuminated from above via a fibre, the wire bond connection is formed at the surface of the silicon which has the highest conductivity due to the exponential absorption of photons in the silicon.

The ball bonding technique is used to wire bond a 2mm by 1mm gold plated silicon die onto copper transmission line. Here the Taconic TLY-5 substrate, $\epsilon_r=2.2$, height=1.15mm is used. In this case a cavity has been made in the transmission line in order to accommodate the silicon chip, so that the contact site is flush with the transmission line. Multiple attempts were made to form wire bonds between the recessed die and copper transmission line, Figure 4.32.

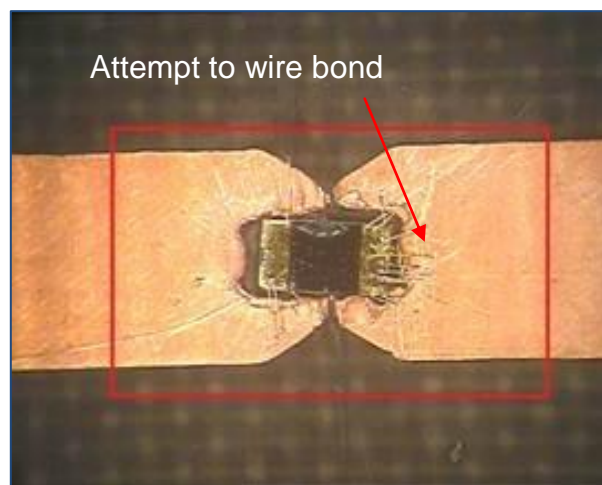


Figure 4.32: Wire bonding to gold contact on silicon die on a recessed transmission line design

However the quality of the bonds was poor. Due to the roughness of the copper surface and the compressible nature of the substrate, this wire bonding technique was found to be unsuitable. Improvements to the process could be made by gold plating the copper track and using a more ridged substrate such as ceramic. For

example, Alumina might be a suitable material which is typically used as a substrate in packaging due to its excellent thermal qualities [50].

4.7 Conclusions

The processing techniques available for improving silicon switch performance have been presented. In order to further investigate the interconnect methods discussed in Chapter 3; methods to deposit contacts onto the silicon have been discussed. These contacts must be compatible with the existing or post-processing fabrication steps such as the passivation or anti-reflective coating which may be applied to the silicon surface.

Passivating the boron doped silicon using silicon dioxide increases the minority carrier lifetime of the silicon by a factor of 2.7 hence reducing switch insertion loss from 1.8dB to 1.3dB. The addition of texturing, increases light absorption but does not improve microwave performance due to the possible effect this process has on recombination velocity of the carriers and also the increase in air gap created between the silicon and copper transmission line by the pyramid structure.

Continuing work on the texturing process is required to see effective results. For example, the increased air gap problem could be mitigated by only texturing the surface of the silicon which is exposed to illumination.

The effect of passivation layer thickness on RF switch performance is also investigated though fabricating capacitively coupled gold switch contacts. The passivated phosphorous doped silicon die was selectively etched so that the anti-reflective layer is maintained, but the capacitance of the contact area is altered. Results indicate that post etching of the silicon dioxide affects insertion loss in an adverse way. However some improvement on insertion loss is observed below 700MHz, hence increasing the useable frequency range of the switch. Ohmic contacts may be a good way to reduce the resistance and capacitance at the interconnect between silicon and metal interface. Further investigation is required to confirm this, as forming ohmic contacts requires removing the passivation layer which leads to decreased carrier lifetime. The injection of doping ions may also degrade performance in terms of lowering the carrier lifetime.

Surface mounting and wire bonding techniques are also investigated. In both cases the performance of the switch is degraded when compared to using silver loaded epoxy as a possible interconnect method. Future work is required to improve the application of these techniques.

4.8 References

- [1] A. Prasad, S. Balakrishnan, S. K. Jain, and G. C. Jain. "Porous Silicon Oxide Anti-Reflection Coating for Solar Cells." *Journal of The Electrochemical Society* 129, no. 3 pp. 596-599, 1982
- [2] M. A. Green, and M. J. Keevers. "Optical properties of intrinsic silicon at 300 K." *Progress in Photovoltaics: Research and Applications* Vol. 3, no. 3 pp.189-192, 1995.
- [3] C. Honsberg and S. Bowden "PV-CDROM: Surface Texturing," Website <http://pveducation.org/pvcdrom/design/surface-texturing>, last accessed: January 2013
- [4] E. A. Taft, "The Optical Constants of Silicon and Dry Oxygen Oxides of Silicon at 5461Å." *Journal of The Electrochemical Society* Vol.125, no. 6 pp. 968-971, 1978.
- [5] J. Schmidt, M. Kerr, and A.Cuevas, "Surface passivation of silicon solar cells using plasma-enhanced chemical-vapour-deposited SiN films and thin thermal SiO₂/plasma SiN stacks," *Semiconductor Science and Technology* Vol. 16, no. 3 pp.164, 2001.
- [6] G. Claudio, P. Kaminski, and K. Bass. "Optical characterisation of aluminium nitride as antireflective coating by a new remote plasma deposition system." *Physica Status Solidi (c)* Vol. 6, no. 12, pp.2665-2667, 2009.
- [7] J. A. Bragagnolo, B. Sopori, E. Eser, T. Hashimoto and I. Sugiyama, "Production technology for passivation of polycrystalline silicon solar cells," 12th Workshop on Crystalline Silicon Solar Cell Materials and Processes, pp. 300-306, 2002

- [8] M. Tao, "A new surface passivation technique for crystalline Si solar cells: Valence-mending passivation," IEEE 33rd Photovoltaic Specialists Conference, PVSC'08, pp. 1-6, 2008.
- [9] E. Cartier, J. H. Stathis, D.A. Buchanan, "Passivation and depassivation of silicon dangling bonds at the Si/SiO₂ interface by atomic hydrogen," Applied Physics Letters Vol. 63, pp.1510–1512, 1993.
- [10] P. Campbell and M. A. Green, "Light trapping properties of pyramidally textured surfaces," Journal of Applied Physics, Vol. 62, pp. 243, 1987.
- [11] P. Papet, O. Nichiporuk, A. Kaminski, Y. Rozier, J. Kraiem, J-F. Lelievre, A. Chaumartin, A. Fave, and M. Lemiti. "Pyramidal texturing of silicon solar cell with TMAH chemical anisotropic etching," Solar Energy Materials and Solar Cells 90, no. 15, pp. 2319-2328, 2006.
- [12] R. Brendel, "A novel process for ultrathin monocrystalline silicon solar cells on glass." Proc. 14th European Photovoltaic Solar Energy Conf., vol. 1354. 1997.
- [13] P. P. Young, R. Magnusson, T. A. Maldonado, and T. R. Holzheimer, "Method for high power illumination of silicon for optically configurable microwave circuits," Proc. SPIE 4768, vol. 74, 2002
- [14] J. R. Flemish, H. W. Kwan, R. L. Haupt, and M.I Lanagan. "A new silicon-based photoconductive microwave switch." Microwave and Optical Technology Letters Vol. 51, no. 1 pp. 248-252, 2009.
- [15] K. S. Kelkar "silicon carbide as a photoconductive switch material for high power applications," Ph.D Thesis Dissertation, University of Missouri-Columbia, Dec. 2006
- [16] B. J. Hughes, I. C. Sage and G. J. Ball, "Optically Controlled Metamorphic Antenna", 5th EMRS DTC Technical Conference Edinburgh, B24, 2008
- [17] Sinton Instruments "WCT100 Wafer Lifetime Equipment," Specification available online <http://sintoninstruments.com/> last accessed 13th June 2014

- [18] R. Sinton, A. A. Cuevas, and M. Stuckings. "Quasi-steady-state Photoconductance, a new method for solar cell material and device characterization." IEEE Photovoltaic Specialists Conference, pp. 457-460, 1996.
- [19] C. J. Panagamuwa, A. Chauraya, and J. C. Vardaxoglou, "Frequency and beam reconfigurable antenna using photoconducting switches," IEEE Trans. Antennas Propagation, vol. 54, no.2, pp. 449-454, 2006.
- [20] E. K. Kowalczyk, R. D. Seager, C. J. Panagamuwa, K. Bass and J. C. Vardaxoglou, "Optimising the performance of an optically controlled photoconductive microwave switch," IEEE Loughborough Antennas and Propagation Conference (LAPC), pp. 1-5, 2012
- [21] D. A. Neamen and B. Pevzner "Semiconductor physics and devices: basic principles," Vol. 3. New York: McGraw-Hill, 2003.
- [22] H. K. Henisch "Semi-conductor contacts : an approach to ideas and models" Clarendon, 1984
- [23] R. Baragiola "Electrical Properties: Electronic Structure of Surfaces" <http://www.virginia.edu/ep/SurfaceScience/electron.html>, Virginia University 2002. Last accessed 15th September 2013
- [24] W. Mönch, "Role of virtual gap states and defects in metal-semiconductor contacts." In Electronic Structure of Metal-Semiconductor Contacts, Springer Netherlands, pp. 224-227, 1990.
- [25] K. C. Saraswat "Metal/Semiconductor Ohmic Contacts," Stamford University EE311 Advanced Integrated Circuit Fabrication Processes Course notes http://www.stanford.edu/class/ee311/NOTES/Ohmic_Contacts.pdf Website last accessed : Dec. 2013
- [26] J. R. Flemish, and R. L. Haupt, "Optimisation of a photonicallly controlled microwave switch and attenuator," IEEE transactions on microwave theory and techniques, vol. 58, No. 10, 2010.

- [27] A. Karabegovic, R.M. O'Connell, and W. C. Nunnally. "Photoconductive switch design for microwave applications." IEEE Transactions on Dielectrics and Electrical Insulation, Vol. 16, no. 4 pp. 1011-1019, 2009.
- [28] J.F.Watts, J.Wolstenholme "An Introduction to Surface Analysis by XPS and AES," Published by Wiley & Sons, 2003
- [29] A. Chauraya, C. Panagamuwa, and J. Vardaxoglou. "Beam scanning antenna with photonicallly tuned EBG phase shifters," IEEE Antennas and Propagation Society International Symposium, pp. 2283-2286, 2006.
- [30] S.R. Wenham and M. A. Green "Method of making buried contact solar cell," United States Patent, 4748130, May 1988
- [31] G. Claudio, K. Bass, K. Heasman, A. Cole, S. Roberts, S. Watson and M. Boreland, "Surface passivation by silicon nitride in Laser Grooved Buried Contact (LGBC) silicon solar cells", Proceedings of the 9th International Workshop on Beam Injection Assessment of Microstructures in Semiconductors, Superlattices and Microstructures, Vol. 45, Issues 4-5, pp. 234-239, April-May 2009
- [32] Y. Tawk, A. R. Albrecht, S. Hemmady, G. Balakrishnan, and C. G. Christodoulou, "Optically pumped frequency reconfigurable antenna design," IEEE Antennas and Wireless Propagation Letters, vol. 9, pp. 280-283, 2010
- [33] A. Chauraya, C. J. Panagamuwa and J.C. Vardaxoglou "Beam Scanning Antenna with Photonicallly Tuned EBG Phase Shifters"IEEE Antennas and Propagation Society International Symposium 2006, pp. 2283, July 2006
- [34] E. K. Kowalczyk, C. J. Panagamuwa, R. D. Seager, and J. C. Vardaxoglou, "Characterising the linearity of an optically controlled photoconductive microwave switch," Loughborough Antennas and Propagation Conference, 2010
- [35] S. S. Gevorgian, "Design considerations for an optically excited semiconductor microstrip gap at microwave frequencies", IEE Proc. Vol 139, No. 2, April 1992

- [36] IMST EMPIRE XCcel version 5.3 -5.51, <http://www.empire.de/>
- [37] D. H. Auston, "Picosecond optoelectronic switching and gating in silicon," *Applied Physics Letters*, vol. 26, pp. 101-103, 1975
- [38] J. R. Flemish, and R. L. Haupt, "Optimisation of a photonicallly controlled microwave switch and attenuator," *IEEE transactions on microwave theory and techniques*, vol. 58, No. 10, 2010.
- [39] H. B. Harrison and G. K. Reeves "Ohmic Contacts Formed on Single- and Polycrystalline Silicon Using Ion Implantation and Low-Temperature Annealing", *IEEE Electron Devices Letters*, Vol. EDL-5, No. 2, Feb. 1984
- [40] L. S. Yu, L. Jia, D. Qiao, S. S. Lau, J. Li, J. Y. Lin, and H. X. Jiang. "The origins of leaky characteristics of Schottky diodes on p-GaN." *IEEE Transactions on Electron Devices*, Vol. 50, no. 2, pp. 292-296, 2003.
- [41] RS Silver loaded epoxy datasheet. Part no. RS 186-3616, Website <http://uk.rs-online.com/web/p/conductive-adhesives/1863616/> last accessed April 2014
- [42] Nondestructive Testing Resource Centre, "Conductivity and Resistivity Values for Misc. Materials," http://www.ndt-ed.org/GeneralResources/MaterialProperties/ET/Conductivity_Misc.pdf
- [43] C. Yang and M. Li. "Conductive Adhesives as the Ultralow Cost RFID Tag Antenna Material." *Current Trends and Challenges in RFID*, Prof. Cornel Turcu (Ed.), ISBN: 978-953-307-356-9, InTech, 2011
- [44] X. Luo, D. Chung "A comparative study of silver-epoxy and tin-lead solder in their joints with copper though mechanic and electrical measurements during debonding", *Kluwer Academic Publishers, Journal of materials science*, Vol. 34, 1999
- [45] G. G. Harman and J. Albers, "The ultrasonic welding mechanism as applied to aluminum- and gold-wire bonding in microelectronics," *IEEE Trans. Parts, Hybrids Package.*, vol. PHP-13, no. 4, pp. 406–412, Dec.1977.

- [46]] L. Levine, "The ultrasonic wedge bonding mechanism: Two theories converge," Proc. SPIE— Int. Soc. Opt. Eng., vol. 2649, pp. 242–246, 1995.
- [47] J. Kim, Bongwon Jeong, Mu Chiao, and Liwei Lin. "Ultrasonic bonding for MEMS sealing and packaging." IEEE Transactions on Advanced Packaging, Vol. 32, no. 2 pp. 461-467, 2009.
- [48] V-PS "Application note: Wire bonding" <http://www.vps.nu/img/image/Docs/safe%20light.pdf> last accessed 1st September 2013
- [49] S. K. Prasad, "Advanced wire bond interconnection technology," Kluwer Academic Publishers, 1st Ed., 2004.
- [50] M. Mirgizoudi, C. Liu, and S. Riches. "Reliability testing of electronic packages in harsh environments." IEEE 12th Electronics Packaging Technology Conference (EPTC), pp. 224-230, 2010.

5 Switch Characterisation

When investigating microwave switches, the primary characteristic of interest to the designer is often the RF transmission of the switch. However, depending on the application, other characteristics may also be of high importance. In this chapter the aim is to characterise the switch in terms of linearity, power handling and switching time.

5.1 Introduction

For applications such as long range high power transmitting antenna, two important figures of merit are power handling and signal distortion for all components in the RF system. The following results ultimately dictate how much power the switch can handle and its linearity response to input signals:

- Insertion loss in the ON state: the signal loss the switch suffers when an RF signal is passed through the switch in the ON state.
- Isolation in the OFF state: the signal leakage appearing at the output when the switch is OFF.
- RF power handling: the behaviour of the switch at high RF powers, particularly with regards to signal compression.
- Harmonic single tone linearity: the appearance of undesired harmonics at multiples of the fundamental test frequency.
- Two tone intermodulation distortion: the distortion caused within the switch when a two-tone signal is passed through the switch.

Insertion loss and isolation have already been reported for various photoconductive switch topologies in Chapter 3. However, very little data is available on the power handling of the photoconductive switch. Hence the characterisation of linearity and compression of the switch will be the focus for the first sections of this chapter.

Presenting research on the linearity of photoconductive switches and proving the current power handling capabilities will increase the applications for such switches. By comparing the results to alternative microwave switches, it can be ascertained whether the photoconductive switch is better in certain applications. The power handling may also give an indication of packaging considerations for dealing with power loss which manifests itself as heat.

The latter part of this chapter will focus on the switching time of the photoconductive switch. Fast switching is essential for cognitive radio applications [8]. The effect switch design and control method have on the rise and fall time of a photoconductive microwave switch at 2GHz is investigated.

5.2 Linearity

For wireless applications which require high power RF signals, linearity is an important device characteristic. Linearity dictates the independence of device impedance from RF input signal power, and is typically monitored through second and third order harmonics as well as intermodulation products. Linearity of photoconductive switches has not been widely reported beyond 1W of incident RF power [2]. Linearity is closely linked to power handling – above a certain power level, the switch may start to exhibit higher levels of insertion loss.

The point at which losses start to increase is referred to as the gain compression of the switch. Above this point there will no longer be a linear relationship between input power and output power. A device may enter this region and continue to serve its function (perhaps with reduced efficiency). However, beyond a certain power damage may be incurred and this is said to be the absolute power handling. Essentially, power handling is defined as the maximum power that the switch can continue to work at.

Signal distortion is an undesired effect caused by non-linearities present in a system. As the signal passes through the system – a switch in this case – it interacts with these non-linearities and the output signal can become distorted. A number of things can be the cause of non-linearity such as changes in material at junction sites, interaction between bias signals, poor contact at junctions and even contaminated surfaces and connectors [3]

5.2.1 Single Tone Linearity

At lower powers the distortion can be very small, however due to the nature by which the distortion is generated, as input power increases by a factor of 1; distortion will increase by a factor of 3. In the case of a single tone input signal, harmonics will be produced at multiples of the fundamental frequency, e.g. $2f_0$, $3f_0$, $4f_0$ etc. Larger harmonics occur at the second ($2f_0$) and third harmonic ($3f_0$).

A usual measure of linearity is the second and third order intercept (SOI / TOI). These are extrapolated values. In terms of the third order intercept it is the theoretical value where if fundamental signal power was increased both fundamental and third harmonic content would be equal. It is also possible to define a second order intercept point SOI which relates to the extrapolated intersection of fundamental signal and second harmonic content.

The following formula, Eq. (5.1), shows how the second order product changes at a rate which is a square of the change of the input signal.

$$V_{out} = a_1 A \cos(\omega t) + a_2 A^2 \cos(2\omega t) + a_3 A^3 \cos(3\omega t) \quad \text{Eq. (5.1)}$$

A is amplitude of input signal, $a_{1,2,3}$ are the transfer functions for the fundamental, second and third harmonics [4]. This demonstrates the relationship between the fundamental and higher order harmonics.

5.2.2 Two-Tone Linearity

Typically, only a broadband system is susceptible to harmonic distortion as single tone harmonics usually occur well away from the input frequency of the signal. For

narrowband systems, two-tone intermodulation is more problematic. The distortion caused when a two-tone signal is applied occurs close to the fundamental frequencies which cause interference in the pass band. The two input signals interact with each other when there are non-linearities present – the theoretical outcome can be calculated using the Volterra series [5]. In general, intermodulation products are multiples of the fundamental frequencies:

1st order f_1, f_2

2nd order f_1+f_2, f_2-f_1

3rd order $2f_1-f_2, 2f_2-f_1$

4th order $2f_2+2f_1, 2f_2-2f_1$

5th order $3f_1+2f_2, 3f_2-2f_1$ etc.

As the fundamental increases by a unit, the intermodulation product of the third order increases three fold. The result can be large intermodulation products in the vicinity of the fundamental signal, causing distortion [6]. Intermodulation is usually measured by extrapolation of the fundamental and intermodulation products. The theoretical point at which these two extrapolated lines intersect is referred to as the third order intermodulation product IP3.

This value can be referenced to either the input (IIP3) or the output signal (OIP3 e.g. output includes the insertion loss of the component under test). A typical intermodulation measurement output is depicted in Figure 5.1. Two main tones can be seen at 2.0095GHz and 2.0105GHz. The intermodulation products occur at 2.0084GHz and 2.0115GHz. These measurements were taken using an Agilent Vector Signal Analyser E4406A. The equipment was borrowed from the University of Westminster to perform preliminary measurements. From these readings it is possible to extrapolate the IP3 values.

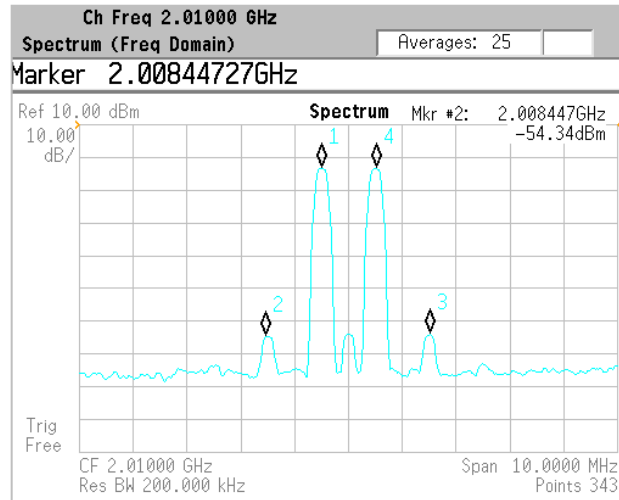


Figure 5.1: Intermodulation products generated when measuring two tone linearity using the Agilent vector signal analyser E4406A at the University of Westminster.

5.3 Switch Linearity and Power Handling Review

Microwave switches such as PIN and varactor diodes, MEMS switches and photoconductive switches are currently used for switching functions in many wireless communication systems. Since linearity of such systems is often limited by the switching device, there is continuous research into improving microwave switch linearity in reconfigurable circuits; a summary of a selection is presented in Table 5.1 in terms of Third Order Intercept (TOI), 3rd Order Intermodulation Product (IP3) and Output IP3 (OIP3).

The linearity and power handling of switch mechanisms is particularly relevant in for high power RF applications. Due to the P-N junction in PIN and varactor diodes, these components are nonlinear and produce distortion. As a solution, alternative topologies are widely being researched to combat this problem.

	Frequency (GHz)	Isolation (dB)	Power (W)	Linearity (dBm)
Heterostructure PCS, single [2]	0.96	-25	>1	TOI 65
Single PIN diode [7]	5.6	-20	>3	IP3 46
4 Varactor stack configuration [8]	1.95	-	>0.2	OIP3 60
Single MEMS [16]	10	40	3 (max)	IIP3 80

Table 5.1: Comparison of Heterostructure photoconductive switch and microwave switches used in reconfigurable applications

Varactor diodes provide an excellent means of continuously tuning frequency but require high voltage bias lines to operate and are inherently non-linear in behaviour, where low power handling is an issue for single varactors. Low power handling is being addressed by incorporating multiple varactors in stacks or incorporating additional passive components [9], however this increases device count and area and may create additional complexities in terms of design and behaviour when components are placed in parallel configurations and signal is split between different paths.

Improving the linearity of diode switches has been a focus of research, resulting in configurations of switches such as reported by Huang *et al.* [8]. A value of 60dBm OIP3 is reported in this instance for a configuration of four diodes, however single switches are far less linear. The principle is based on back-to back configuration resulting in cancellation of distortion currents. The downside of this approach is that no two devices will exhibit the same distortion so cancellation will not be absolute. Multiple devices are required which increase complexity and footprint of the switching mechanism.

Since RF power is dissipated in the form of heat in the junction resistance of these devices they have a lower mean time to failure [11] compared to junctionless switches.

Furthermore, the effect of distortion of the switch mechanism has been investigated by Yong *et al.*[12]. The example of a varactor diode in a reconfigurable patch antenna is used to demonstrate the non-linear effects on antenna performance. From the perspective of Electromagnetic Interference (EMI) conformity issues, Kalialakis *et al.* [13] report on the importance of harmonic performance for a quarter-wavelength microstrip antenna switched via varactor diode.

PIN diodes are a more popular choice in reconfigurable circuits when compared to varactor diodes as they require bias lines with lower voltage, however they display higher loss due to their ON state resistance, compromising performance. PIN diodes also suffer similar linearity and distortion problems as varactor diodes. Generally, PIN diodes are mainly constructed to exhibit fast switching speeds, which require a small intrinsic layer and a small carrier lifetime. These values have a direct effect on the tendency to retain a quiescent level of stored charge, and hence create distortion [14]. PIN diode distortion is at its worst at the intermediate levels of bias where the PIN diode's resistance is some moderate value. Since the distortion level of PIN diodes also heavily depends on the forward current in the device, IP3 can vary from 31-65dBm in any given diode depending on this current value and on its resistance [15]. In this case, maximum power handling is 250mW.

In the application of reconfigurable circuits, a PIN diode used in series for a tuneable filter has a reported IP3 of 46dBm and distortion free output tested up to 2W [7].

Conversely, MEMS switches demonstrate high linearity, as there are no semiconductor junctions in these components. Typical intermodulation intercept point values are tested to above 65dBm for a 1MHz tone spacing at 1GHz [31]. These devices have been incorporated into reconfigurable circuits and antennas as is demonstrated by a monolithic integration approach by Crusats *et al.* [17].

MEMS switches have excellent insertion loss and isolation values and display far more linear behaviour, particularly as an alternative to varactor diodes. However they often display problems such as self-actuation when handling higher input powers.

For example DeNatale [18] reports the self actuation of a MEMS at ~3W when hot switched, limiting their reliability. They are also more difficult to integrate into reconfigurable circuits, requiring high voltage biasing lines.

Due to self-actuation issue and increased distortion at higher temperatures [19], the use of these components in high power applications is limited. More recently, there are a few candidates that can handle RF power up to 10W [20]. In this instance the reliability of the MEMS switch was said to be compromised by the build-up of contaminants on the contact surface. To solve these reliability issues hermetic packaging is required which is expensive to implement [21]

Currently, a heterostructure light activated microwave photoconductive switch design [2] with flip chip light source has a reported third order intercept (TOI) of 65dBm, extrapolated from measurements taken up to 1W.

The photoconductive switch consists simply of silicon, and does not require the presence of a p-n junction to work. The switch does not incorporate moving parts and so should be less expensive to manufacture and not suffer failure due to self-actuation under high power signals. In addition to this, due to the absence of a junction in a photoconductive silicon die switch, the voltage at which the switch experiences breakdown is considerably higher. Hence there is potential for greater power handling capability from photoconductive switches.

5.4 Single tone linearity test setup

In this section, the single tone linearity of the photoconductive switch is further investigated. Parameters including insertion loss, isolation measurements and second and third order intercept (SOI/TOI) measurements are determined using the measurement platform illustrated in Figure 5.2.

An Anritsu 37397D Vector Network Analyser measures the S-Parameter values to determine feed-through response in both on and off switch states. For the harmonic testing, signal is generated using a Continuous wave signal generator, HP 83650L, and is boosted to produce 1W by external amplification using a combination of amplifier modules.

A high directivity 22dB directional coupler is used to couple a portion of the input signal entering the switch to determine an accurate power reading just before the switch. The output signal is fed into the Spectrum Analyser, Advantest R3132 to measure power at the fundamental frequency f_0 , 2GHz, and second and third harmonics at $2f_0$ (4GHz) and $3f_0$ (6GHz).

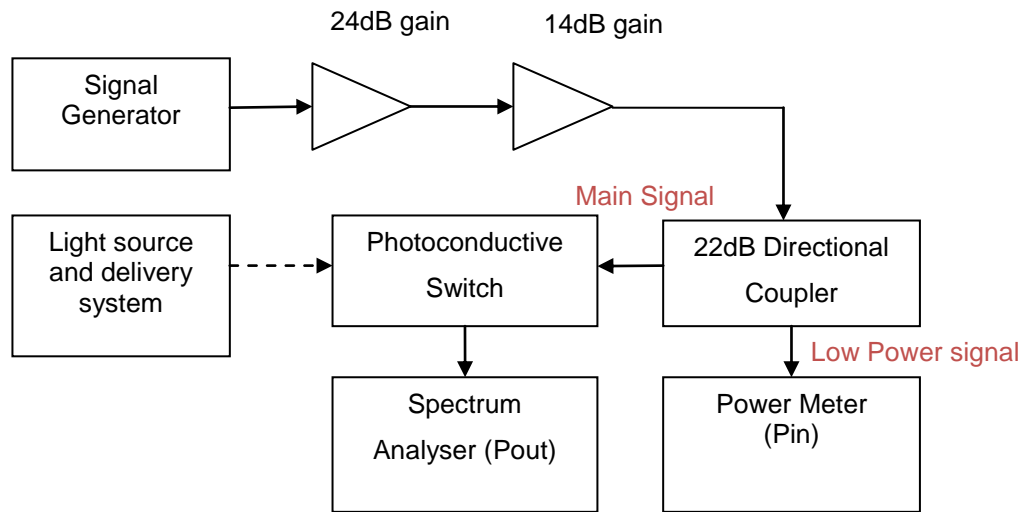


Figure 5.2: Measurement platform for single tone linearity measurements on a photoconductive switch

5.4.1 High Directivity Coupler

A high directivity coupler based on work by Baek *et al.* [22] was used to accurately sample incident power to the switch for measurement with a power meter. The novel design enables high directivity through use of a capacitive interdigitated gap, overall increasing the isolation and minimising S_{11} and S_{41} while maintaining a 20dB coupling between 1.5-2.2GHz. AWR Microwave Office [23] was used to initially estimate coupler dimensions, shown in Figure 5.3.

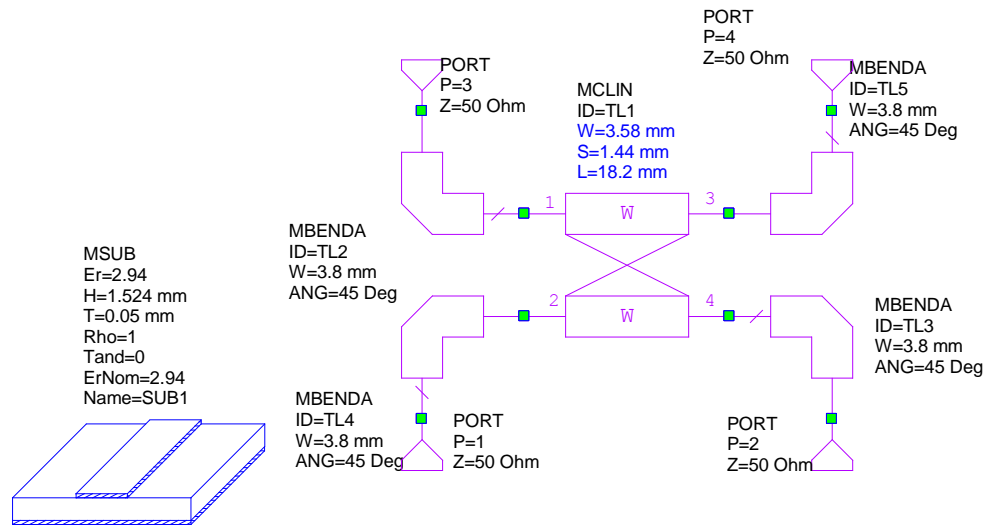


Figure 5.3: AWR Microwave Office design of a 2GHz coupler

The analytical model can be used to quickly investigate the geometry required to achieve an acceptable performance based on the criteria below:

- Gap between coupled lines determines the level of coupling, 20dB in this case.
- Length of line determines the frequency at which coupling is achieved
- Width of coupled line controls the reflection coefficient, e.g. line impedance

This simplified model does not include material losses, but takes into account the discontinuities of a bend in the coupler design. The design can then be further optimised using 3D EM simulation.

The design – in particular the interdigitated gap parameters – was modified according to the substrate material through parameter sweep adjustment using EMPIRE XCcel version 5.3 [12], see Figure 5.4 and Figure 5.5 for the final design, simulation and actual performance. The final design established a 22dB coupled output and an insertion loss of 0.2dB.

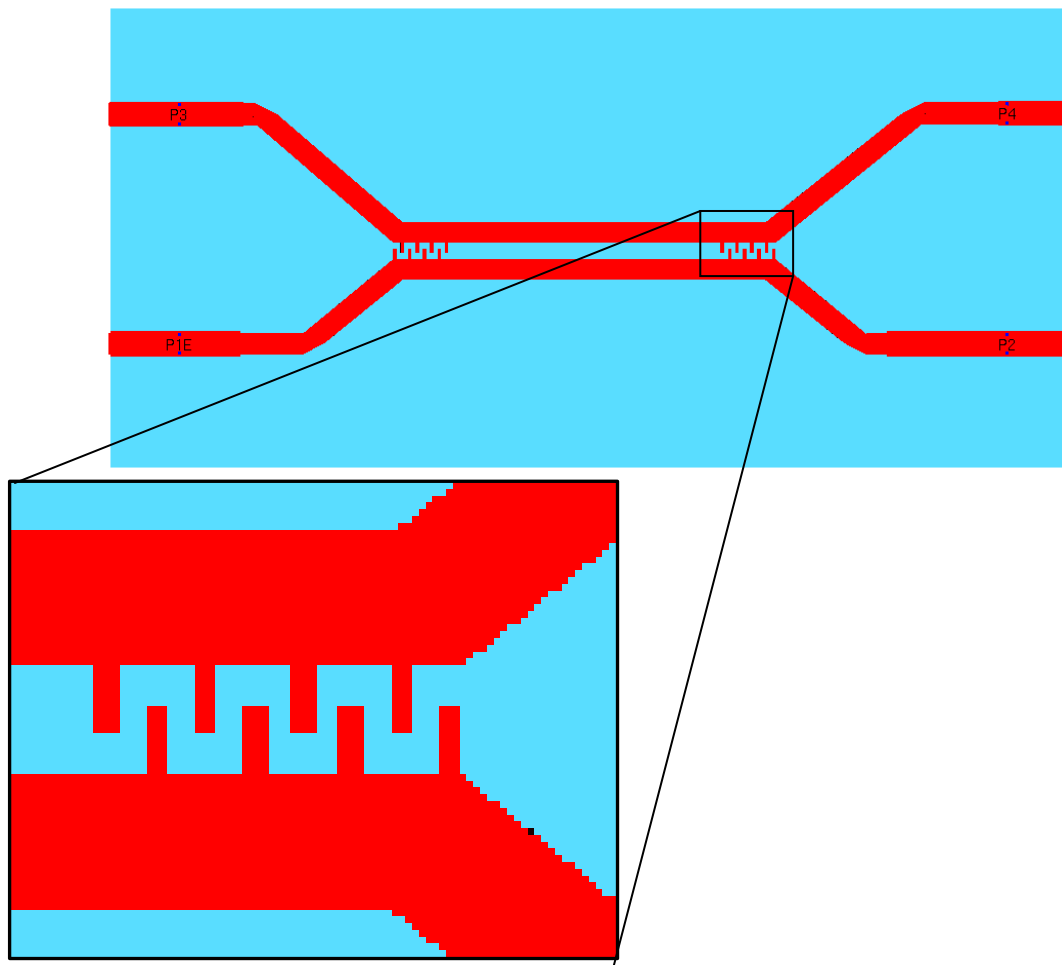


Figure 5.4: Final design in EMPIRE XCcel of the 20dB directional coupler

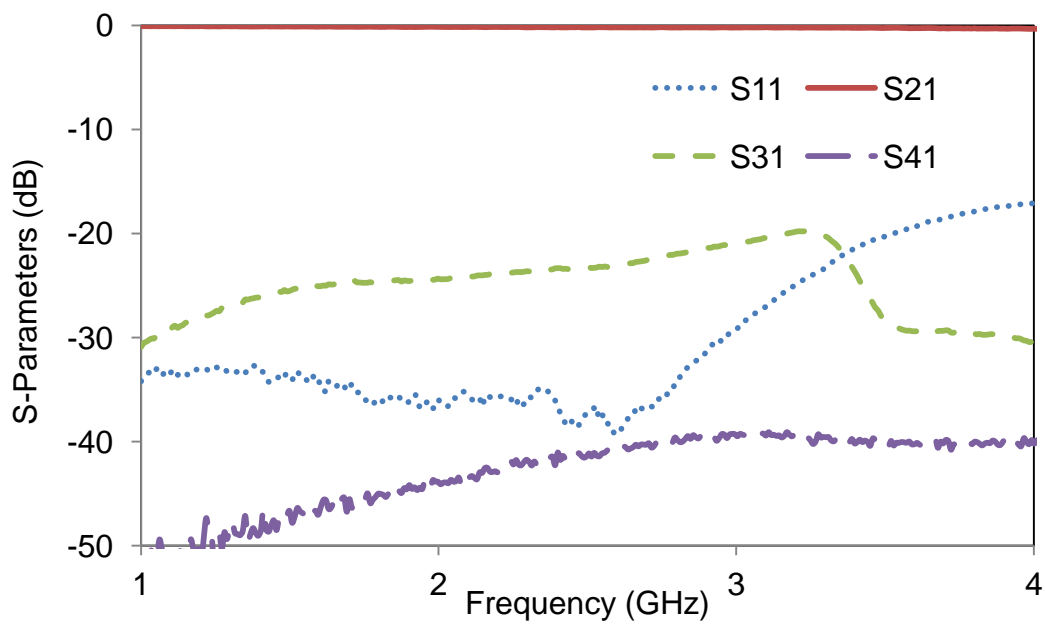


Figure 5.5: Measured s-parameters for the directional coupler design

5.4.2 Wilkinson Combiner Amplifier

The power amplifier was designed to amplify the signal from the signal generator up to 1W to provide sufficient signal strength to detect second and third harmonics using the Advantest Spectrum Analyser. Given the poor thermal conductivity of the substrates available and the limited power output of readily available MMIC amplifiers a power combiner was designed to combine the output of two MMIC amplifiers to achieve a 1W RF signal at 2GHz. This was designed as a bespoke solution at the start of the doctoral study an alternative to buying an off-the-shelf amplifier.

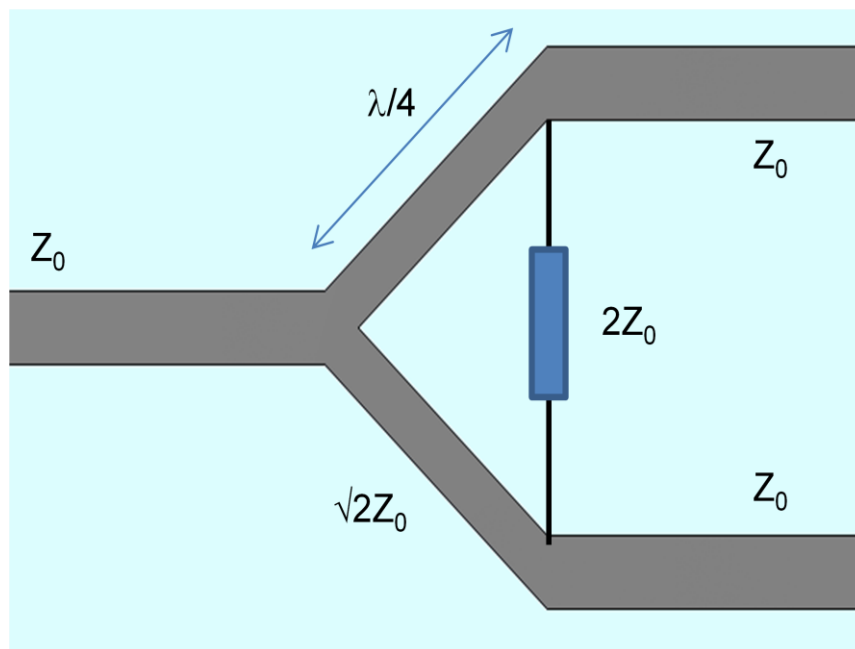


Figure 5.6 : Wilkinson Divider Theory

Figure 5.6, based on theory from Pozar [24], is used to design the Wilkinson divider/combiner circuitry, where Z_0 is the characteristic impedance (50Ω) and λ is the guide wavelength. To ensure a smooth RF path the divider was designed with a curved transmission line, Figure 5.7. Since the final design contains an active device to achieve amplification which cannot be simulated using EMPIRE XCcel, the simulated and measured result cannot be compared. For measured results refer to Figure 5.8.

The input signal is amplified by 14.6dB at 2GHz. In order to reach 1W (30dBm), a 15.4dBm signal is used as the input signal to the Wilkinson Divider circuit.

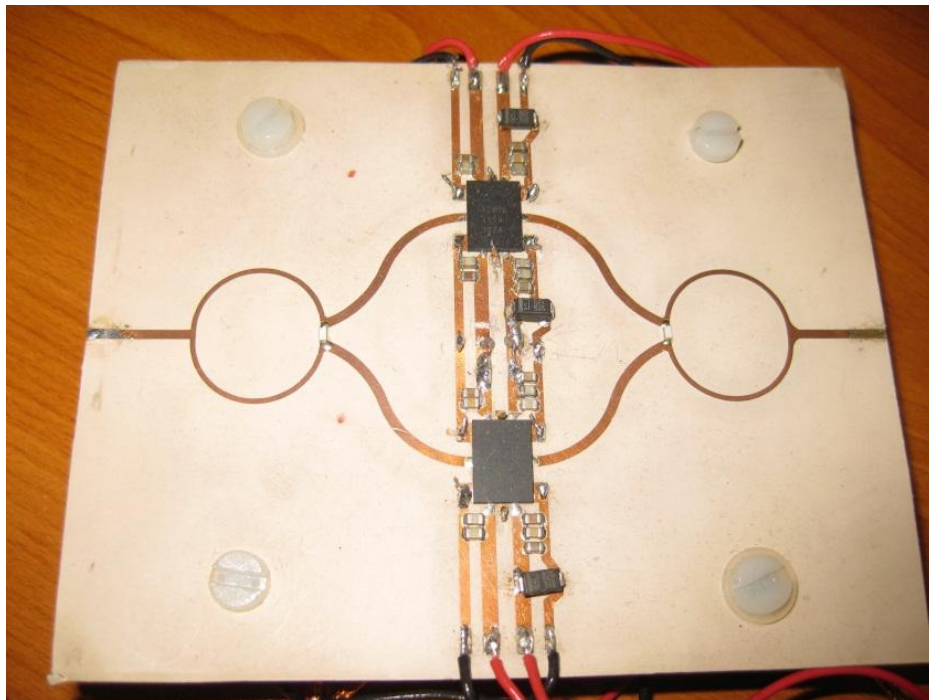


Figure 5.7: Fabricated Wilkinson divider/combiner including MMIC amplifier chips

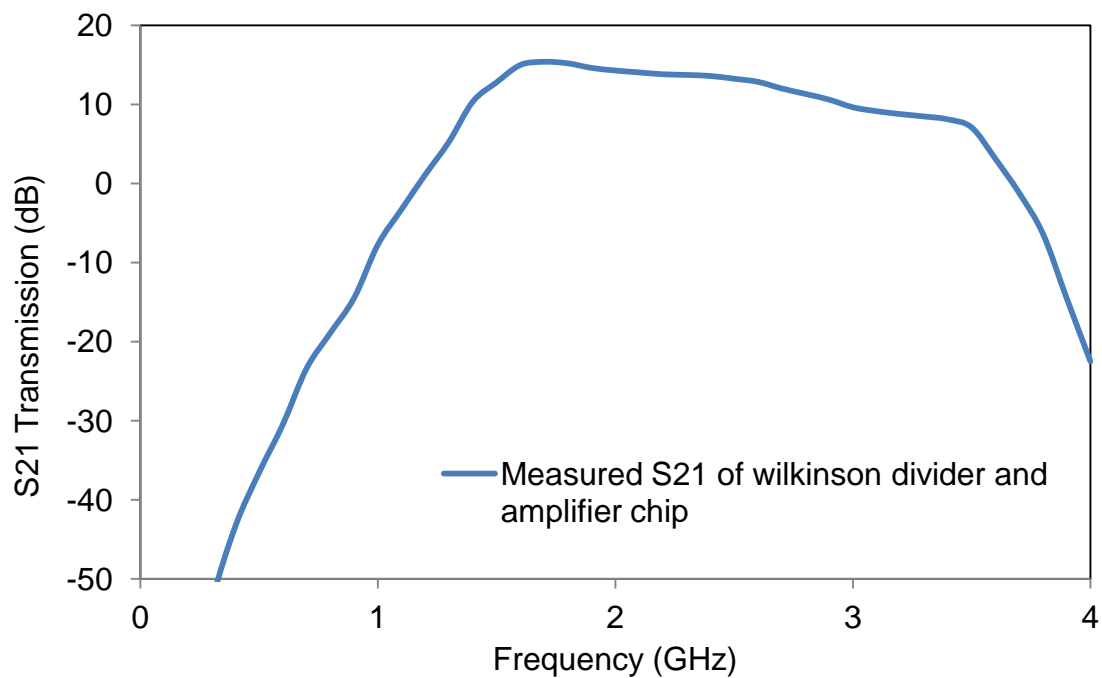


Figure 5.8: Measured transmission performance of Wilkinson divider and amplifier chip

5.4.3 Low Pass Filter

In order to reduce the harmonics generated by the signal generator and amplifier modules, a low pass Chebyshev filter was designed in AWR Microwave Office, Figure 5.9. A fifth order cascade filter with a 0.5dB pass band ripple was designed using segments of transmission line with differing widths. The cut-off frequency was designed to be 2.2GHz, frequencies above this value are reflected due to the change in impedance of the differing transmission line segments. Two such filters were used in series, Figure 5.10. This results in a reduction of second harmonic at 4GHz by 47dB, and third harmonic at 6GHz by 20dB. Insertion loss is 0.5dB at 2GHz. The filter wizard functionality was used to produce the low pass filter, however the response of the filter is more similar to a band stop filter – the pass band returns at 6.5GHz. This is a simple filter employing high and low line impedances to act as series inductors and shunt capacitors. The lines are designed to be $\lambda/4$ in length and hence the pass band returns at multiples of the design frequency.

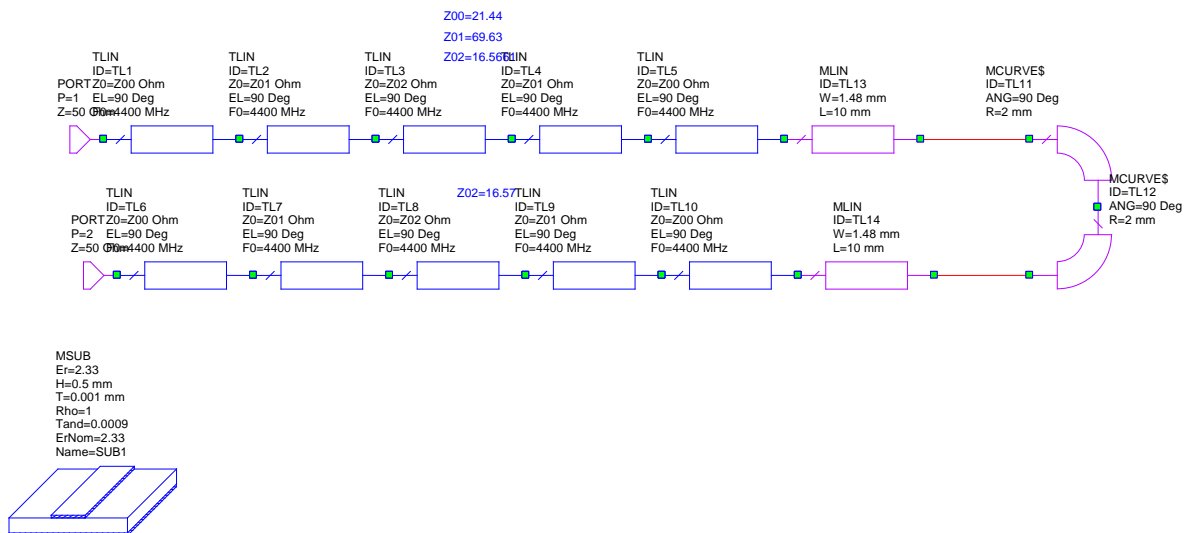


Figure 5.9: Cascaded low pass filter designed in Microwave Office

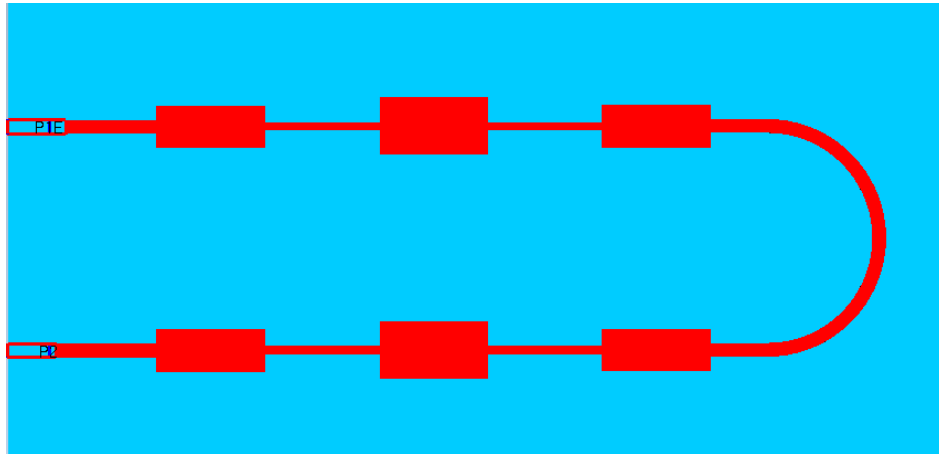


Figure 5.10: Layout of planar filter

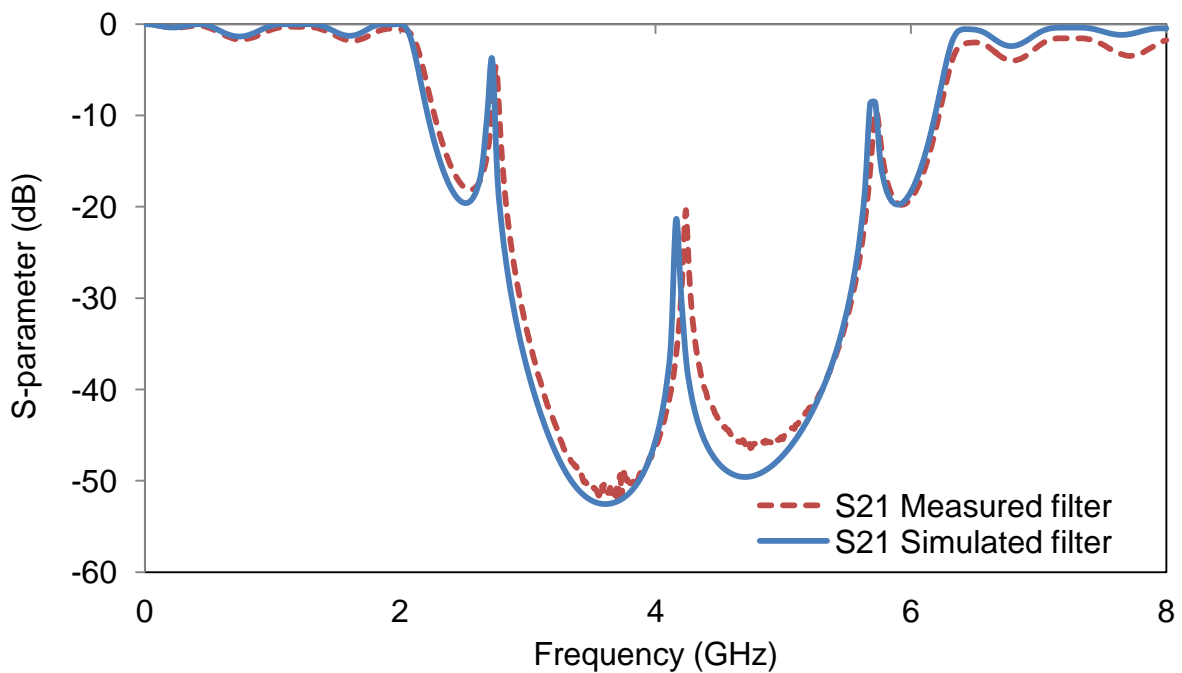


Figure 5.11: Simulated and measured transmission response of the low pass filter

5.4.4 Conditions and Limitations

To determine the effect of radiant flux on switch linearity, radiant flux is varied between 10mW and 200mW and applied for 5 minutes before taking measurements so as to limit the effects of laser source radiant flux fluctuations. Insertion loss measurements are taken first to ensure optimum positioning of the fibre optic cable followed by power in/out measurements at the fundamental and second and third

order harmonic readings. To ensure high accuracy, harmonic measurements are taken from the signal generator and both power amplifiers to eliminate their effects on results, for further measures taken to ensure accuracy, please refer to Table 5.2.

All measurements are taken at ambient temperature in a fan ventilated room, $\sim 23^{\circ}\text{C}$, with the switch located inside a laser safe structure. The third order intercept point is independent of frequency as well as capacitance value and so is suitable measure of linearity.

Error Source	Mitigation
Different calibration dates on measuring equipment	Equipment was tested under like circumstances and differences in readings were noted
The attenuation used of equipment to give most accurate results	At least 10dB attenuation can give improved results on Spectrum analyser
Cable loss in cables and microwave components	Cable loss was measured for all cables and components
Equipment being overdriven and producing their own harmonics	The input to test equipment was limited to 28.5dBm
The fluxuating intensity of laser light	Laser light was left on during the experiments to reach a constant level
The equipment and components heating up and giving different results	The amplifier equipment was given sufficient time to cool down between experiments – none the less this will still affect the results
Improper alignment of fibre optic	Output was measured by the spectrum analyser several times to ensure optimum alignment
Fluctuating output from power amplifier	This element is uncontrollable
Rogue harmonics of the signal generator / power amplifier	A filter was designed to cut out harmonics from the signal generator and amplifier

Table 5.2: Sources of error in measurement and steps taken to prevent their occurrence

5.5 Single Tone Linearity Measurements and Discussion

The single tone linearity is investigated for two different switch topologies. The first is the switch designed on Taconic TLY-5 substrate with a permittivity of 2.2 and thickness of 1.15mm. The second is the optimised transmission line topology, designed on Rogers R3003 which has been discussed in Chapter 3. A 2GHz signal is investigated with corresponding harmonics being generated at 4 and 6GHz.

5.5.1 Isolation and Insertion Loss

The switch topology designed on the TLY-5 substrate is presented in Figure 5.12. Isolation results in the switch OFF state are presented in Figure 5.13. Transmission results in the ON state are presented in Figure 5.14.

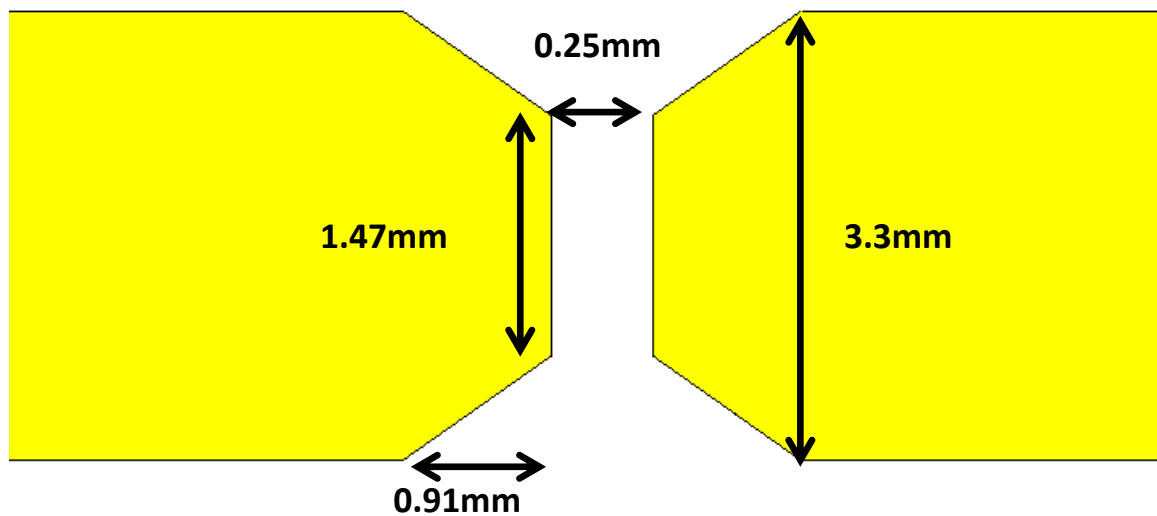


Figure 5.12: Switch topology on TLY-5 substrate (not to scale)

The isolation in the OFF state is measured at 15.5dB at 2GHz. The reflected signal, S_{11} in the off state is -0.19dB. The insertion loss whilst controlled by 200mW of radiant flux is 0.69dB. Only a small amount of power is dissipated, hence system efficiency is not compromised by the switch. As minimum power is dissipated in the switch, there is also reduced thermal contribution that could potentially raise the

temperature of the wireless system. S_{11} of the switch in the ON state is -20.2dB. As radiant flux decreases, insertion loss increases as demonstrated in Figure 5.14. At the minimum radiant flux of 10mW, insertion loss is 3dB; this supports work conducted by Panagamuwa *et al.* [6].

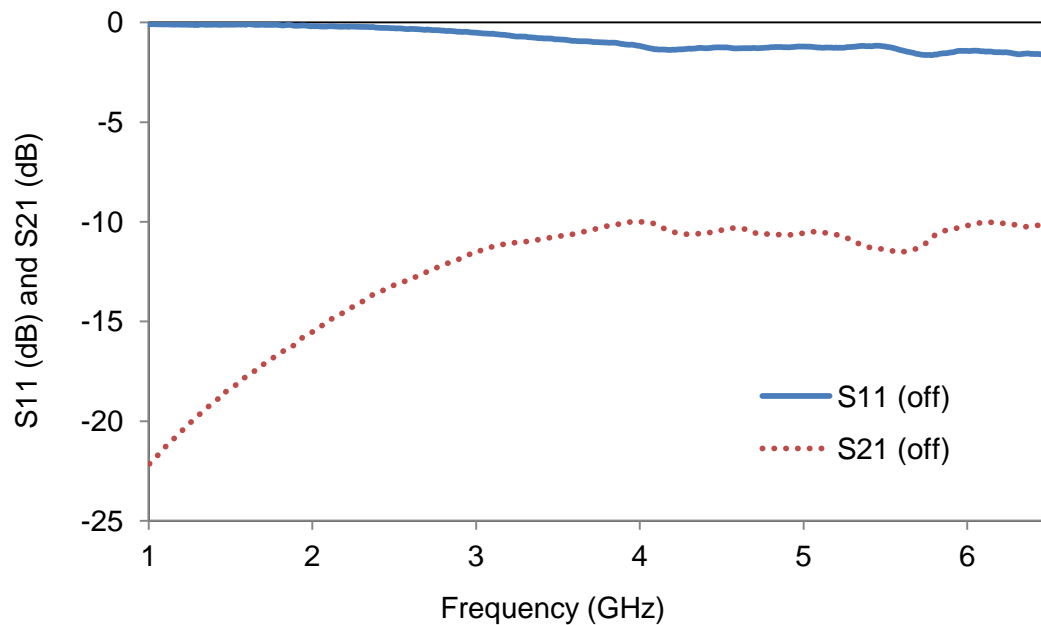


Figure 5.13: OFF state S-Parameter performance for TLY-5 substrate PCS

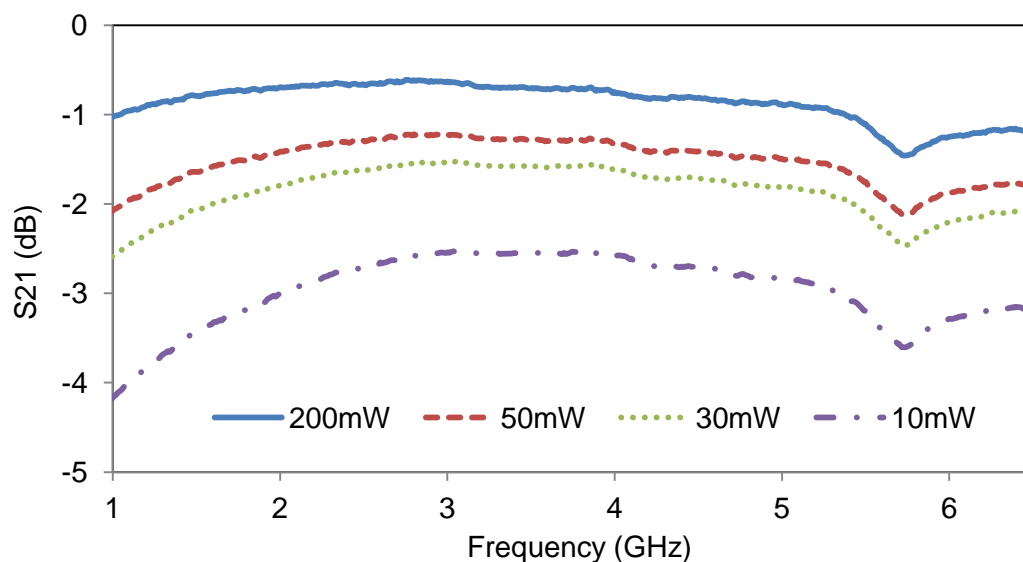


Figure 5.14: Various ON state S-Parameter performances for TLY-5 substrate PCS

5.5.2 The SOI / TOI Linearity

The fundamental output power versus input power is presented in Figure 5.15 for a radiant flux of 200mW. The switch remains linear over the full range of measurements and beyond 1W. In Figure 5.15, the second and third order harmonics are also displayed and have been extrapolated to provide the second and third intercept points, 63dBm and 70dBm respectively referenced to the switch's output power [27]. These measurements were taken with the switch under a radiant flux of 200mW, note that the insertion loss of the switch at the second harmonic frequency (4GHz) is 0.75dB and the corresponding insertion loss at the third harmonic frequency (6GHz) is 1.25dB, refer back to Figure 5.14.

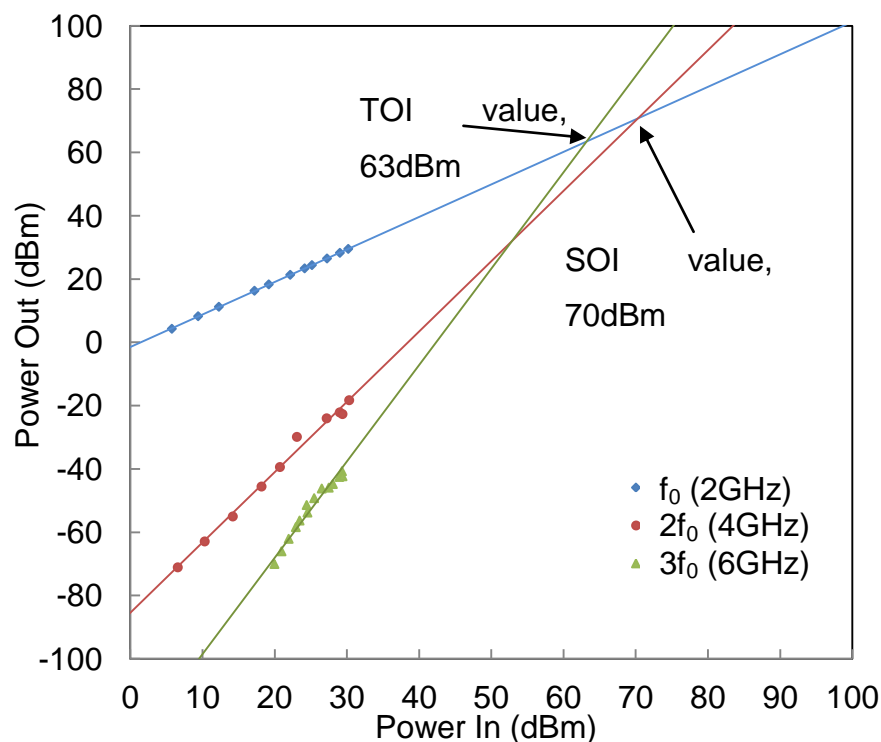


Figure 5.15: Extrapolated second and third order intercept result for a single tone linearity measurement. Silicon topology type 1 under 200mW of radiant flux.

Figure 5.16 presents varying TOI with respect to radiant flux. It can be observed that as illumination increases, linearity remains constant presenting the switch as a reliable mechanism for handling high power under any radiant flux above 10mW. Linearity is independent of the control method. This contrasts with other microwave switches where device resistance is dependent on current (pin diode) or voltage

(varactor diode) supplied to the switch – linearity of a pin diode, for example, can be improved by increasing the supply current [11]

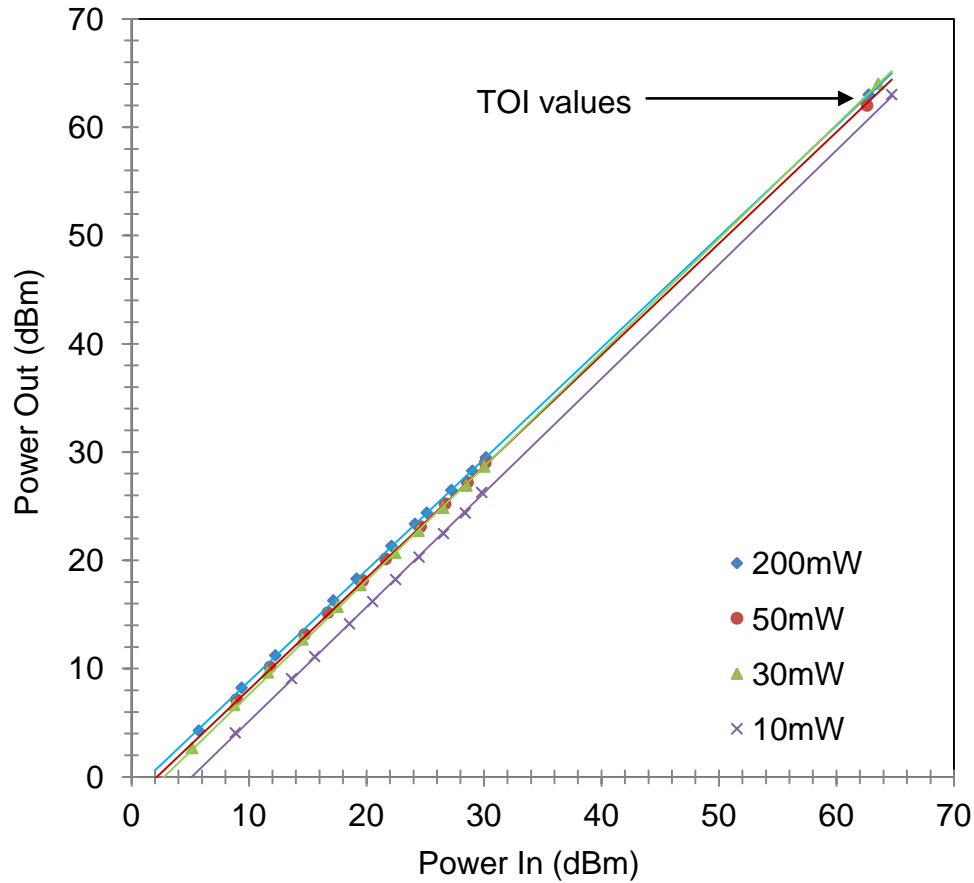


Figure 5.16: Extrapolated TOI values for differing illumination intensities (10, 30, 50 and 200mW of radiant flux)

The same single-tone measurement was performed on the optimised switch topology described in Chapter 3, Section 3.2. This has been optimised based on both transmission in the OFF and ON state. The transmission line has been tapered to better facilitate the coupling across the gap, where the silicon die dimensions are $1 \times 1 \times 0.3\text{mm}$, Figure 5.17.

For the maximum radiant flux of 200mW the value for TOI is 74dBm. The value for Second Order Intercept which has an expected slope gradient of two is 105dBm, Figure 5.18. These values indicate the switch is linear by nature.

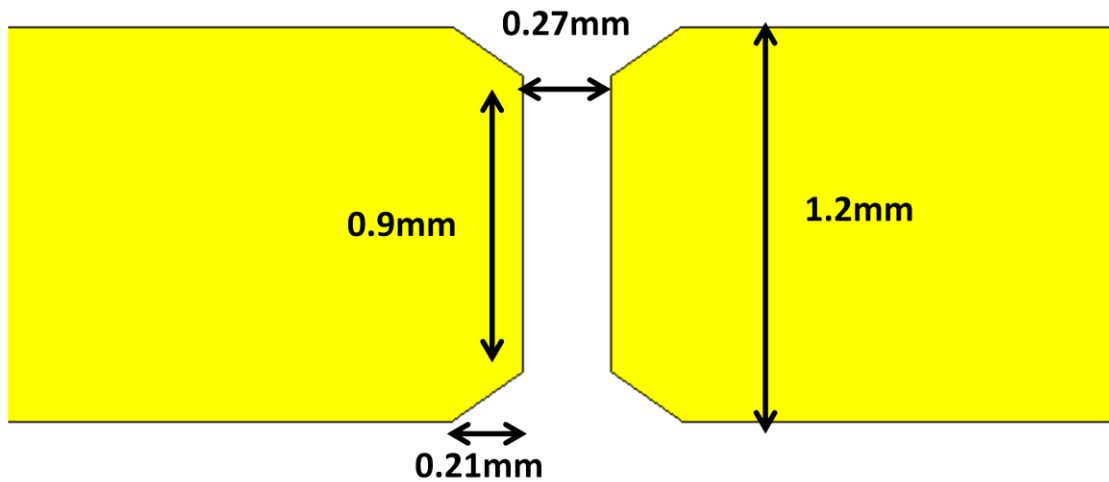


Figure 5.17: Switch topology on R3003 Substrate (0.53mm thick). The end of the transmission lines has been slightly chamfered to facilitate signal coupling into the silicon die – these values have been measured after fabrication

The optimised switch shows slightly better linearity performance than the original Taconic TLY-5 Switch, which could potentially be due to a number of reasons. Linearity is dependent on the interconnect method, which is not strictly regulated in the case of these photoconductive switches. The silver epoxy may contain traces of contaminants, or may contain differing quantities of conductive and adhesive, which would affect linearity performance.

The size of the silicon die also differs between the two photoconductive switches. This means the conductivity profiles of the two silicon die will differ. Potentially this change in conductivity could cause non-linear behaviour, and explain the difference in TOI and SOI values. None the less these switches indicate the region in which linearity falls for a typical photoconductive switch.

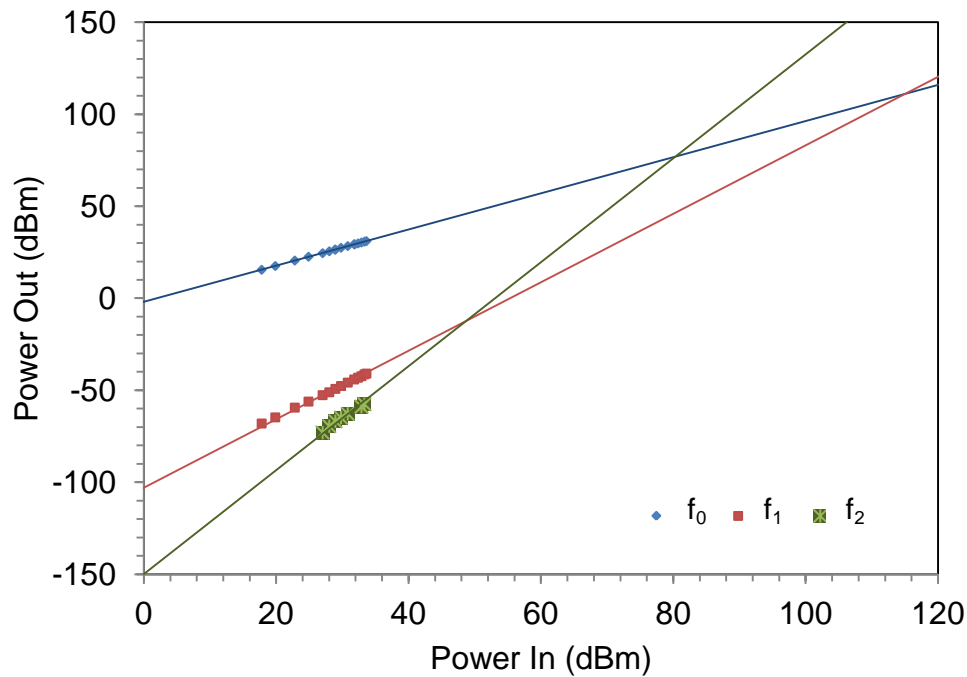


Figure 5.18: Extrapolated second and third order intercept result for a single tone linearity measurement. Optimised switch topology under 200mW of radiant flux

5.6 Two Tone Third Order Intermodulation Product

Typically, only a broadband system is susceptible to harmonic distortion, as single tone harmonics usually occur well away from the input frequency of the signal. When utilising the switch in a narrow band application, the intermodulation distortion is also of concern.

5.6.1 Two Tone Setup

The Rohde and Schwarz ZNB8 four port vector network analyser was used to perform the two-tone linearity characterisation. Two internal signal generators were used to generate the two tones based around a centre frequency of 2GHz and spaced 1MHz apart. The signals were combined using a power combiner and connected to the switch, as is shown in Figure 5.19 and Figure 5.20. A 20dB attenuator was placed on the input to the ZNB8 in order to reduce distortion at the receiver.

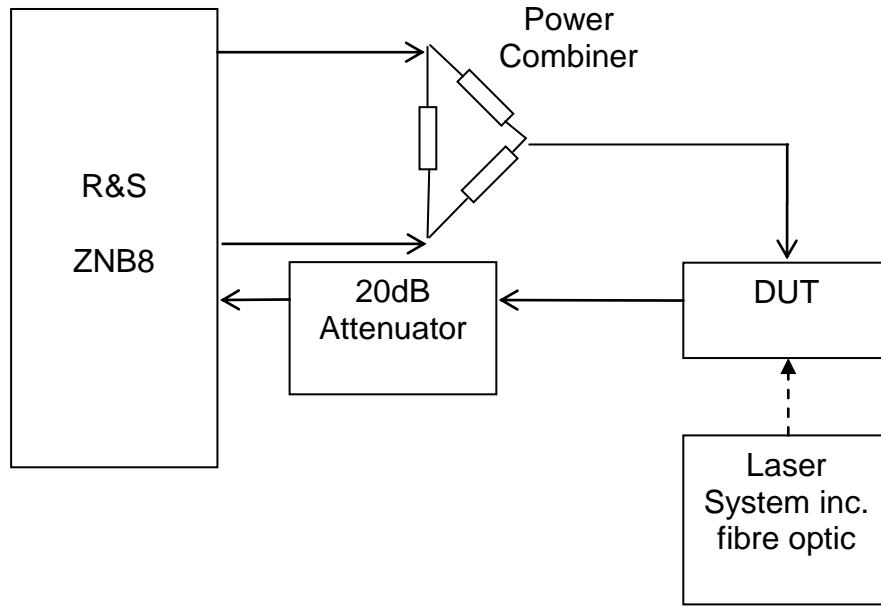


Figure 5.19 : Two-tone IM Distortion measurement platform

Power calibration of the system was performed in order to remove cable losses and effect of the attenuator on the results. The linearity of the test setup was calculated by placing a transmission line between the input and attenuator. Several readings were recorded for varying input powers to allow P_{in} against P_{out} to be plotted.

The linearity of the switch was then measured by replacing the transmission line with the switch. The silicon was illuminated with 50mW of radiant flux – as input power was varied the fundamental power output and intermodulation products appearing either side of the main tones were recorded.

The power was swept between 0 – 6dBm and the level of the intermodulation product was recorded at $2f_1 - f_2$ and $2f_2 - f_1$. f_1 refers to the frequency of the lower tone (1.9995GHz) and f_2 relates to the frequency of the upper tone (2.0005GHz).

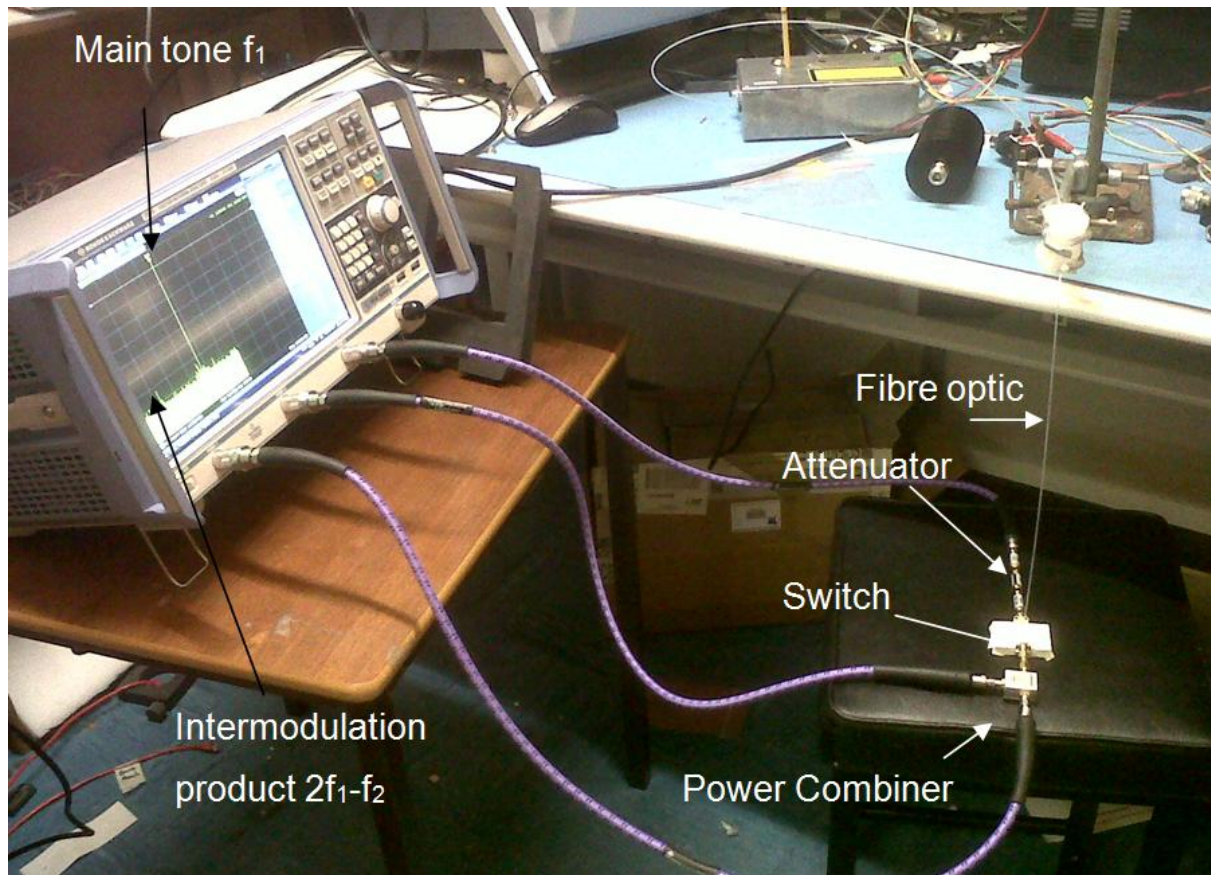


Figure 5.20: two-tone IM Distortion measurement setup in the process of capturing data. Equipment was setup to allow minimum noise floor

5.6.2 Two tone Results

In order to eliminate the test setup non-linearities, the transmission line output intermodulation products were subtracted from the switch intermodulation products, as it is assumed that a transmission line is a linear component which does not exhibit non-linear distortion. Similarly to the single tone harmonics, the measured intermodulation distortion is expected to increase at a gradient of three as input signal is increased by a factor of 1, Figure 5.21 and Figure 5.22. Results agree with the theoretical gradient of three, the graphs also present the line of best fit equation which confirms this. With an input of 6dBm, the third order intermodulation product occurs at -96dBm for the lower-tone, as seen in Figure 5.23. The extrapolated value of intercept point is $58\text{dBm} \pm 3\text{dBm}$. This is with reference to the input power. Distortion values for the upper tone were similar to the lower tone output as expected.

The lower tone distortion product was measured at 1.9985GHz, whereas the upper tone distortion product was measured at 2.0014GHz. Fundamental tone spacing is 1MHz.

The level of the intermodulation products (IP) is similar when 30, 50 and 200mW of radiant flux is applied. Although the general trend shows that when a higher radiant flux of 200mW is applied this produces slightly higher distortion, Figure 5.23. At 32dBm input power, the result for 200mW of radiant flux shows a corresponding intermodulation product at ~-86dBm, whereas for the 30mW of radiant flux the IP at 32dBm is ~ -97.5dBm. When 50mW of radiant flux is applied the intermodulation product is ~-100dBm when the input power is 32dBm.

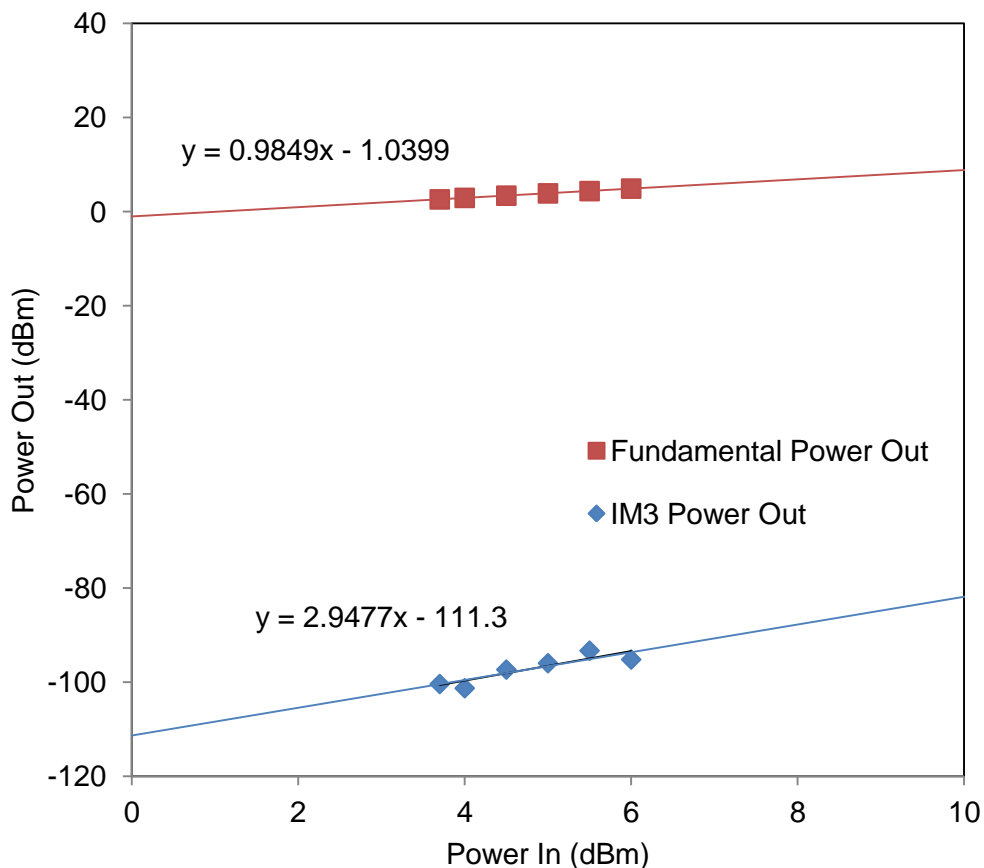


Figure 5.21: Two tone intermodulation results and fundamental input tone at 1.9995GHz

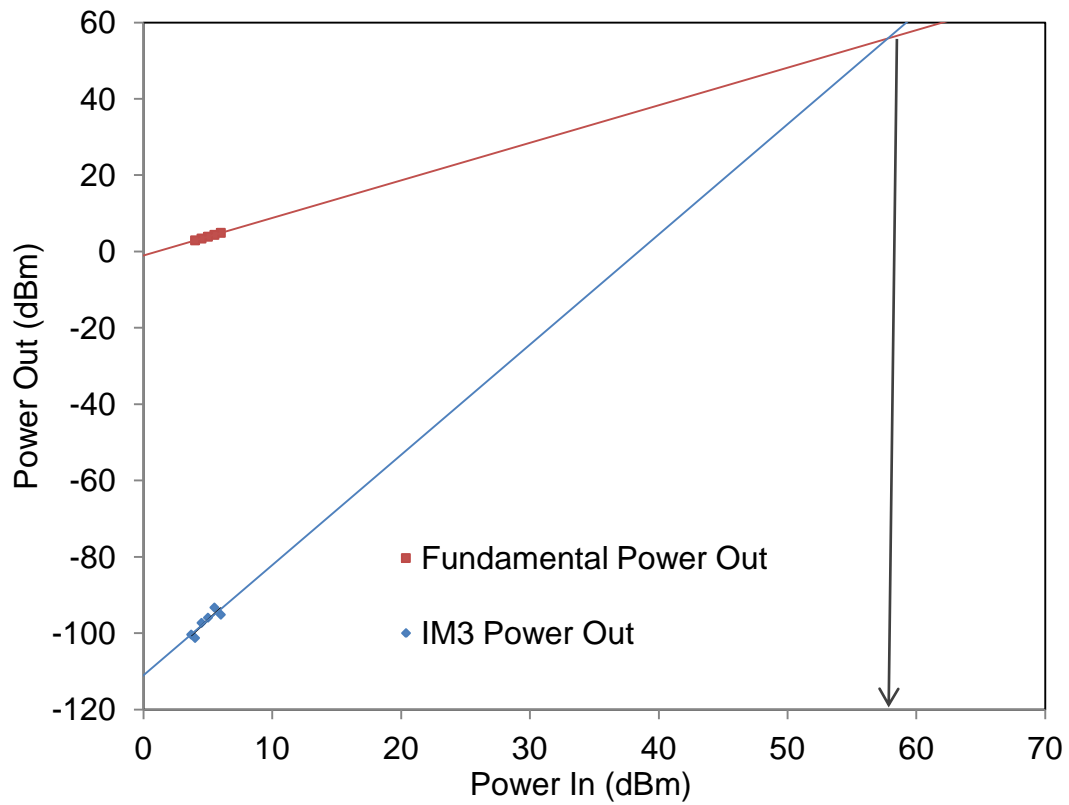


Figure 5.22: Extrapolated IP3 value from fundamental signal at 1.9995GHz and corresponding intermodulation distortion at 1.9985GHz

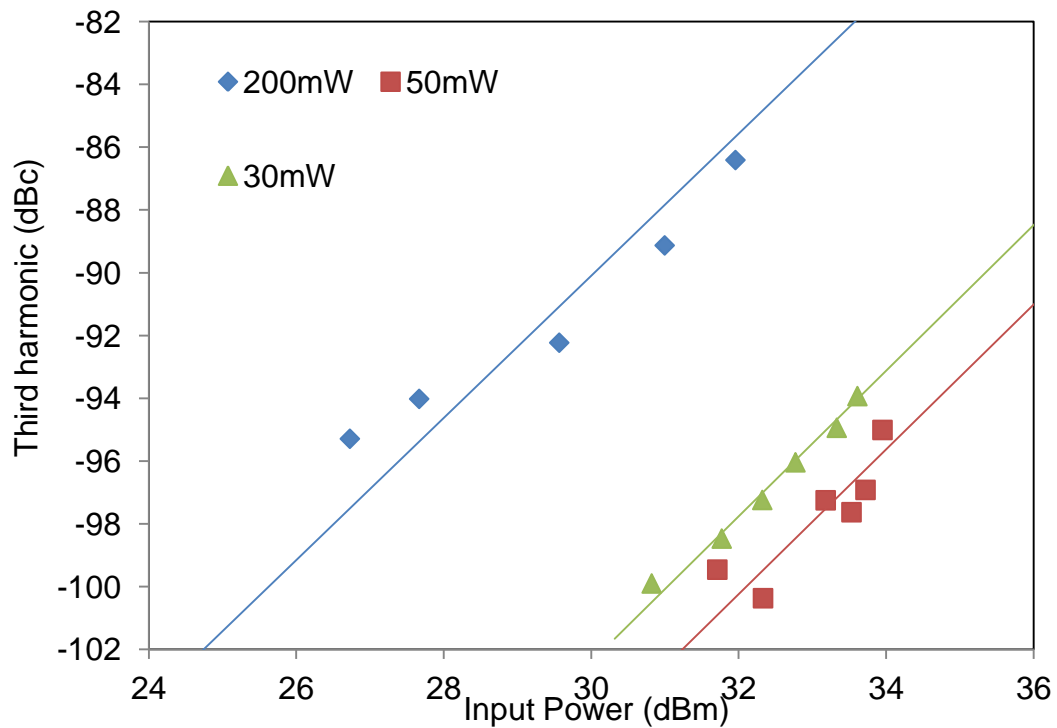


Figure 5.23: Third intermodulation products at 30, 50 and 200mW of radiant flux

5.6.3 Discussion on two-tone Intermodulation

Many types of RF switches exist and have been optimised for different purposes. Table 5.3 presents a general view of the types of commercial switches that are available and indicates their linearity performance for a basic comparison. In general, the photoconductive switch has better linearity values when compared to commercially available PIN switches.

Switch type	Insertion loss (dB)	Isolation (dB)	1dB compression (dBm)	IP3 (dBm)
MEMS[31]	0.17	23	40	>65
PIN diode [6]	1.4	35	33	46
PCS [28]	0.4	18	40	58

Table 5.3: Typical linearity and power handling results for various microwave switches

A possible reason as to why photoconductive switches create less distortion to the input signal is their structure. Generally non-linearity occurs in a component when there is a change in material. For example, the PIN diode contains a P and an N doped region, separated by an intrinsic region (un-doped). Here a junction exists where a change in doping of the material is apparent. The non-linear behaviour occurs at the junction in PIN diodes due to the change in impedance as the signal is propagating through the switch. More specifically, in a PIN diode, the impedance changing could be due to a number of factors such as forward biasing resistance or capacitance [15].

Ultimately, non-linearities can cause a change in the output signal's shape. Hence from a transient point of view, it is ideal if the PIN diode can retain its quiescent level of stored charge as the signal propagates through the switch. This leads to less change in the impedance of the diode. There are three factors which can affect this charge level and hence create distortion of the signal.

- The first is carrier lifetime – a longer carrier lifetime produces less distortion.
- The second is width of the intrinsic layer – thicker intrinsic layer increases the transmit time through the switch and hence improves the switch ability to hold charge.
- Lastly, purity also affects the distortion; if the silicon has fewer defects it will tend to produce less distortion.

Firstly, a PN junction does not exist in the type of photoconductive switch which is presented in this study, as the silicon consists of one type of near intrinsic silicon.

Secondly, it can be assumed that the same factors which affect a PIN diode's linearity will also have an effect on the photoconductive microwave switch. Hence, the carrier lifetime, the size of the intrinsic layer and the purity all affect distortion levels within the switch and how a signal propagates through the photoconductive silicon.

The carrier lifetime of the switch discussed in this work has been increased by using the float-zone method to grow the wafer. The high carrier lifetime of the silicon also improves distortion performance. For semiconductors with a larger carrier lifetime, the capacitance value within the device remains more constant and hence distortion is less prevalent.

The quasi-steady state photoconductance method was used to monitor the minority carrier lifetime in the un-diced silicon wafer used to produce the photoconductive switch. This value is measured as $\sim 600\mu\text{s}$, and directly affects the carrier concentration in the illuminated silicon. This initial value is just an indication of the actual carrier lifetime within the switch as when the silicon is diced, the damage caused will reduce the carrier lifetime. The silicon has been designed to have a high carrier lifetime to improve conductivity and has the added benefit of producing reduced distortion.

The large near intrinsic layer in the silicon means less quiescent charge is lost in the switch and hence non-linearity due to change in impedance is reduced. Typically for the switch the width of the switch is 1mm, which is much larger than the intrinsic (or depletion) layer within a PIN diode.

The introduction of doping atoms is intentional, but these atoms can act as defect sites as they are different in nature to the silicon atoms. The doping concentration for this photoconductive switch is relatively low; meaning the distortion within the switch can be kept to a minimum with regards to the presence of impurities.

Although fairly linear in nature, there is still a low level of third order intermodulation products which are produced. It is speculated that the cause of this distortion in the photoconductive switch may arise from the differing conductivity and permittivity profiles generated within the silicon when illuminated [29] and [30]. This difference in material properties could potentially cause impedance change in the switch, which has been identified as a cause for non-linearity.

The silicon dimensions have been matched to the fibre dimensions, hence a more uniform lateral conductivity profile is created across the length of the silicon. A higher wavelength of light also produces a more uniform conductivity profile throughout the depth of the silicon. This can be deduced from findings in Chapter 2 which indicate that lower wavelengths of illumination produce higher conductivity in the top few μm that are close to the surface of the silicon. Whereas the majority of the silicon die has low conductivity. Future work may involve the effect that conductivity profile has on the linearity performance of a photoconductive switch in order to verify this.

5.6.4 Two Tone Linearity using separate RF sources

An alternative experimental setup was also used to validate the linearity performance for the two tone intermodulation. The setup involved separate RF generators (HP83650L Series Swept CW Generator and a Marconi 10MHz – 20GHz microwave test set 6200) which output two tones separated by 1MHz, with a centre frequency of 2GHz. The measurement platform is outlined in Figure 5.24. In this case isolators and low pass filters are included to reduce effects of intermodulation products generated by the source.

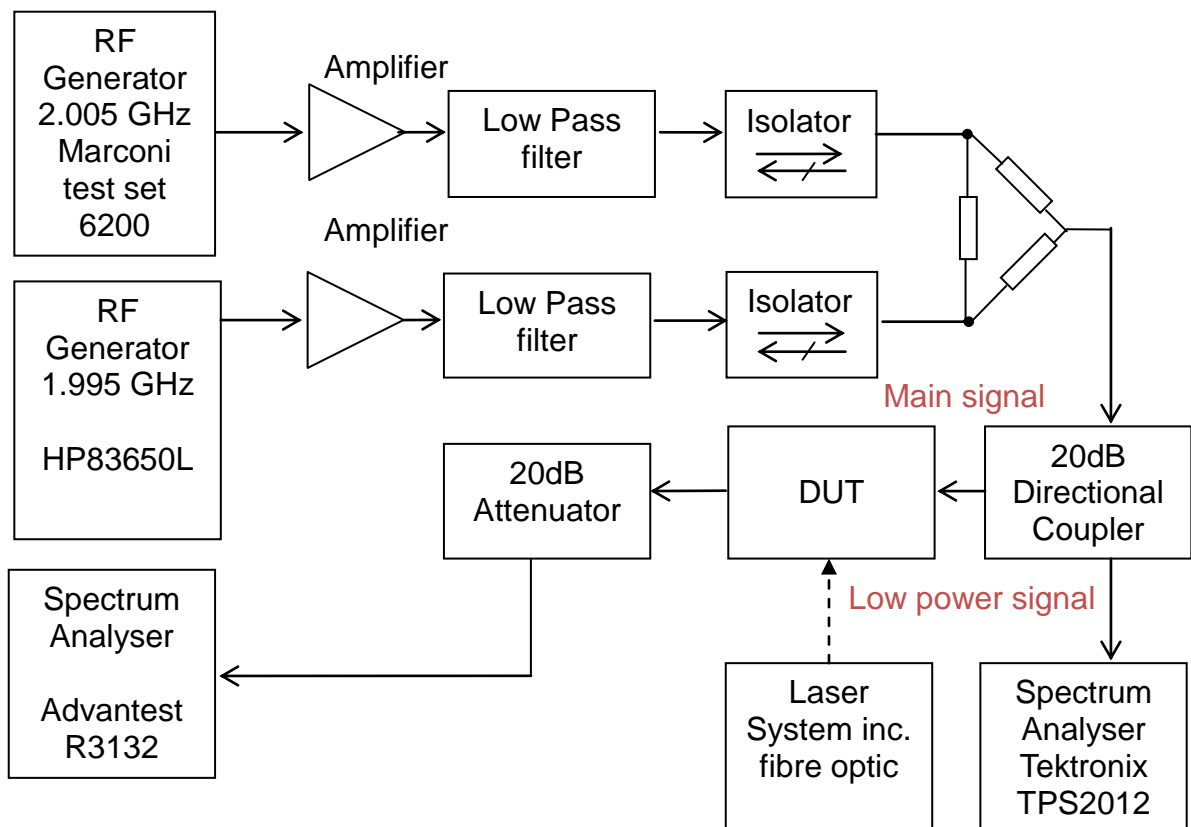


Figure 5.24: Measurement platform for two tone linearity using two separate sources

Results of the extrapolated intermodulation product are presented in Figure 5.25. In this case the extrapolated IP3 is 54dBm which is comparable to the IP3 of 58dBm extrapolated when using the ZNB VNA measurement in section 5.6.2. In this case it was necessary to make some correction to the output power measurements, as there is some non-linearity associated with the spectrum analyser.

In order to reduce the error, the linearity of a transmission line was first recorded using this test setup. Since a transmission line is linear, this result was subtracted from the measurement results obtained when the transmission line was replaced with a photoconductive switch, hence eliminating error due to the test equipment.

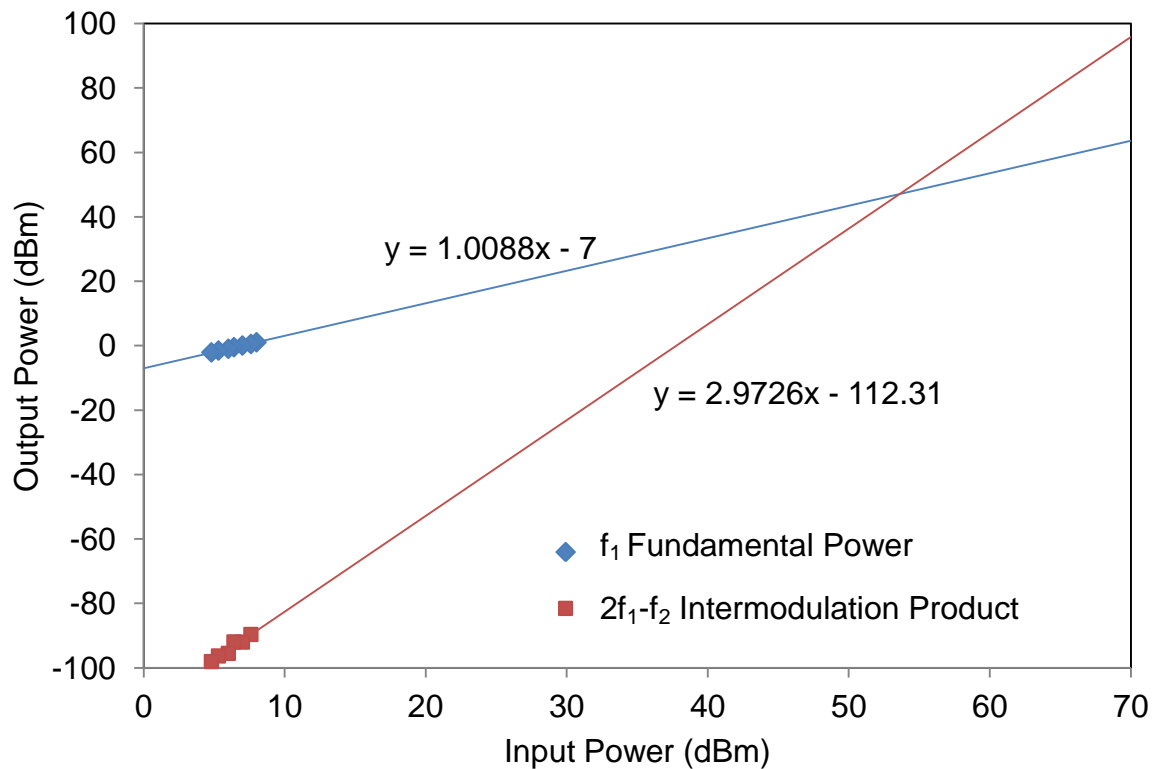


Figure 5.25: Extrapolated IP3 value for an alternative experimental setup involving separate sources. The graph also displays the equation for the line of best fit for the fundamental and third order intermodulation products.

5.7 1dB Compression Point

The output of linear devices is a fixed fraction of the input power. In the case of non-linear devices, such as amplifiers, mixers and switches, the output behaviour is more complex. Generally, these type of devices become more lossy as input power to the device is increased, which implies linear amplitude reduction. This response can be measured as the 1dB compression point.

The 1dB compression point is where the actual output signal of the switch is 1dB below the extrapolated small signal gain of the switch (e.g. the switch's linear response). Usually after this point the device is expected to saturate e.g. the output power starts to level off, and does not increase with increasing input power. In this region the device is totally non-linear in behaviour.

5.7.1 Experiment Setup for 1dB Testing

The 1dB compression point was measured using the Anritsu 37397D Lightning series VNA [31]. The measurement setup is shown in Figure 5.26. The VNA was set to maximum attenuation of 40dB and a 30dB attenuator was also used to ensure input to the equipment remained under 1W. A circulator was used to ensure any power that may be reflected from the switch or a short circuit does not flow back to

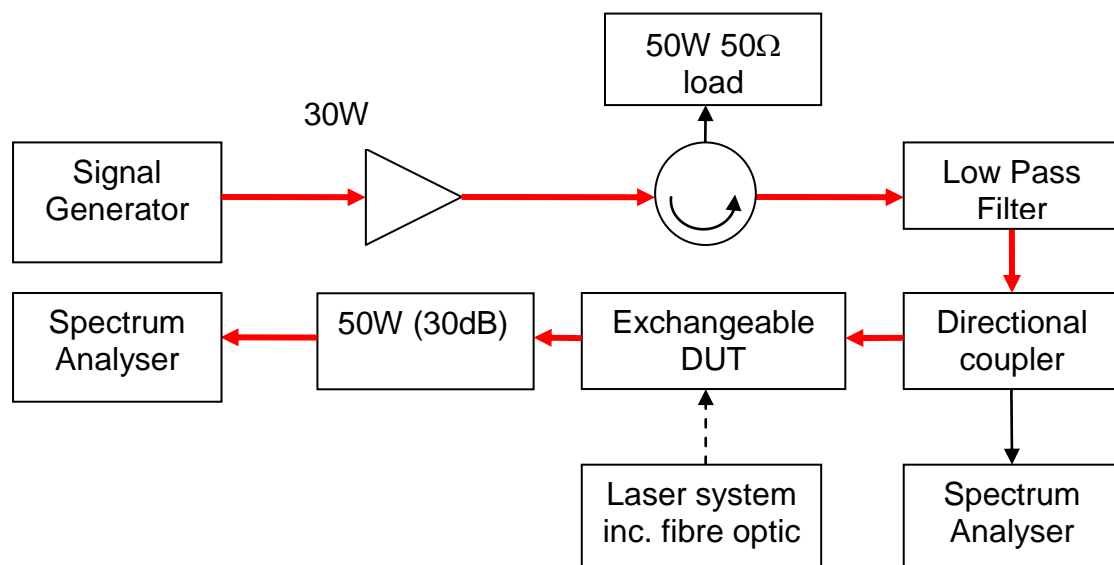


Figure 5.26: Measurement platform for 1dB compression and power handling test

the input of the VNA. The coupler and filter were also used as in previous measurement setups to increase accuracy.

The power in and power out behaviour of the system without a switch was first characterised, and then the same measurements were taken with the switch. To eliminate the effects of the amplifier switch results were subtracted from results taken from the system without the switch.

The RF input power to the switch was swept between -25dBm – 0dBm at 2GHz which is then fed into the amplifier. To turn the switch ON, 200mW of radiant flux was used to illuminate the switch.

5.7.2 1dB compression Results

Figure 5.27 shows the high power performance of the switch compared to the extrapolated small signal performance of the switch. A linear output power response is seen as input power is increased up to 31dBm. The loss in the switch starts to increase at this point. The 1dB compression point is where the actual output signal of the switch is 1dB below the extrapolated small signal gain of the switch. The 1 dB compression point occurs at 36dBm.

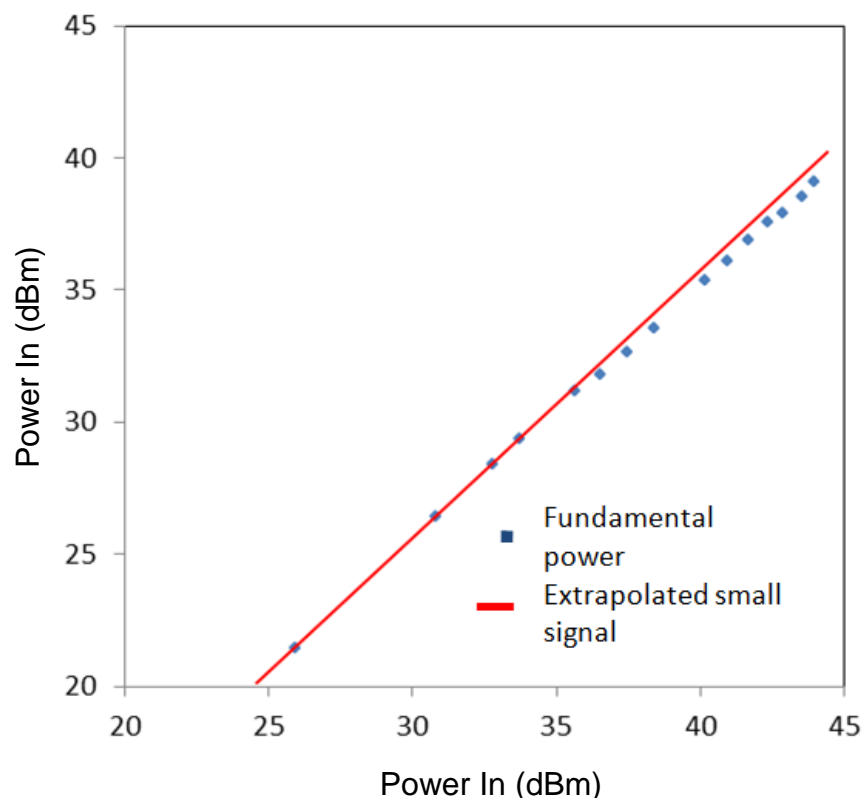


Figure 5.27: Power handling up to 44dBm. Fundamental power deviating away from small signal

There is no saturation of the switch up to the maximum power tested, 44dBm. However at 42dBm input power (15.8W) the gradient of the power out is no longer unity, a 1dB reduction in switch performance beyond this power level is evident when compared to small signal performance. It is expected that loss increases at these input powers as heating of the device and silver epoxy interconnect affects performance.

Through inspection of the switch the silver epoxy element appears to have degraded from the increases in heat. This reduction is likely the response to a build-up of heat in the silicon, silver epoxy and substrate, degrading switch performance. As the switch has no junction the linearity response is generally superior to PIN diodes. In this experiment the fibre optic was not in an optimised position to give maximum signal transmission, which explains the discrepancy between input power and output power. This is because in this experiment it was not possible to capture the S-Parameter performance directly in order to minimise insertion loss.

In the future, possible alternatives to the silver epoxy interconnect can be investigated such as wire bonding and surface mounting to the transmission line itself. These methods, particularly surface mounting reduce the resistance encountered by the RF signal as metal connections are more electrically and thermally conductive.

Passive intermodulation may also be the cause of non linearities observed here – this could be in the form of contaminated silver epoxy or a contaminated silicon surface.

5.8 Absolute Power Handling

Absolute power handling refers to the power the switch is able to handle before it becomes irrevocably damaged and unable to function in the way it is intended. Using the setup in Figure 5.26, the switch was tested up to 44dBm (25W), where failure occurred due to the silver loaded epoxy connection. Wireless systems that require long range communications could require high power output, particularly in a military application such as the software defined antenna [32] mentioned in Chapter 1.4.1 or an RF system installed at a base station. Build-up of heat in the switch damaged the silver epoxy and destroyed the switch. Thermal management methods such as careful placement of bond pads and heat sinks [33], could potentially improve the switch's absolute power handling.

Figure 5.28 shows the damage to the switch. Insertion loss increased by 17dB after switch failure, isolation also increased in the OFF state from 18dB to 21dB, indicating

that there may have been breakdown in the silver loaded epoxy bonding to the right side of the silicon, and hence reduced signal throughput.

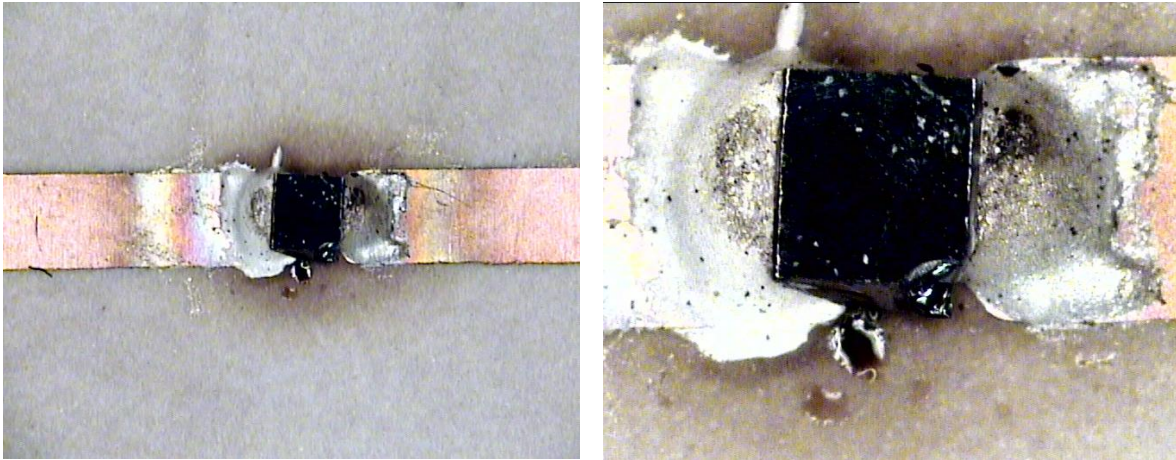


Figure 5.28: Power handling of the switch, visual results

5.9 Switch Rise and Fall Time

This study aims to evaluate the effect switch design and control conditions have on rise and fall time of the photoconductive switch. Better understanding in this area will allow the system designer to choose an appropriate photoconductive switch optimised for the characteristic of interest e.g. short switching time or low insertion loss. To this end, the transmission performance of the switch is also quoted alongside the switching time as there is some correlation between the two.

5.9.1 Review of Switching Times

Another figure of merit for microwave switches is time taken to turn OFF and ON. Certain applications such as microwave generation using gallium arsenide (GaAs) switches require switching speeds in the region of ps. For example, Frankel *et al.* [34] describe picoseconds switching as a way to apply large-signal nonlinear device characterisation with bandwidths in the hundreds of gigahertz. An application which requires slower switching in the nanosecond range is utilising the switch as a pumping source for electrical-discharge lasers [35].

There are applications for which fast switching is desirable, but not a necessity. For example, the reconfiguration mechanism should be fast for cognitive radio

applications in order to minimise downtime [36], however switching in the range of μs is acceptable.

There are a number of different parameters which affect the rise and fall time of a photoconductive switch [37]:

- Radiant flux and wavelength of the illumination source
- Switch geometry
- Contact type – capacitive, Schottky or ohmic
- Silicon treatment – doping and passivation

Karabegovic *et al.* [38] report on the impact of semiconductor dimensions and light intensity of the control illumination source on switching time for a GaAs switch used to generate 10GHz microwave signal. The width of the switch in this case dictates OFF switching speed as the electrons are swept out of the GaAs as opposed to allowing recombination to occur. Rise times of 4.8ps are achieved.

Flemish *et al.* [30] investigate the effect that contact type has on both transmission performance and switching speeds for an optically controlled attenuator [39]. A pulsed LED was used to control the switch, which is fabricated on silicon substrate. In this case, ohmic contacts produced faster switching time of 8-14 μs , however insertion loss and isolation were degraded when compared to capacitively coupled contacts. In this case, a minimum turn ON time of ~65 μs was observed.

Tawk *et al.* [40] discuss switching speeds for a phosphorous doped un-passivated silicon switch for use in cognitive radio. Switching times in the region of 8-20 μs are demonstrated at 8.4GHz under 50mW of radiant flux. The corresponding difference in return loss between ON and OFF state is 10dB. These switching speeds illustrate that photoconductive switches are a candidate for use in cognitive radio applications.

FET microwave switches exhibit fast switching speeds as the depletion layer can be modulated very rapidly by control voltage. Charge carriers must be conducted out of the intrinsic region and hence it is this depletion layer thickness which dictates switching speed. Consequently devices such as PIN diodes have larger intrinsic layers and are slower to switch [41]. Typical switching times are in the region of 10ns

in terms of rise and fall time of the switch and 100ns for the total switch ON time [42]. This corresponds to an insertion loss of 0.4dB and an isolation of 22dB at 2GHz.

Typical switching times for diodes are also in the nanosecond range. For example, the SKY12210 PIN diode has a switching time of 157ns, with a corresponding insertion loss of 0.4dB and isolation of 44dB at 2GHz [43].

The switching time of MEMS switches is slower than PIN and varactor diodes. Typical switching times for MEMS vary between 2-40us [44]. Switch time is generally longer as a mechanical movement of the switch lever (or membrane) is required for switch operation. Typically the membrane is connected via a folded spring, the force contained in the spring dictates the voltage needed to switch and also the switching time. Typical ON state insertion loss is 0.1dB and OFF state isolation is 55dB, at ~2GHz. Table 5.4 gives an overview of the different switching times of typical microwave switches.

Switch	Insertion loss	Isolation	Switching Time
Photoconductive Si substrate switch [39]	0.4dB	20 dB	~65us
Photoconductive Si die switch (unpassivated) [40]	5 dB	8 dB	~20us
FET Switch [42]	0.4 dB	22 dB	~100ns
PIN diode [43]	0.4 dB	44 dB	~150ns
MEMS switch [44]	0.1 dB	55 dB	~40us

Table 5.4: Comparison of switching times for various microwave switches

5.9.2 Influences of switching time of a photoconductive switch

The switching times of various photoconductive switches are investigated in this section. Different applications may require different levels of isolation and insertion loss. On the other hand, for certain applications this value may not be absolute – in that it is possible to accept a higher insertion loss to obtain a faster switching speed.

It is expected the amplitude of the transmitted signal in the ON and OFF states (hereafter referred to as the ON-OFF voltage) will have an effect on rise and fall times of the switch. An amplitude change from 5mV to 1mV will have a shorter switching time when compared to an amplitude change of 20mV to 1mV. So a switch which has a higher dynamic range, will naturally take longer to switch.

The primary aim of this study is to discuss the effects that radiant flux, geometry and fabrication techniques have on rise and fall times of a photoconductive switch. However consideration is also given to the effect that these criteria have on the ON-OFF voltage ratio, which also has a bearing on switching times. For a photoconductive switch this ratio is easily adjustable. To put into context why this is important, an amplitude change from OFF to ON state of 1mV to 5mV will naturally take a shorter period of time than a 1mV to 20mV amplitude change. Hence rise and fall time should always be noted alongside a switch's dynamic range i.e. difference in OFF state isolation and ON state transmission levels.

The time taken to switch ON is dependent on how fast electrons are promoted to the valence band. Since silicon is an indirect bandgap material this is dictated by the energy from incoming photons and the presence of phonons. After a certain period of illumination, steady state conductivity is reached within the silicon, which is dependent on size of the silicon die and the rate of recombination due to trap density. There are two main mechanisms controlling the time taken to switch off a photoconductive switch, recombination time of the carriers and sweep-out time due to electric field.

Recombination is dependent on the carrier lifetime of the silicon which is affected by silicon quality and the Auger recombination effect at high injection of carriers. Sweep out time is dependent on the length of the semiconductor that the carriers must traverse through and the mobility of the carrier which is affected by carrier concentration.

5.9.3 Experimental Switch Time Setup

Three types of silicon are presented in this work to investigate the effect doping and passivation has on rise and fall time of the switch. Each silicon die is mounted over

varying transmission line gap widths using silver loaded epoxy. The different switches along with radiant flux values are presented in Table 5.5:

Switch Name	Silicon dimension (mm)	Doping type (Resistivity)	Silicon Passivation - carrier lifetime (μ s)	Gap between lines (mm)	Radiant Flux (mW)
A	1×1×0.3	Phosphorous (10000 Ω /m)	600	0.27	55
B	1×1×0.3	Phosphorous (10000 Ω /m)	600	0.27	80
C	1×1×0.3	Phosphorous (10000 Ω /m)	600	1	55
D	1×1×0.3	Phosphorous (10000 Ω /m)	600	1	80
E	1×1×0.53	Boron (10000 Ω /m)	36	0.27	80
F	1×1×0.53	Boron (10000 Ω /m)	14	0.27	80

Table 5.5 Types of silicon switch and experimental setup. Variation includes carrier lifetime of the silicon, gap between the transmission line, illumination and ON and OFF state voltage for an input signal of 2GHz

The substrate is Rogers 3003, $\epsilon_r=3$, thickness = 0.53mm. The transmission line is designed to be matched to 50 Ω . An OSRAM near-IR LED [41] with a centre wavelength of 850nm is used to illuminate the die. The LED is pulsed with a 50:50 duty cycle at a frequency of 100kHz to promote conductivity within the die. Two different radiant flux values are applied, 55mW and 80mW.

The radiant flux is measured using a radiant flux meter. Optimum coupling between light source and die is not the focus of this paper, so the assumption is made that the same majority of light is coupled into the die for both the radiant flux values.

Rise and fall time is measured using a LeCroy Serial Data Analyser, SDA 18000, displaying both the triggering pulse and 2GHz signal envelope of the switch response. The experimental setup is detailed in Figure 5.29. The ON-OFF amplitude is used to defined the rise and fall time

The rise time is defined as the time taken for the ON-OFF amplitude to change from 10% of the total amplitude (ON voltage – OFF voltage) to 90% of its total amplitude.

The fall time is defined as the time taken for the total RF signal amplitude to change from 90% of its total amplitude value to 10% of this total amplitude.

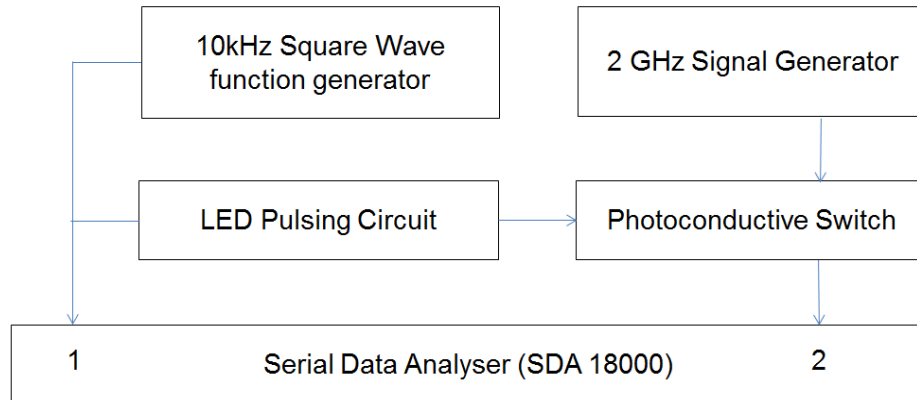


Figure 5.29: Experimental setup for measuring the rise and fall time of the photoconductive switch

5.9.4 S-Parameter Performance

For the present study, measured S21 results are presented for Switch A and B listed in Table 5.5. Both these switches have identical dimensions, doping and gaps in the transmission lines (0.27mm gap); only the radiant flux is changed. S21 result under pulsed LED operation is presented in Figure 5.30.

In the case of Switch A, using a radiant flux of 55mW, the S21 at 2GHz is -2.8dB. The corresponding S11 at 2GHz is -11.6dB. With regards to Switch B where an increased radiant flux of 80mW is used, the S21 in the ON state is improved to -1.8dB. S11 in this instance is -14.8dB. For both cases, the corresponding OFF state S21 is -18dB, and S11 is -0.19dB at 2GHz, Figure 5.31.

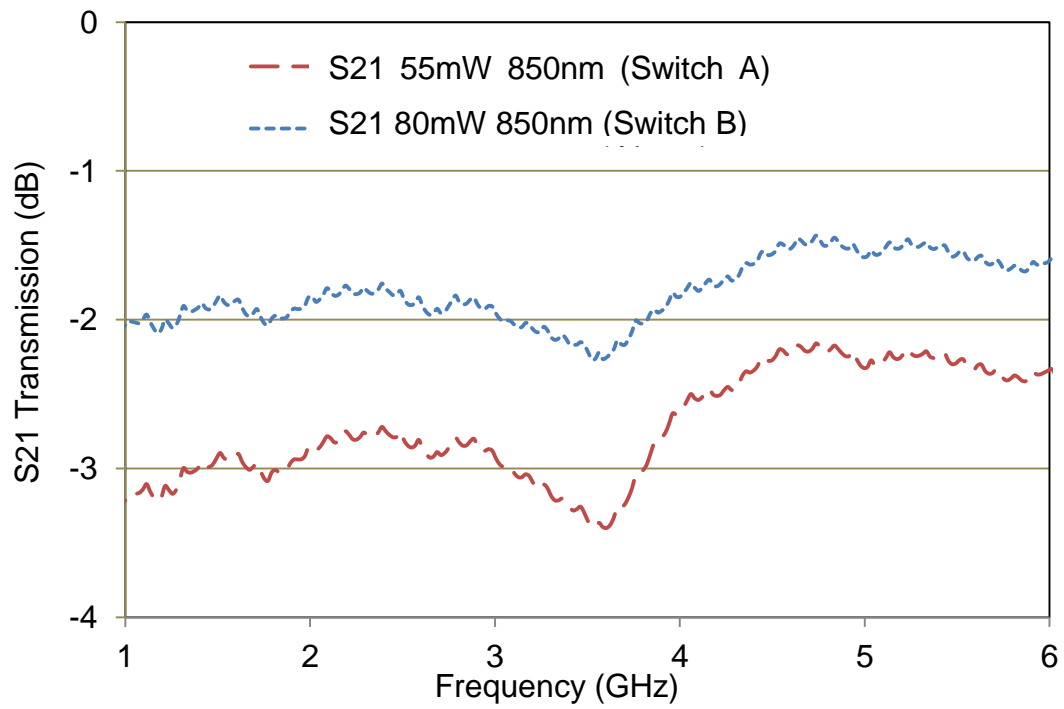


Figure 5.30: S-parameter performance of switch types A and B under 850nm LED illumination (10kHz pulse cycle)

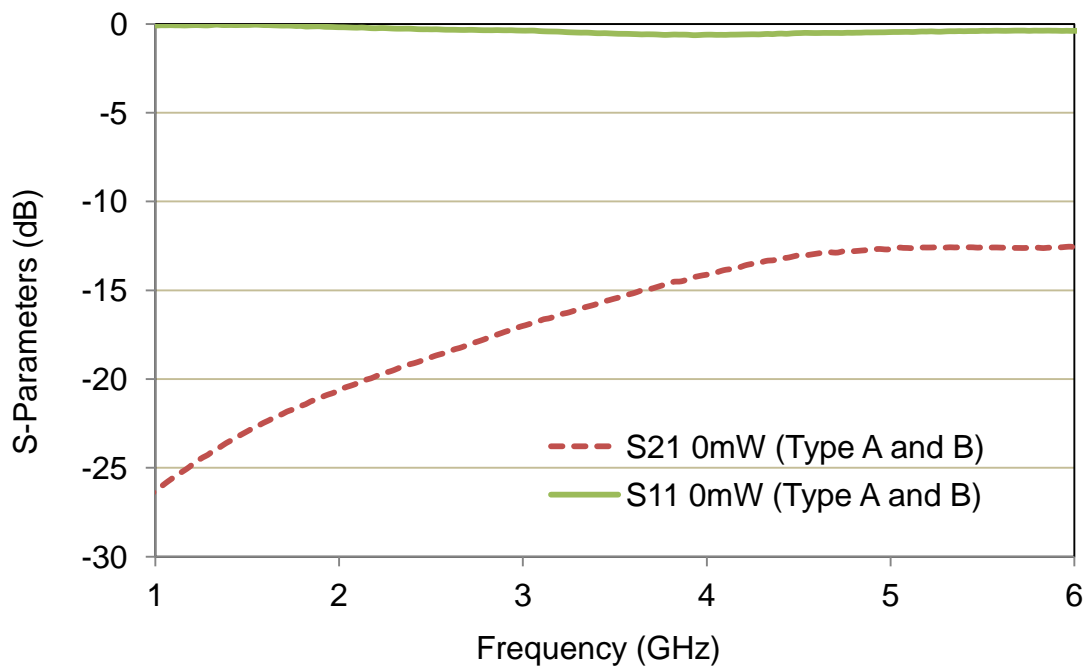


Figure 5.31: S-parameter performance of switch types A and B under 0mW of radiant flux

5.10 Switching Time Results

Rise and fall times were calculated for the six variations in silicon passivation quality, switch geometry and varying illumination intensities. The switching graphs for Switch A are presented in Figure 5.32 and Figure 5.33 which correlate to the S-parameter results presented in Figure 5.30 and Figure 5.31. In this case, rise time is measured to be $17\mu\text{s}$ and fall time is measured to be $76\mu\text{s}$. Further analysis of the other switches follows.

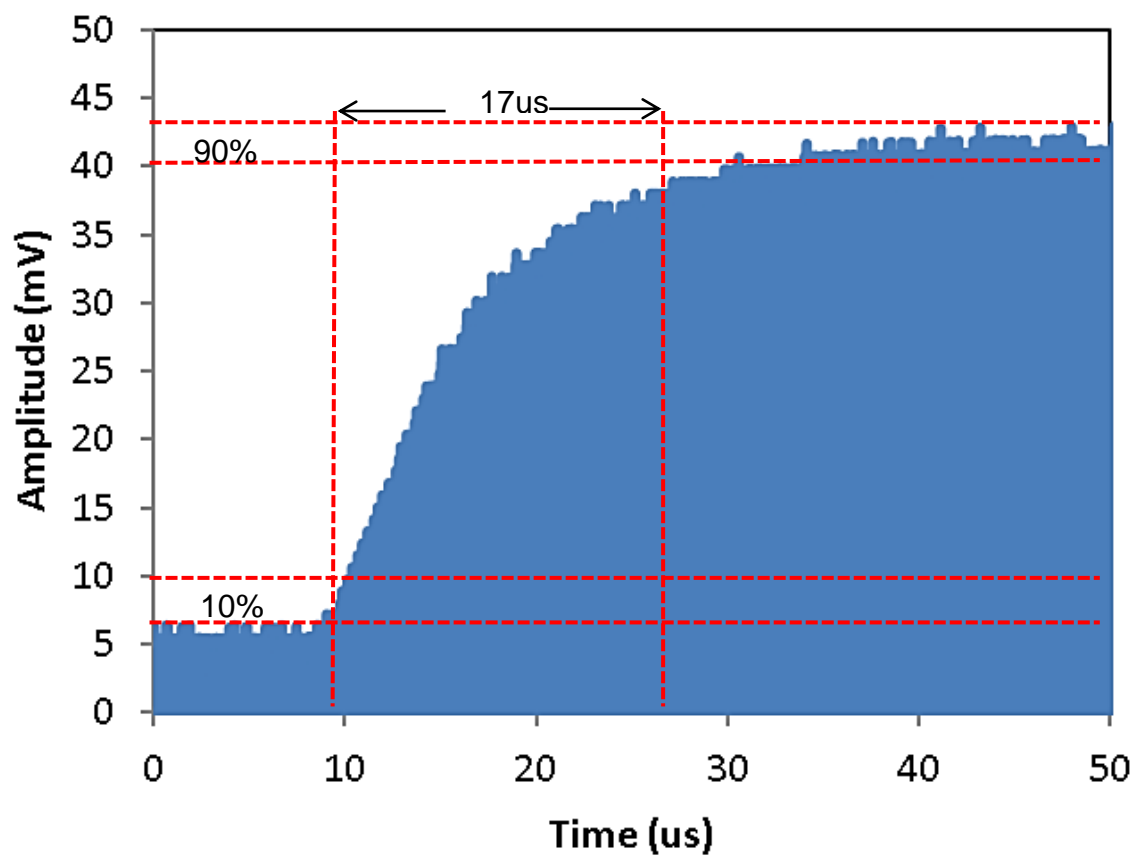


Figure 5.32: ON-OFF amplitude for a 2GHz signal passing through silicon type A (0.27mm gap, radiant flux is 55mW)

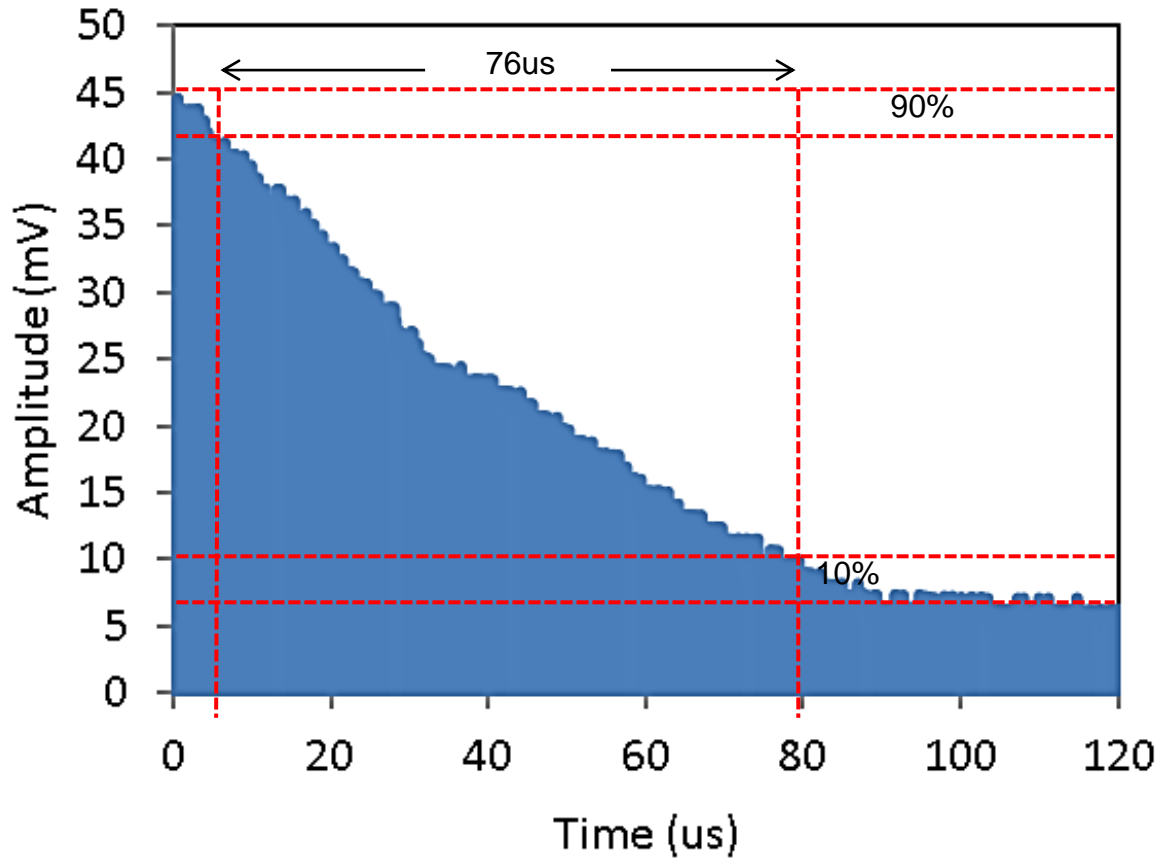


Figure 5.33: OFF-ON amplitude for a 2GHz signal passing through silicon type A (0.27mm gap, radiant flux of 55mW)

5.10.1 Switch dimensions and radiant flux

Optical radiant flux dictates the rate at which photons are injected into the silicon and has a direct effect on the number of free carriers generated in the silicon. Along with switch width, optical radiant flux controls the ON impedance of the switch. In this section switches A, B, C and D are investigated.

As shown in Figure 5.34, for the case of the 0.27mm gap geometry, when the 55mW of radiant flux is used (Switch A) a fall time of 76 μ s is observed. When the radiant flux is increased to 80mW (Switch B), the fall time is increased to 89 μ s. This is an increase of 17% in the switching time.

Note that when gap width is increased in the case of the 55mW of radiant flux (switches A and C) the fall time is reduced by 13 μ s (17%). For the case of the 80mW of radiant flux (switches B and D) the fall time is reduced by 20 μ s (22%).

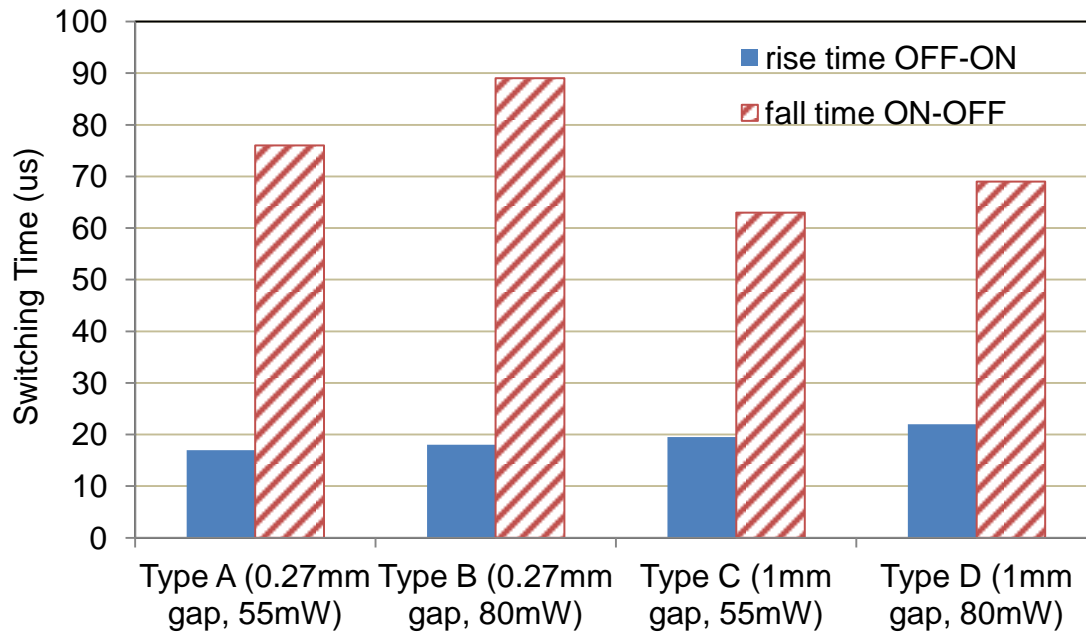


Figure 5.34: Rise and fall times for switches which have either a 0.27mm or 1mm gap. Two radiant flux values are investigated, 55mW and 80mW.

5.10.2 Passivation

In order to quantify the effect passivation has on switching time, three samples with varying degrees of passivation are investigated as described in Table 5.5.

In this section switch variations B, E and F are investigated. The level of passivation is quantified in terms of carrier lifetime. Measurements were taken using the Quasi-steady state photo conductance method. Quoted values are for wafer samples prior to dicing. It is expected the carrier lifetime will be reduced by the sawing process, however the initial carrier lifetime gives some indication of the quality of the silicon. The results for rise and fall times for each switch are presented in Figure 5.35. In this scenario, the silicon die is illuminated with a radiant flux of 80mW and the gap size is kept at 0.27mm.

The type of silicon used in Switch B has been processed to contain the least density of traps using a dry oxidisation process in order to form a layer of silicon oxide on the surface which both acts as passivation and an anti-reflection coating. It has a measured wafer carrier lifetime of 600 μ s. The corresponding measured fall time is 89 μ s.

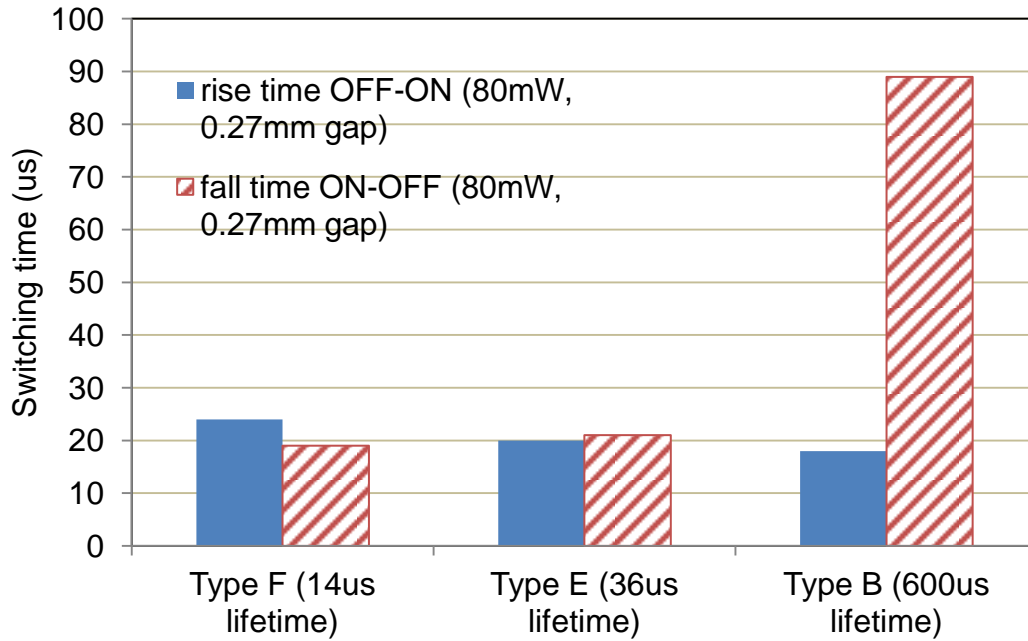


Figure 5.35: Rise and fall times for switches incorporating silicon which has been passivated in different ways and under radiant flux of 80mW.

The basic passivated silicon used in Switch E has undergone a less expensive, less rigorous passivation process when compared to Switch B. This process involves a mixture of wet and dry oxidation processes and has a measured carrier lifetime of 36 μ s and a fall time of 21 μ s. Switch F is made from unpassivated silicon (carrier lifetime 14 μ s) – there is a native oxide of ~2nm and has a fall time of 19 μ s. The reflectance and carrier lifetime description is listed in Chapter 4, section 4.3.1.

The fall time for the high carrier lifetime silicon (Switch B) is three times longer when compared with switches E and F. Since passivation improves the quality of the silicon by eliminating defects at the surface, the electrons and holes take longer to recombine, leading to a longer switch fall time. If the free carriers are not swept out of the system, then switch fall time is dictated by natural recombination. Also of particular note, is the voltage difference between ON and OFF state Δ voltage (ΔV), listed in Table 5.5. Generally, photoconductive switches which have a large difference between ON and OFF voltage will take longer to turn ON and OFF. This is because the number of free carriers is directly related to the ON voltage. The OFF voltage is only achieved once the majority of carriers have recombined.

This is why in the case of passivation, larger ΔV also results in a longer fall time of the switch. Hence a reduced fall time in the switch can be achieved by using silicon

which does not have a long carrier lifetime. The OFF time is more affected by the carrier lifetime than the ON time as carriers are generated faster than they recombine in high quality, passivated silicon.

Therefore, in contrast to the differing fall time for the passivated and non-passivated samples, the rise time for the three switches are relatively similar. They are 24 μs , 20 μs and 18 μs for Switch F, E and B respectively. In the case of rise time, as ΔV increases rise time reduces - the opposite to what is observed for the fall time.

The focus of this section is to concentrate on rise and fall time with regards to radiant flux, switch geometry and silicon quality. However all these switch types include differing ON and OFF state voltage levels. Hence the rate of change of voltage with respect to time ($\Delta V/\Delta t$) for the rising and falling edges may be a more suitable parameter for comparing different switch rise and fall times. This eliminates the effect that a large ΔV will have on switching rise and fall times.

5.10.3 ON-OFF State Voltage Difference

It is clear that the difference in transmitted RF signal amplitude between the ON and OFF state (referred to as $\Delta \text{voltage}$ or ΔV) has a large bearing on switching time. As is expected those switches with larger ON-OFF voltage differences have longer switch OFF times, however there is less variation in switch ON time. In order to study this further the rising and falling edge gradients for all six switch types have been calculated using the Eq. (5.2):

$$\text{Rising (falling) edge gradient} = \frac{\Delta \text{voltage}}{\text{Rise (fall) time}} \quad \text{Eq. (5.2)}$$

The results are shown in Table 5.5. The gradient of the rising and falling edges of each switch are independent of the ON-OFF voltage values. This makes it plainly clear that the dependence is also linked to other factors such as switch geometry, radiant flux and passivation quality.

First investigating the radiant flux aspect, in the case of the 0.27mm switch with 600 μs lifetime (switch A and B), there is a 14% increase in rising edge gradient between 55mW and 80mW of radiant flux.

Switch Name	Short Description *	ON voltage (mV)	OFF voltage (mV)	Δ voltage (mV)	Rise Time (μ s)	Fall Time (μ s)	Rising edge $\Delta V/\Delta t$ (V/ms)	Falling edge $\Delta V/\Delta t$ (V/ms)
A	0.27mm gap 55mW, 600us	42	6	36	17	76	2.12	0.47
B	0.27mm gap 80mW, 600us	50	6	44	18	89	2.44	0.49
C	1mm gap 55mW, 600us	32	5	27	19.5	63	1.38	0.43
D	1mm gap 80mW, 600us	43	5	38	22	69	1.73	0.55
E	0.27mm gap 80mW, 36us	29	7	22	20	21	1.1	0.1
F	0.27mm gap 80mW, 14us	17	6.5	10.5	24	19	0.44	0.55

Table 5.5: Rising and falling times along with ON-OFF voltage values. Rising and falling speeds are presented by taking into account the voltage difference

For switch C and D, the 1mm geometry switch, the corresponding increase is 20%. Increase in radiant flux leads to a steeper rising edge gradient. Increasing the radiant flux increases the rate at which photons enter the silicon. This corresponds to faster generation of free electrons, which is finally observed as a decrease in the rise time.

In terms of geometry of the gap, the gradient of the line decreases as gap width increases. Comparing switch type A and C there is a 35% reduction in the rising edge gradient. For the higher radiant flux of 80mW the difference in rising edge gradient of switch type B and D is 29%. Maximum coupling between the transmission line and the silicon die is achieved faster for the smaller gap geometry. This is likely because the free electrons created in the silicon diffuse within the die. More of the bottom surface of the die is in contact with the transmission lines in the 0.27mm gap geometry (switches A and B), hence rising edge gradient is increased.

For the three different carrier lifetimes of silicon, there is also marked variation in the rising edge gradient. For the highest carrier lifetime of 600 μ s (switch B) the gradient is 2.44V/ms. For switch E which corresponds to the carrier lifetime of 36 μ s the rising edge gradient is 1.1V/ms. Switch F (lifetime of 14 μ s) exhibits a rising edge gradient of just 0.44V/ms.

As the silicon carrier lifetime increases, the gradient of the rising edge also increases –switch rise time is reduced. The probable cause relates to the fact that trap density is reduced in samples A and B due to high quality passivation. Hence, recombination of carriers in the silicon due to the Shockley-Read-Hall recombination mechanism is less likely to occur.

Falling edge gradient is similar for all the switches if the result for switch E is disregarded. This suggests that the fall time is largely dictated by the difference in voltage between OFF and ON state, and not the geometry or the radiant flux applied to the switch. Once illumination is removed, the radiant flux value has no effect on the rate of recombination. Hence rate of change of voltage for the falling edge does not vary between switches to such an extent as for the rising edge.

5.10.4 Discussion on switching times

Generally, applying a higher radiant flux results in a steeper rising edge gradient. It also has the effect of increasing switch transmission. The higher ON-OFF ratio created by this scenario means fall time increases.

The use of passivation reduces rise time of the switch. However silicon which has an increased carrier lifetime due to the passivation process has a corresponding higher transmission and longer switch fall time. Increasing the transmission line gap width increases the rise time of the switch, correspondingly the fall time of the switch is reduced.

Should fast switching speeds be required for a particular application the choice of fabrication method and geometry of the switch design should be considered. For such switching time critical applications, it has also been demonstrated that the designer should implement the minimum ON-OFF transmission needed to ensure the fastest possible switching speeds.

In contrast to photoconductive switches, PIN diodes and MEMS switches generally do not have the ability to control the ON voltage, or transmission, in the ON state. Hence photoconductive switches are highly configurable in terms of controlling both transmission and switching speed – both of which are application dependent.

5.11 Conclusions

The linearity in terms of harmonics generated by single tone inputs, and intermodulation generated by two-tone input has been presented. The third order intercept for a single tone, 2GHz input is extrapolated to be 74dBm. Corresponding second order intercept is 105dBm. These results indicate the switch is highly linear in nature. In terms of two tone input, an intermodulation product intercept is extrapolated to be 58dBm \pm 3dBm. Nevertheless, this is more linear than many junction based PIN or varactor diodes. Non-linearities may be caused by the silicon-passivation junction that the signal must couple over in the switch. There are also dissimilar materials such as the epoxy interconnect which may have non-linear characteristics.

The power handling has also been reported. The 1dB compression point of the switch is demonstrated to be in the region of 42dBm input power. The switch experienced non-reversible damage at an input of 44dBm. Other microwave switches such as MEMS switches cannot handle high powers, due to self actuation. There is the potential to increase the power handling by investigating thermal management measurements in order to remove heat from the switch more efficiently.

Lastly, the switch rise and fall time is presented for different topologies and fabrication processes of the photoconductive switch. The rise and fall time has been presented for six different variations of a photoconductive switch for an input RF signal of 2GHz. The effect of illumination in terms of radiant flux applied has been reported for the switch incorporating silicon which has a high level of passivation. For silicon with 600 μ s carrier lifetime the fall time is 89 μ s. This compares to a fall time of 21 μ s for a non passivated switch with carrier lifetime of 14 μ s. Generally, the limiting factor on switching time is the turn OFF time. This is because the carriers recombine naturally, and for high carrier lifetime silicon materials, there are less defect sites for recombination to occur. The effect of gap width and passivation is also considered. Generally, applying a higher radiant flux results in a steeper rising edge gradient. It also has the effect of increasing switch transmission. The higher OFF-ON ratio created by this scenario means fall time increases

5.12 References

- [1] Y. Tawk, A. R. Albrecht, S. Hemmady, G. Balakrishnan and C. G. Christodoulou, "Optically Pumped Frequency Reconfigurable Antenna Design", IEEE Antennas and Wireless Propagation Letters, vol. 9, pp. 280-283
- [2] Y. Kaneko, T. Takenaka, T.S. Low, Y. Kondoh, D.E. Mars, D. Cook and M. Saito, "Microwave switch: LAMPS (light activated microwave photoconductive switch)," IEEE Electronic Letters, June 2003.
- [3] R. Rice, "Intermodulation Distortion in RF Connectors," available online <http://www.rfp2.com/pdf/tech-wp-Intermodulation.pdf> website last accessed Nov. 2012
- [4] Anritsu "Amplifier Testing with the 37300C VNA" Application Note <http://www.us.anritsu.com>, last accessed Aug. 2010, published 2003
- [5] M. Schetzmen, "The Volterra and Winner Theories on Nonlinear Systems," Wiley, New York, 1st Ed., 1980.
- [6] S. A. Maas, "Nonlinear microwave and RF circuits," Artech House, 1st Ed., 2003.
- [7] C. Lugo Jr. and J. Papapolymerou, "Electronic switchable bandpass filter using PIN diodes for wireless low cost system-on-a-package applications," IEEE Proceedings Microwave Antennas Propagation, Vol. 151, No. 6, December 2004
- [8] C. Huang et al., "Ultra linear low-loss varactor diode configurations for adaptive RF systems," IEEE transactions on microwave theory and techniques, Vol. 57, No. 1, January 2009.
- [9] E. R. Brown, "RF-MEMS switches for reconfigurable integrated circuits," IEEE Transactions on microwave theory and techniques, Vol. 46, No. 11, November 1998
- [10] K. Buisman, C. Huang, A. Akhnoukh, M. Marchetti, L.C.N de Vreede, L.E. Larson and L.K. Nanver, "Varactor topologies for RF adaptivity with improved

- power handling and linearity,” IEEE/MTT-S International Microwave Symposium, pp. 319 - 322 , June 2007.
- [11] C. L Lim, “PIN diode switches for high-linearity applications,” in EE Times-India, November 2008.
 - [12] S. Yong, “Design and analysis of pattern null reconfigurable antennas,” Ph.D. dissertation, Dept. Elect. and Comp. Eng., Illinois Univ., Urbana-Champaign, IL, 2012.
 - [13] C. Kalialakis and P. S. Hall, “Analysis and experiment on harmonic radiation and frequency tuning of varactor-loaded microstrip antennas,” IET Microw. Ant. and Prop., vol. 1, no. 2, pp. 527-535, 2007.
 - [14] Hewlett Packard “Applications of PIN Diodes” Application note 922, Nov. 1999.
 - [15] Infineon datasheet “Silicon PIN Diode bar 64” available online <http://www.infineon.com>, published June 2013, last accessed April 2014.
 - [16] Radant MEMS “RMSW100HP High Power MEMS,” available online www.radant.com, last accessed October 2012
 - [17] G. Crusats, L. Jofre, and N. Biyikli, “RF MEMS Integrated Frequency Reconfigurable Annular Slot Antenna,” IEEE Trans. Antennas Propagat. Vol. 58, No. 3, pp. 626-632, March 2010
 - [18] J. DeNatale, “RF MEMS Circuits: Applications of MEMS switch and tunable capacitor,” Rockwell Scientific, June 2004, available online <http://www.iversensor.org>, last accessed June 2010
 - [19] Y. Zhu and H. D. Espinosa, “Reliability of capacitive RF MEMS switches at high and low temperatures” Wiley Periodicals, pp. 317-328, 2004
 - [20] C. D. Patel, and G. M. Rebeiz, “An RF-MEMS switch for high-power applications,” IEEE MTT-S Int. Microwave Symposium Digest (MTT), 2012

- [21] K. Persson and K. Boustedt, "Fundamental requirements on MEMS packaging and reliability" Proc. On 8th International Symposium on Advanced Packaging Materials, pp 1-7, March 2002
- [22] D. Baek and Y. Kim, "Symmetric Microstrip interdigital capacitor-compensated high directivity directional-coupler," Microwave and optical technology letters, Vol 50, No 11, November 2008
- [23] AWR Microwave Office version 9, <http://www.awrcorp.com>
- [24] IMST EMPIRE XCcel version 5.3, <http://www.empire.de/>
- [25] D. Pozar "Microwave Engineering", Third Edition, John Wiley and Sons, pp. 318, 2005
- [26] C. J. Panagamuwa, A. Chauraya and J.C. Vardaxoglou, "Frequency and beam reconfigurable antenna using photoconducting switches" IEEE Trans. Antennas Propagat., vol. 54, no.2, pp. 449-454, 2006.
- [27] E. K. Kowalczyk, C. J. Panagamuwa, R. D. Seager, and J. C. Vardaxoglou, "Characterising the linearity of an optically controlled photoconductive microwave switch," IEEE Loughborough Antennas and Propagation Conference (LAPC), 2010
- [28] E. K. Kowalczyk, C. J. Panagamuwa, R. D. Seager, "Intermodulation Distortion in a Photoconductive Microwave Switch," Unpublished journal
- [29] W. Platte "Effective photoconductivity and plasma depth in optically quasi-CW controlled microwave switching devices" IEE Proceedings J, Optoelectronics, Vol.135, Issue 3, pp. 251 – 254, June 1988
- [30] C. Lee, P. Mak, A. Defonzo "Optical control of millimeter-wave propagation in dielectric waveguides," IEEE Journal of Quantum Electronics, Vol. 16, Issue 3, pp.277-288, March 1980, Vol. 14, No. 18, August 1978
- [31] Anritsu "Amplifier Testing Application Note" Published September 2003, available online <http://www.anritsu.com/en-US/Downloads/Application-Notes/Application-Note/DWL1277.aspx> last accessed April 2014

- [32] S. P. Benham, D. P. Atkins, E. J. Totten, G.A. Pettitt and P. Cushnaghan, "Software Defined Antenna", IEEE Loughborough Antennas and Propagation conference, pp 489-492, November 2009
- [33] K. F. Harsh, Bingzhi Su, Wenge Zhang, Victor M. Bright, and Y. C. Lee. "The realization and design considerations of a flip-chip integrated MEMS tunable capacitor," A-Physical Sensors and Actuators, Vol. 80, no. 2 pp. 108-118, 2000.
- [34] M. Y. Frankel, J. F. Whitaker, G. A. Mourou, F. W. Smith, and A. R. Calawa, "High-voltage picosecond photoconductor switch based on low-temperature-grown GaAs," IEEE Transactions on Electron Devices, Vol. 37, no. 12 pp. 2493-2498, 1990.
- [35] W. C. Nunnally and R. B. Hammond, "Optoelectronic switch for pulsed power," in Picosecond Optoelectronic Devices, C. H. Lee, Ed. Orlando, FL: Academic Press, pp. 373-398, 1984.
- [36] F. K. Jondral, "Software-defined radio: basics and evolution to cognitive radio." EURASIP Journal on Wireless Communications and Networking, no. 3 pp. 275-283, 2005.
- [37] E. K. Kowalczyk, C. J. Panagamuwa and R. D. Seager, "Design and operation influences regarding rise and fall time of a photoconductive microwave switch," IEEE Loughborough Antennas and Propagation Conference (LAPC), pp. 149-154, 2013.
- [38] A. Karabegovic, R. M. O'Connell, and W. C. Nunnally, "Photoconductive switch design for microwave applications," IEEE Trans. Dielectrics and Electrical Insulation, vol. 16, No. 4, 2009
- [39] J. R. Flemish, and R. L. Haupt, "Optimisation of a photonicly controlled microwave switch and attenuator," IEEE transactions on microwave theory and techniques, vol. 58, No. 10, 2010.
- [40] Y. Tawk, S. Hemmady, C. G. Christodoulou, and G. Balakrishnan, "Measuring the transition switching speed of a semiconductor-based photoconductive

switch using RF techniques,” IEEE international Symposium on Antennas and Propagation, pp. 972-975, July 2011

- [41] R. Cory and D. Fryklund “Solid State RF/Microwave Switch Technology: Part 2” available online www.mpdigest.com, p.p. 34, published June 2009, last accessed July 2012.
- [42] Skyworks “AS179-92LF: 20 MHz-3.0 GHz GaAs SPDT Switch” datasheet available online <http://www.skyworksinc.com/uploads/documents/200176G.pdf>, last accessed October 2013
- [43] Skyworks “SKY12210-478LF: 0.9-4.0 GHz, 100 W High Power Silicon PIN Diode SPDT Switch,” datasheet available online <http://www.skyworksinc.com/uploads/documents/200176G.pdf>, last accessed October 2013
- [44] G. M. Rebeiz, and J. B. Muldavin. "RF MEMS switches and switch circuits," IEEE Microwave Magazine, Vol. 2, no. 4 pp. 59-71, 2001.
- [45] OSRAM LED datasheet “SFH 4232, IR LED Emitter, 850nm 120deg “available online <http://uk.rs-online.com/web/p/ir-leds/6811244/> last accessed June 2013.

6 Conclusions and Future Work

In this thesis the simulation, fabrication and performance of a photoconductive microwave switch is discussed and implemented as an optically controlled transmission line. To briefly summarise, the complete design cycle of the switch is considered in order to optimise and find strategies to best proceed with development of the switch, potentially as a commercial product. The benefit to using this switch is that it does not require metallic biasing lines to operate – meaning that the radiation pattern of the RF system is not compromised by the presence of the switch. In RF systems, especially antenna applications, the presence of metallic biasing lines are currently one of the disadvantages for commercial switches such as PIN diodes and Micro Electro-Mechanical Systems (MEMS) switches.

The analytical nature of photoconduction within semiconductors is discussed and then implemented in order to investigate conductivity profile with regards to varying radiant flux and wavelength. This profile is then applied to a simulation model in order to investigate the benefits of signal planarity as a packaging strategy. This is important if this switch is ever to be implemented in a RF product.

In order to realise a packaged switch, fabrication techniques are investigated in terms of interconnect method. These are implemented on an optimised transmission line topology along with an optimised die which includes a passivation layer. Finally, the switch is characterised – an important step which enables RF designers to make a decision on which switch to use for their application. The contributions and conclusions for this work are highlighted in the upcoming sections.

6.1 Auger term considered in generating conductivity profile

Semiconductor theory is considered when selecting a suitable material in order to maximise conductivity and hence provide a low insertion loss switch. Silicon wafers which are formed with high quality processing steps that create a high carrier lifetime are investigated analytically using equations that relate the quality of silicon and properties of the illumination to the carriers generated in the semiconductor. In Chapter 2, the addition of the Auger recombination term is factored into Platte's equation, as the number of carriers created in the silicon indicates that this form of recombination will have a significant effect on the carriers generated and hence the maximum conductivity of the silicon.

The main outcome is that the Auger term significantly decreases the conductivity of the silicon when compared to using the equation without this recombination term when higher levels of radiant flux are applied. However, the Auger recombination has little effect on a $1\text{mm} \times 1\text{mm} \times 0.3\text{mm}$ silicon sample which is illuminated by 10mW of radiant flux. If higher levels of radiant flux are being applied to control the switch, then the Auger recombination term should be considered for a more realistic conductivity profile.

Lastly, the wavelength of the light is also investigated for the silicon used in this thesis. It is demonstrated that for a given thicknesses of silicon there is a limited range of wavelengths that produce a maximum average conductivity. For example, for 0.3mm thick silicon, the ideal optical wavelength is 930nm and for 0.53mm thick silicon, it is 960nm. This highlights that the light source must be considered when designing the switch. Ideally a light source producing a wavelength between 900-1000nm will produce the highest average conductivity in the silicon.

6.2 Simulating packaging strategy based on conductivity profile

Chapter 3 also introduces an optimised transmission line design in order to maximise isolation in the OFF state and minimise insertion loss in the ON state. A transmission line that is a similar width as the silicon die is shown to maximise the switch's dynamic range in terms of transmission. A line which is slightly narrower than the die is ideal.

The conductivity profile generated with the inclusion of the Auger term is used to build up a simulation model for the photoconductive switch. This is of benefit for RF designers who want to accurately simulate the effect of the photoconductive switch in their antennas or RF systems. It is also necessary to understand the switch behaviour in order to design and optimise a package design for the photoconductive switch.

The simulation model includes a six layer dielectric die structure which is modelled with varying real and imaginary permittivity. A 200nm insulating vacuum layer is also included around the die to represent the passivation. This improves correlation between simulation and measurement at low frequencies (<500MHz). At higher frequencies (>5GHz), correlation between simulation and measurement is improved by simulating both SMA connectors. The designer will need to weigh the gains made by improved correlation over a broad bandwidth with the increase in simulation time. If the design specification is for a small bandwidth, it may be sufficient to omit the SMA connectors.

Having achieved reasonable agreement between simulation and measurement, the packaging aspect of the switch is investigated. The concept of planarity is investigated with relation to the conductivity profile. Here it is found that designing the switch with the highest conductivity in closest to the copper transmission line slightly reduces insertion loss by 0.18dB at 2GHz. However, when implementing the optical feed method practically, some of this advantage is negated, especially at higher frequencies.

The implementation of a Light Emitting Diode (LED) as the illumination source below the ground plane is investigated – LEDs much less sensitive to electrostatic discharge and are less expensive than laser diodes. However, high power LEDs also have a relatively large diameter which is found to degrade transmission performance due to the hole in substrate and ground plane required to accommodate them. Measurement of this setup also highlights that shadowing of transmission lines prevents maximum light delivery to the silicon die if the optical feed method is from below the silicon die. This could partly be addressed by aligning the optical feed to be at a 45° angle. This would provide a larger footprint in

terms of illumination area on the die whilst maintaining the same size hole in the substrate.

6.3 Analysing passivation and interconnect methods

Chapter 4 concentrates on the effect that passivation and carrier lifetime can have on switch performance. It is found that a high carrier lifetime is desirable when continuous wave illumination of the switch is implemented and minimum insertion loss is the goal. This is demonstrated by comparison of passivated (carrier lifetime $600\mu\text{s}$) and unpassivated silicon die ($13.4\mu\text{s}$). The reflectivity of the die is also demonstrated – the passivated die has a reflectivity of 15% compared to an unpassivated die of 35%. The passivated switch is more efficient as more photons enter the silicon due to this layer acting as an anti-reflection coating. Consequently applying the passivation reduces insertion loss by 0.5dB. If maximising transmission in the ON state is the goal then passivation of the silicon is an important fabrication step to consider.

A texturing technique is also applied to the silicon surface, which is successful in increasing the amount of light entering the silicon. It is also apparent that the reflection from the surface of the silicon is improved across a broader bandwidth of the light spectrum when compared to only applying an anti reflective coating which is targeted at one wavelength. Hence a broadband light source emitting white light could be used instead of a single wavelength laser source. However, the texturing also damages the silicon surface, potentially increasing the number of recombination sites in the silicon, which reduces the carrier lifetime. This technique also decreases the surface area of silicon which is in contact with the copper transmission line, which could potentially decrease signal coupling from transmission line to the silicon die, increasing insertion loss. Hence the use of this technique requires further refinement.

In order to explore packaging techniques further, gold contacts are fabricated onto the die using photolithography and evaporation techniques. This enables an investigation of surface mount techniques – replacing the silver loaded epoxy interconnect with a solder based interconnect. The solder is far more conductive than the silver epoxy and requires less preparation in terms of curing. It is found

that the soldering technique does not yield better transmission when compared to the epoxy method. This may be due to the difficulty in soldering the bare die to the transmission line which requires the use of flux which may contaminate the die.

In order to further investigate this, other methods of applying the gold contacts could be explored to verify if a better interconnect can be formed when compared to the silver epoxy method.

6.4 Linearity and switching time characterisation

Lastly, the single tone and two-tone linearity of the optimised photoconductive switch is presented. The single tone third order intercept is reported to be 74dBm. It is clear that the linearity performance is generally higher than PIN diodes, with a third order intermodulation product of 58dBm. The power handling is ~25W, making it suitable for use in systems where these levels of power are required. The linear response also indicates that this switch is ideal to use in applications which require signal distortion to be kept to a minimum.

The switching performance is dependent on ON-OFF voltage ratio, applied radiant flux, passivation and transmission line topology. Best transmission performance is achieved with a high ON-OFF voltage ratio, high radiant flux value, high quality passivation (long carrier lifetime) and small gap in transmission line. This leads to a switch on time of 19 μ s, which is one of the fastest times for all the switch types investigated. However, it also yields the longest switch OFF time, with a measured value of 89 μ s.

Clearly, there is a trade-off between low insertion loss and fast switching time. The benefit of the photoconductive switch is that applied radiant flux can easily be varied. Hence the RF designer can control both insertion loss and switching time depending on the importance of these criteria for the chosen certain application. More specifically, if transmission is to be maximised then a high radiant flux and high quality silicon with a small gap should be used. If switching time should be kept to a minimum, then a non passivated die should be used and ON-OFF ratio should be kept to a minimum (applied radiant flux should be kept low).

6.5 Future Work

Based on the research presented in this thesis the following sections discuss potential ways this research could be extended.

6.5.1 Transparent Materials and Silicon Processing Techniques

Further investigation of transparent substrates and metals could negate the need to drill holes in the substrate to realise an optical feed technique from below the silicon. It has been shown in this work, that these disruptions in the signal path can increase insertion loss. Hence if they can be avoided, the benefit of maintaining signal planarity can be realised without modifying the transmission line.

Texturing showed promising results in terms of allowing more photons to enter the silicon die. However one of the perceived problems was that the surface area of the silicon in touch with the transmission line is reduced. This could further be investigated by masking the underside of the silicon, so that the texturing is only applied to the surface of the silicon which is subjected to the illumination source. This should have the effect of reducing insertion loss.

6.5.2 Silicon Quality and Die Size

One of the factors which reduce the conductivity within the silicon is identified as the defects, which are created by the wafer sawing process which is required to manufacture the photoconductive switch. Potential ways to improve the quality at these surfaces, and hence increase effective carrier lifetime, is to process these edges after the sawing process. This could be done using a reactive ion etch process and further passivation techniques. Such processes are technically challenging and expensive to implement on small dice, but may yield better insertion loss performance when using low radiant flux.

Alternatively, larger die size could also be investigated. It is assumed that when photons are absorbed in the silicon and create free carriers, these carriers diffuse throughout and to the edges of the silicon, hence encountering trap sites at the sawn edges of the silicon. If the illumination is applied to the centre of a larger die, then there is less probability that the carriers diffuse to the trap sites at the edge of

the silicon die and recombine. This has the benefit of increasing effective carrier lifetime and hence increasing conductivity realised in the photoconductive switch.

6.5.3 Ohmic Contacts

Packaging techniques could further be explored through the type of contact formed, potentially benefitting performance and allowing easier integration of the switch into an RF system. Metallised ohmic contacts on the silicon could improve switch performance in terms of interconnection methods. A capacitive method of contact is investigated in this work, so as not to degrade the silicon quality through removal of the passivation layer. However, an ohmic contact could provide a signal path with less resistance and potentially a reduced insertion loss at low frequencies. This could be realised by employing a laser groove technique, as is common in the photovoltaic industry. This involves creating a groove on the silicon surface with a laser, doping the groove area and then electroplating the groove with multiple metal layers. An alternative doping process is ion implantation, which is a far more accurate way of achieving a particular doping profile.

6.5.4 Wire Bonding

Wire bonding should further be investigated. In this case, the die should be mounted on a more rigid substrate, such as alumina to perform the wire bonding. A more rigid structure will not absorb the ultrasonic energy used to form the wire bond connection. It is also critical to ensure contamination of the die and transmission line is kept to a minimum and that the materials used are compatible. The wire bonding process may be more successful when using a gold plated transmission line, which is compatible with standard gold wire bonds and the gold contacts on the silicon.

6.5.5 Characterisation

Further characterisation of the switch may also be investigated. Future work could involve investigating the effect different light sources have on the overall switching time of the photoconductive switch. In this thesis the rise and fall times have been investigated, however sometimes the switch time including the time taken for the light source to switch is of interest. The effect of different pulsing frequencies for the light source may also yield a similar performance to the continuous wave

illumination approach, but draw less current. This may provide further information on which illumination sources provide the fastest switch ON and OFF time and the best transmission performance with relation to current consumption.

Finally, this work has concentrated on the performance of an optically controlled transmission line. This work can be extended in terms of characterisation of linearity and switching time for different applications such as antennas and filters. This gives a better indication of how the switch performs in these structures and highlights the main benefit of using such a switch – the elimination of metallic biasing lines which can cause perturbation of the RF radiation performance.